SUBCRITICAL REACTIVITY MEASUREMENTS ON FUEL STORAGE ARRAYS IN THE DIMPLE REACTOR

A Thesis submitted for the award of the degree of Doctor of Philosophy of the University of London

by

John P Taggart, BSc

Nuclear Power Section
Department of Mechanical Engineering
Imperial College of Science and Technology

April 1988

ABSTRACT

The storage in skips of spent fuel from thermal reactors is an important aspect of the nuclear fuel cycle. It is necessary to evaluate methods for assessing the subcriticality of fuel storage arrays.

One method is the modified source multiplication technique, in which count rates from detectors in the subcritical array of interest are compared with count rates from a slightly subcritical, or reference array for which the subcriticality is known. It is necessary to use, additionally, calculated correction factors to account for differences in the neutron flux distributions in the arrays and to show their validity when the above differences are large.

Work on fuel skips in the DIMPLE reactor has shown that with the use of localised neutron sources and several detectors, the subcritical reactivity of arrays with k-eff in the range of 0.76-0.91 can be determined by the modified source multiplication technique to an accuracy of 7-10% standard deviation.

Two sets of axially spread sources provided neutrons. Count rates from detectors in fuel clusters were summed and for each configuration a single correction factor, calculated by diffusion theory was used. The correction factor appropriate to the entire fission rate in an array was shown to be well predicted. This allowed estimation of calculational systematic errors from the range of k-eff values given by individual in-cluster detectors. These errors were significant but the use of transport theory reduced them, giving an overall error slightly greater than that due to experiment. Also it was found that four radial source positions in different skip compartments are an improvement on two.

K-eff values for most of the arrays lie between transport and diffusion theory predictions. This behaviour is consistent with the respective estimation, by the calculations and experiment, of flux levels in different environments.

Acknowledgements

I would like to thank Dr C B Besant of the Department of Mechanical Engineering, Imperial College for his constant guidance and encouragement throughout this project.

Thanks are also due to many of the staff of AEE Winfrith, particularly Mr G Ingram, Mr J M Stevenson and Mr B M Franklin for many valuable discussions during the course of this work.

I am also grateful to the experimental staff of the DIMPLE reactor for their co-operation with the experimental work.

Finally I must express my thanks to Mrs L Alford and Mrs S White for the typing of this thesis.

CONTENTS

1. Introduction: Fuel Storage and the DIMPLE Reactor

1.1 Properties and Safety Considerations of Thermal Reactor Fuel Storage Systems

1.1.1 Storage of Spent Fuel

Prolonged use of thermal reactor fuel in a power reactor causes the build-up of fission products. Some of these are strong neutron absorbers, such as samarium 149 and xenon 135, and can cause significant deterioration in the performance of the reactor. The fuel must therefore be removed and purified, i.e. reprocessed, to remove these and other poisons. Before reprocessing, however, the fuel must be stored for a period. This is for several reasons (1):

(i) To allow the decrease of activity of certain transuranic nuclides;

(ii) To allow the decay of fission products, principally iodine 131 and xenon 135.

Typically, from a thermal reactor, many thousands of fuel pins are removed at a time for storage and reprocessing. During the storage period significant heat is generated from the spent fuel and it is necessary to submerge the pins in a coolant. The most convenient coolant, water, is also a moderator and tends to increase considerably the neutron production due to fission of an array of fuel pins.

In order to store large numbers of pins in compact spaces, use is made of fuel skips, containing inserts which are compartmental boxes with neutron-absorbing walls. The pins are generally placed in clusters inside cans, one can to a compartment in a skip.

A typical fuel storage skip, contained in a flask, is shown in Fig. 1.1. This skip is of the type used widely by the Central Electricity Generating Board. The concentration of natural boron in the skip insert walls is typically about 1%; an excessive concentration of natural boron in steel significantly reduces the strength of the steel.

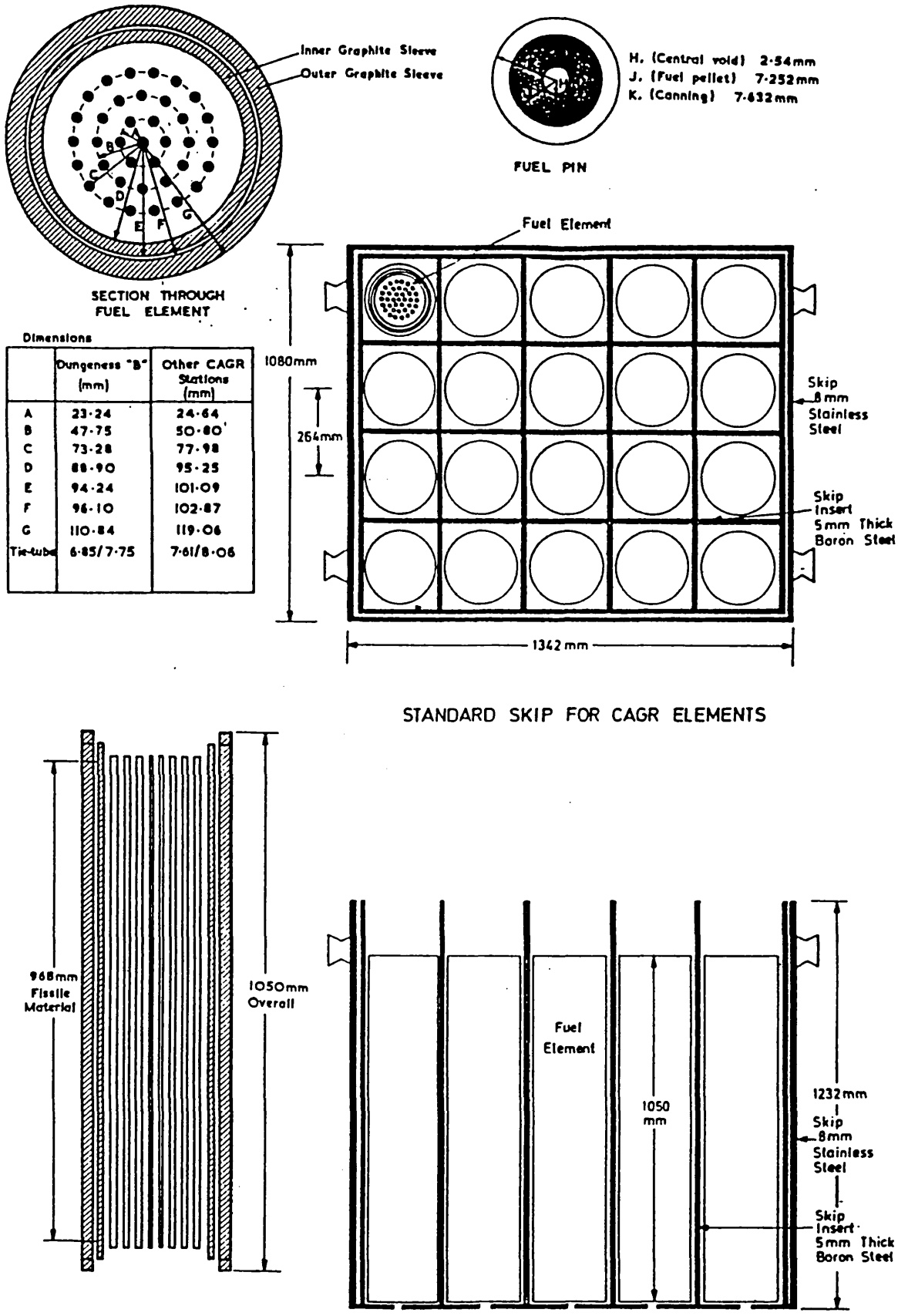

Fig. 1.1. Schematic of CAGR Skip and Skip Insert.

The walls are roughly 0.5cm thick, so an estimation can be made of their permeability to thermal neutrons.

Thermal absorption cross-section of boron 10≃4000 x 10^{-24} cm^2.

Number density of boron 10 in steel = (density of steel x proportion by weight of natural boron x proportion of boron 10 in natural boron/gram molecular weight of boron 10) x 6.03 x 10^{23} atoms cm^{-3}

$$= \frac{7.8 \times 0.01 \times 0.18}{10} \times 6.03 \times 10^{23} \text{ atoms } cm^{-3}.$$

Probability of transmission of neutron through absorber =
e $^{-}$(no. density x absorption cross-section x thickness)
= e^{-a} (where a = 4000 x 10^{-24} x 7.8 x 0.01 x 0.18 x 10^{-1}
x 6 x 10^{23} x 0.5) = 0.2.

Hence thermal neutrons are absorbed strongly in the boron steel. Fast neutrons, however, can penetrate it easily.

The cans are not necessarily restrained inside the compartments, so it is not necessarily the case that significant slowing-down occurs before fission neutrons reach the skip walls. The entire skip, encased in its outer shielding may be used in its fully loaded state to transport spent fuel elements to a reprocessing plant, and hence there is at least some likelihood of pins moving inside the skip during the storage period.

1.1.2 Neutron Populations in Spent Fuel

During the fission process in a thermal reactor, transuranic elements are produced. This is due largely to the following chain reactions (2):

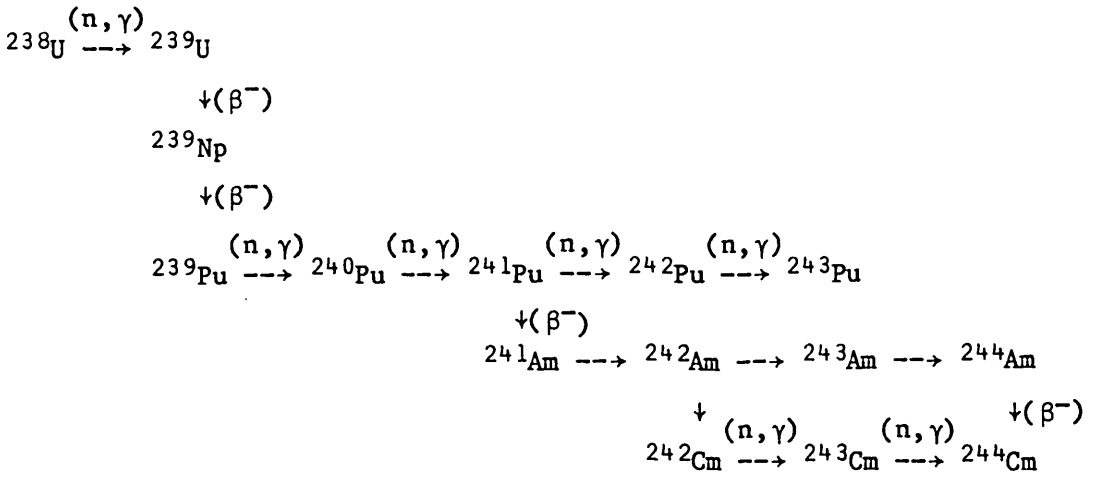

Uranium 238 has an absorption cross-section of about 10×10^{-24} cm^2 to thermal neutrons; it does not undergo fission at all with neutrons below about 1MeV. The product uranium 239 beta-decays through neptunium 239 to produce plutonium 239. Now plutonium 239 is an alpha particle emitter: certain nuclides such as oxygen 18 can undergo (α,n) reactions, producting neutrons. Plutonium 239 is transmuted to plutonium 240 and plutonium 241 by neutron absorption. Isotopes of americium and curium are then produced by successive beta-decay and neutron absorption.

Typically in spent thermal reactor fuel, the following proportions of transuranic nuclides, which are also significant spontaneous neutron emitters, are present (Table 1.1). Their half-lives for spontaneous fission, and neutrons per spontaneous fission are given also (3).

The total neutron emission per tonne is of the order of 5×10^7 s^{-1} (4).

Table 1.1 Significant Spontaneous Neutron Emitters in Spent Fuel

Nuclide	Proportion in Grams Per Tonne	$t_{\frac{1}{2}}$(Spontaneous Fission)
Pu238	23	4.9×10^{10} years
Pu240	1450	1.34×10^{11} years
Pu242	145	7.1×10^{10} years
Cm242	0.8	7.2×10^{6} years
Cm244	1.45	1.35×10^{7} years
Cm246	2×10^{-3}	1.7×10^{7} years

In spent thermal reactor fuel curium 242 and curium 244 are the dominant neutron sources. Typically a fuel skip might contain 1 tonne of spent fuel. The spontaneous source due to curium 244 is:

(mass of spent fuel in grams x proportion by mass of curium 242/gram atomic weight of curium 242) x 6.03×10^{23} x 0.7 x no. of neutrons produced in curium 242 fission/curium 242 half life ≈

$$= \frac{10^6 \times 0.8 \times 10^{-6}}{242} \times \frac{6.03 \times 10^{23} \times 0.7 \times 3.0 ns^{-1}}{7.2 \times 10^6 \times 3 \times 10^7} \approx 2 \times 10^7 ns^{-1}$$

Hence spent thermal reactor fuel is an appreciable neutron emitter. Assuming that irradiated fuel exists throughout the skip, then there will be an appreciable steady-state neutron flux level existing in it.

The flux level in the skip depends not only on the neutron source strength, however, but also on the neutron multiplication of the skip and its contents. A convenient measure of neutron multiplication is the k-eff value which can be defined loosely as the average number of neutrons produced for every neutron absorbed in, or leaking from the system.

Hence, S neutrons introduced into a system produce, in successive generations, S x k-eff, S x $(k\text{-eff})^2$, S x $(k\text{-eff})^3$ neutrons, and so on. The total number of daughter neutrons due to an initial number of neutrons, S, in a system with k-eff less than unity, is given by:

Total no. of daughter neutrons = S x k-eff + ... + S x $(k\text{-eff})^n$

$$= \frac{S \times k\text{-eff}}{1 - k\text{-eff}}. \qquad (1.1)$$

It is noticeable that a k-eff of unity gives a self-sustaining production of neutrons in successive generations. In this condition the system in question is said to be critical.

Depending on their history, Commercial Advanced Gas Reactor (CAGR) fuel elements typically have enrichments of 2-3%. It is possible in a CAGR skip to incorporate enough pins of 3% enrichment to achieve criticality (5). However, this requires pins to be evenly spread throughout the whole of every compartment. With pins in clusters, and separated from the compartmental walls by water gaps, values of k-eff appear to be in the range 0.7-0.9 (6).

1.1.3 Safety Considerations

The most important safety consideration is that the fuel storage array should not go critical. This is self-evident, but can be elaborated upon somewhat. Given that an array is subcritical, or possessing a k-eff of less than unity, is not sufficient; there must be a minimal chance that, in an accident situation, the array, by suffering an increment in k-eff, will become critical. It is possible in principle to place approximate probabilities on this, for a given array. Note that this probability does not necessarily become greater with increasing k-eff: it depends on the detailed geometry of the fuel storage array, and on operational considerations.

In order to nominate a fuel storage array as being within set safety limits, it is necessary to:

(i) Determine its k-eff value;
(ii) Show that the probability of criticality due to accident is low enough.

The first of these steps is the aim of this work. The k-eff value itself, however, is not measured directly. Experimentally the multiplication of neutrons over all generations is usually measured. This multiplication is characterised by a quanitity called reactivity which is related to the k-eff by the equation:

$$\rho = \frac{\text{k-eff} - 1}{\text{k-eff}}. \qquad (1.2)$$

Measurements of k-eff are thus, to be strict, referred to as reactivity measurements.

The second of the above criteria is covered to a moderate degree, experimentally; more extensive calculated evidence is available elsewhere (7,8).

Implicitly, it is important not only to have an experimentally derived value of k-eff, it is also important to be able to substantiate k-eff calculations which must of necessity take place before loading a skip.

On the face of it, due to the static geometry of a typical fuel storage array, the experimental determination of k-eff can include some reliance on supporting calculation. Clearly, however, in the general case, this must not be too great, since the range of possible accident situations must include the loading, by mistake, of increased enrichment fuel, for example, giving an unseen increase in k-eff.

Safety considerations concerning, for example, inherent source strengths, or mechanical considerations, may limit severely the range of experimental techniques available to measure k-eff.

It may also be desirable to have an approximate means of determining k-eff rapidly during loading of a skip. Such a means can scarcely rely on supporting calculation.

1.2 The DIMPLE Reactor and The Fuel Storage Arrays

1.2.1 The DIMPLE Reactor

Reactivity measurements were performed on mock-ups of actual fuel storage arrays in a reactor called DIMPLE. This is a zero-power, water-moderated reactor owned by the UKAEA and located at Winfrith in Dorset (9).

Figure 1.2 shows the construction of DIMPLE. Multiplying assemblies can be housed inside an aluminium tank, 2.6m in diameter and 4m high, contained within a steel-lined concrete block shield. Moderator is accommodated at shutdown in dump tanks, linked to the reactor tank by stainless-steel pipes through dump valves. The moderator can be heated, cooled or cleaned up by additional circuits.

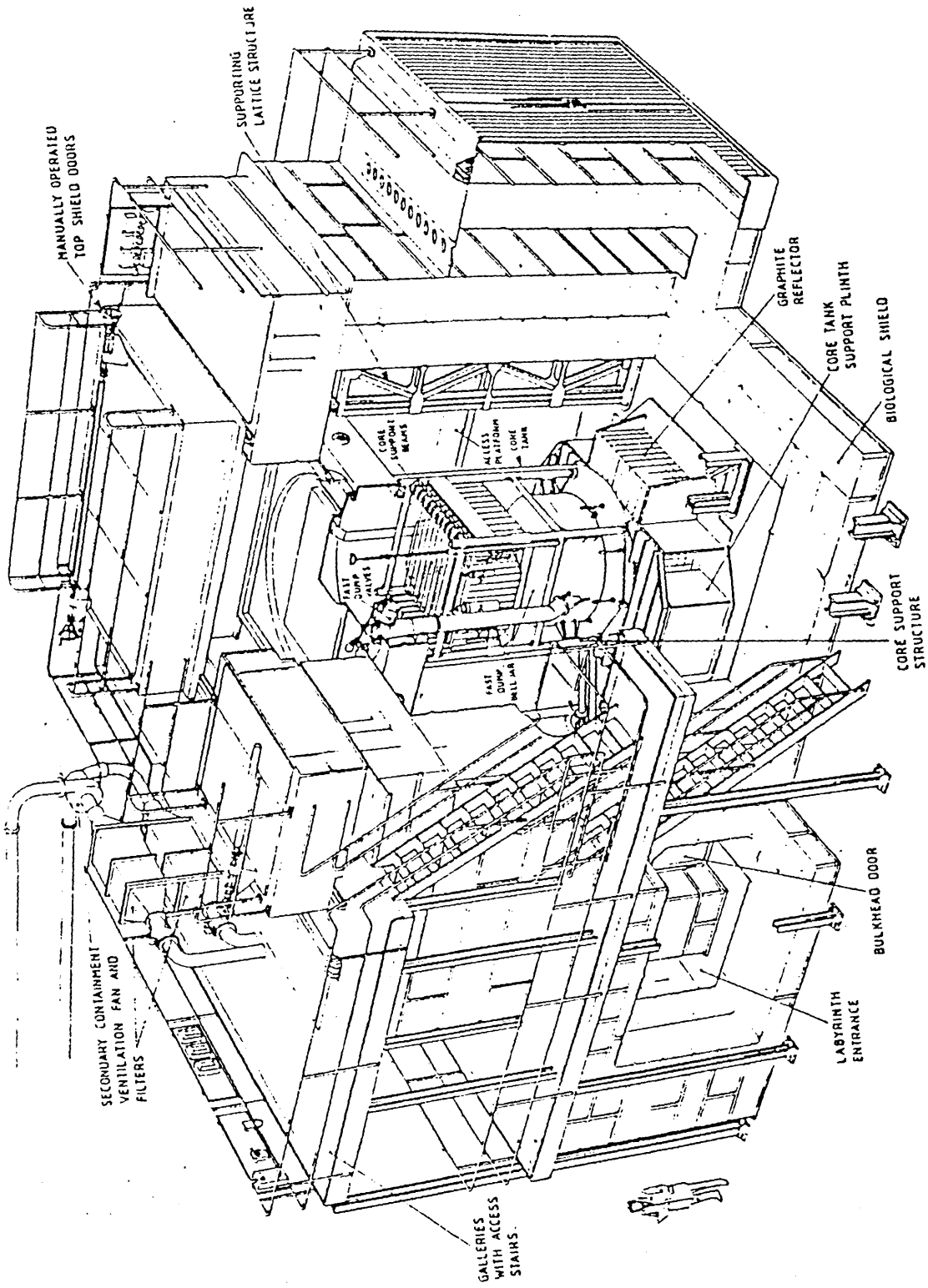

Fig. 1.2. General View of the DIMPLE Reactor.

To maintain clean-core geometries no control rod facilities exist in DIMPLE; reactivity changes over periods of seconds are made by adjustment of the moderator level in the tank. To achieve this, two pumps, one for large changes in level, ie greater than several centimetres, and one for small changes in level, ie less than several centimetres, are available. The water level is monitored by depth probes, the most precise of these, the precise level gauge (PLG), giving readings to ±0.1mm.

Reactor instrumentation consists of several boron detectors housed in submersible pods in the reactor tank. If any of these detectors gives a count rate corresponding to a predetermined maximum allowed fuel flux, or a count rate increase corresponding to a maximum allowed positive period, the reactor is automatically shutdown.

Shutdown is by means of a fast dump system which lowers the water level in the reactor tank by at least 10cm in 0.6 sec and 30 cm in about 1 sec.

U-shaped aluminium beams spanning the reactor tank support lattice plates which can house fuel pins in precise positions, and act as support for other components of assemblies placed in the tank.

1.2.2 The Fuel Storage Arrays

A CAGR fuel skip insert was placed in DIMPLE. This skip insert consisted of welded boron-steel plates ≈5mm thick and containing ~1% by weight of natural boron. The plates formed a 5 x 4 square compartmental box as in Figure 1.1. To accommodate the skip conveniently in the tank, it was necessary to shorten it axially to a height of about 70cm. Details of the skip insert dimensions and density are given in Table 1.2 (10).

The fuel pins, contained within the skip, consisted of 3% enriched uranium oxide fuel. The fuel was in pellet form, wrapped in adhesive aluminium foil, contained in stainless-steel cans with an inside radius

of 5.191mm and an outside radius of 5.462mm. The pellets extended over a height of 69cm and were retained by plugs at the top and bottom of the can. The pins were of half the cross-sectional area of CAGR pins. Details of their dimensions, material consituents, and the moderator surrounding them are given in Table 1.3 (10). The fuel was unirradiated and thus had negligible spontaneous neutron source strength.

No details here are given of the beams, the plugs of the cans or the reactor instrumentation, though details are contained in Ref. (11). All these components are known to have very little effect on the reactivity of the assemblies in DIMPLE (10).

Details of measurements on 6 fuel storage arrays built in DIMPLE are included in this work. These arrays were named SO2/A, SO2/B through to SO2/G. A list of them is given in Table 1.4. Diagrams of these six arrays are shown in Figs 1.3 to 1.8. Measurements were also performed on several further arrays. These additional measurements, however, do not affect the results of this work.

Table 1.2 Skip Dimensions, Density and Main Material Constituents

Density (g/cc)	Measurement	Dimension (mm)	Main Material Constituents (%)
7.81	Length	1323.3	B(natural):1.04
	Width	1059.5	Cr: 20.02
	Height	743.0	Fe: 67.33
	Wall Thickness	5.23	Ni: 9.91
	Compartmental Internal Width	258.4	Mn: 1.64

Table 1.3 Pin Dimensions, Densities and Main Material Constituents

Region	Density (g/cc)	Measurement Dimension (mm)	Main Material Constituents by Weight (%)
Fuel	10.45	Radius 5.062 Height 692.8	U238:85.37, U235:2.656 O:11.91
Aluminium foil, glue + gap	0.901	Radius 5.062→ 5.191	AL;84.73, C:12.76, H:2.13
Steel Can	7.80	Radius 5.191→5.462 Height 717.4	Fe:67.33, Ni:11.18, Cr:18.00 Mn:1.66, Ti:0.67, Al:0.25
Water	0.998	Height 768.0	O:88.81, H:11.19

Table 1.4 The Fuel Storage Arrays

Official Name	Description	Water Height(s) up Pins (cm)	Abbreviated Name
SO2/A (also SO2/F)	196 pins per compartment	49, 33	196/49, 196/33
SO2/B	112 pin clusters, centred	76	112/76 (CTD)
SO2/C	112 pin clusters, groups of four	76	112/76 (G4)
SO2/D	112 pin clusters, moved to skip centre	76	112/76 (CC)
SO2/E	112 pin clusters, moved to skip centre with 96 pins added	76	112/76 (CCD)
SO2/G	221 pin clusters, centred	76	221/76 (CTD)

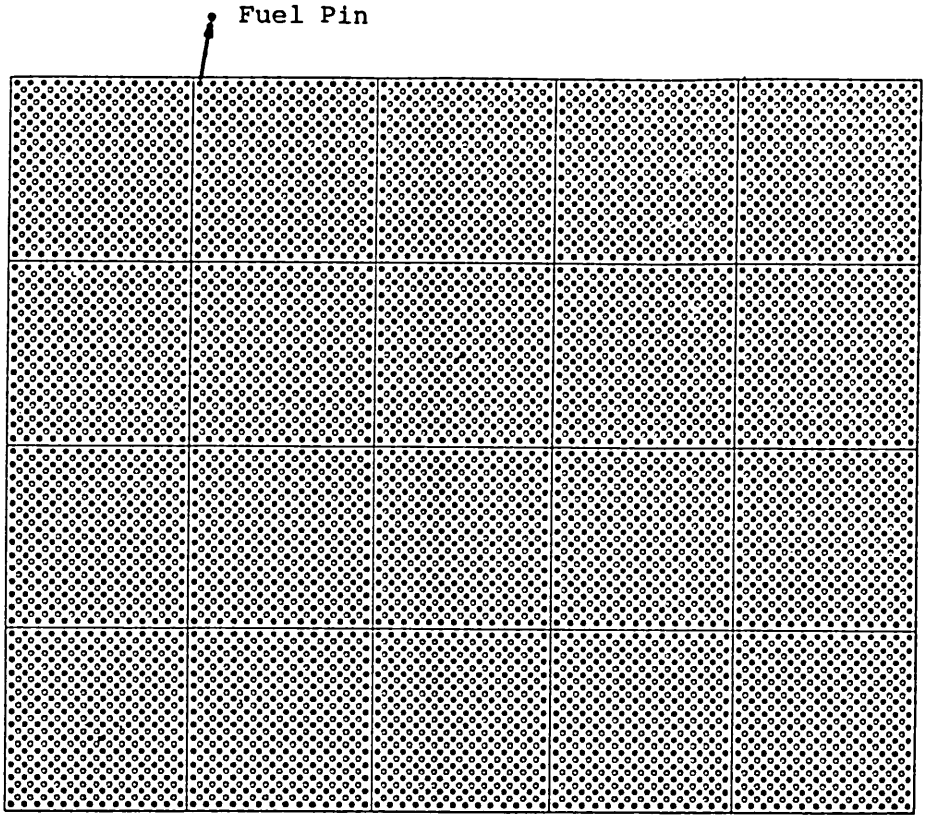

Fig. 1.3. 196 Pins Per Compartment Array.

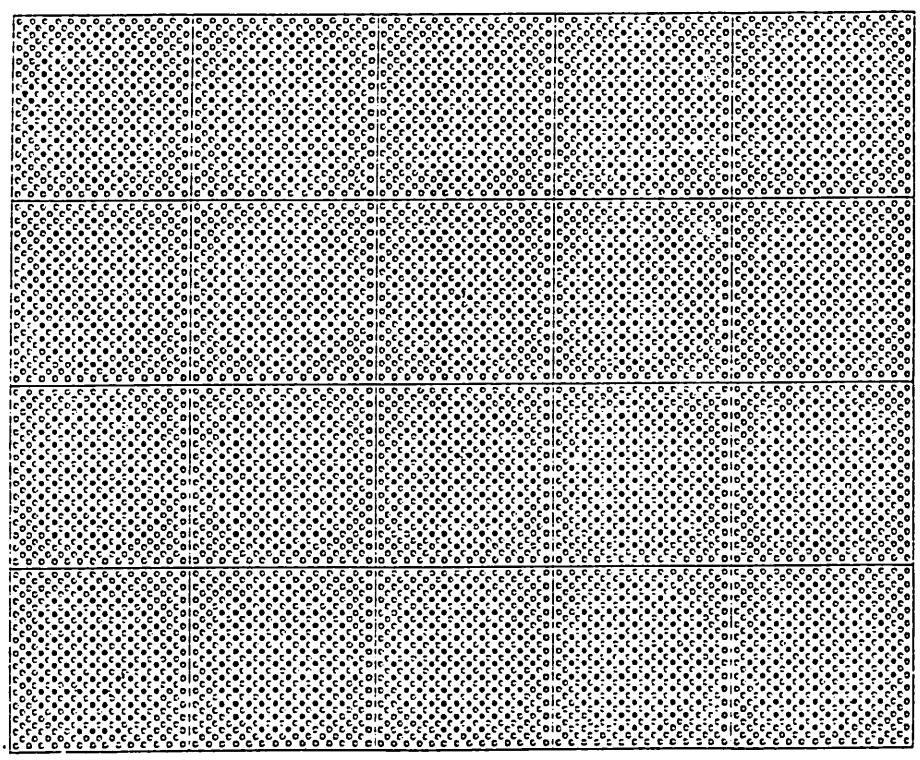

Fig. 1.4. 112 Pin Clusters, Centred Array.

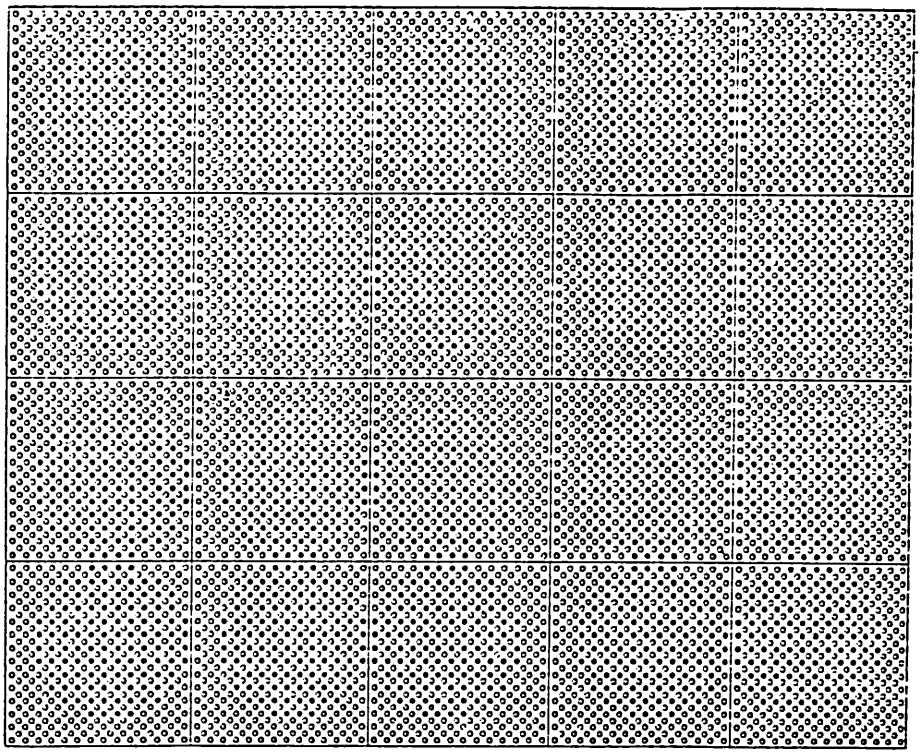

Fig. 1.5. 112 Pin Clusters, Groups-of-Four Array.

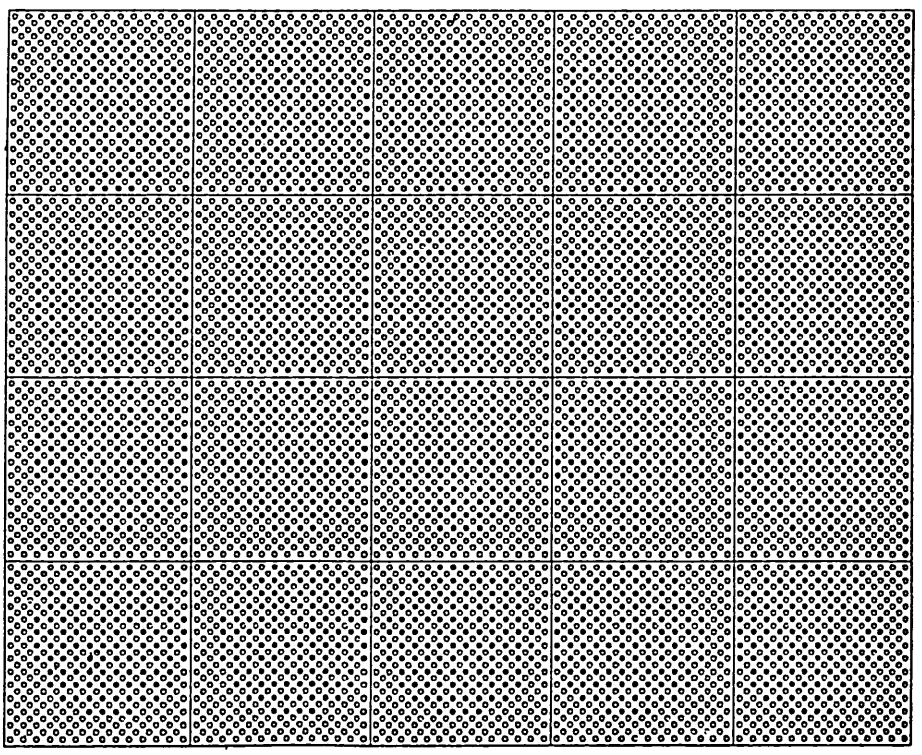

Fig. 1.6. 112 Pin Clusters, Closest-to-Centre Array.

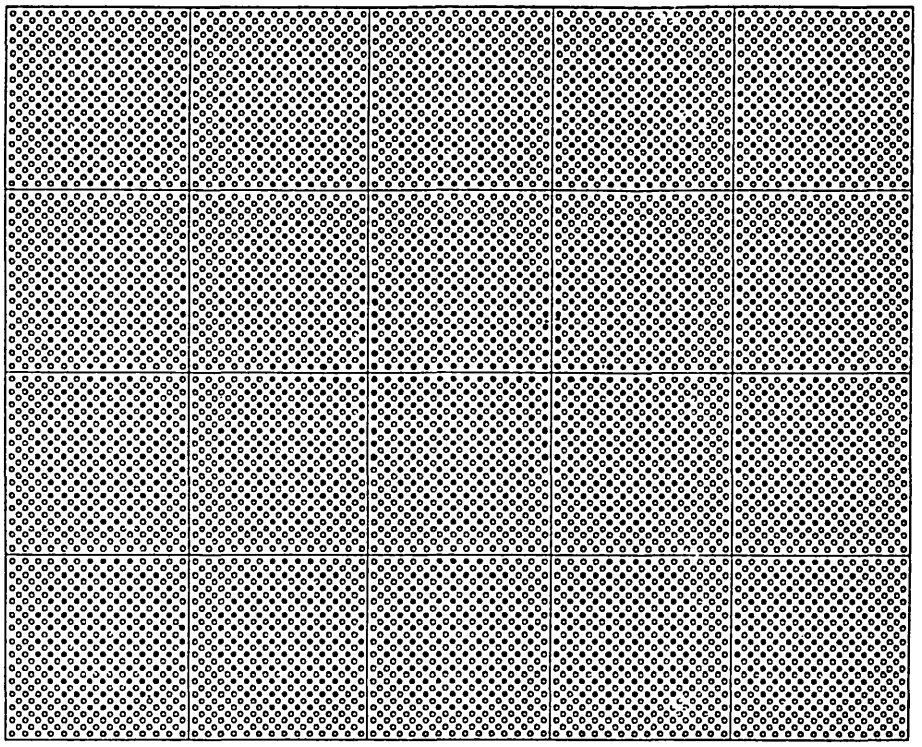

Fig. 1.7. 112 Pin Clusters, Dropped Pins Array.

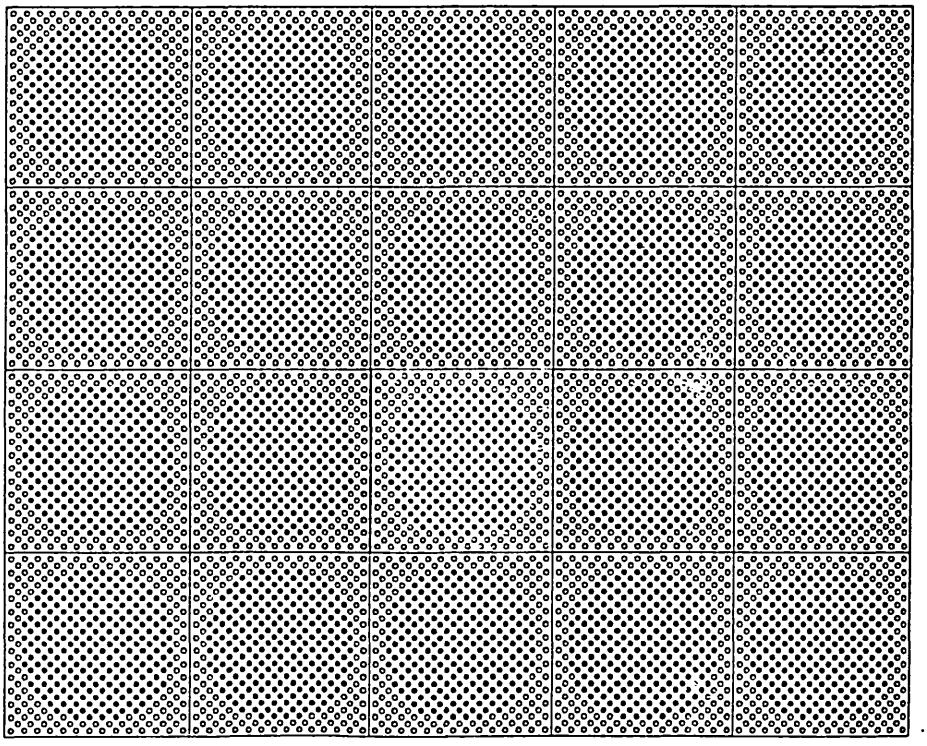

Fig. 1.8. 221 Pin Clusters, Centred Array.

Except for SO2/A and SO2/F all arrays were variants of a basic 112 or 221 pins per compartment array corresponding to 56 or 110 CAGR pin arrays. The pin pitch was 1.79cm in the 196 and 112 pins per compartment arrays and 1.2657cm in the 221 pins per compartment arrays. No steel cans were present around the clusters. The moderator height in all the 112 and 221 pins per compartment arrays was 76cm above the bottom of the fuel pins - hence 7cm of water was entirely above the fuel pins. Water extended also to an effectively infinite distance around and below the skip outer walls.

Three of the arrays (SO2/C, SO2/D and SO2/E) simulated possible accident situations in which clusters are slumped against skip compartmental walls after an impact of the skip. Of these, the array with dropped pins (SO2/E) simulated an accident situation in which extra pins are dropped into the centre of the skip.

The 196 pins per compartment array was the only array capable of being taken critical by use of moderator alone (5). By using a moderator height of 49cm up the fuel pins, a slightly subcritical version of this array was created for the measurements. A well-subcritical version of this array was created by lowering the moderator about 19cm from its critical height, that is, to 33cm up the fuel pins.

In the context of the measurements the arrays, with moderator included are referred to as 'configurations' since the term 'array' strictly refers to the arrangement of fuel pins alone. Abbreviated names for the configurations including the water height, are given in Table 1.4, these proving convenient in some of the tables in this work.

2. Concepts of Subcritical Reactor Theory

It has been stated that the purpose of this work was to measure the k-eff values of subcritical fuel storage arrays. Before describing the measurements it is necessary to give definitions of the fundamental physical parameters which characterise subcritical assemblies. A discussion is then made of the basic neutronic properties of such assemblies.

2.1 The Neutron Transport Equation, Linearity and Separation into Time- and Space-Dependent Parts

The neutron transport equation for the flux distribution in an assembly is (1):

$$\frac{1}{v}\frac{d\phi(r,E,\Omega,t)}{dt} + \Omega \cdot \nabla\phi(r,E,\Omega,t) + \Sigma_t(r,E)\,\phi(r,E,\Omega,t) =$$

$$\int_{4\pi} d\Omega' \int_0 dE' \Sigma_s(E' \to E, \Omega' \to \Omega)\,\phi(r,E',\Omega',t) +$$

$$\chi(E) \int_{4\pi} d\Omega' \int_0^\infty dE' \nu\Sigma_f(r,E')\,\phi(r,E',\Omega',t), \qquad (2.1)$$

where: $\phi(r,E,\Omega,t)$ is the angular flux at position r, energy E, angle Ω and time t;
$\Sigma_t(r,E)$ is the transport removal cross-section at r and E;
$\Sigma_s(E' \to E, \Omega' \to \Omega)$ is the scatter cross-section from (E',Ω') to (E,Ω); and
$\chi(E)$ is the emergence spectrum at E.

No imposed source term has been included; the definitions which follow refer to the assembly alone. Delayed neutrons have not been included explicitly.

If the assumption is made that burn-up is negligible, and that no mechanical change is being made to the assembly, then the cross-sections appearing in Equation 2.1 are essentially constant. The angular flux can be split into a space-dependent and a time-dependent part:

$$\phi(r,E,\Omega,t) = \phi(r,E,\Omega)\, n(t), \tag{2.2}$$

where: $\phi(r,E,\Omega)$ is the space and energy dependent flux shape which remains constant; and

$n(t)$ is the level of the flux which tends to change with time.

Substituting Equation 2.2 into Equation 2.1 and multiplying throughout by $\frac{v}{n(t)\phi(r,E,\Omega)}$ gives:

$$\frac{1}{n(t)}\frac{dn(t)}{dt} = \frac{v}{\phi(r,E,\Omega)}\left[-\Omega\cdot\underline{\nabla}\phi(r,E,\Omega) - \Sigma_t(r,E)\,\phi(r,E,\Omega)\right.$$

$$+ \int_{4\pi} d\Omega' \int dE'\ \Sigma_s(E'\rightarrow E, \Omega'\rightarrow\Omega)\,\phi(r,E'\Omega')$$

$$\left. + \chi(E)\int_{4\pi} d\Omega' \int_0^\infty dE'\ \nu\Sigma_f(r,E')\,\phi(r,E'\Omega')\right]. \tag{2.3}$$

The left hand side of Equation 2.3 is dependent on time only whereas the right hand side is dependent only on position, energy and angle. Both sides are thus equal to a constant. Writing this constant as λ results in

$$\frac{1}{n(t)}\frac{dn(t)}{dt} = \lambda \text{ or } n(t) = n(o)e^{\lambda t}. \tag{2.4}$$

The constant λ is called the time eigenvalue of the linear system.

The spatial part of the equation can be written:

$$\Omega\cdot\underline{\nabla}\phi(r,E,\Omega) + \Sigma_t(r,E)\,\phi(r,E,\Omega) + \frac{\lambda}{v}\,\phi(r,E,\Omega)$$

$$= \int_{4\pi} d\Omega' \int_0^\infty dE'\,\Sigma_s(E'\rightarrow E, \Omega'\rightarrow\Omega)\,\phi(r,E',\Omega') +$$

$$\chi(E)\int_{4\pi} d\Omega' \int_0^\infty dE'\ \nu\Sigma_f(r,E')\,\phi(r,E',\Omega'). \tag{2.5}$$

This equation, characterising the distribution of neutrons in a linear assembly, is equivalent to the transport equation for a fictitious assembly with no time dependence, and with identical properties aside from the provision of an extra absorption term. Only in an assembly with time eigenvalue zero is the extra absorption term also zero.

2.2 Modal Solutions

Equation 2.5 in fact has an infinite, though non-analytical, series of solutions for $\phi(r,E,\Omega)$. These solutions have been shown to be orthogonal (2) and in many cases to form a complete set (3). No general proof of completeness of the eigenfunctions has yet been found, though there are physical reasons to believe that they form such a set. Equation 2.5 can thus be rewritten using $\phi_n(r,E,\Omega)$ where n is the index of the eigenfunction:

$$\Omega\cdot\nabla\phi_n(r,E,\Omega)+\Sigma_t(r,E)\,\phi_n(r,E,\Omega)+\frac{\lambda}{v}\phi_n(r,E,\Omega)$$

$$= \int_{4\pi} d\Omega' \int_0^\infty dE' \; \Sigma_s(E'\to E,\Omega'\to\Omega)\,\phi_n(r,E',\Omega') +$$

$$\chi(E)\int_{4\pi} d\Omega' \int_0^\infty dE' \,\nu\Sigma_f(r,E')\,\phi_n(r,E',\Omega') \qquad (2.6)$$

The solutions ϕ_n are referred to as modes, or harmonics. Only one of the modes has positive values over the whole assembly and thus a separate physical existence. It is called the fundamental mode. It has the largest time eigenvalue (Equation 2.4); the time eigenvalues decrease with increasing n, or number of zero-crossing regions between the boundaries of the assembly (4): eventually merging into a continuum:

$$\lambda_0 > \lambda_1 > \ldots\ldots\ldots\ldots > \lambda_n \quad \ldots \qquad (2.7)$$

A schematic diagram of the first three flux modes of an assembly is shown in Fig. 2.1.

Modes other than the fundamental are often referred to as 'higher modes'. Often, use is made of the terms 'radial modes' and 'axial modes'. These refer to assemblies whose geometry is constant over their height. Functions characterising flux distributions can thus be split into the product of two functions, one giving the radial, and the other the axial distribution.

2.3 Neutron Multiplication

The modal neutron multiplication per generation, k_n, is equal to the quotient of the total neutron production and the total neutron absorption plus leakage for the flux distribution $\phi_n(r,E,\Omega)$:

$$k_n = \frac{\langle \chi(E) \int_{4\pi} d\Omega' \int_0^\infty dE' \; \nu\Sigma_f(r,E')\phi_n(r,E',\Omega') \rangle}{\langle \Omega \cdot \underline{\nabla}\phi_n(r,E,\Omega) + \Sigma_a(r,E)\phi_n(r,E,\Omega) \rangle} . \qquad (2.8)$$

The brackets denote integration over all position, energy and angle. Note that scatter takes no part in the overall production or loss of neutrons from the system, so that Σ_t, the transport removal cross-section has become the absorption cross-section, Σ_a.

Hence there exists an infinite series of values of k_n, each corresponding to a time eigenvalue λ_n. k_0, the multiplication per generation characterising a fundamental mode distribution in the assembly, is the largest, while the others decrease with increasing n, merging into a continuum. Generally the neutron multiplication per generation of the fundamental mode is significantly greater than that of any of the higher modes. This results from the fact that the flux gradients and hence neutron leakage increases sharply when the number of zero-crossing regions increases from nought (Fig. 2.1). The parameter

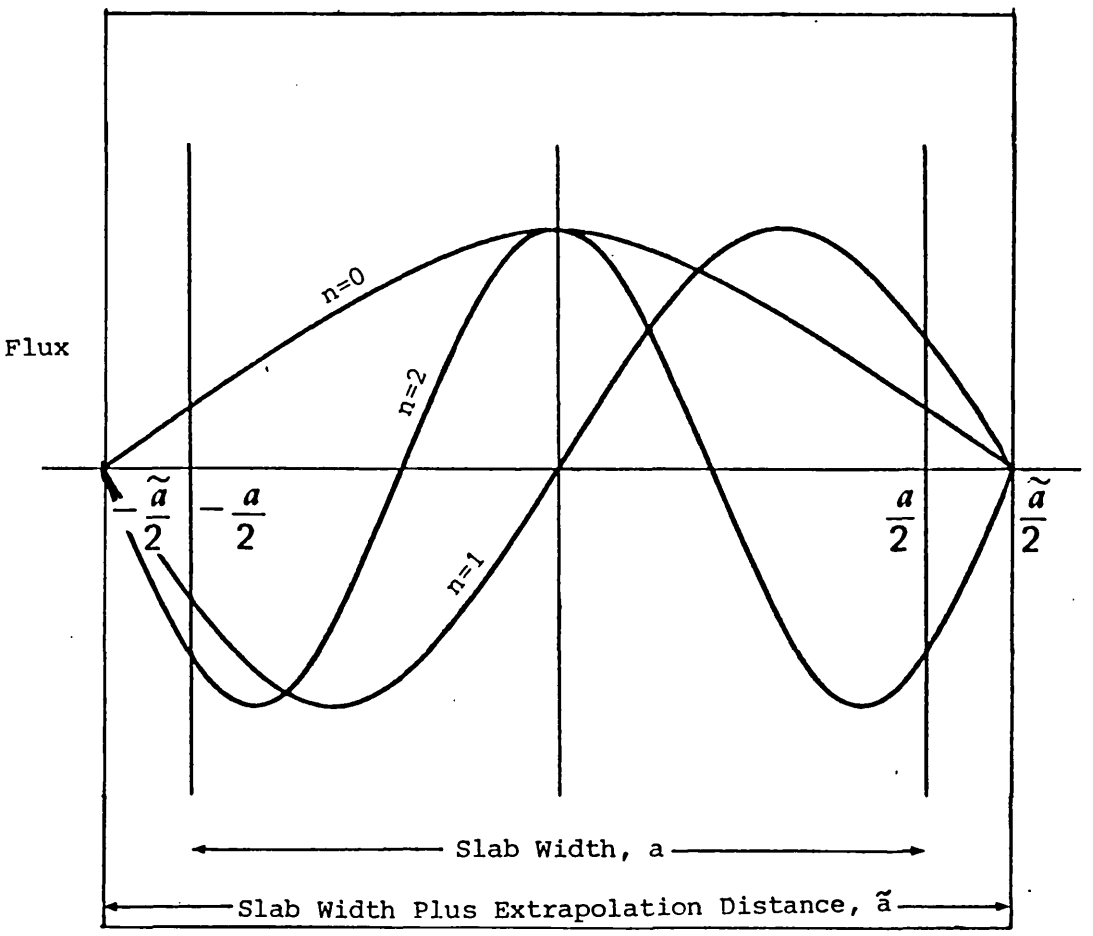

n=0: Fundamental Mode.

n=1: First Higher Mode.

n=2: Second Higher Mode.

Fig. 2.1. The First Three Flux Modes For a Slab Geometry.

k_0 is usually simply called 'k-effective' or 'k-eff'. This is a more rigorous definition of k-eff than that given in Chapter 1. Note that it is only correct to describe the multiplication per generation of a neutron distribution in terms of the k-eff value if that distribution is the fundamental mode.

It must be noted that the neutron multiplication per generation is not an eigenvalue of the neutron transport equation. In neutronics calculations, an assembly is usually characterised by a simplified form of the following eigenvalue equation:

$$\Omega \cdot \underline{\nabla} \phi'(r,E,\Omega) + \Sigma_t(r,E)\,\phi'(r,E,\Omega) =$$

$$\int_{4\pi} d\Omega' \int_0^\infty dE'\ \Sigma_s(E' \to E, \Omega' \to \Omega)\,\phi'(r,E',\Omega') +$$

$$\frac{1}{k}\,\chi(E) \int_{4\pi} d\Omega' \int_0^\infty dE'\ \nu\Sigma_f(r,E')\,\phi'(r,E',\Omega'). \qquad (2.9)$$

This is often referred to as an eigenvalue mode equation. It differs from the static form of the neutron transport equation (Equation 2.5) in that the time absorption term has been replaced by an artificial multiplication of the fission source. Clearly the reciprocal of the eigenvalue ($^1/k$) can, from Equation 2.9, be expressed in the form of Equation 2.8. However, it is characterised by the artificial fundamental mode distribution ϕ', which is not by definition the same as the fundamental mode distribution, ϕ, in the neutron transport equation.

This disparity between the definitions of neutron multiplication per generation in reactor calculations and in the true physical situation is further discussed in the next chapter.

2.4 Criticality and the Definition of a Subcritical Assembly

The criticality of an assembly is defined in terms of the fundamental mode neutron multiplication per generation or k-effective. If k-eff >1, the assembly is supercritical, if k-eff = 1 the assembly is critical and if k-eff <1 all higher mode multiplications are also less than one and hence the neutron distribution, which is composed of a linear superposition of modes, since they form a complete set, tends to decrease with successive generations. A subcritical assembly is thus one in which any distribution of neutrons tends, if left to itself, to die away with time.

By Inequality 2.7, the fundamental mode tends to die away more slowly than the higher modes; for this reason it is often referred to as the persisting mode.

2.5 Modal Reactivity

The modal reactivity, ρ_n, of an assembly is the net production of neutrons divided by the total production of neutrons per generation in that assembly:

$$\rho_n = \frac{\langle \chi(E) \int_{4\pi} d\Omega' \int_0^\infty dE' \nu\Sigma_f(r,E') \phi_n(r,E',\Omega') - \Omega \cdot \underline{\nabla} \phi_n(r,E,\Omega) - \Sigma_a(r,E) \phi_n(r,E,\Omega) \rangle}{\langle \chi(E) \int_{4\pi} d\Omega' \int_0^\infty dE' \nu\Sigma_f(r,E') \phi(r,E',\Omega') \rangle} . \tag{2.10}$$

ρ_n thus bears a simple relationship to the modal neutron multiplication per generation, k_n:

$$\rho_n = \frac{k_n - 1}{k_n} \tag{2.11}$$

The fundamental mode reactivity is often referred to as the static reactivity, or simply reactivity, ρ.

$$\rho = \frac{\text{k-eff} - 1}{\text{k-eff}}. \qquad (2.12)$$

In a subcritical assembly all the modal reactivities are negative, since k-eff, and hence all other values of k_n are less than unity, and the static reactivity thus has the smallest absolute value.

In Chapter 1, the static reactivity was mentioned as characterising the multiplication of neutrons summed over all generations in a subcritical assembly. Due to the fact that the static reactivity relates to the k-eff alone, this is only the case when a fundamental mode is present in isolation. In the following sections, a general expression for the multiplication of neutrons in a subcritical assembly for a non-fundamental mode distribution is derived. It will be shown that the modal reactivities play an important part in this expression.

2.6 Introduction of Sources into a Subcritical Assembly

The inclusion of a steady state source term $S(r,E,\Omega)$ in the transport equation (Equation 2.1) results in:

$$\frac{1}{v}\frac{d\phi}{dt}(r,E,\Omega,t) = -\Omega\cdot\underline{\nabla}\phi(r,E,\Omega,t) - \Sigma_t(r,E)\,\phi(r,E,\Omega,t)$$

$$+ \int_{4\pi} d\Omega' \int_0^\infty dE' \Sigma_s(E'\to E,\Omega'\to\Omega)\,\phi(r,E',\Omega',t)$$

$$+ \chi(E) \int_{4\pi} d\Omega' \int_0^\infty dE' \nu\Sigma_f(r,E')\,\phi(r,E',\Omega',t) + S(r,E,\Omega). \qquad (2.13)$$

If the assembly is subcritical then the terms on the right hand side of the above equation, which are dependent on neutron flux must have a net negative value since the flux distribution is a superposition of modes which, left to themselves, tend to die away with time (section 2.4).

The introduction of the source causes the magnitude of the flux in the assembly to increase initially. This continues until the terms dependent on flux, which are negative, balance the source term. A steady state flux distribution is thus reached in the assembly, governed by the following equation:

$$-\Omega\cdot\underline{\nabla}\phi(r,E,\Omega)-\Sigma_t(r,E)\phi(r,E,\Omega)$$

$$+\int_{4\pi}d\Omega'\int_0^\infty dE'\Sigma_s(E'\rightarrow E,\Omega'\rightarrow\Omega)\phi(r,E',\Omega')+$$

$$\chi(E)\int_{4\pi}d\Omega'\int_0^\infty dE'\nu\Sigma_f(r,E')\phi(r,E',\Omega')+S(r,E,\Omega). \qquad (2.14)$$

The flux distribution characterised by Equation 2.14 can be expanded as a linear sum of the flux modes of the assembly, since they form a complete set:

$$\phi(r,E,\Omega)=\sum_n n_n\phi_n(r,E,\Omega). \qquad (2.15)$$

2.7 Importance

The expansion coefficients, or levels, n_n of the flux modes in a subcritical assembly can be found using any complete set of eigenfunctions mutually orthogonal to the flux eigenfunctions ϕ_n; there is one set, the importance eigenfunctions, which have this property and hence enable determination of n_n. The importance of a neutron at r,E,Ω,t, or $\phi^*(r,E,\Omega,t)$ is defined as its expected or probable contribution to a future meter reading (4). The importance can be shown to obey the equation which is adjoint to Equation 2.1 (4). The adjoint equation for a linear system has an orthogonal and complete set of eigenfunctions $\phi_n^*(r,E,\Omega)$. Moreover, the eigenfunctions $\phi_n^*(r,E,\Omega)$ are mutually orthogonal with $\frac{1}{v}\phi_n(r,E,\Omega)$ (1):

$$\langle\phi_n^*(r,E,\Omega)\frac{1}{v}\phi_m(r,E,\Omega)\rangle=0 \text{ for } n\neq m. \qquad (2.16)$$

By the definition of importance above, each importance eigenfunction ϕ_m^* is the contribution of a neutron distribution to some imaginary detector distribution. By choosing an arbitrary flux distrubtion $\phi = \Sigma n_n \phi_n$ it is possible to determine what this detector distribution is:

$$<\phi_m^*(r,E,\Omega)\ \frac{1}{v}\ \phi(r,E,\Omega)> = <\phi_m^*(r,E,\Omega) \sum_n n_n\ \frac{1}{v}\ \phi_n(r,E,\Omega)>$$

$$= <\phi_m^*(r,E,\Omega) n_m\ \frac{1}{v}\ \phi_m(r,E,\Omega)> \text{ by Equation 2.16}$$

$$= n_m <\phi_m^*(r,E,\Omega) \frac{1}{v}\ \phi_m(r,E,\Omega)>. \qquad (2.17)$$

If ϕ_m and ϕ_m^* are normalised so that $<\phi_m^*(r,E,\Omega)\ \frac{1}{v}\ \phi_m(r,E,\Omega)> = 1$ then, from Equation 2.17, $<\phi^*_m(r,E,\Omega)\ \frac{1}{v}\ \phi\ (r,E,\Omega)> = n_m$ which is merely the level of the m^{th} mode. So the m^{th} importance mode is merely the contribution of any arbitrary flux distribution $\phi(r,E,\Omega)$ to the m^{th} flux mode. Note that the normalisations of ϕ_m^* and ϕ_m are entirely arbitrary: their normalisation is accompanied by a dependent normalisation of the level n_m.

2.8 Modal Flux Distribution in a Subcritical Assembly in the Presence of a Steady State Source

The neutron transport equation (Equation 2.1) can be rewritten, with the inclusion, for completeness, of delayed neutron and source terms, as:

$$\frac{1}{v}\ \frac{d\phi}{dt}(r,E,\Omega,t) + (\Omega\cdot\underline{\nabla} + \Sigma_t(r,E))\phi(r,E,\Omega,t)$$

$$= \int_{4\pi} d\Omega' \int_0^\infty dE' \Sigma_s(E'\to E, \Omega'\to\Omega)\,\phi(r,E',\Omega',t)$$

$$+ (1-\sum_{i=1}^{D'} \beta_i)\chi(E) \int_{4\pi} d\Omega' \int_0^\infty dE'\, \nu\Sigma_f(r,E')\,\phi(r,E'\Omega',t)$$

$$+ \sum_{i=1}^{D'} \lambda_i C_i(r,E,\Omega,t) + S(r,E,\Omega), \qquad (2.18)$$

where: B_i is the neutron fraction in the i^{th} delayed neutron group;

D' is the number of delayed neutron groups;

λ_i is the decay constant of the i^{th} delayed neutron group; and

C_i is the precursor concentration for the i^{th} delayed neutron group.

An expression for the level of each mode is now derived from the above equation. The derivation follows the same lines as that in Ref. (5) which is simplified in that a diffusion theory equation for the fundamental mode only has been used. It should be noted that the following derivation results in point kinetics equations for the flux level.

Multiplying Equation 2.18 by $\phi_m^*(r,E,\Omega)$ and integrating over all space, energy and angle:

$$<\phi_m^*(r,E,\Omega,)\frac{1}{v}\frac{d\phi(r,E,\Omega,t)}{dt}> = <\phi_m^*(r,E,\Omega)\left[\left(-\Omega\cdot\underline{\nabla}-\Sigma_t(r,E)\right)\phi(r,E,\Omega,t)\right.$$

$$+\int_{4\pi}d\Omega'\int_0^\infty dE'\,\Sigma_s(E'\rightarrow E,\Omega'\rightarrow\Omega)\,\phi(r,E',\Omega',t)$$

$$+(1-\sum_{i=1}^{D'}\beta_i)\,\chi(E)\int_{4\pi}d\Omega'\int_0^\infty dE'\,\nu\Sigma_f(r,E')\,\phi(r,E',\Omega',t)$$

$$\left.+\sum_{i=1}^{D'}\lambda_i C_i(r,E,\Omega,t)+S(r,E,\Omega)\right]>. \qquad (2.19)$$

Using orthogonality, and dividing throughout by the importance-weighted spatial function $\langle \phi_m^*(r,E,\Omega) \frac{1}{v} \phi_m(r,E,\Omega) \rangle$ gives the level of the m^{th} mode alone on the left hand side:-

$$\frac{dn_m(t)}{dt} = \langle \phi_m^*(r,E,\Omega) \left[\left(-\Omega \cdot \underline{\nabla} - \Sigma_t(r,E)\right) \phi_m(r,E,\Omega) n_m(t) \right.$$

$$+ \int_{4\pi} d\Omega' \int_0^\infty dE' \Sigma_s(E' \rightarrow E, \Omega' \rightarrow \Omega) \phi_m(r,E',\Omega') n_m(t)$$

$$+ (1 - \sum_{i=1}^{D'} \beta_i) \chi(E) \int_{4\pi} d\Omega' \int_0^\infty dE' \nu\Sigma_f(r,E') \phi_m(r,E',\Omega') n_m(t)$$

$$\left. + \sum_{i=1}^{D'} \lambda_i C_i(r,E,\Omega) + S(r,E,\Omega) \right] \rangle \; / \; \langle \phi_m^*(r,E,\Omega) \frac{1}{v} \phi_m(r,E,\Omega) \rangle . \quad (2.20)$$

Taking into account the fact that (scatter in - transport out) = (scatter in - (scatter out + absorption)) = (-absorption) when integration over all space, energy and angle occurs, the above can be written:

$$\frac{dn_m(t)}{dt} = \langle \phi_m^*(r,E,\Omega) \left[\left(-\Omega \cdot \underline{\nabla} - \Sigma_a(r,E)\right) \phi_m(r,E,\Omega) n_m(t) \right.$$

$$+ (1 - \sum_{i=1}^{D'} \beta_i) \chi(E) \int_{4\pi} d\Omega' \int_0^\infty dE' \nu\Sigma_f(r,E') \phi_m(r,E',\Omega') n_m(t) + \sum_{i=1}^{D'} \lambda_i C_i \; (r,E,\Omega)$$

$$\left. + S(r,E,\Omega) \right] \rangle \; / \; \langle \phi_m^*(r,E,\Omega) \frac{1}{v} \phi_m(r,E,\Omega) \rangle . \quad (2.21)$$

The sum of the first three terms on the right hand side of Equation 2.21 giving the leakage, absorption and prompt neutron production can be related to the m^{th} modal reactivity of the assembly, if they are divided by the prompt neutron production instead of the neutron population. Accordingly, Equation 2.21 can be written:

$$\frac{dn_m(t)}{dt} = \langle \phi_m^*(r,E,\Omega) \left[\left(-\Omega\cdot\underline{\nabla} - \Sigma_a(r,E)\right)\phi_m(r,E,\Omega) n_m(t) \right.$$

$$\left. + \left(1-\sum_{i=1}^{D'} \beta_i\right)\chi(E) \int_{4\pi} d\Omega' \int_0^\infty dE' \nu\Sigma_f(r,E')\phi_m(r,E',\Omega') n_m(t) \right] \rangle$$

$$/ \langle \phi_m^*(r,E,\Omega)\chi(E) \int_{4\pi} d\Omega' \int_0^\infty dE' \nu\Sigma_f(r,E')\phi_m(r,E',\Omega') \rangle$$

$$\times \frac{\langle \phi_m^*(r,E,\Omega)\chi(E) \int_{4\pi} d\Omega' \int_0^\infty dE' \nu\Sigma_f(r,E')\phi_m(r,E',\Omega') \rangle}{\langle \phi_m^*(r,E,\Omega) \frac{1}{v} \phi_m(r,E,\Omega) \rangle}$$

$$+ \frac{\langle \phi_m^*(r,E,\Omega)\lambda_i C_i(r,E,\Omega) \rangle}{\langle \phi_m^*(r,E,\Omega) \frac{1}{v} \phi_m(r,E,\Omega) \rangle} + \frac{\langle \phi_m^*(r,E,\Omega) S(r,E,\Omega) \rangle}{\langle \phi_m^*(r,E,\Omega) \frac{1}{v} \phi_m(r,E,\Omega) \rangle} \cdot \quad (2.22)$$

Equation 2.22 for the m^{th} mode level can be simplified to an equation involving the m^{th} modal reactivity, the prompt neutron generation time and the contribution of the delayed neutrons and the imposed source. Firstly the terms before the multiplication sign on the right hand side are equivalent to the m^{th} modal reactivity if the subtraction of the delayed neutrons is ignored:

$$\frac{\langle \phi_m^*(r,E,\Omega)\left[\left(-\Omega\cdot\underline{\nabla}-\Sigma_a(r,E)\right)\phi_m(r,E,\Omega)+\chi(E)\int_{4\pi} d\Omega' \int_0^\infty dE' \nu\Sigma_f(r,E'\Omega')\phi_m(r,E',\Omega')\right]\rangle}{\langle \phi_m^*(r,E,\Omega)\chi(E)\int_{4\pi} d\Omega' \int_0^\infty dE' \nu\Sigma_f(r,E')\phi_m(r,E'\Omega')\rangle}$$

$= \rho_m$ as in Equation 2.10 (4).

The delayed neutron term which is subtracted is merely the importance-weighted fraction of fission neutrons which are delayed. This can be defined as βeff_m, the effective delayed neutron contribution for the m^{th} mode.

$$\beta eff_m = \frac{\langle \phi_m^*(r,E,\Omega)\sum_{i=1}^{D'} \beta_i \chi(E) \int d\Omega' \int dE' \nu\Sigma_f(r,E')\phi_m(r,E',\Omega')\rangle}{\langle \phi_m^*(r,E,\Omega)\chi(E) \int d\Omega' \int dE' \nu\Sigma_f(r,E')\phi_m(r,E',\Omega')\rangle} \qquad (2.23)$$

also, the quotient $\dfrac{\langle \phi_m^*(r,E,\Omega)\chi(E)\int_{4\pi} d\Omega' \int_0^\infty dE' \nu\Sigma_f(r,E')\phi_m(r,E'\Omega')\rangle}{\langle \phi_m^*(r,E,\Omega)\frac{1}{v}\phi_m(r,E,\Omega)\rangle}$

when multiplied top and bottom by the m^{th} modal level n_m, becomes m^{th} modal (effective production rate/effective population), or 1/neutron generation time, ℓ_m^*, for the m^{th} mode.

The last two terms in Equation 2.22 are merely the effective precursor concentration decay rate and effective source strength in the m^{th} mode:

$$C_{ieffm}(t) = \frac{\langle \phi_m^*(r,E,\Omega)\ C_i(r,E,\Omega)\rangle}{\langle \phi_m^*(r,E,\Omega)\frac{1}{v}\phi_m(r,E,\Omega)\rangle}, \qquad (2.24)$$

$$\text{and} \quad S_{effm} = \frac{\langle \phi_m^*(r,E,\Omega)\ S\ (r,E,\Omega) \rangle}{\langle \phi_m^*(r,E,\Omega)\ \frac{1}{v}\ \phi_m(r,E,\Omega) \rangle}. \tag{2.25}$$

Equation 2.21 thus becomes:

$$\frac{dn_m(t)}{dt} = \left[\frac{\rho_m - \beta_{effm}}{\ell_m^*} \right] n_m(t) + \lambda_i C_{ieffm}(t) + S_{effm}. \tag{2.26}$$

By similar reasoning, it can be shown that the corresponding equation for delayed neutron terms is (5):

$$\frac{dC_{ieffm}(t)}{dt} = \frac{\beta_{ieffm}}{\ell_m^*}\ n_m(t) - \lambda_i C_{ieffm}(t). \tag{2.27}$$

Equations 2.26 and 2.27 are merely the general modal forms of the reactor point kinetics equations.

For a subcritical reactor with a steady-state source, after the initial transient has died away,

$$\frac{dn_m(t)}{dt} = \frac{dC_{ieffm}(t)}{dt} = 0 \text{ and so } n_m = -\frac{S_{effm}\ell_m^*}{\rho_m}, \tag{2.28}$$

$$\text{or, } n_m = -\frac{\langle \phi_m^*(r,E,\Omega)\ S\ (r,E,\Omega) \rangle}{\langle \phi_m^*(r,E,\Omega)\chi(E)\int_{4\pi} d\Omega' \int_0^\infty dE'\, \nu\Sigma_f(r,E')\phi_m(r,E',\Omega') \rangle} \times \frac{1}{\rho_m}.$$

The level, n_m in Equation 2.28, is dependent on the normalisation of ϕ_m; however, the total flux is not dependent on this normalisation:

$$\phi(r,E,\Omega) = \sum_m n_m \phi_m(r,E,\Omega) =$$

$$\sum_{m(-\rho_m)} \frac{1}{} \quad \frac{\langle \phi_m^*(r,E,\Omega)S(r,E,\Omega) \rangle}{\langle \phi_m^*(r,E,\Omega)\chi(E)\int_{4\pi} d\Omega' \int_0^\infty dE'\, \nu\Sigma_f(r,E')\phi_m(r,E',\Omega') \rangle}\ \phi_m(r,E,\Omega). \tag{2.29}$$

This is the equation for the total flux distribution in a subcritical assembly with a steady state source. It can be seen that the flux distribution consists of a superposition of modes. Each mode has a level proportional to the contribution of the source distribution to that mode. The level of each mode is also inversely proportional to the modal reactivity; this expresses the multiplication of neutrons in that mode.

2.9 Basic Characteristics of Flux Distributions in Subcritical Assemblies

In an assembly with k-eff just less than 1, it is generally the case that the multiplication of the fundamental mode $(1/\rho_0)$ is much greater than the multiplication of each of the higher modes, since the higher modes are generally characterised by values of k_n significantly less than the k-eff. This in turn results from the significantly larger flux gradients occurring in the higher modes, giving greater neutron leakage (Fig. 2.1). Hence the fundamental mode flux distribution may dominate even for a source distribution which is itself very different from a fundamental mode. Now the fundamental mode distribution in an assembly tends to be spread over the fissile regions. Hence for the fuel storage configurations in DIMPLE a localised source distribution was expected to be very different from the fundamental mode distribution. However, if the subcritical reactivity is sufficiently low, the flux distribution due to such a source will be a fundamental mode distribution.

The physical significance of the above is that whatever the initial source distribution, its resultant fission chain is long enough to spread into the persisting neutron distribution of the assembly, provided the subcritical reactivity is sufficiently low.

For assemblies which are far from critical, the level of the fundamental mode is not, in general, so dominant and may not even dominate at all. Hence the flux distribution is likely to be significantly different from a fundamental mode, unless the source distribution itself is close to a fundamental mode distribution. This can be explained as follows.

Higher modes have both positive and negative regions over an assembly, (Fig. 2.1), and their levels can be small if the source distribution is spread over the whole assembly. A highly localised source, however, will give a significant contribution of higher mode flux contamination. This manifests itself usually in a high flux fall-off away from the source: the higher modes tend to have a positive contribution to the flux close to the source, and a negative contribution far away from it.

This situation occurs when the average length of the fission chains is significantly smaller than the linear dimensions of the fissile regions of the assembly. The length of the fission chains is determined both by the neutron multiplication and the mean distance each neutron travels from birth to absorption. The root-mean-square distance travelled by a neutron from birth to capture is equal to six times the migration length squared (6). For example, in a well-subcritical, water-moderated assembly such as some of the assemblies built in DIMPLE, the average length of the fission chains is likely to be only a small multiple of the migration length which is about 6cm for water (7), and probably no more than 8cm for the fuel and water environment existing in some of the DIMPLE assemblies, amounting to say 30cm altogether. This compares with the length of the skip which is in the region of 1 metre (Table 1.2).

In Fig 2.2 are schematic diagrams of flux distributions in two subcritical assemblies, one just subcritical and the other well subcritical.

It is convenient to refer to a subcritical assembly in terms of its fundamental mode reactivity, or alternatively its k-eff, since this directly expresses the departure of the assembly from criticality in terms of neutron multiplication per generation, even though the fundamental mode may not be an easily attainable neutron distribution for that assembly.

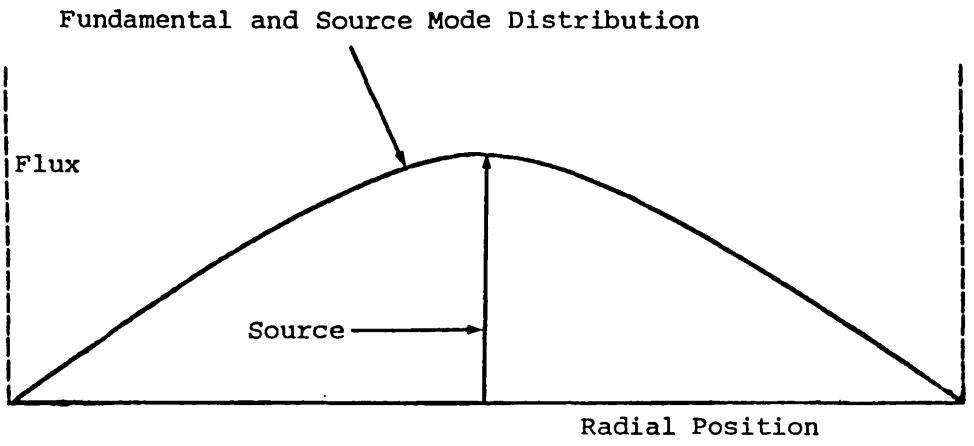

Slightly Subcritical Assembly.

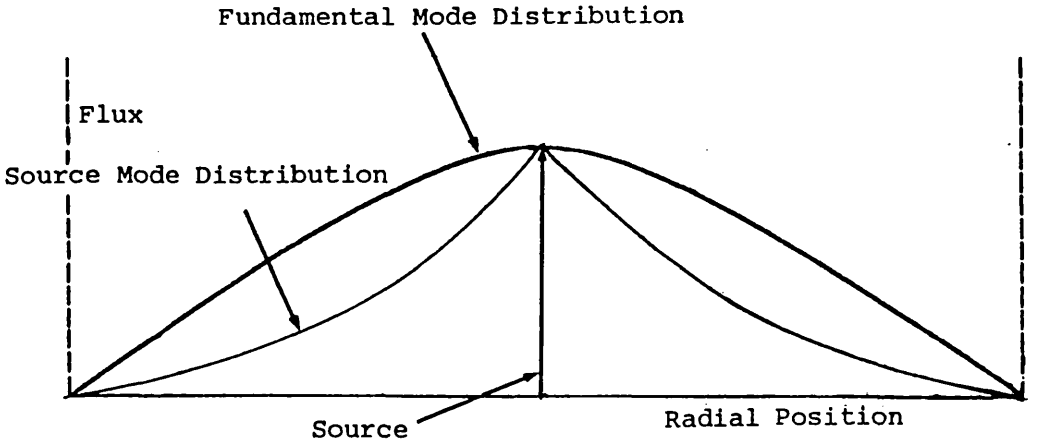

Well-Subcritical Assembly.

Fig. 2.2. Flux Distributions in Subcritical Assemblies (Schematic).

3. Introduction to the Subcritical Reactivity Measurements

In this chapter the aims of the subcritical reactivity measurements in DIMPLE are described fully. The theory of the techniques used for the measurements are explained; this follows to a large extent from the derivation of the flux level in a subcritical assembly in section 2.8.

3.1 The Aims of the Measurements

The experimental program on the fuel storage arrays had, essentially, three aims:-

(i) To determine experimentally the values of k-eff for the storage arrays in question, and thus to validate a technique for this determination.

(ii) To compare these k-eff values with those produced from calculation.

(iii) To examine the feasibility of producing a plant instrument to monitor subcritical reactivity (1).

Regarding the first aim, it is clear that a range of techniques exist, in principle, for determining the degree of subcritical reactivity (2). It was decided to concentrate largely on the modified source multiplication, or MSM technique (3), for several reasons:

(i) The hardware required is very simple, being no more than sources and detectors capable of location in and around the skip.

(ii) The technique had been demonstrated successfully on assemblies with k-eff as low as 0.9 (3). However, there appeared to be no systematic validation of the technique for well-subcritical assemblies. As will be seen, the provision of such a validation is a principal part of this thesis.

It was thought probable that reliable values of k-eff would not be forthcoming from any of the other techniques. Capabilities for producing noise correlation functions existed (4) and it was planned to gather some more of this type of data from the skip arrays.

Due to time limitations, none of the other techniques (2) were explored. Nevertheless, it was expected that the use of the modified source multiplication technique would provide valuable data in an application in which experimental data is scarce.

Regarding the second of the above aims, it is important to have prior knowledge of the criticality properties of a fuel storage array before loading and this must come from calculation, assuming no previous experimental data is available for that array. The skip insert experiments gave a very good chance to test the accuracy of calculational methods. For all the configurations studied, it was aimed to produce calculations using diffusion theory, transport theory and Monte Carlo methods to determine which would produce the most accurate k-eff values. Additionally, results from detectors in different environments could give information on the performance of these calculations in modelling neutron transport in skip type geometries.

The final aim was largely conceptual in nature: actual fuel storage arrays used by the CEGB and British Nuclear Fuels differ from the fuel storage arrays in DIMPLE in that in general a significant spontaneous source is present in the fuel and constraints on placing of sources and detectors may be strict. The experience gained in the application of modified source multiplication and noise correlation function techniques could be used to produce recommendations of methods for monitoring subcritical reactivity. This might be an instrument which would produce k-eff values without resort to a calculated model of the assembly, or in view of the fact that storage arrays are static in nature, one which places reliance on calculated parameters.

Incorporated within these general aims are subsidiary aims; these will be discussed with the description of the implementation of the subcritical reactivity measurements (Chapter 4).

Since the subcritical reactivity measurements used primarily the modified source multiplication technique, the noise measurements are not included in this thesis. They will be described fully in a document in preparation.

3.2 The Modified Source Multiplication Technique

3.2.1 Derivation

In section 2.8, the modal flux level in a subcritical assembly was expressed in terms of the reactivity, effective source strength and prompt neutron generation time. Any determination of fundamental mode reactivity and hence the k-eff ideally involves a fundamental mode neutron distribution only; considering for the moment the fundamental mode only (Equation 2.28):

$$\rho = - \frac{Seff\ \ell^*}{n}. \qquad (3.1)$$

The count rate of a detector in the assembly can be expressed in terms of the flux level, n:

$$CR = \int_{v\ detector} \int_{o}^{\infty} \int_{4\pi} \Sigma_{det}(r,E) n \phi(r,E,\Omega) dr\ dE\ d\Omega, \qquad (3.2)$$

where: CR is the count rate of the detector; and
Σ_{det} is the macroscopic neutron detection cross-section and integration has been made over the detector volume.

An expression for the flux level n can be derived as follows.

Firstly $CR.\ell^* =$

$$\frac{\int_{v\ detector} \int_{o}^{\infty} \int_{4\pi} \Sigma_{det}(r,E) n \phi(r,E,\Omega) dr\ dE\ d\Omega\ \langle \phi^*(r,E,\Omega) \frac{1}{v} \phi(r,E,\Omega) \rangle}{\langle \phi^*(r,E,\Omega) \chi(E,\Omega) \int_{4\pi} d\Omega' \int_{o}^{\infty} dE'\ \nu\Sigma_f(r,E') \phi(r,E',\Omega') \rangle}$$

$$= \frac{n.\int_{v\ \text{detector}} \int_{o}^{\infty} \int_{4\pi} \Sigma_{det}(r,E) n\phi(r,E,\Omega) dr\ dE\ d\Omega \cdot \langle \phi^*(r,E,\Omega) \frac{1}{v}\ \phi(r,E,\Omega) \rangle}{\langle \phi^*(r,E,\Omega) \chi(E,\Omega) \int_{4\pi} d\Omega' \int_{o}^{\infty} dE'\ \nu\Sigma_f(r,E') n\phi(r,E',\Omega') \rangle} \cdot \tag{3.3}$$

Now ϕ and ϕ^* have arbitrary normalisations; these can be made so that

$$\langle \phi^*(r,E,\Omega) \frac{1}{v}\ \phi(r,E,\Omega) \rangle\ = 1, \tag{3.4}$$

$$\text{and } \langle \phi^*(r,E,\Omega) \chi(E,\Omega) \int_{4\pi} d\Omega' \int_{o}^{\infty} dE'\ \nu\Sigma_f(r,E') \phi(r,E',\Omega') \rangle$$

$$= \langle \chi(E,\Omega) \int_{4\pi} d\Omega' \int_{o}^{\infty} dE'\ \nu\Sigma_f(r,E) \phi(r,E',\Omega') \rangle. \tag{3.5}$$

Hence:-

$$\text{CR.}\,\ell^* = \frac{n.\int_{v\ \text{detector}} \int_{o}^{\infty} \int_{4\pi} \Sigma_{det}(r,E) n\phi(r.E,\Omega) dr\ dE\ d\Omega}{\langle \chi(E,\Omega) \int_{4\pi} d\Omega' \int_{o}^{\infty} dE'\ \nu\Sigma_f(r,E') n\phi(r,E,\Omega,) \rangle} \cdot \tag{3.6}$$

Now the detector efficiency, $W = \dfrac{\text{detector count rate}}{\text{assembly fission rate}}$

$$= \frac{\int_{v\ \text{det}} \int_{o}^{\infty} \int_{4\pi} \Sigma_{det}(r,E) n\phi(r,E,\Omega) dr\ dE\ d\Omega}{\int_{v\ \text{assembly}} \int_{o}^{\infty} \int_{4\pi} \Sigma_f(r,E) n\phi(r,E,\Omega) dr\ dE\ d\Omega}. \tag{3.7}$$

and the mean number of neutrons per fission, $\bar{\nu}$ =

$$\frac{\text{assembly neutron production rate}}{\text{assembly fission rate}}.$$

$$= \frac{\int_{v\ \text{assembly}} \int_{o}^{\infty} \int_{4\pi} \nu\Sigma_f(r,E) n\,\phi(r,E,\Omega) dr\ dE\ d\Omega}{\int_{v\ \text{assembly}} \int_{o}^{\infty} \int_{4\pi} \Sigma_f(r,E) n\,\phi(r,E,\Omega) dr\ dE\ d\Omega} . \qquad (3.8)$$

Inserting Equation 3.7 and Equation 3.8 into Equation 3.6 gives:

$$CR.\ell^* = \frac{n.W}{\bar{\nu}} \text{ or } n = \frac{CR.\ell^*.\bar{\nu}}{W} . \qquad (3.9)$$

Hence the flux level n has been related to a count rate in the assembly.

Putting Equation 3.9 into Equation 3.1:

$$\rho = -\frac{S_{eff}\ W}{\bar{\nu}\ CR} . \qquad (3.10)$$

This is the basic source multiplication equation. The reactivity is expressed as the quotient of the effective source strength and the neutron production rate, or the inverse multiplication of the source. With a knowledge of detector efficiency, effective source strength and mean number of neutrons per fission, the reactivity of an assembly can be related to an experimental count rate.

3.2.2 Need for a Calibration

It is, however, difficult to obtain directly a calculated value of the factor $\frac{WS_{eff}}{\bar{\nu}}$ for several reasons:

(i) The efficiency of a detector depends on its absolute sensitivity which in turn depends on the amount of detection material within it. This is not usually well known for any given detector.

(ii) The detector itself makes a localised perturbation to the neutron flux. Perturbations involving localised changes in flux are usually difficult to calculate accurately.

(iii) The strength of the imposed or spontaneous source in an assembly is not usually well known.

Both conditions (i) and (iii) can be met, by separate calibrations, though (ii) cannot easily be circumvented by direct experimental methods.

Fortunately, it is possible to eliminate all the above difficulties, by means of a close-to-critical calibration. The reactivity of a slightly subcritical configuration can be obtained by making use of delayed neutron effects in the kinetic behaviour. In addition an experimental count rate can be obtained by imposing a steady-state source on the slightly subcritical configuration.

Choosing the suffix '1' for the slightly subcritical configuration: and '2' for the subcritical assembly, for which the reactivity is to be determined gives:

$$\rho_1 CR_1 = -\left(\frac{WS_{eff}}{\bar{\nu}}\right)_1 \text{ which is determined experimentally.} \quad (3.11)$$

$$\text{Obviously, } \rho_2 CR_2 = -\left(\frac{WS_{eff}}{\bar{\nu}}\right)_2 = \rho_1 CR_1 \left(\frac{\rho_2 CR_2}{\rho_1 CR_1}\right). \quad (3.12)$$

The quotient $\left(\frac{\rho_2 CR_2}{\rho_1 CR_1}\right)$ which is required instead of $\rho_2 CR_2$ does not depend on detector sensitivity, detector perturbation, or source strength, provided they are common to both assemblies, ie:

(i) The same detector is used in both slightly subcritical and unknown assemblies.

(ii) The detector has the same local environment in both assemblies.

(iii) Both assemblies are driven by the same source.

This quotient is thus much more easily calculated than the term $(\frac{WS_{eff}}{\bar{\nu}})$.

The source multiplication equation (Equation 3.10) thus becomes, using the experimental values of ρ_1 and CR_1:

$$\rho_2 = \rho_{1\ expt} \left(\frac{\rho_2 CR_2}{\rho_1 CR_1}\right)_{calc} \times \frac{CR_{1expt}}{CR_{2expt}}. \qquad (3.13)$$

Equation 3.13 is called the 'modified source multiplication equation'.

Henceforth in this work, an assembly for which the reactivity is to be determined is called an 'unknown subcritical assembly' or a 'well-subcritical assembly'. The slightly subcritical configuration is termed the 'reference configuration' since it is being referred to in the determination of the reactivity of the unknown subcritical assembly. The term $\left(\frac{\rho_2 CR_2}{\rho_1 CR_1}\right)_{calc}$ is termed the 'correction factor'. In the modified source multiplication equation (Equation 3.13) the reactivity of the unknown subcritical configuration is first given experimentally by an expression containing a calibrated reactivity and a ratio of the count rates. This expression is then modified by a correction factor which accounts for the change of detector efficiency and effective source strength between the reference and unknown subcritical configurations. The steps necessary for the determination of modified source multiplication reactivity are illustrated schematically in Figure 3.1.

It is evident from the derivation of the modified source multiplication equation that the reactivity of a subcritical assembly is given individually by each of any number of detectors. This fact is of importance in any practical modified source multiplication measurement, as will be shown presently.

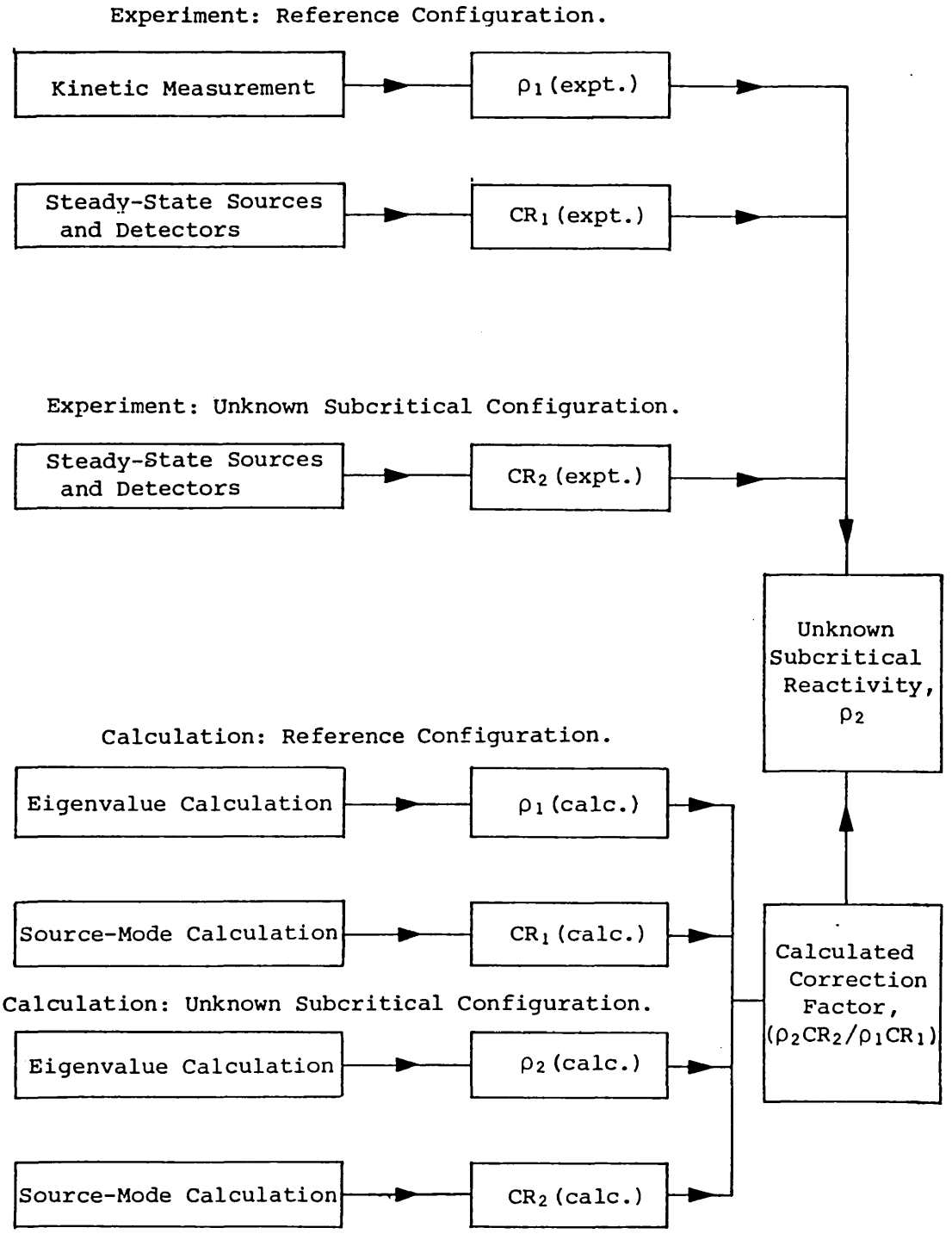

Fig. 3.1. The Determination of Reactivity by the Modified Source Multiplication Technique.

At this point it is necessary to consider the disparity in definition between the physical and calculated k-eff and hence reactivity as mentioned in section 2.3. This is because it has a possible effect on the validity of the calculated correction factor.

Consider the reactivity of the reference configuration. Since it is by definition near to critical, the time absorption is a small fraction of the total losses occurring in the static neutron transport equation (Equation 2.5). Hence the replacement of this term by an increment of the fission source should introduce a correspondingly small disparity in reactivity.

For an assembly which is well-subcritical, the disparity is still probably small, provided that the fission source extends over the whole assembly as does the time absorption. In the fuel storage configurations in DIMPLE this is certainly the case (Figs.1.3 to 1.8).

3.2.3 Properties of the Modified Source Multiplication Equation

The determination of subcritical reactivity by the modified source multiplication technique results from determinations of three quantities: the measured reactivity of the reference configuration, an experimental count rate ratio or ratios, and the corresponding calculated correction factor or factors. Hence the total error depends on the errors in each of these three quantities. As will be seen in the analysis of the DIMPLE measurements, the experimental errors are easily quantified. Less easily quantified is the error in the correction factor, of which a preliminary discussion is given here. Firstly it should be noted that provided a fundamental mode only is present, the correction factor has no explicit dependence on reactivity, as shown below:

$$\rho CR = \frac{WS_{eff}}{\bar{\nu}} = \frac{\int_{v\ detector} \int_{o}^{\infty} \int_{4\pi} \Sigma_{det}(r,E) n\phi(r,E,\Omega) dr\ dE\ d\Omega}{\int_{v\ assembly} \int_{o}^{\infty} \int_{4\pi} \Sigma_{f}(r,E) n\phi(r,E,\Omega) dr\ dE\ d\Omega}$$

$$x\ \frac{<\phi^*(r,E,\Omega) S(r,E,\Omega)>}{<\phi^*(r,E,\Omega)\ \frac{1}{v}\ \phi^*(r,E,\Omega)>}$$

$$x\ \frac{\int_{v\ assembly} \int_{o}^{\infty} \int_{4\pi} \Sigma_{f}(r,E) n\phi(r,E,\Omega) dr\ dE\ d\Omega}{\int_{v\ assembly} \int_{o}^{\infty} \int_{4\pi} \nu\Sigma_{f}(r,E) n\phi(r,E,\Omega) dr\ dE\ d\Omega}$$

$$= \int_{v\ detector} \int_{o}^{\infty} \int_{4\pi} \Sigma_{det}(r,E) n\phi(r,E,\Omega) dr\ dE\ d\Omega$$

$$x\ \frac{<\phi^*(r,E,\Omega) S(r,E,\Omega)>}{<\chi(E) \int_{4\pi} d\Omega \int dE' \nu\Sigma_{f}(r,E') n\phi(r,E'\Omega')>} . \qquad (3.14)$$

The normalisation assumptions in Equations 3.4 and 3.5 have been used above. Both the numerator and the denominator of the correction factor depend on normal and adjoint flux profile over the assembly and on source strength and detector cross-section, though the correction factor does not depend on the last two quantities if the same detectors and sources are used in both configurations.

Now, if the unknown subcritical configuration has a similar flux profile to the reference configuration, the errors in the normal and adjoint flux estimation in the unknown subcritical and reference configurations will largely cancel, and the overall correction factor is likely to be accurate. Because of the similarity of flux profiles in the two

configurations, the correction factor for a given detector is also likely to be close to unity. This situation is illustrated in Figure 3.2. The flux profile in the unknown subcritical configuration is similar to the flux profile in the reference configuration. The level of the flux is lower in the former configuration by a factor equal to the ratio of the reactivities of the two configurations, ρ_2/ρ_1.

It is worthwhile examining more closely the conditions necessary for this situation. The similarity of flux profile implies a similarity both of geometry and of source distribution in the two configurations. For the flux levels to differ in the ratio of the respective reactivities, the source strength must also be the same in each configuration. The first of these conditions, that of similarity of geometry, limits the degree of subcriticality possible in the unkown subcritical configuration, since the reference configuration is by necessity only slightly subcritical. Finally, the required predominance of the fundamental mode also limits the subcriticality of the unknown subcritical configuration, by the arguments of section 2.9.

In practice the similarity of the flux profile in the two configurations is observed by means of the count rates from detectors distributed over each configuration. For each detector which is in the same location in both configurations, the ratio of the two count rates is similar, as shown schematically in Fig. 3.2. Obviously there must exist some difference in flux profile between the two configurations and this will be evident close to any regions in which the geometric changes are made to produce the unknown subcritical configuration from the reference configuration.

Because of the strict constraints necessary for the occurrence of the situation illustrated in Fig. 3.2, it is necessary to consider the application of the modified source multiplication equation to situations in which these contraints are not satisfied. The lower the k-eff of the unknown subcritical configuration, the greater are the probable differences between its flux profile and that of any reference configuration used for the calibration. This is due both to the geometrical changes necessary to lower the k-eff from a value just less

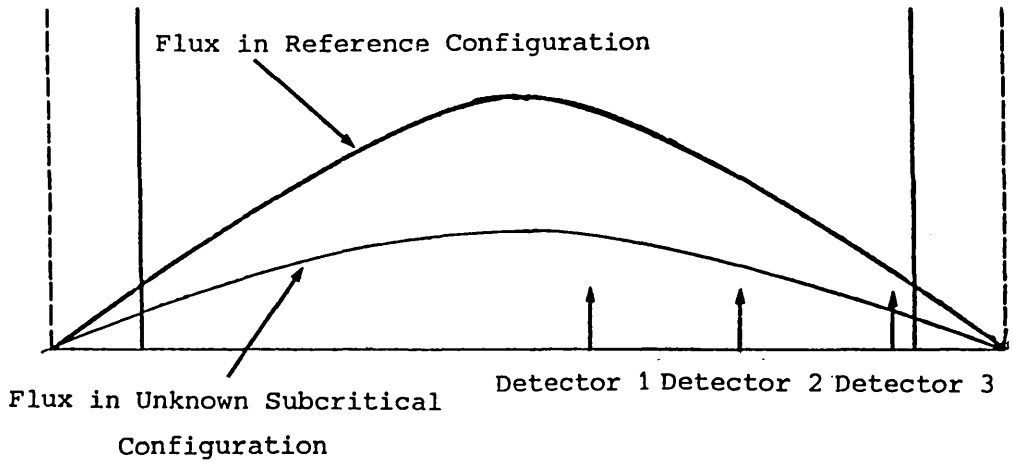

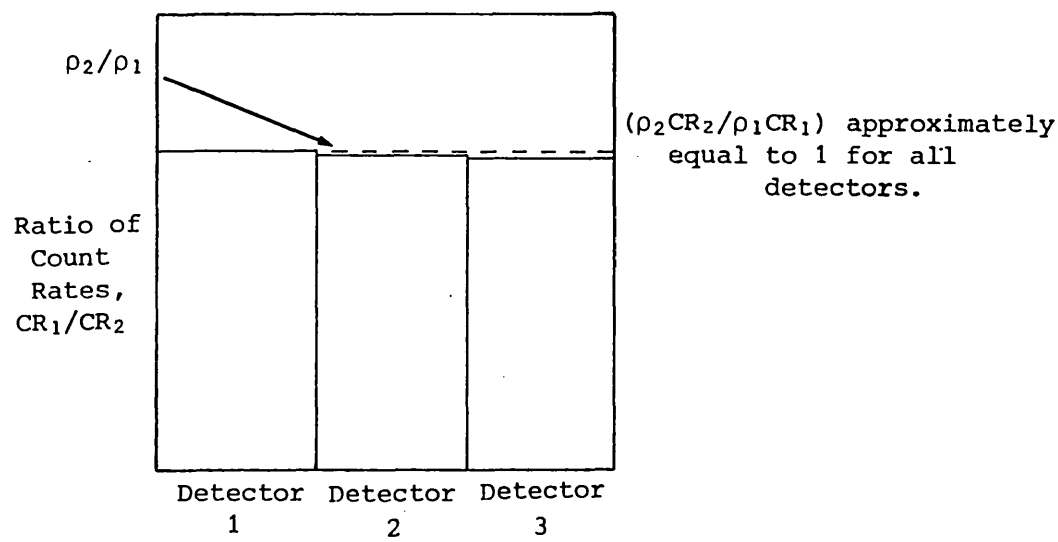

Fig. 3.2. The Modified Source Multiplication Technique: Small Changes in Flux Profile.

than unity to what may be a significantly lower value, and to the increasing importance of higher modes in the flux distribution. Higher mode contamination is likely to be particularly important if the flux distribution originates from localised sources (section 2.9). This situation is illustrated schematically in Figure 3.3. It must also be noted that the flux distribution in the reference configuration itself is not necessarily a fundamental mode. This situation is presumably possible if the assembly is very large and is driven by localised sources.

Considering firstly the validity of the modified source multiplication equation where higher modes are significant, it is clear that the derivation used in section 3.2.1 does not work. However, if the correction factor is accurate, then the reactivity from the MSM equation (Equation 3.13) is, by cancellation, equal to the true reactivity of the unknown subcritical configuration. This is the case irrespective of the higher mode contamination in the source mode flux distribution which gives the count rates. In principle then the modified source multiplication equation is valid for significant higher mode contamination provided that the calculated correction factors can be shown to be accurate.

Unfortunately the presence of the higher modes causes the correction factor, in general, to be dependent on reactivity. The modal generalisation of Equation 3.1,

$$\rho_n = - \frac{S_{eff\ n}\ \ell^*_n}{n_n}, \qquad (3.15)$$

leads to

$$CR_n = - \frac{W_n\ S_{effn}}{\bar{\nu}\ \rho_n}. \qquad (3.16)$$

In Equation 3.16, CR_n is the contribution of the n^{th} flux mode to the count rate.

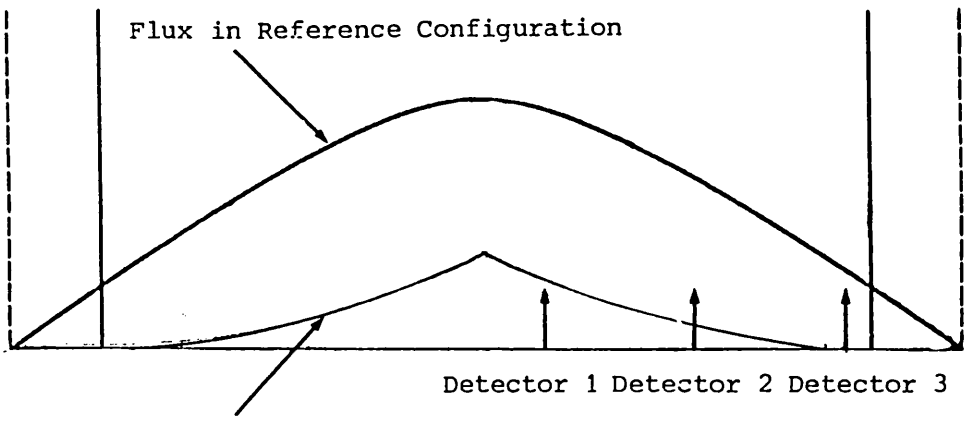

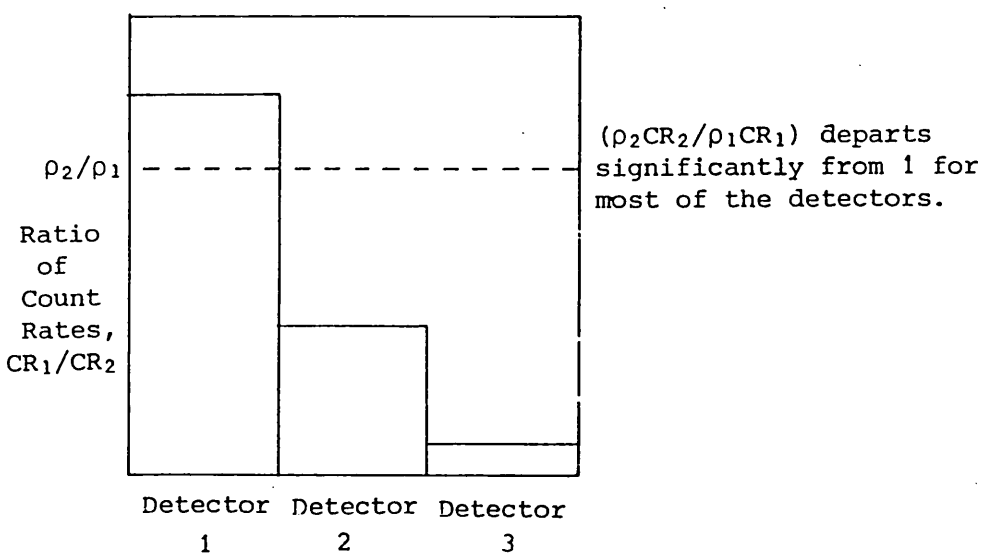

Fig. 3.3. The Modified Source Multiplication Technique: Large Changes in Flux Profile.

$$\text{Now } CR = \sum_{n=1}^{\infty} CR_n = \sum_{n=1}^{\infty} \frac{W_n S_{effn}}{\bar{\nu}\,\rho_n} \tag{3.17}$$

$$\text{and } \rho\, CR = \frac{WS_{eff}}{\bar{\nu}} + \sum_{n=2}^{\infty} \frac{\rho}{\rho_n} \frac{W_n S_{effn}}{\bar{\nu}}. \tag{3.18}$$

As a result of this dependence on calculated reactivity, errors in the correction factors due to calculational deficiencies are more likely to be significant. The significant presence of higher modes additionally means that the distribution of sources and detectors becomes important. As was shown in section 2.9, the levels of the higher modes depend on the source distribution and so a preference appears to be indicated towards a source distribution which minimises the presence of the higher modes. Furthermore, for a given source distribution in an assembly the proportion of the flux due to the higher modes varies with position. This is evident from Figure 2.2 in which the flux departs more and more from that due to a fundamental mode once a certain distance from the source is exceeded. Thus the systematic errors due to calculation may vary with the position of the detector in the assembly.

From these general arguments previous experience in the modified source multiplication technique can be examined.

3.2.4 Experience with the Modified Source Multiplication Technique

There appears to be no experience of the modified source multiplication technique on fuel storage arrays of the type built in DIMPLE. The principal characteristics of the DIMPLE fuel storage arrays from the point of view of modified source multiplication measurements are:

(i) The large geometric departure of most of the subcritical configurations from the reference configuration (Figs. 1.3 to 1.8).

(ii) The absence of a spontaneous source in the fuel used, resulting in the use of localised sources for subcritical measurements.

(iii) The large degree of subcriticality of many of the configurations.

Nevertheless, much experience of the modified source multiplication technique has been gained, particularly on assemblies in which the unknown subcritical configuration is produced from a slightly subcritical configuration by the lowering of control rods (5, 6). Several examples of the technique pertain to fast assemblies: an important characteristic of these assemblies is the presence of a spontaneous neutron source spread throughout the fuel. This tends to minimise higher mode contamination, resulting in a largely fundamental mode distribution even in well-subcritical configurations, as explained in Ref. (6). Typically, the changes in flux profile are not particularly large for such assemblies, for example in Ref. (3), the range of correction factors used in the modified source multiplication measurements is from about 0.6 to about 1.3, it being remembered that small differences in flux profile result in correction factors of unity (Fig. 3.2).

The greater difficulties encountered in making modified source multiplication measurements in water-moderated assemblies driven by localised sources are implied in Ref. (7). In general, detector count rates are not inversely proportional to subcritical reactivity, but depart from this behaviour due to the presence of higher modes.

Most of the accounts of the modified source multiplication technique describe measurements in which the detectors are distributed over the entire assembly, though in all the fast assembly measurements, no marked preference for certain detector locations is stressed. In contrast Ref. (7) stresses the need to choose proper source and detector locations to minimise the higher mode contamination in the count rates; this is presumably a result of the measurement being dependent on a flux distribution originating from a localised source.

It is noted in Ref. (7) that for approaches to critical in water-moderated assemblies, total count rates from detectors distributed throughout fuel regions have been used. These total count rates tend to be closer to inverse proportionality with subcritical reactivity, than the individual count rates in general. This is because higher flux modes tend to have a reduced effect over the whole of an assembly since they individually have both positive and negative flux values in different regions (Fig. 2.1).

With regard to the determination of the reactivity and thus the k-eff value of an assembly from the individual reactivities given by each of a distribution of detectors, the usual method has been to take the arithmetic mean of the individual reactivities (3), with their standard deviation being a measure of the errors due to calculation. Quantification of the errors in this way assumes the true reactivity of the assembly to be bracketed by the reactivities obtained from the individual detectors. This, however, is not necessarily the case if the correction factor calculations model two widely different flux profiles, since significant systematic errors may be present.

The correction factor calculations used in the past have generally been multigroup diffusion theory or transport theory calculations. In several examples sensitivity studies of the correction factors to the calculational methods used have been made (3,5).

Finally several variants of the modified source multiplication technique have been suggested (8).

It is apparent that a systematic interpretation of the modified source multiplication technique is required for the case of well-subcritical fuel storage arrays driven by localised sources. Given that significant higher mode contamination is present, this interpretation will include a diagnosis of preferred source and detector positions for the measurements probably suppressing the effects of the higher modes, so as to minimise the systematic errors in the correction factors due to calculational deficiencies. By implication, a reliable means of assessing these systematic errors is required.

As will be seen, the DIMPLE measurements and their analysis concentrate on these fundamental aspects of the technique.

3.3 The Near-to Critical Calibration

As explained earlier, it is necessary in the conventional modified source multiplication technique to determine experimentally the reactivity of a slightly subcritical assembly. Several different methods for so doing exist (2). All of these methods involve making a

reactivity perturbation to the critical assembly. Provided that the reactivity is somewhat less than the delayed neutron fraction, all of the methods have accuracies controlled by knowledge of delayed neutron fractions and half-lives.

The only rapid and convenient means of changing the reactivity of the near-to-critical configuration in the skip insert was by means of water height alteration. Facilities for performing the inverse kinetics technique existed (9), but this technique was deemed inappropriate for the following reason. Prior to calibration using inverse kinetics, the assembly is balanced at critical by raising the water height. A negative reactivity change is then made, by lowering water. The result depends on two measurements, one made after a rise in water height, the other after a drop. Due to capillary action, the extent of the drop cannot be accurately determined under such circumstances.

As a result, an alternative method, using positive periods, whereby all measurements are made after rises in water height, so causing capillary effects to cancel, was used. The theory is described below.

A slightly supercritical reactor can be prompt subcritical, provided that $\rho < \beta_{eff}$. Such an assembly has divergent kinetic behaviour which is controlled by delayed neutrons and is thus not strongly dependent on prompt neutron lifetime.

The reactor point kinetics equations can be written:

$$\frac{dn}{dt} = \left(\frac{\rho - \beta}{\ell^*}\right) n + \sum_{i=1}^{D} \lambda_i C_i, \qquad (3.19)$$

$$\text{and } \frac{dC_i}{dt} = \frac{\beta_i n}{\ell^*} - \lambda_i C_i, \qquad (3.20)$$

where i is the number of the delayed neutron group and D is the number of delayed neutron groups.

Note that these equations assume a fundamental mode flux distribution. This is valid for the case of a slightly supercritical assembly.

Assuming that the prompt and delayed neutron levels can be represented by the exponential expressions $n = n_o e^{st}$ and $C_i = C_{io} e^{st}$ gives:

$$sn_o e^{st} = \left(\frac{\rho - \beta}{\ell^*}\right) n_o e^{st} + \sum_i \frac{\lambda_i n_o \beta_i}{\ell^*(\lambda_i + s)} e^{st} \qquad (3.21)$$

$$\text{or } s\ell^* = \rho - \beta + \sum_i \frac{\lambda_i \beta_i}{\lambda_i + s} \qquad (3.22)$$

$$\text{Hence } \rho = s\ell^* + \sum_i \frac{\beta_i(s+\lambda_i)}{\lambda_i+s} - \sum_i \frac{\lambda_i \beta_i}{\lambda_i+s} = s\ell^* + \sum_i \frac{s\,\beta_i}{\lambda_i+s} \qquad (3.23)$$

$$= \frac{\ell^*}{\tau} + \sum_i \frac{\beta_i}{1+\lambda_i\tau} \quad \text{where } \tau \text{ is the reactor period, } 1/s.$$

In water-moderated assemblies such as the fuel storage configurations in DIMPLE, the prompt neutron generation time is of the order of 2×10^{-5} secs (10). For small degrees of supercriticality the period of the assembly is of the order of several seconds. Hence the term proportional to the prompt neutron generation time in Equation 3.23 can be ignored, giving:

$$\rho = \sum_i \frac{\beta_i}{1+\lambda_i\tau}. \qquad (3.24)$$

The period of the supercritical assembly can be computed by fitting an exponential function to the time-dependent count rates from one or more detectors. The reactivity due to the rise in water height from the initial water height is thus determined from Equation 3.24, giving a reactivity against water height gradient ($d\rho/_{dh}$).

In order to determine the reactivity of a slightly subcritical configuration, it is necessary to obtain $d\rho/_{dh}$ values at the subcritical water height, at the critical water height and possibly at intermediate water heights so that an approximation to the equation below can be made:

$$\rho_{\text{subcritical}} = \int (d\rho/dh)_h \, dh \cong \sum_{i=1}^{n} \frac{d\rho}{dh}_i \Delta h_i . \qquad (3.25)$$

Here the $d\rho/dh$ integral has been split into n finite areas with a value $(d\rho/dh)_n$ being a mean value for that area. This procedure is illustrated in Figure 3.4.

Values of $(d\rho'_{dh})$ at the subcritical water height can be obtained by altering the assembly to make it critical at that height, as shown schematically in Fig 3.5. The departure of the experimental $(d\rho/dh)$ value from the true$(d\rho/dh)$ value is of the order of the proportional change made in k-eff to make the period measurement at the reduced water height possible, ie 1%.

Values of $d\rho'_{dh}$ at the water heights lower than the critical water height for the reference configuration geometry can be obtained as follows. The reference configuration geometry, while unflooded, is made potentially more reactive eg by the addition of fuel. A period measurement is then made at a slightly lower water height than the critical water height for the reference configuration geometry. This slightly lower water height is now the critical water height because of the reactivity insertion, enabling the period measurements to be made. This process is illustrated schematically in Fig. 3.5.

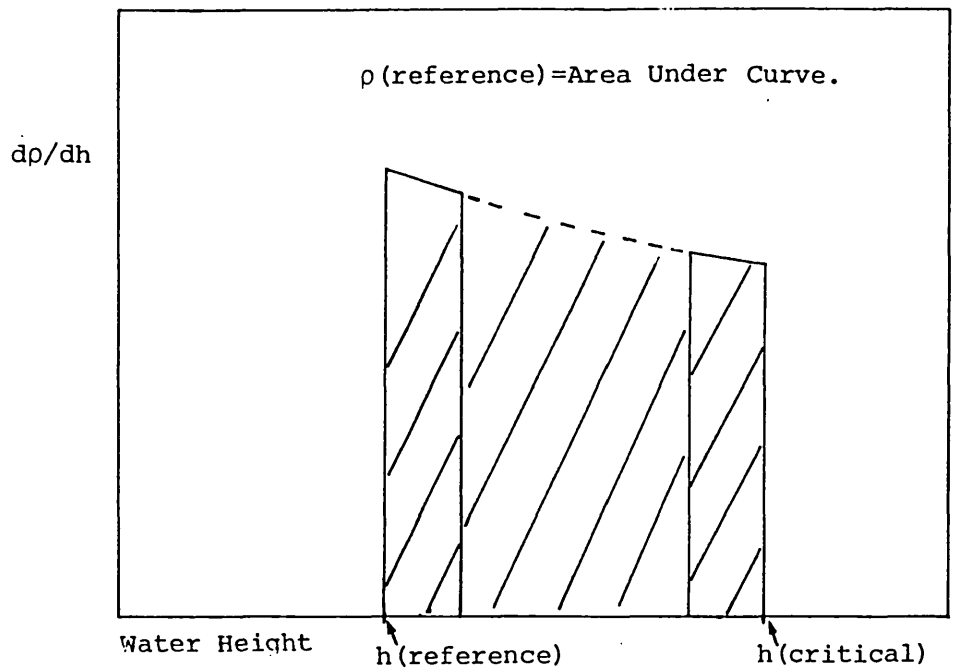

Fig.3.4. The Determination of the Reactivity of the Reference Configuration.

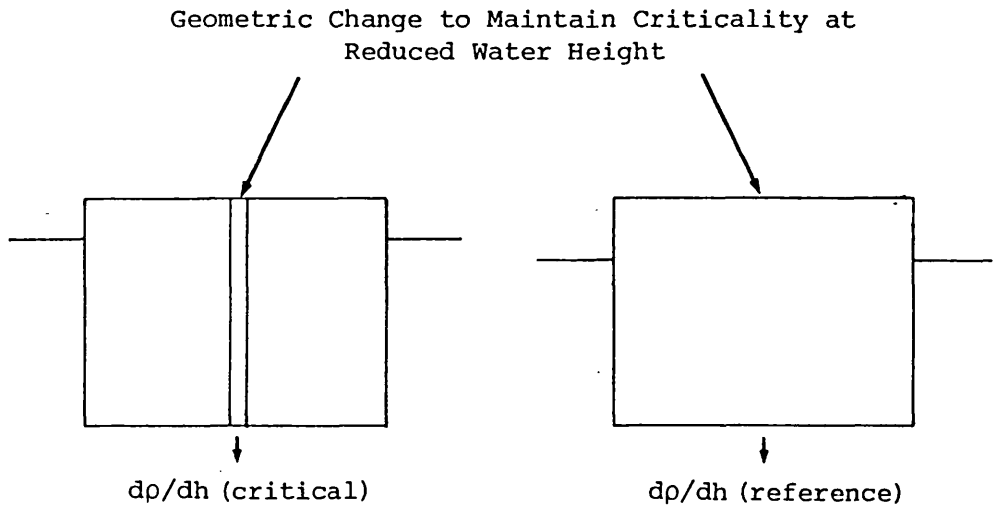

Fig. 3.5 The Production of dρ/dh Values Over the Required Height Range (Schematic).

4. Procedure for the Modified Source Multiplication Measurements

Both the aims of the subcritical reactivity measurements and the theory of the techniques used have been established. The procedures for the measurements are now described. In this chapter are included the methods by which the experimental count rates, the correction factors and hence the reactivities from the MSM technique for the fuel storage configurations in DIMPLE were obtained. Details of the close-to-critical calibration and various subsidiary measurements and calculations are given in the following chapters.

4.1 Production of Experimental Count Rates

Count rates were obtained by imposing sources on all the well-subcritical configurations listed in section 1.2.2, and also on a reference configuration which was the 196 pins per compartment array with the water lowered a few centimetres from the critical height (section 1.2.2).

4.1.1 Sources

For the production of count rates six californium 252 sources were used (1). Californium 252 undergoes spontaneous fission and is thus a neutron emitter. It has a half life of 2.65 years, largely due to its alpha decay. For the purpose of providing neutrons for count rates in subcritical assemblies any small, steady-state source is sufficient; the californium sources were those most readily available.

The sources were contained in small capsules, which themselves were positioned by means of spacers in two large stainless-steel tubes, three to a tube, each of which was located in the skip by means of a dowel at the bottom and retained at the top by the top lattice plate (Fig. 4.1).

In order to test the accuracy of the modified source multiplication technique with different source positions, two radial arrangements of the source tubes were used (Figures 4.2 and 4.3). The standard source positions (Figure 4.2), were in the centres of the centremost two compartments. This was to produce a symmetric neutron distribution in

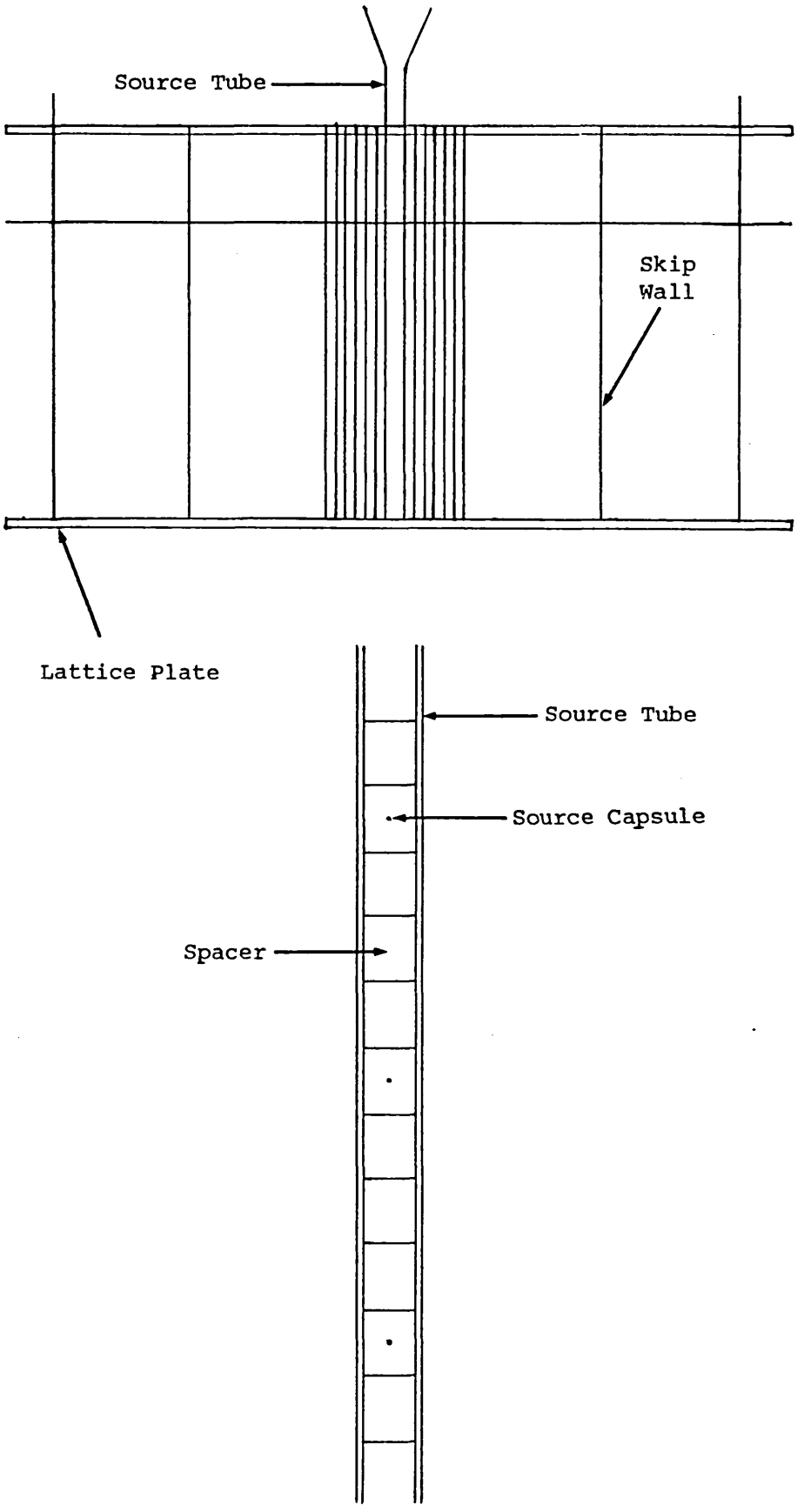

Fig. 4.1. Side View of the Skip and Source Tube.

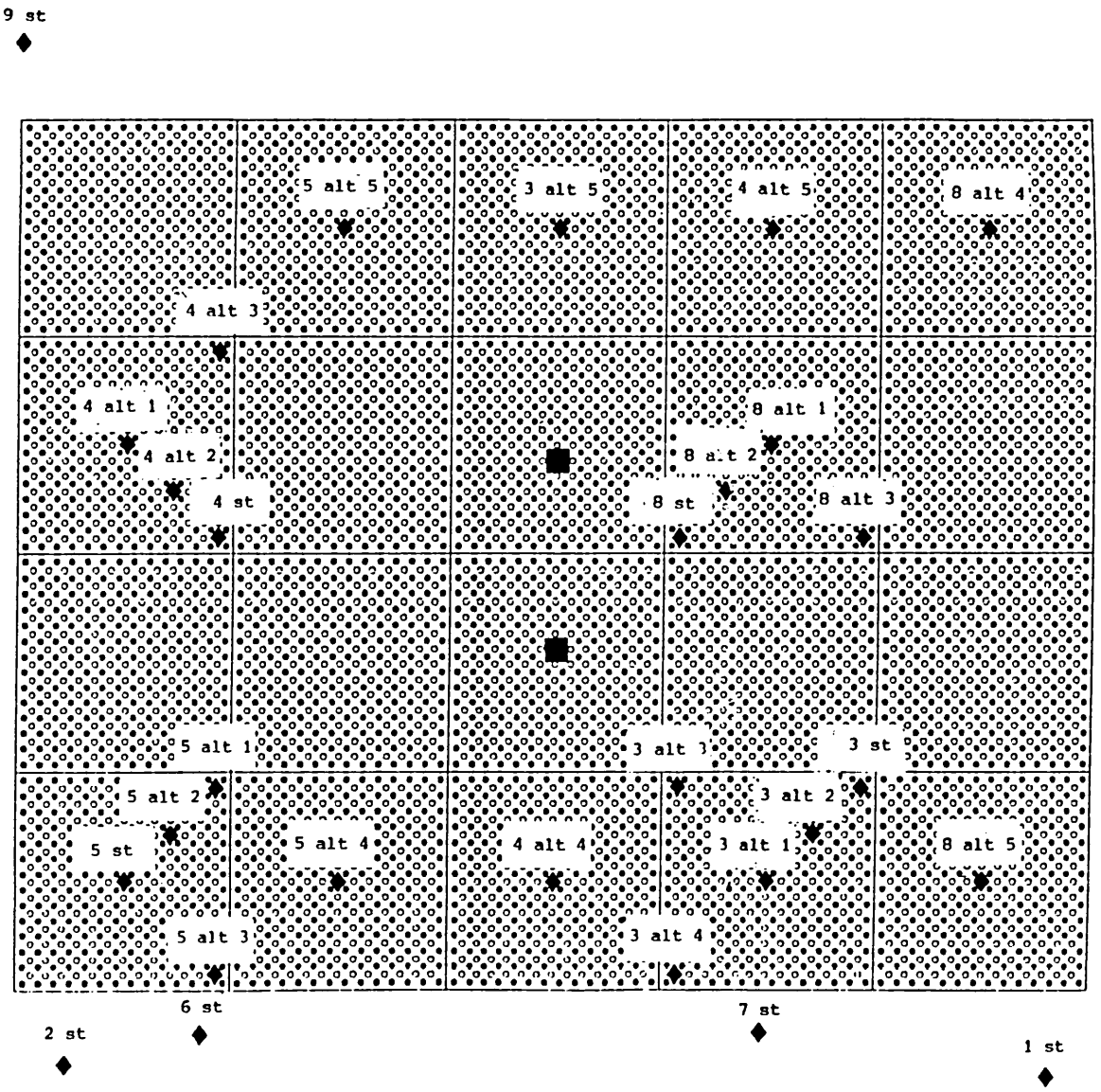

Fig. 4.2. Standard Source Positions and Associated Detector Positions.

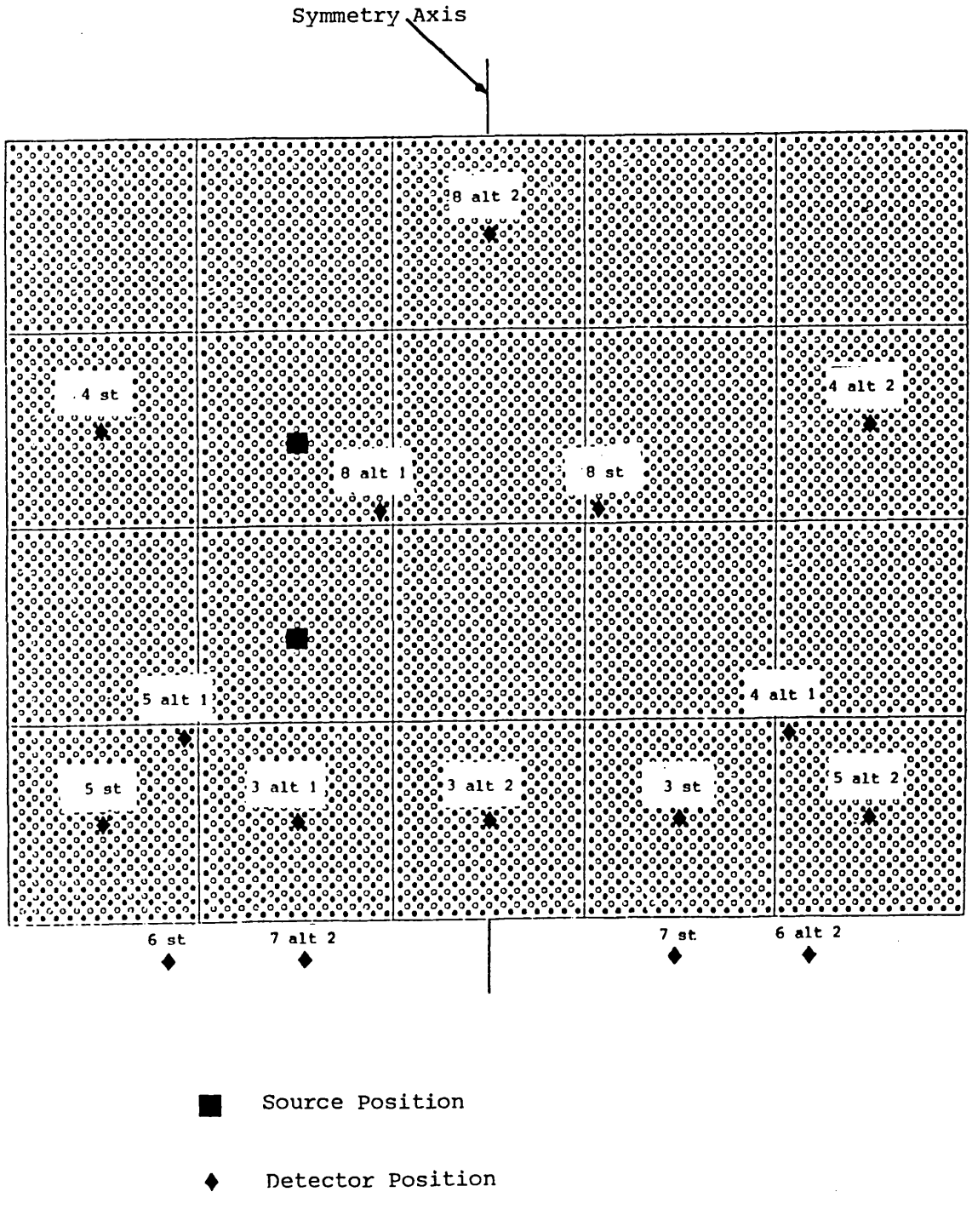

Fig. 4.3. Alternative Source Positions and Associated Detector Positions.

the skip, which was itself symmetric for most of the configurations studied and hence was expected to possess a symmetric fundamental mode. The alternative source positions (Figure 4.3) were in the centres of the two adjacent compartments on the left. Use was made of the symmetry of the skip configurations about the axis marked and by summing count rates from detectors in symmetric positions about this axis, results appropriate to four radial source positions were obtained. This arrangement was expected to yield a neutron distribution closer to a fundamental mode and hence to give greater accuracy of results. It was employed only for both the 196 pins per compartment configurations, and for the centred 112 and 221 pin clusters configurations.

The sources were axially spread in the tubes; in this way, it was aimed to minimise higher axial modes (section 2.2). The axial positioning of the sources is shown in Figure 4.4.

It was realised that the source tubes made a reactivity perturbation to each of the assemblies; for the 196 pins per compartment configuration at the critical water height this was equal to 0.4% $\Delta k/k$ (2). For the entire course of the measurements the k-eff value of each configuration was taken to mean the k-eff value of that configuration with the source tubes. The perturbations of the source tubes in the alternative positions were slightly smaller than in the standard positions. Accordingly, the reference configuration for the alternative source positions, employed a water height slightly different from that used for the standard source positions, to give the same negative reactivity.

4.1.2 Detectors

With the sources in their standard positions, a total of 29 count rates were obtained for each configuration. These comprised 24 positions inside the skip and 5 positions outside the skip (Figure 4.2). The detector positions were in several different environments, and were at a variety of distances from the sources. They were thus expected to provide information on the optimum detector positions for the measurements. A total of 9 experimental channels were available to produce the count rates. Of these four used 5EB40/6 detectors (3).

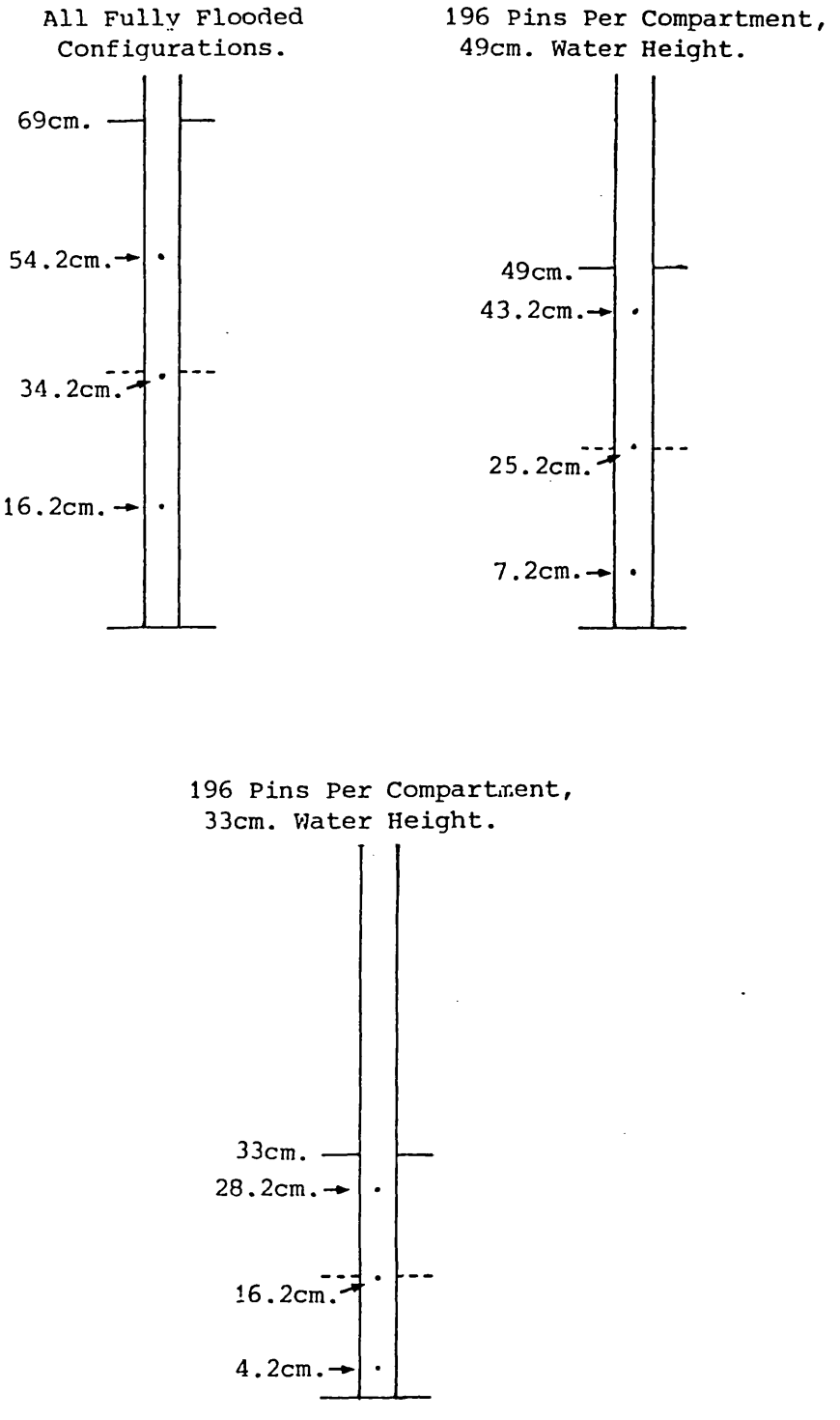

Fig. 4.4. Axial Source Positions.

These detectors, with diameters of 0.6cm, were small enough to be placed inside fuel-pin cans and hence be positioned in the fuel clusters. All 24 count rates in the skip were from these four detectors. As can be seen in Figure 4.2, a total of 6 positionings of these detectors, one standard and five alternative, were used. The five count rates outside the skip were taken from larger detectors of which three were installed instrumentation (detectors 1, 2 and 9). The two others (detectors 6 and 7) were large detectors placed in pods attached to the outer wall of the skip.

A table of the detectors corresponding to each detection channel is given below: the dimensions of each detector are also given.

Table 4.1 Detector Types and Dimensions

Channel	Detector Type	Dimensions (cm)		
		Active Length	Diameter	Total Length
1	FC165	5.7	3.0	20
2	P7	22.0	~2.5	~25
3	5EB40/6	5.0	0.6	14
4	5EB40/6	5.0	0.6	14
5	5EB40/6	5.0	0.6	14
6	12B70	12.0	2.5	22
7	12B20	12.0	2.5	22
8	5EB40/6	5.0	0.6	14
9	12EB20	12.0	2.5	21

The detectors on channels 1 and 2 were fission counters using uranium 235 as the active material.

All of the remaining detectors used boron triflouride as the active material; with the low count rates expected in well-subcritical configurations it was thought desirable to use detectors of as high a sensitivity as possible, compatible with mechanical constraints.

With the sources in the alternative positions, a total of 16 count rates in symmetric pairs of positions were obtained (Figure 4.3). Of these 12 were in the skip and 4 were outside the skip; two of the positions were on the axis of symmetry and hence corresponded singly to a pair of positions. A total of 9 count rate pairs were thus produced.

The axial positions of the detectors are shown in Figure 4.5. The 5EB40/6 detectors were supported in the tubes by means of perspex spacers. Three different spacer lengths were used altogether, one for each of the three water heights used in the measurements (section 1.2.2). The lengths were chosen so as to position the detector active material close to half-way up the flooded fuel in each assembly for the following reason.

An assembly with constant radial geometry over most of its height has an axial fundamental mode which is close to a cosine function. This has been demonstrated in arrays of fuel pins in water (4). The maximum value of the cosine function is half-way up the flooded fuel in such assemblies, and the function is quite flat in this region. It was expected that such a distribution would obtain in the fuel storage configurations, and so an exact knowledge of the axial positions of the detector active material would not be required for the correction factor calculations.

The detectors on channels 6 and 7 were also positioned close to the midplane of each of the assemblies by means of three different sets of perspex spacers. All the installed detectors (detectors 1, 2 and 9) were immovable and remained at the same positions throughout the measurements.

4.1.3 Experimental Procedure

Precautions were taken to ensure that the sensitivity of each of the detectors remained as stable as possible. The settings of all the experimental channels are shown in Table 4.2 and were those used at the beginning of the measurements.

Discrimination levels were set to coincide with the pulse heights between the noise and the pulses resulting from neutron detection (Figure 4.6). The noise resulted from gamma-ray induced events in the boron triflouride detectors and alpha particles in the fission counters. Few pulses were evident at these levels, rendering the detection channels insensitive to small changes in amplifier gain. All detection channels and pulse height spectra were checked on every day of the measurements.

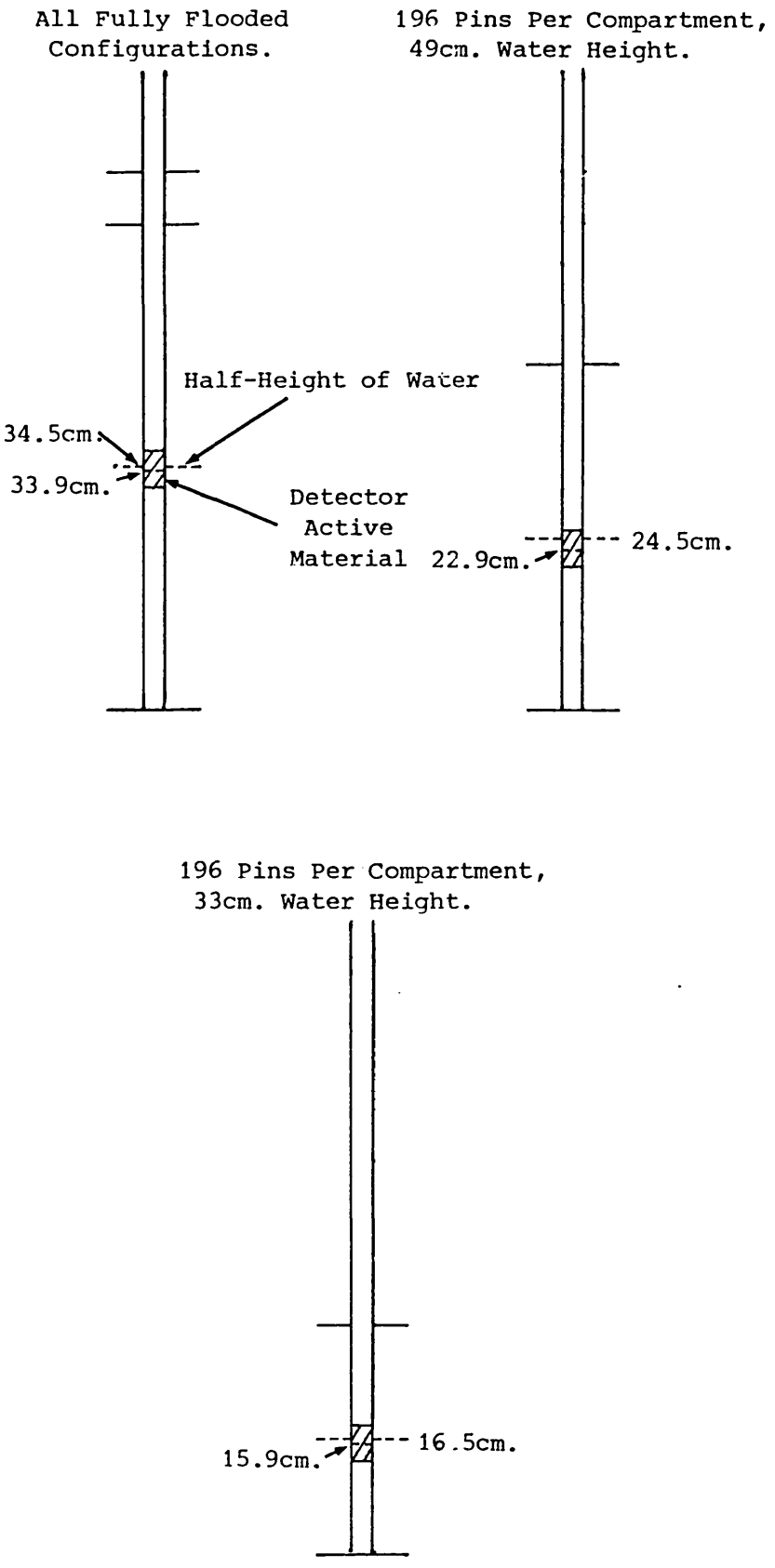

Fig. 4.5. Axial Detector Positions in the Skip.

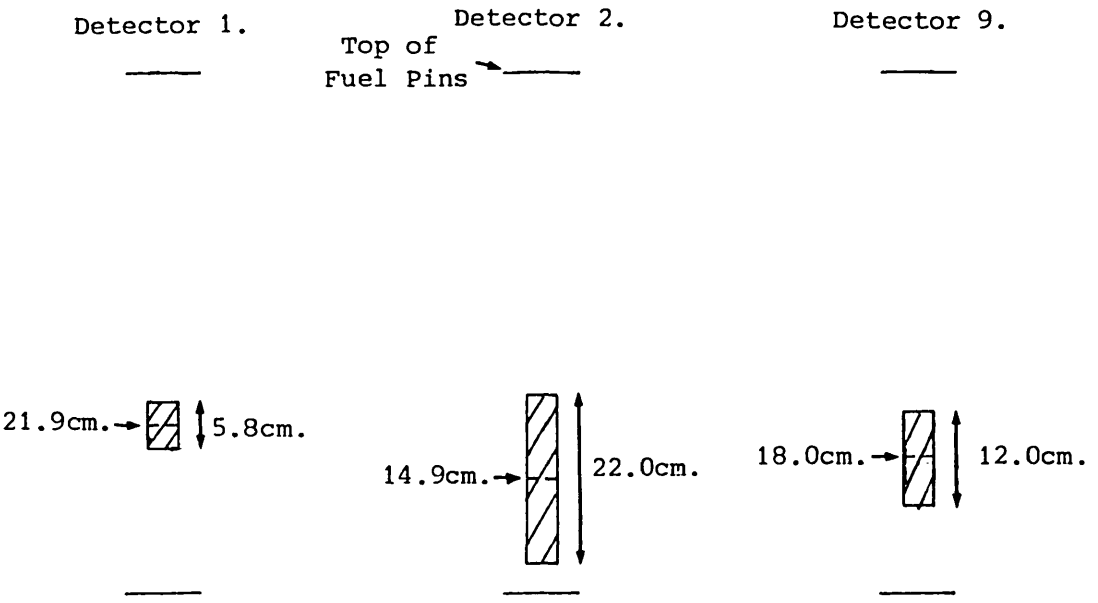

Fig. 4.5.(Contd.) Axial Detector Positions Outside the Skip.

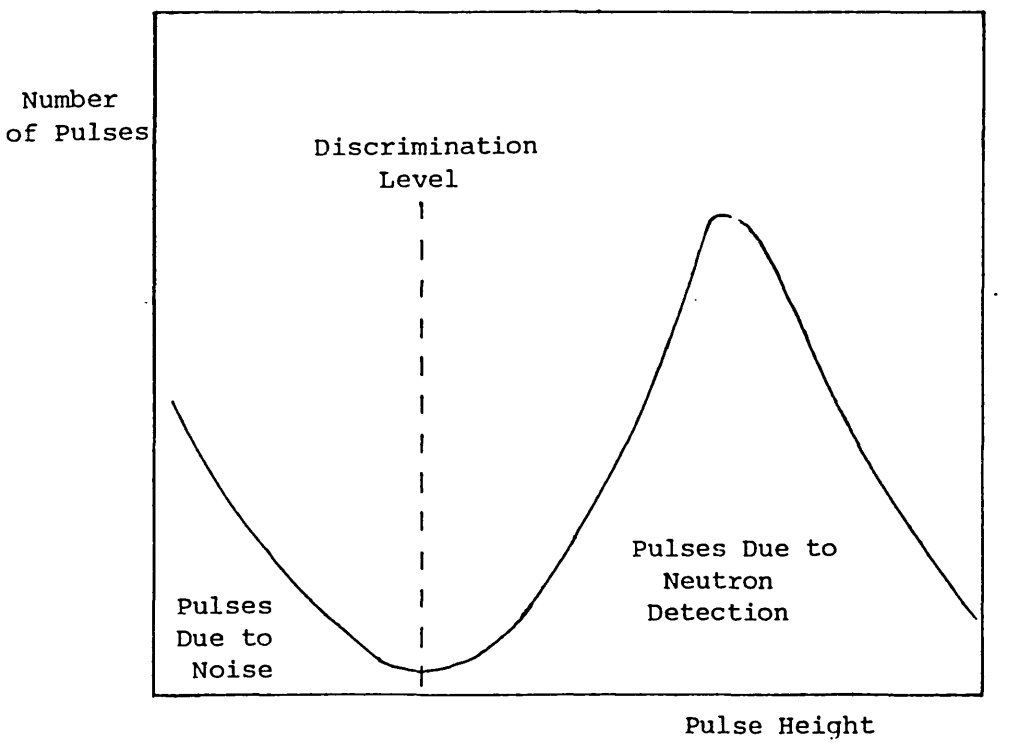

Fig. 4.6. Typical Pulse Height Spectrum.

Table 4.2 Typical Channel Settings

Channel	Detector	EHT (Volts)	Discrimination Level	Pulse Peak (MCA channel no)	Sensitivity of Count Rate to Gain Change of 10% (%)
1	FC165	300	0.254	322	0.8
2	P7	300	0.26	362	1.0
3	5EB40/6	950	0.245	375	1.0
4	5EB40/6	940	0.23	274	1.8
5	5EB40/6	940	0.265	374	0.9
6	12B70	2300	0.26	515	0.8
7	12B20	1300	0.25	580	0.6
8	5EB40/6	940	0.255	410	0.6
9	12EB20	--	--	--	--

Failure of components occurred occasionally throughout the measurements. Sometimes the detectors themselves experienced breakdown and were rendered useless. Cross-calibration between detectors was made at the start of the measurements and each time a detector was replaced, in order to correct for the resultant change in detector sensitivity; the procedure for this is described in the next section. Sometimes head or main amplifiers failed. Each time a replacement was made the main amplifier gain was adjusted to bring the pulse height peak close to its previous value.

Care was taken in the handling of the detectors, especially the 5EB40 detectors which were moved frequently. Plugs were regularly checked and moisture and dirt removed.

Count rates were obtained using a standard counting program on a PDP11 computer, linked to the detection channels via CAMAC interfaces. The program made dead-time corrections. The dead-times of the detectors were 1.4μs for the boron triflouride detectors and 1.25μs for the fission detectors; even with the count rates obtained in the reference configuration the dead-time corrections were small. Enough counts were taken from each detector to obtain a standard deviation on each count rate of about 1% or less, this being a much smaller error than that associated with the calibration of the reference configuration due to delayed neutron data (section 3.3). This required about an hour of counting for the lowest count rates in the well-subcritical configurations.

From the actual count rates, corrected experimental count rates were produced by dividing by relative detector sensitivity (the assignment of relative detector sensitivities is described in section 4.1.4) and a source decay factor:

$$\text{Corrected experimental count rate} = \frac{\text{Actual experimental count rate}}{\text{Detector sensitivity x source decay factor}}. \qquad (4.1)$$

The source decay factor was to correct for the changes in source strength which occurred throughout the measurements due to the decay of the californium 252 constituting the sources. On the first day of the measurements, the source decay factor was assigned a value of unity, and thereafter as calculated from the expression:

$$\text{Source decay factor} = \exp\left(-0.693.nw/(2.65x52.2)\right), \qquad (4.2)$$

where nw is the number of weeks elapsed from the beginning of the measurements.

4.1.4 Cross-Calibration of Detectors

As mentioned in the previous section, occasionally detectors were replaced, and so a means was found to compare experimentally the sensitivities of the new and old detectors.

For a detector (a), its count rate is given by:

$$CR_a = \iiint \Sigma_{da}(r,E)\,\phi(r,E,\Omega)\,d\Omega\,dE\,dr \qquad (4.3)$$

where $\Sigma_{da}(r,E)$ is the detection cross-section of detector (a) at r and E. This equation similarly applies to another detector (b):

$$CR_b = \iiint \Sigma_{db}(r,E)\,\phi(r,E,\Omega)\,d\Omega\,dE\,dr. \qquad (4.4)$$

Now if detector (b) replaces detector (a) in a certain position, then the flux remains the same, provided the two detectors are geometrically similar and that a large change in absorption by the detection material does not take place. The sensitivities can be related by means of a constant if they result from the same detection material:

$$\Sigma_{db}(r,E) = k\Sigma_{da}(r,E). \tag{4.5}$$

$$\text{Hence } k = \frac{\Sigma_{db}(r,E)}{\Sigma_{da}(r,E)} = \frac{CR_b}{CR_a}. \tag{4.6}$$

The relative sensitivities of two detectors of similar geometry and detection material can thus be found by swapping their positions. This, of course generates two count rate ratios and hence two sensitivity ratios which should be the same.

At the beginning of the measurements the relative sensitivities of all the 5EB40/6 detectors in the skip were found by swaps as were those of the 12B20 and 12B70 detectors outside the skip. The relative sensitivities of any new detectors of these types as introduced were then computed by swaps with the remaining detectors.

Examples of the sensitivities computed for the various detectors are shown in Table 4.3. The sensitivities of the four detectors in the skip were relative to a nominal sensitivity of 1.000 for detector 3 in the 112 pin clusters, centred configuration. Each of the detectors outside the skip was assigned a nominal sensitivity of 1.000 at the beginning of the measurements. The absolute value of this nominal sensitivity is not important: it is only the ratio of the sensitivities featuring in any count rate ratio that is important in the modified source multiplication equation (Equation 3.13). The errors quoted for the sensitivities in Table 4.3 result from the difference between the two sensitivity ratios given by each swap. The nominal sensitivities for the detectors outside the skip, not resulting from intercalibration, do not have these errors.

Table 4.3 Examples of Detector Sensitivities

Configuration	Det 3	Det 4	Det 5
196/49, 196/33	1.318(±1.4%)	1.138(±1.0%)	0.336(±1.7%)
112/76 (CTD)	1.000(-)	''	1.252(±1.0%)

Configuration	Det 8	Det 6	Det 9
196/49, 196/33	1.123(±1.4%)	1.000(-)	1.000(-)
112/76 (CTD)	''	1.000(-)	1.000(-)

4.2 Correction Factor Calculations

The computation of correction factors for the modified source multiplication measurements was carried out using, in two-dimensional geometry, the diffusion theory code SNAP (5) in eigenvalue and source modes. These calculations required the prior preparation of cross-sections for the materials comprising the fuel skip configuration modelled by each calculation.

4.2.1 Cross-Section Preparation

Multigroup cross-sections were prepared for each configuration using the PERSEUS collision probability module of LWRWIMS, a thermal reactor code (6). The models for the 112 pin clusters, centred, and the 221 pin clusters, centred configurations, are shown in Figs 4.7 and 4.8. In the initial fine spectrum calculation, 5 radial meshpoints defined a fuel pin surrounded by its clad and water, a pin cell covering an area of one pin pitch squared in each configuration. Two pin cell types were defined for the centred configurations, one for the pin cells adjacent to the water surrounding the clusters and one for the remaining pin

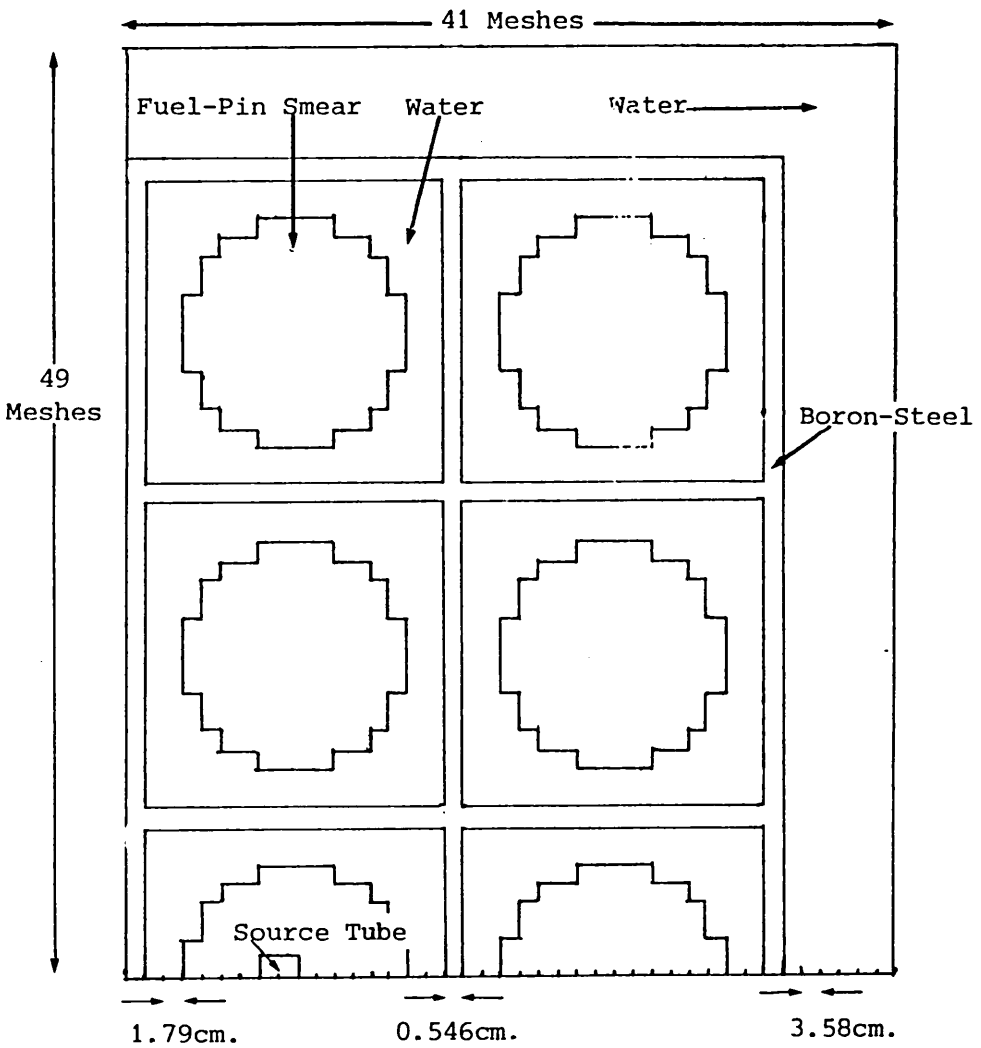

Fig. 4.7. Calculational Model for the 112 Pin Clusters, Centred Configuration.

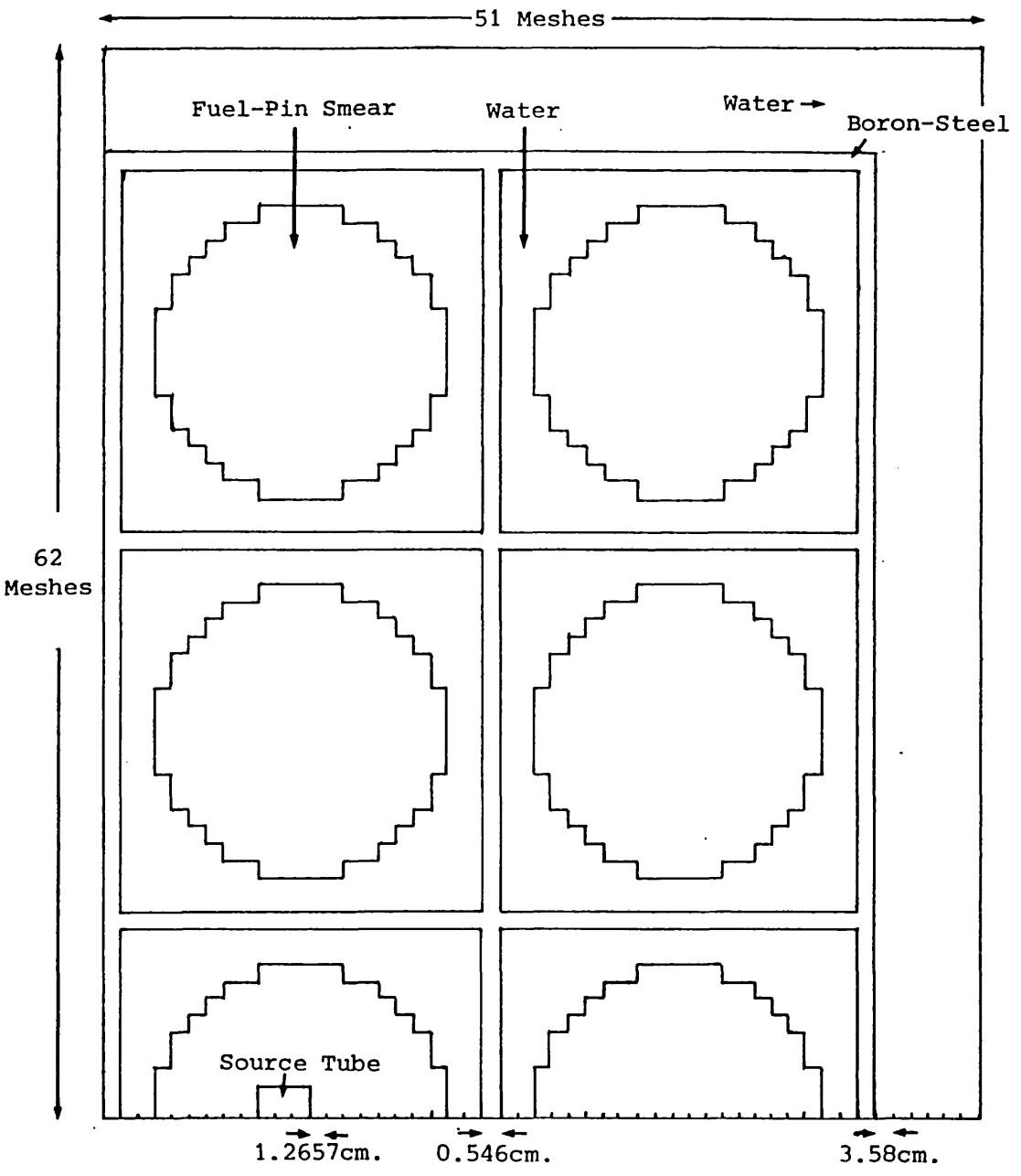

Fig. 4.8. Calculational Model for the 221 Pin Clusters, Centred Configuration.

cells. For the closest-to-centre configurations an additional pin cell type was defined for those pins closest to the boron-steel walls. This procedure was adopted to take account of the differing spectra in the different fuel positions.

The boron-steel walls were one mesh thick and a single material type was defined for them. Two different water types were defined, one for water inside the skip and the other for water outside the skip. The source tube occupied 4 meshes in the 196 pins per compartment and the 112 pin clusters configurations, and 9 meshes, corresponding to approximately the same area, in the 221 pin clusters configurations.

Compositions of each of the materials were taken from an earlier and sightly different version of the data already given in Table 1.3. For the source tube meshes a mixture of stainless-steel, air and water corresponding approximately with the estimated actual proportions in the tube and surrounding water was used (Table 4.4).

Table 4.4 Material Composition of the Source Tube Meshes

Material and Constituent Elements	Fraction of Mass of Source Tube Material (%)
Steel (as in Table 1.3): radius 3.1cm, inner radius 1.9cm	87.7
Water (as in Table 1.3)	12.3
Air: 25% O 75% N	0.005 (ignored in calculations)

Finally, the model assumed full reflection about the left-hand and bottom boundaries.

The PERSEUS module was run in 8 energy groups. Details of the group structure are given below: it was based on the recommended 6-group structure for thermal reactor calculations (6). Two extra groups were used in the thermal region, it being thought that the presence of strongly absorbing material would warrant extra energy definition in this part of the spectrum.

Table 4.5 Group Structure for the Diffusion Theory Calculations

Group in Correction Factor Calculations	LWRWIMS 69 Group Library Groups	Energy Range (eV)
1	1-5	1.0×10^{7}-8.21×10^{5}
2	6-14	8.21×10^{5}-9.0×10^{3}
3	15-27	9×10^{3}-4.0
4	28-45	4.0-0.625
5	46-52	0.625-0.25
6	53-58	0.25-0.067
7	59-64	0.067-0.025
8	65-69	0.025-0.0

4.2.2 Diffusion Theory Calculations

The only code readily available to produce both fundamental mode reactivities and source mode fluxes for the calculation of correction factors was the diffusion theory code SNAP. The multigroup finite-difference diffusion equation used by the code can be written (5):

$$\sum_{n=1}^{N} \bar{D}_{on} \left(\phi_n^{(g)} - \phi_o^{(g)}\right) S_{n/L_n} + V_o \Sigma_o^{(g)} \phi_o = V_o Q_o,$$

where: $$Q_o = \sum_{h=1}^{G} \Sigma_o^{(hg)} \phi_o^{(h)} + \frac{1}{k} \sum_{m=1}^{M} \chi_o^{(mg)} \sum_{h=1}^{G} (\nu\Sigma_f)_o^{mh} \phi_o^{h}, \quad (4.7)$$

where: $\bar{D}_{on}$ is the diffusion coefficient characterising neutron leakage from a cell to its n^{th} immediate neighbour;

N is the number of immediate neighbours a cell has and is equal to four for a two-dimensional rectangular geometry;

$\phi_o^{(g)}$ is the flux in cell o in group g;

$\phi_n^{(g)}$ is the flux in cell o's n^{th} neighbour in group g;

S_n is the area of the surface common to cells o and n;

L_n is the distance between the centres of cells 0 and n;

V_o is the volume of cell o;

$\Sigma_o^{(hg)}$ is the scatter cross-section from group h to group g in cell o;

$\chi_o^{(mg)}$ is the emergence spectrum into group g in cell o for material m; and

$(\nu\Sigma_f)_o^{mh}$ is the production cross-section for group h in cell o for material m.

The above equation is the computational form of the neutron diffusion equation in eigenvalue mode:

$$-D(r,E)\underline{\nabla}\phi(r,E)+\Sigma_r(r,E)\phi(R,E) = \int_o^\infty dE' \Sigma_s(E'\rightarrow E)\phi(r,E')$$

$$+ \frac{1}{k}\chi(E)\int_o^\infty dE' \nu\Sigma_f(r,E')\phi(r,E'). \qquad (4.8)$$

This is itself a simplification of the corresponding neutron transport equation in section 2.1.

The diffusion coefficient $\bar{D}_{on}$ is the harmonic mean diffusion coefficient for leakage between cells o and n (Fig. 4.9) and is given by:

$$\frac{\Delta x_o + \Delta x_n}{\bar{D}_{on}} = \frac{\Delta x_o}{D_o} + \frac{\Delta x_n}{D_n}, \qquad (4.9)$$

where D_o and D_n are the diffusion coefficients for cells o and n.

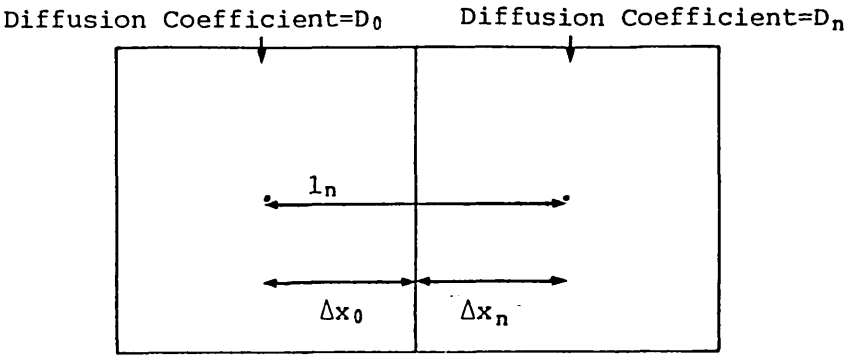

Fig. 4.9. Leakage Between Cells in the Diffusion Theory Calculations.

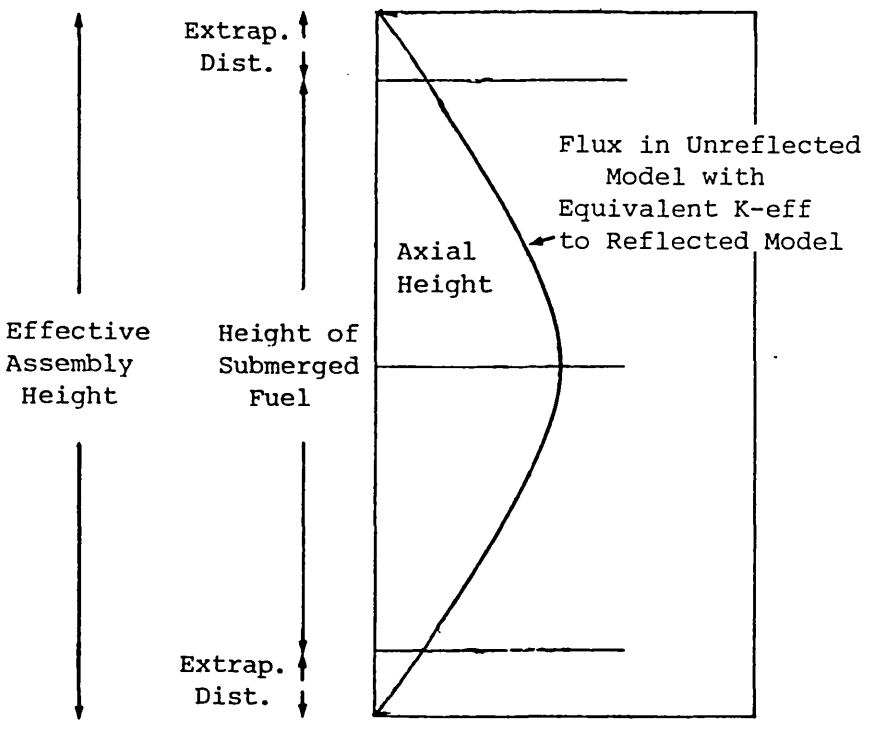

Fig. 4.10. The Effective Assembly Height.

The multigroup finite-difference equations can also be run in source mode using SNAP in which case there is no eigenvalue k and an extra term not containing neutron flux is added to the right hand side to represent the imposed source:

$$Q_o = \sum_{h=1}^{G} \Sigma_o^{(hg)} \phi_o^{(h)} + \sum_{m=1}^{M} \chi_o^{(mg)} \sum_{h=1}^{G} (\nu\Sigma_f)_o^{mh} \phi_o^{h} + R_o, \qquad (4.10)$$

where R_o is the imposed source in cell o in neutrons sec^{-1} unit $volume^{-1}$.

For the correction factor calculations it was assumed that each assembly was effectively of constant composition axially, justifying the use of two-dimensional models. To account for the finite axial height of each assembly, an axial buckling was used appropriate to the assumed cosine-shaped persisting axial distribution of neutrons (section 4.1.2). The value of the buckling was calculated from:

$$B_a^2 = (\pi/H)^2, \qquad (4.11)$$

where H = water height + bottom extrapolation distance + top extrapolation distance.

This is illustrated in Figure 4.10 (previous page).

For all the fully flooded configurations, the extrapolation distance was estimated to be 7cm (7) giving an axial buckling of $0.00143cm^{-2}$. In the 196 pins per compartment, 33cm water height configuration, the extrapolation distance was taken as 7.18cm giving an axial buckling of $0.0044cm^{-2}$. For both versions of the reference configuration, the axial buckling was adjusted to correspond to a height smaller than the actual water height plus extrapolation distances, in order that the calibrated reactivity was yielded by the eigenvalue calculation:-

(i) Reference configuration, standard source positions: $B_a^2=0.00294cm^{-2}$, corresponding to 49cm water height +4.47cm top and bottom extrapolation distance.

(ii) Reference configuration, alternative source positions: $B_a^2=0.00300cm^{-2}$, corresponding to 48.2cm water height +4.58cm top and bottom extrapolation distance.

These reduced extrapolation distances were necessary since a buckling corresponding to the actual extrapolation distance gave k-eff > 1 in each diffusion theory calculation. For a supercritical assembly the neutron flux is time dependent and thus not suitable for a correction factor calculation.

For all the configurations the same radial geometry was used in the diffusion theory calculations as in the cross-section preparations; the large amount of water (17.5cm) outside the skip in the model was sufficient to contain easily the positions of the detectors outside the skip.

No account was made in the diffusion theory calculations of the detectors themselves. For all detectors in the same environment in both the reference and unknown subcritical configurations, the perturbation of the detector to the flux was expected to be the same in both cases. This is clearly not true for the detectors in the clusters in the 221 pin cluster configurations and for all detectors in the compartmental corners. Accordingly, subsidiary calculations were performed to determine the perturbations of the detectors. These calculations are described in Chapter 7.

To produce the correction factors, one eigenvalue and one source calculation was run using SNAP for each configuration, both sets of fluxes being stored on disk. The model described above was used for both eigenvalue and source calculations with an imposed source being additionally included for each source calculation. The source strength per unit volume was equated with the actual source strength by the following relation:

$$R \times A \times 2^n \times \int_{-H/2}^{+H/2} \cos^2 \frac{\pi x}{H}\, dx = \sum_{i=1}^{N} S_i \cos \frac{\pi x_i}{H}, \qquad (4.12)$$

where: R is the source strength per unit volume in the two-dimensional calculation;

A is the total area of the source meshes (Figs. 4.7 and 4.8);

n is the number of planes of reflection (equal to two);

H is the effective height of the assembly, related to the axial buckling by $H=\pi/\sqrt{B_a^2}$;

S_i is the actual strength of the i^{th} source;

N is the number of sources; and

X_i is the distance of the i^{th} source from the midplane of the assembly.

The left hand side in Equation 4.12 represents the three-dimensional model equivalent to the two-dimensional model used in the source calculations. This model is of constant composition axially, and of height given by the axial buckling (Equation 4.11). The source strength has the same axial variation as the flux, that is, a cosine function.

Hence the effective three-dimensional source is equal to

$$R \times A \times 2^n \times \int_{-H/2}^{+H/2} \cos \frac{\pi x}{H}\, dx.$$

Since the importance varies axially as a cosine function in this model also, the importance-weighted source strength is as on the left hand side of Equation 4.12.

The right hand side of Equation 4.12 represents a three-dimensional model in which the experimental sources are explicitly represented. The importance weighting is assumed to be the same function as on the left hand side. This was thought to be a valid assumption provided that the model has no axial variation in composition over most of its height.

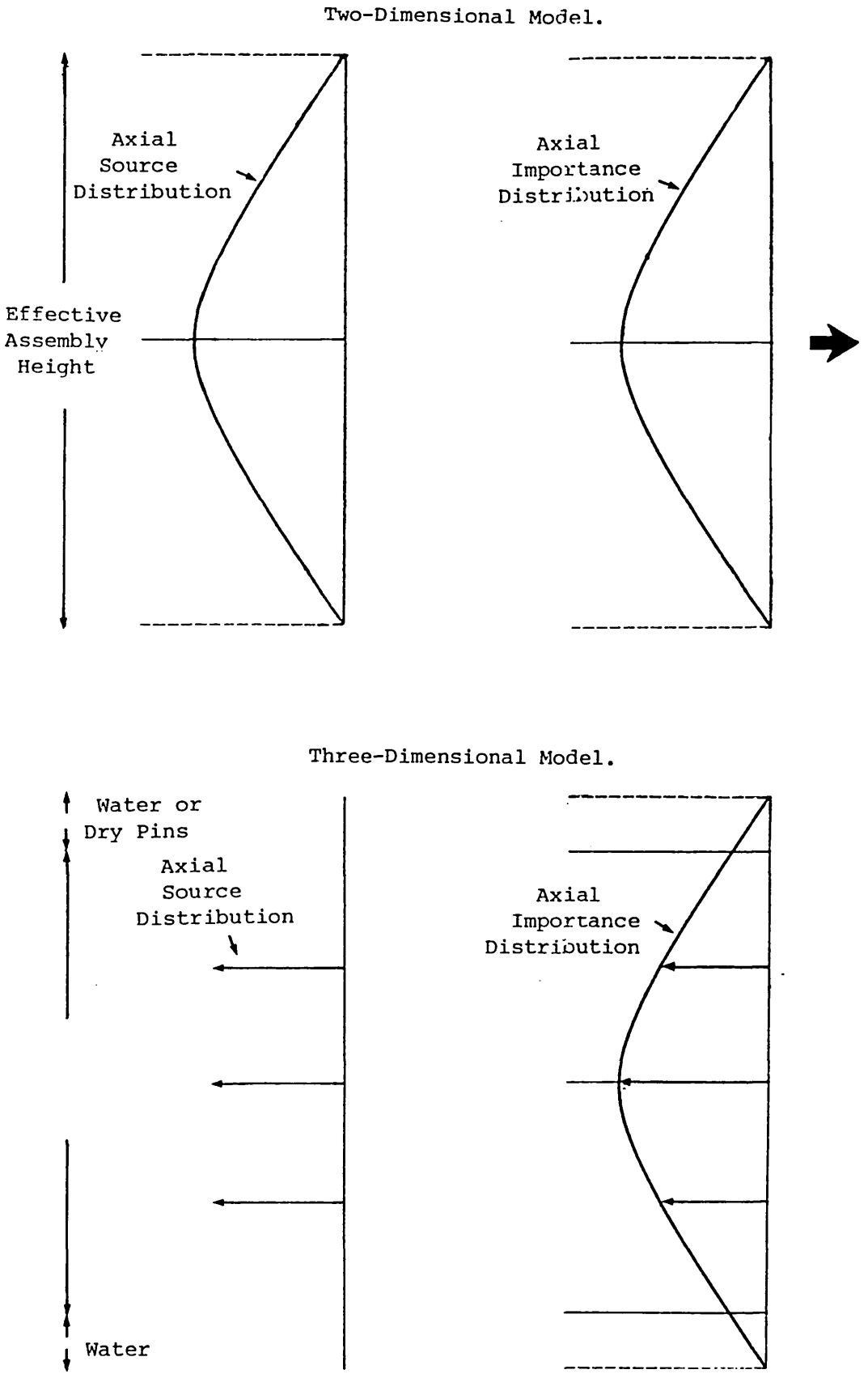

Fig. 4.11. The Equivalence of Source Strength in the Two-Dimensional and Three-Dimensional Models.

This is the case for the skip configurations studied. However, it was expected that close to the sources the assumption of a cosine function for the axial importance would be invalid.

The equivalence of the two models represented in Equation 4.12 is illustrated schematically in Fig. 4.11 (previous page).

An analysis of the validity of Equation 4.12 for the detector positions used was undertaken by comparisons of two-dimensional and three-dimensional calculations. These are described in Chapter 7.

Below are the actual source strengths employed both experimentally and in the measurements.

Total experimental source strength, beginning of measurements = $4.17 \times 10^{7} ns^{-1}$, divided evenly between the two source tubes.

Table 4.6 Experimental and Calculational Source Strengths

Configuration	Height of Assembly in Calculation	$\sum_{i=1}^{N} S_i \cos\left(\frac{\pi x_i}{H}\right)$ (ns^{-1})	R, $ns^{-1}\ cm^{-3}$
Reference, standard sources	(49+2x4.47)cm	2.967×10^{7}	3.996×10^{4}
Reference, alternative sources	(48.2+2x4.58)cm	2.940×10^{7}	3.996×10^{4}
Fully flooded configurations	(69+2x7.0)cm	3.562×10^{7}	3.345×10^{4} (112 pin clusters) 2.973×10^{4} (221 pin clusters)
196 pins per compartment, 33cm water height	(33+2x7.18)cm	3.350×10^{7}	5.519×10^{4}

Note that the lower values for importance-weighted experimental source strength in the reference configurations results from the greater degree of spreading of the sources in the reference configurations (Figure 4.4). The two different values of source strength per unit volume in the fully flooded configurations result from the differing areas of the source meshes in the 112 and 221 pin cluster models (Figs. 4.7 and 4.8).

The imposed sources were split between energy groups 1 and 2 in the SNAP source calculations in the ratio 4.089:1. This was estimated from a graph of the californium 252 emission spectrum (8). Finally, it is noted that the normalisation of the above source strengths is of no consequence to the correction factors since they only depend on the ratio of two calculated count rates.

It was realised that problems would be experienced in the convergence of the source mode calculations for the two reference configurations (9). Use of the coarse-mesh rebalance facility (5) in these calculations was thus made, the aim being that accelerated elimination of higher modes would force the flux solution rapidly to the presumed fundamental mode in these configurations.

4.2.3 Detector Cross-Sections

Separate PERSEUS calculations were run in selected configurations to prepare boron 10 and uranium 235 cross-sections for conversion of the SNAP source mode fluxes to reaction rates. (The term reaction rate is the calculated equivalent of an experimental count rate.) The configurations used in these calculations were the 196 pins per compartment, the 112 pin clusters, centred, and the 221 pin clusters, centred. Low density boron 10 and uranium 235 were incorporated in selected meshes corresponding to the positions of some of the detectors in the measurements (Figure 4.12).

It was assumed that the cross-sections would be dependent only on immediate environment, making superfluous the modelling of every configuration for their prepartion. Additionally the densities of the

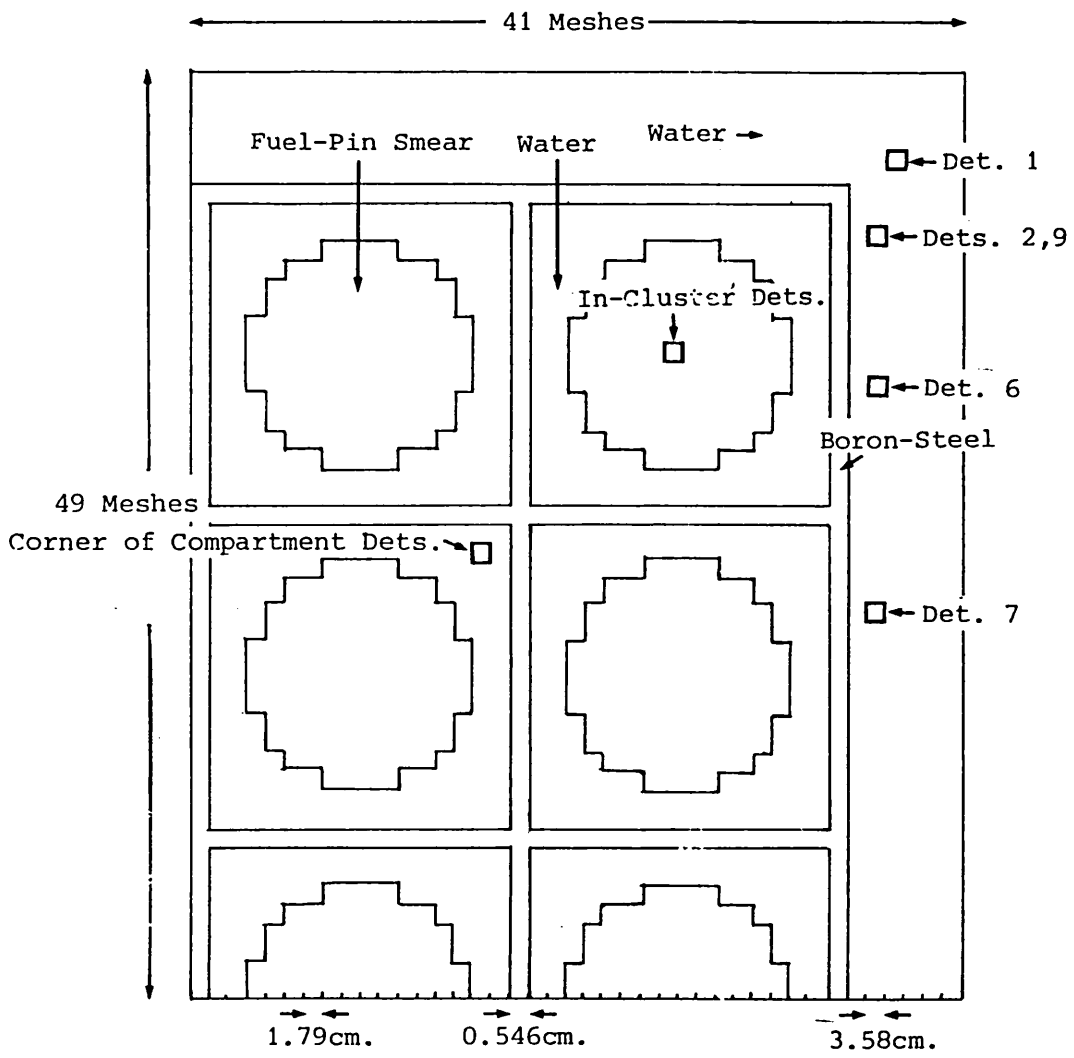

Fig. 4.12. Calculational Model to Produce the Detector Cross-sections.

detection materials as modelled were arbitrary, since the correction factors depend only on ratios of reaction rates.

4.2.4 Computation of Correction Factors and Modified Source Multiplication Reactivities

A FORTRAN program, 'MSM', converted source mode fluxes to reaction rates, and using experimental count rates and the calibrated reactivity of the reference configuration, produced a modified source multiplication reactivity for each of the detectors. This comprised the production of a file containing information from the reference configuration, and secondly, the production of reactivities from this file and from data for the unknown subcritical configuration. The process is illustrated in Figure 4.13.

The radial positions of the detectors were defined by specifying a square of 2x2 meshes and corresponding weights for each mesh. Each weight was proportional to the inverse lateral distance of the measured centre of the detector from the centre of the mesh (Figure 4.14).

In Figure 4.14, the weights assigned to the fluxes ϕ_{11}, ϕ_{12}, ϕ_{21}, ϕ_{22} are $W_{11}=1$, $W_{12}=Y_1/Y_2$, $W_{21}= X_1/X_2$, $W_{22} = x_1Y_1/x_2Y_2$. (4.13)

This analysis assumes:

(i) Linear interpolation of flux between mesh centres;

(ii) Separate x- and y-axis flux dependence over the four mesh points ie:

$$\phi_{22} = \phi_{11} \times \frac{\phi_{12}}{\phi_{11}} \times \frac{\phi_{21}}{\phi_{11}}. \qquad (4.14)$$

The average flux in group g for the detector is thus:

$$\overline{\phi_{dg}} = \frac{W_{11}\phi_{11g} + W_{12}\phi_{12g} + W_{21}\phi_{21g} + W_{22}\phi_{22g}}{W_{11} + W_{12} + W_{21} + W_{22}}. \qquad (4.15)$$

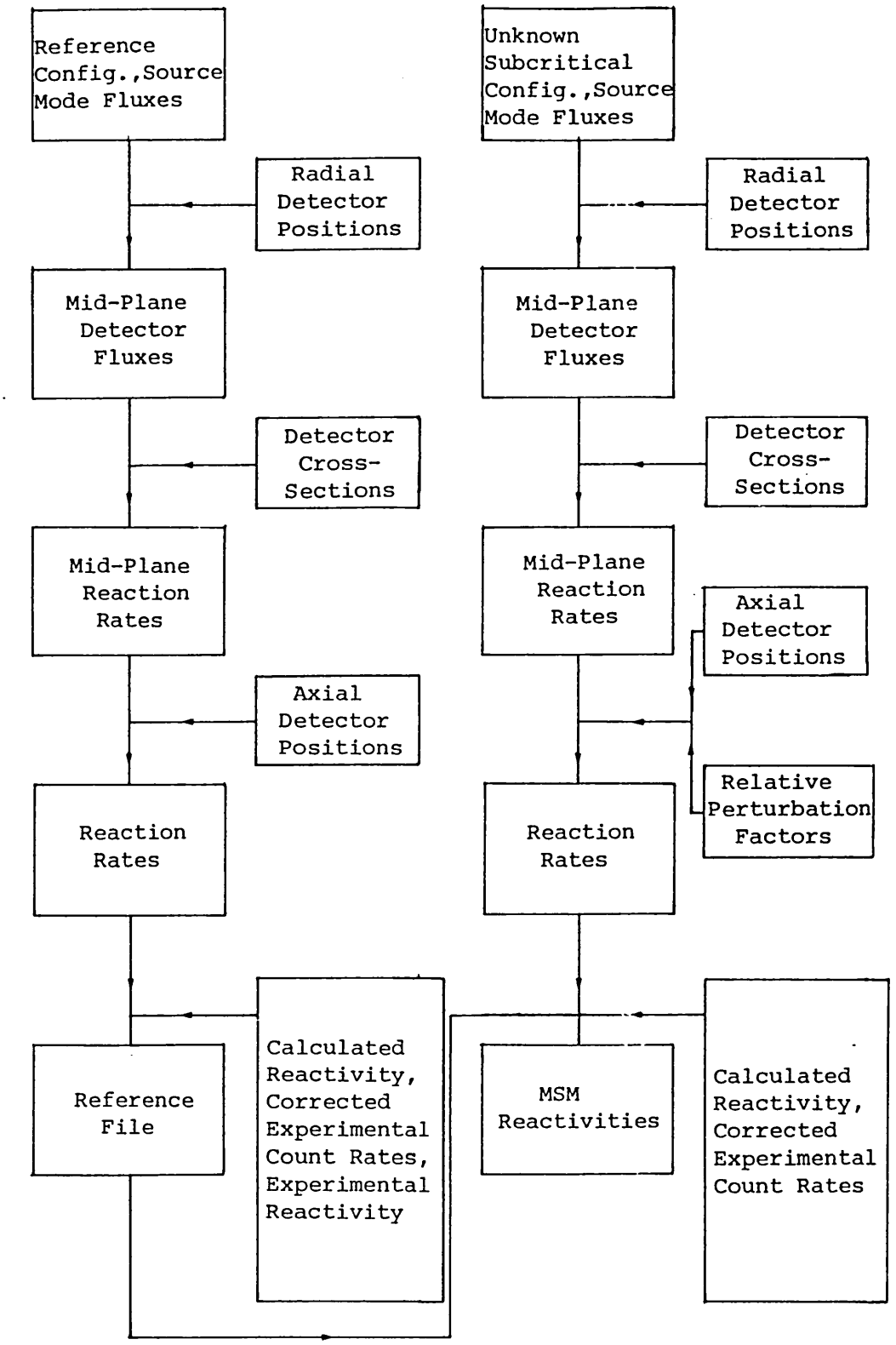

Fig. 4.13. The Calculation of Reactivities from the MSM Technique

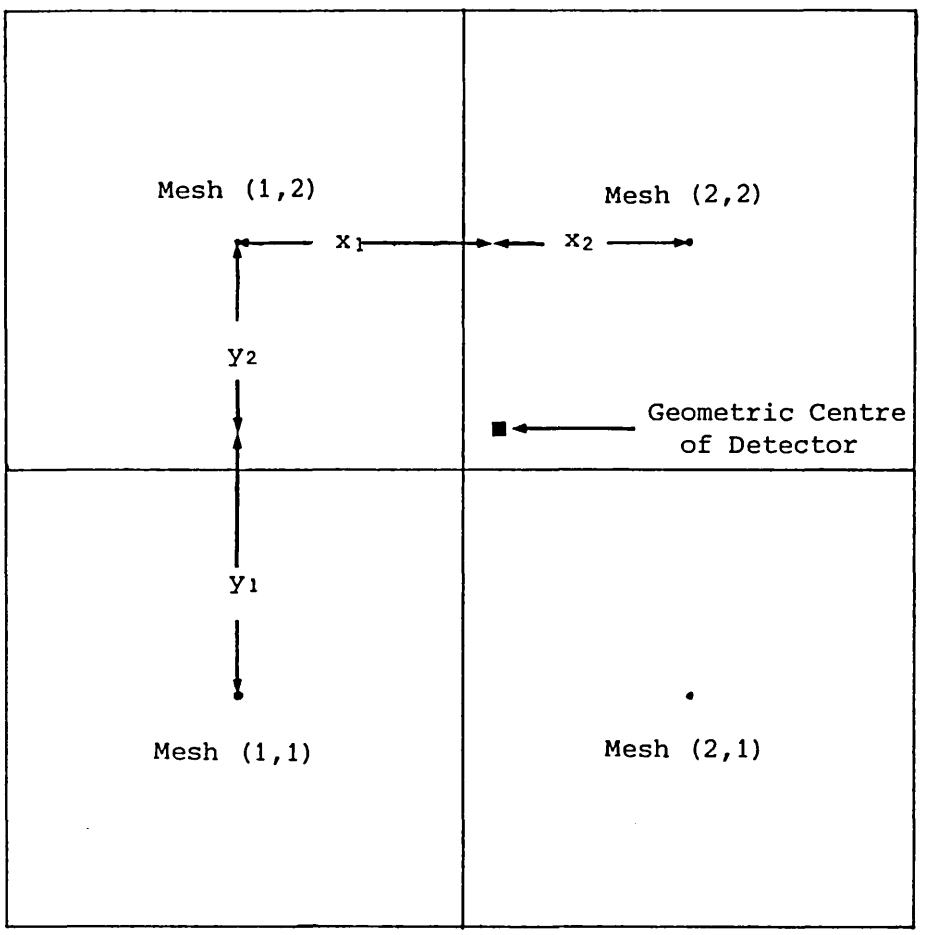

Fig. 4.14. The Representation of Detector Positions in the Correction Factor Calculations.

Detector cross-sections produced using PERSEUS (section 4.2.3) were normalised by a factor constant for each detector to bring them close to the nominal sensitivity of the detector in counts sec^{-1} unit thermal $flux^{-1}$ (3). Note that this normalisation does not affect ratios of reaction rates. It was carried out to gain an idea of whether count rates might eventually be predicted absolutely, a purpose examined at the end of this thesis.

Midplane count rates were then produced by the operation:

$$RCR_d = \sum_{g=1}^{G} \overline{\phi_{dg}}\ \sigma_{dg}, \qquad (4.16)$$

where: RCR_d is the midplane count rate for a detector; and
σ_{dg} is the normalised detector cross-section in group g, calculated using PERSEUS.

Finally, the midplane count rates were converted to reaction rates by multiplying by a factor to account for the expected cosine-shaped axial flux distribution in each assembly. According to Equation 4.12, the source mode fluxes calculated using the source strength R are those appropriate to the midplane of the assembly. The average flux over a detector's active length is thus not $\overline{\phi_{dg}}$ but $\overline{\phi_{dg}} \cdot \cos_d$ where

$$\cos_d = \int_{\text{active length}} \cos \frac{\pi x}{H}\, dx, \qquad (4.17)$$

where x is the distance from the midplane of the assembly.

Cosine factors for all detectors were calculated from measured detector heights (section 4.1.2) and the heights of the assemblies as modelled in the calculations (Table 4.6). The reaction rates were given by:

$$CR_d = RCR_d \times \cos_d, \qquad (4.18)$$

where CR_d is the reaction rate for the detector.

Correction factors were then computed from the reaction rates and the calculated reactivities:

$$CF_d = \frac{\rho_2 \, CR_{2d}}{\rho_1 \, CR_{1d}}, \tag{4.19}$$

where CF_d is the correction factor for a detector.

The suffixes '2' and '1' refer to the unknown subcritical and reference configurations respectively.

In the case of each detector which was in a different environment in the unknown subcritical and the reference configuraitons, the correction factor was adjusted by a relative perturbation factor to account for the different perturbations of the detector in the two configurations:

$$CF_d = \frac{\rho_2 \, CR_{2d}}{\rho_1 \, CR_{1d}} \times RPF_d, \tag{4.20}$$

where RPF_d is the relative perturbation factor for the detector.

The relative perturbation factors were produced from subsidiary calculations of detector perturbations described in chapter 7.

A reactivity for each detector was calculated from the equation:

$$\rho_{2d} = \rho_{1expt} \times CF_d \times \frac{CR_{1d\ expt}}{CR_{2d\ expt}}, \tag{4.21}$$

which is the modified source multiplication equation applied to detector d.

Alternatively groups of detectors were considered as one:

$$\rho_{2g} = \rho_{1expt} \times \left(\frac{\rho_2 \sum_{d=1}^{nd} CR_{2d}}{\rho_1 \sum_{d=1}^{nd} CR_{2d}} \right)_{calc} \times \frac{\sum_{d=1}^{nd} CR_{1d\ expt}}{\sum_{d=1}^{nd} CR_{2d\ expt}} \qquad (4.22)$$

where nd is the number of detectors in the group.

5. The Calibration of the Reference Configuration

It was stated in the previous chapter that two versions of the reference configuration were used, one for the standard source positions and the other for the alternative source positions. This was because the change in the positions of the source tubes meant that a different water height was required to attain the same value of subcritical reactivity which was desired for each of the two versions. The calibration of the reference configuration for the alternative source positions was made by a simple adjustment to the data used for the former version of the reference configuration.

5.1 The Reference Configuration for the Standard Source Positions

A two-stage process determined the water height for the reference configuration using the standard source positions. Firstly, with both the sources and detectors in their standard positions in the 196 pins per compartment configuration, the critical water height was found by extrapolation. This technique relies on the fact that for very small degrees of subcritical reactivity, the count rate of any detector is inversely proportional to subcritical reactivity (section 3.2.3). Additionally, for small water height changes close to the critical water height, the value of $d\rho/dh$ was known to be almost constant (1). Hence, by plotting the reciprocals of the count rates of several detectors against water height, a value for the critical water height was found. This is illustrated schematically in Fig. 5.1.

Secondly, the water-height drop from the critical water height was selected with two considerations in mind:

(i) Changes in reactivity due to small temperature shifts were to be small.

(ii) The value of $d\rho/dh$ was to be determined over the range of water heights between that of the reference configuration and the critical water height (section 3.3).

With regard to the first consideration, the change in reactivity with temperature was expected to be virtually constant over small changes in

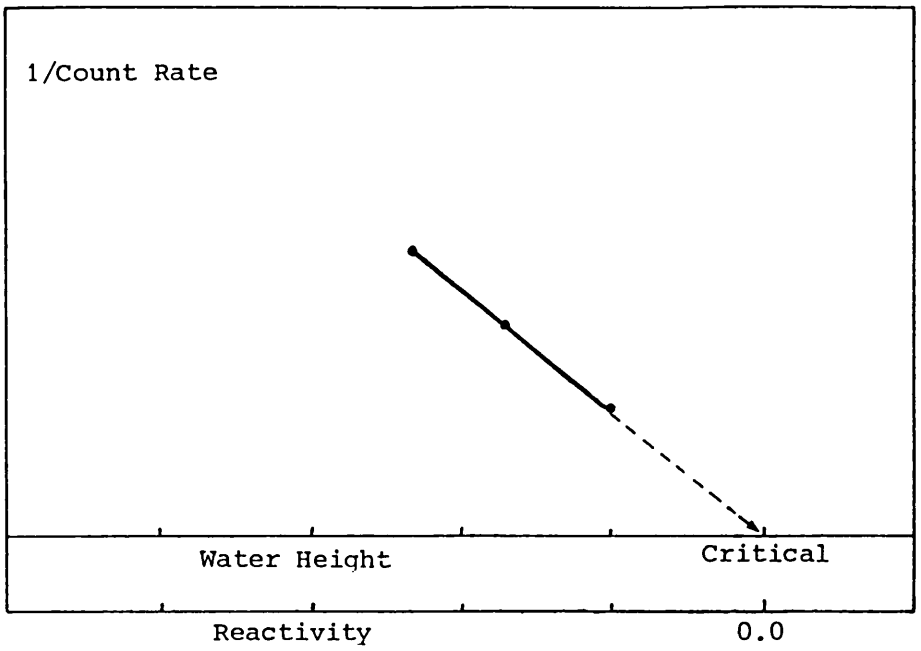

Fig. 5.1. The Determination of the Critical Water Height By Extrapolation.

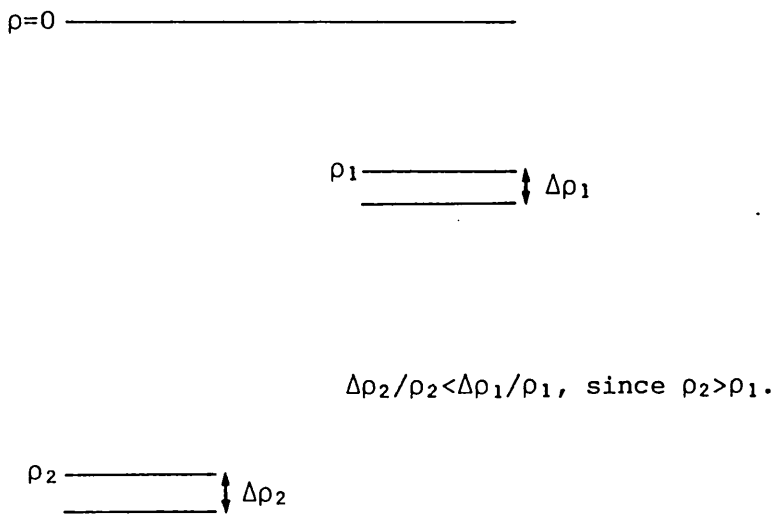

Fig. 5.2. The Sensitivity of Reactivity to Temperature Changes.

water height. This, however, means that the proportional change in reactivity with temperature becomes larger with decreasing reactivity, as shown schematically in Fig. 5.2. Accordingly, the subcritical reactivity of the reference configuration was to be sufficiently large so as not to be substantially affected by changes in the environmental temperature around the skip.

The experimental results which led to the determination of the reference configuration are now examined.

5.1.1 Determination of Water Height

At a temperature of 18.3°C, the critical water height was found by extrapolations using the count rates from a number of detectors to be 52.26cm up the fuel pins, measured as 186.01cm±0.005cm on the precise level gauge. Experimental $d\rho/dh$ values had been obtained previously for the same assembly at water heights of 52.09cm, 50.52cm and 49.96cm up the fuel pins, from period measurements (1,2). (These heights were measured respectively as 185.84cm, 184.27cm and 183.71cm on the precise level gauge). To make period measurements possible at the above three water heights, the assembly was made more reactive by replacing one source tube and then both source tubes with fuel pins. The $d\rho/dh$ values are tabulated below, with the number of source tubes included.

Table 5.1. Experimental $d\rho/dh$ Values

Precise Geometry of Assembly	Water Height Above Bottom of Fuel (cm)	PLG Height (cm)	$d\rho/dh$ (dρ/cm)
2 source tubes (containing steel spacers)	52.09	185.84	0.001960±0.000028
1 source tube (empty)	50.52	184.27	0.002108±0.000033
No source tubes	49.96	183.71	0.002239±0.000029

The main random contribution to the uncertainty in $d\rho/dh$ was the uncertainty in water height measurement which was approximately ±0.01cm for a single reading. Though repeated determinations might have lowered this value, experience suggested caution (1) and the single reading error was taken, resulting in an uncertainty of roughly 1.5% as above.

Also associated with these results is a systematic error of 5% r.m.s. due to errors in the delayed neutron data (3). It should also be noted that two of the values of $d\rho/dh$ in Table 5.1 are appropriate to one or no source tubes in the skip instead of the two source tubes in the reference configuration. The shift in $d\rho/dh$ at a given water height due to the replacement of one or both source tubes with fuel pins can be given as follows:

$$\text{Firstly, } d\rho/dh = d\rho/dB^2 \times dB^2/dh, \tag{5.1}$$

where B^2 is the axial buckling. Now on the right hand side of equation 5.1, only $d\rho/dB^2$ may change at a given water height due to a change in the geometry of the assembly. For k-eff ≈ 1,

$$d\rho/dB^2 \approx d\ (1-1/k\text{-eff})/dB^2 \approx d\ ((1+M^2B^2)/-k_\infty)/dB^2, \tag{5.2}$$

where k_∞ is the k-infinity of the assembly geometry and M^2 is the migration area. The leakage relation in the above equation is approximate (4).

$$\text{Hence } d\rho/dB^2 \approx -M^2/k_\infty. \tag{5.3}$$

Considering the right hand side of Equation 5.3, the replacement of one or both source tubes changes the proportion of water in the assembly by a small fraction of one percent, and thus has a correspondingly small effect on the migration area. However, at a given water height, the k-infinity changes in the same proportion as the k-eff, since the leakage fraction remains constant. Hence $d\rho/dB^2$, and therefore $d\rho/dh$, changes by up to about 0.4% (section 4.1.1) due to the replacement of the source tubes.

The calculated value for the temperature coefficient of reactivity in the critical configuration was found to be 2×10^{-4} $\delta\rho/°C$ (5). Hence in order to restrict the proportional change in reactivity due to a temperature shift of 1°C to, say, 2%, a subcritical reactivity of 0.01 was required. However, the experimental $d\rho/dh$ values in Table 5.1 extended only to (52.26-49.96)cm = 2.30cm below the critical water height, corresponding to a negative reactivity of about 0.005.

As a compromise a water height of 3.26cm below the critical water height was chosen, it being assumed that the $d\rho/dh$ values at heights below 49.96cm up the fuel pins would not depart too greatly from the value of 0.002239 $\delta\rho$/cm at that height. The proportional change in the reactivity of the reference configuration due to a temperature shift of 1°C was thus approximately $2\times10^{-4}/(3.26\times0.002)$ = 3%.

Finally it should be noted that the values of $d\rho/dh$ in Table 5.1 applied to temperatures about 2°C different from the temperature of 18.3°C used for the critical water height and the reference configurations. From Equation 5.3, the change in $d\rho/dh$ with temperature can be derived since only $d\rho/dB^2$ and not dB^2/dh varies with temperature.

$$d/dT\ (d\rho/dB^2) \approx d/dT\ (-M^2/k_\infty). \qquad (5.4)$$

On the right hand side of Equation 5.4 the fractional change with temperature is dominated by that of the age-to-thermal which amounts to roughly 1.6×10^{-3}/°C (6). Hence the fractional change in $d\rho/dh$ due to the temperature shift of 2°C is roughly 0.3%.

5.1.2 Determination of Reactivity

The reactivity at the chosen water height of (52.26-3.26)cm = 49 cm up the fuel pins was determined by integration of the $d\rho/dh$ vs precise level gauge height curve as shown in Fig. 5.3. Linear interpolation was made between the three known $d\rho/dh$ values, and extrapolation made to a value at 49.00cm. Calculation of the area under the graph then gave the reactivity at 49.00cm:

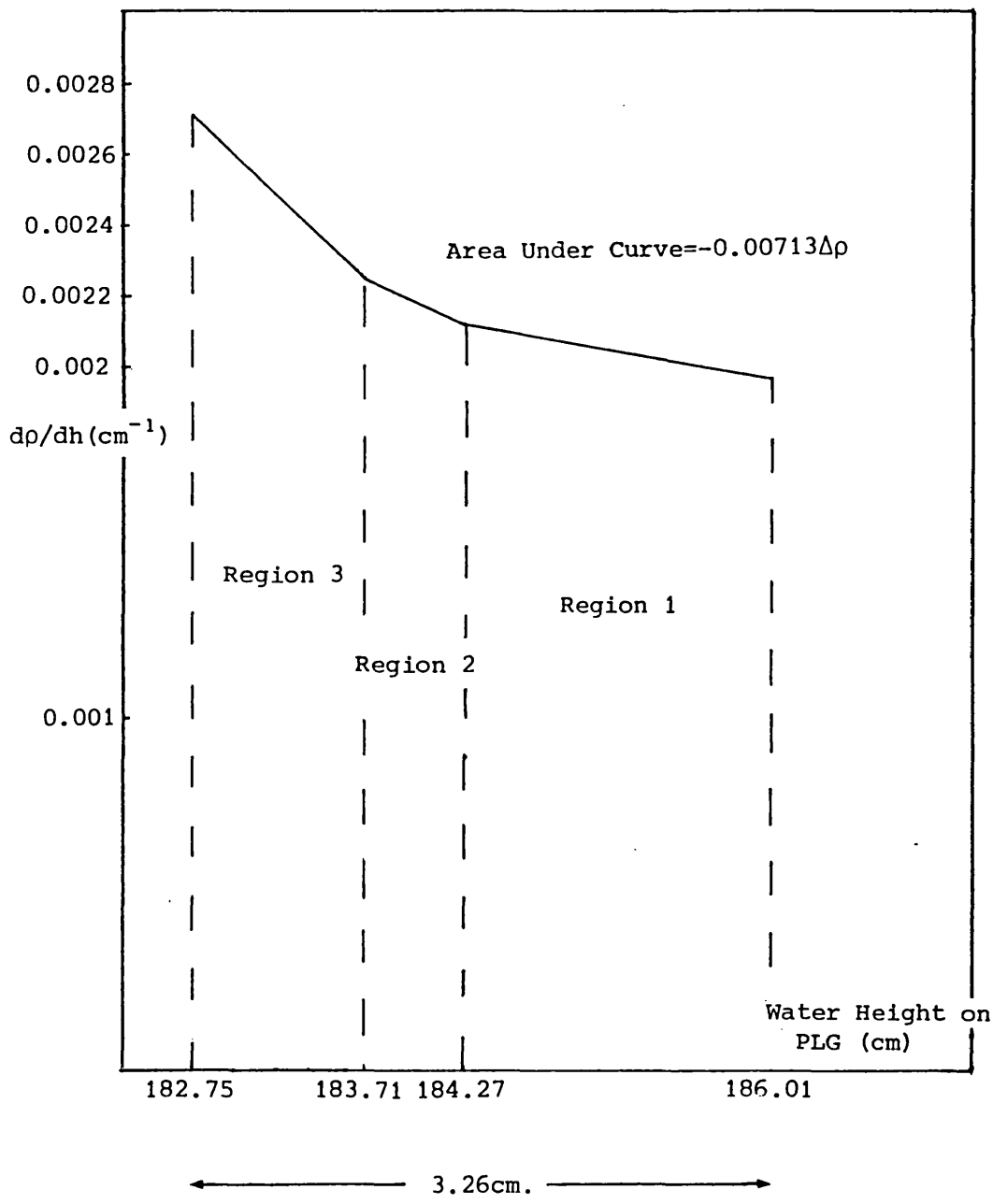

Fig. 5.3. Integration of the dρ/dh Curve to Give the Reactivity of the Reference Configuration.

Table 5.2 Integration of $d\rho/dh$ Curve to Give the Reactivity of the Reference Configuration

Region Under Curve (Fig. 5.3)	$\overline{d\rho/dh}$ in Region ($\delta\rho$/cm)	Δh (Width of Region) (cm)	Area of Region $=\overline{d\rho/dh}\ \Delta h(\delta\rho)$
1	0.002034	1.74	0.00354
2	0.002174	0.56	0.00122
3	0.002470	0.96	0.00237
			0.00713

Hence the reactivity of the reference configuration was determined as -0.00713.

Errors due to the linear interpolations between 52.09cm and 49.96cm are clearly small. The assumed value of $d\rho/dh$ at 49.00cm has an estimated error of 8% resulting in a 4% error in the area of region 3 and thus a 1.5% error in the reactivity, for the fractional area of region 3.

A summary of the errors in the reactivity of the reference configuration is given below.

Table 5.3 Errors in the Reactivity of the Reference Configuration

Nature of Error	% of ρ
Determination of water height in extrapolations	0.2
Delayed neutron data	5
Determination of water height in period measurements	1.5
Determination of area under $d\rho/dh$ curve	1.5
Geometry changes in period measurements	0.4
Temperature dependence of $d\rho/dh$	0.3

These give a total error of 5.5% r.m.s, and the reactivity of the reference configuration for the standard source positions is thus $-(0.713\pm0.039)\times10^{-2}$ at a temperature of 18.3°C. An alternative determination of this reactivity was also made using the mean value of $d\rho/dB^2$ over the water height drop (Appendix B).

5.1.3 Alternative Determination of Reactivity

Another method was also used to determine the reactivity of the reference configuration (7). In this method a calculated reactivity was corrected by the ratios of experimental and calculated $d\rho/dh$ values over the range of water heights involved. Calculations using the two-dimensional model described in the last chapter, and the transport theory code TWOTRAN (8) gave the following k-eff values for the 196 pins per compartment configuration:

Table 5.4 Calculated k-eff Values Close to the Critical Water Height

Water Height, Calculated from Axial Buckling (cm)	k-eff
52.26	1.0123
49.00	1.0045

The calculated reactivity decrement for the water height drop from critical to the reference configuration was thus -0.00768. In Table 5.5 are the calculated and experimental $d\rho/dh$ values over this range:

Table 5.5 Comparisons of Calculated and Experimental $d\rho/dh$ Values

Water Height (cm)	Calculated $d\rho/dh$ ($\delta\rho$/cm)	Experimental $d\rho/dh$ ($\delta\rho$/cm)	Calculated $d\rho/dh$/ Experimental $d\rho/dh$
52.09	0.00211	0.001960	1.077
50.52	0.00231	0.002108	1.096
49.91	0.00240	0.002239	1.072

The mean ratio of calculated and experimental $d\rho/dh$ values over the range of 52.26cm-49.00cm was equal to 1.08. Thus the reactivity of the reference configuration is equal to -0.00768/1.08 or -0.00711. Errors inherent in this method differ from those in the original method in that the errors introduced in extrapolating to a $d\rho/dh$ value at 49.00cm and interpolating between known $d\rho/dh$ values have been replaced by errors in the calculated/experimental ratios. These are insensitive to changes in

water height in this range, and hence the second method is probably marginally the better of the two.

5.2 The Reference Configuration for the Alternative Source Positions

With the source tubes in the alternative positions (Fig. 4.3), the critical water height was found by extrapolation to be 51.33cm up the fuel pins, measured as 185.08cm on the precise level gauge or 0.93cm lower than the critical water height for the standard source positions. It was decided to use, for the alternative source positions, the same reactivity in the reference configuration as for the standard source positions.

The required drop from the critical water height was calculated using the following relation:

$$h_a = \frac{h_s \cdot \overline{(d\rho/dh)}_s}{\overline{(d\rho/dh)}_a} \approx \frac{h_s \cdot (d\rho/dh)_{calc,s}}{(d\rho/dh)_{calc,a}} , \qquad (5.5)$$

where: h_a is the required water height drop using the alternative source positions;

h_s is the water height drop (3.26cm) used for the standard source positions (h_a and h_s are illustrated schematically in Figure 5.4);

$\overline{(d\rho/dh)}_s$ is the mean $d\rho/dh$ value over the water height drop using the standard source positions;

$\overline{(d\rho/dh)}_a$ is the mean $d\rho/dh$ value over the water height drop using the alternative source positions;

$(d\rho/dh)_{calc,s}$ is the calculated $d\rho/dh$ value at the critical water height using the standard source positions; and

$(d\rho/dh)_{calc,a}$ is the calculated $d\rho/dh$ value at the critical water height using the alternative source positions.

Equation 5.5 is valid provided that the ratio of average $d\rho/dh$ values over the respective water height drops is well represented by the ratio of calculated $d\rho/dh$ values at the critical water heights. It has

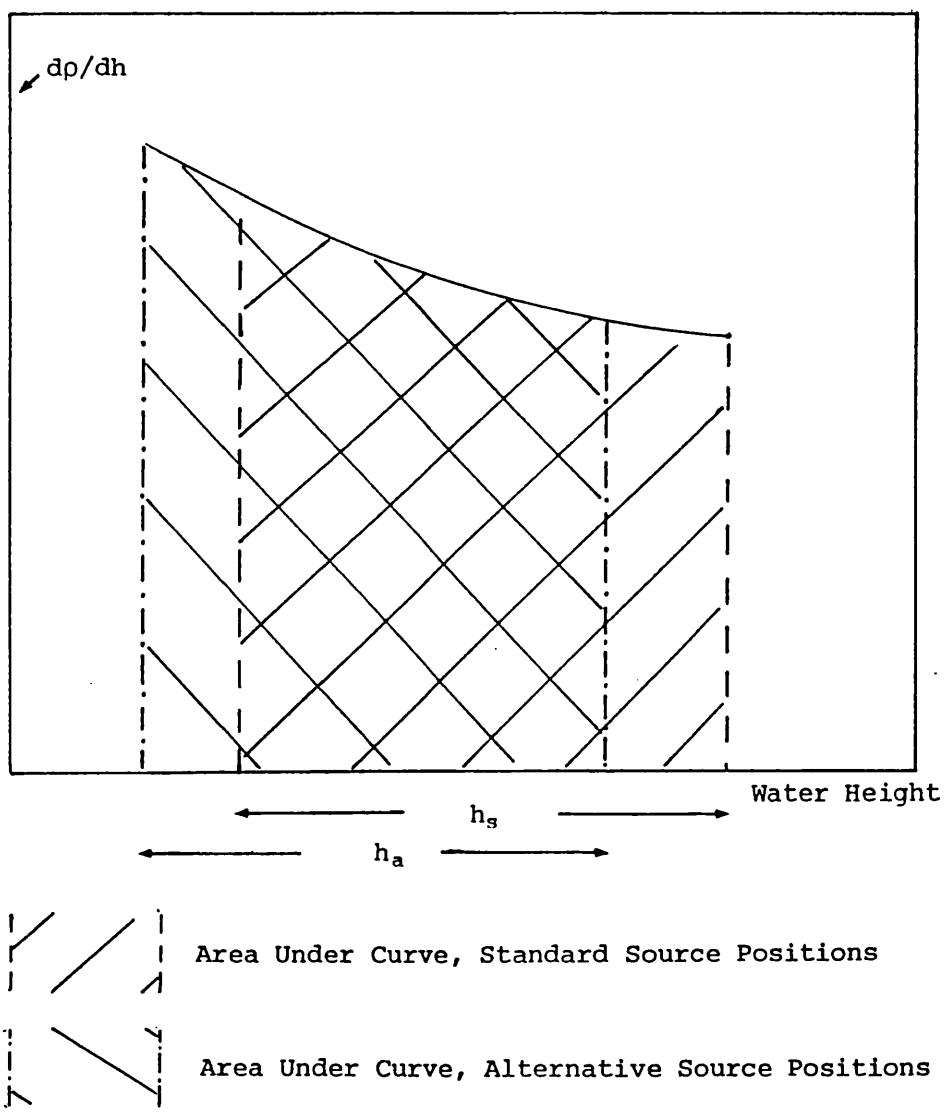

Fig. 5.4. The Water Height Drops For the Two Versions of the Reference Configuration.

already been shown, however, that the ratio of calculated/experimental $d\rho/dh$ values is almost constant over the range of water heights in question (Table 5.5) and so only a small error is introduced by the use of Equation 5.5.

The value of $d\rho/dh$ at the critical water height using the alternative source positions was found to be equal to 0.00220 by TWOTRAN calculations which modelled the source tubes in their alternative positions. Hence the required water height drop was equal to 3.26cmx0.00211/0.00220 or 3.13cm, where the calculated value of $d\rho/dh$ for the critical water height using the standard source positions has been derived from Table 5.5. This water height drop corresponded to a height of (51.33-3.13=48.2)cm up the fuel pins which was the height used for the reference configuration.

6. Subsidiary Measurements

In addition to those measurements necessary for the determination of reactivities using MSM, a number of subsidiary measurements were carried out. These were primarily to quantify the experimental errors aside from those associated with the calibration of the reference configuration. They were thus concerned with the corrected experimental count rates featuring in the calculations of modified source multiplication reactivities (Equation 4.21) and are now described.

6.1 Reproducibility of Count Rates

Apart from the random counting errors, which were in all cases less than about 1%, as explained in section 4.1.3, each count rate contained errors associated with its reproducibility. In general, if a count rate from a detector in a given assembly is repeated at a later date, the count rate differs; this difference is governed by the reproducibility of:

(i) The detector environment if the assembly is rebuilt;

(ii) The detector position, which in the case of the detectors in the skip is influenced by the possible bending of the pin can containing the detector;

(iii) The detector geometry, which may have changed due to the replacement of the tube, or the plug or cable;

(iv) The detector sensitivity. This was examined in section 4.1.4 and was shown to contribute an error of about 1% to a ratio of corrected experimental count rates, when a change of detector occurred.

Of the first three contributions to count rate reproducibility, that due to detector positioning is considered first since the other two contributions implicitly contain detector positioning errors also.

6.1.1 Detector Positions

Of the nine detectors only the four inside the skip were repositioned with their tubes in the measurements. Accordingly, in most of the fully flooded configurations, repeat count rates were taken in the standard detector positions, after all the count rates in the alternative detector positions had been obtained. These count rates were compared with the original count rates to give the approximate reproducibility errors due to detector positioning. In the table below are the percentage changes in count rates from the detectors in the skip on their repositioning. No corrections have been made for source decay since the count rates were obtained within a few days of one another in each case.

Table 6.1 Percentage Count Rate Changes for Detector Repositioning

Configuration	Percentage change on repositioning			
	Det 3	Det 4	Det 5	Det 8
112/76 (CTD)	+0.9	-5.5	-1.0	+0.9
112/76 (G4)	-0.3	+0.9	-4.0	-0.7
112/76 (CC)	+2.9	-0.5	-0.9	-0.8
112/76 (CCD)	-0.6	-0.5	+0.0	+0.1
Root mean square change	1.6	2.8	2.1	0.7

It was concluded that the contribution to the total reproducibility error for each detector in the skip due to its positioning was about 2% r.m.s.

6.1.2 Detector Geometry

On one occasion the tubes containing the detectors in the skip were replaced. Count rates were recorded before and after the change to show the reproducibility error due to changes in detector geometry. In Table 6.2 are the percentage changes in count rate, on the replacement of the tubes.

Table 6.2 Percentage Count Rate Changes due to Replacement of Tubes

Configuration	Percentage Change on Tube Replacement			
	Det 3	Det 4	Det 5	Det 8
221/76 (CTD)	+0.7	+13.3*	-2.4	+2.2

*After this count rate was recorded, the pin can containing the detector was found to be misplaced; hence the result was ignored.

The above results inevitably include the errors due to detector positioning, and it was concluded that no extra error resulted from the changing of the tubes.

6.1.3 Rebuilding of Assemblies

Repeat count rates were taken for the detectors in the standard positions from the rebuilds of the 196 pins per compartment and 112 pin clusters, centred configurations. These count rates were corrected for source decay, and detector sensitivity where necessary as described in section 4.1.3. The changes in the corrected count rates are shown in Table 6.3.

Table 6.3 Percentage Count Rate Changes in the Rebuilds of Assemblies

Configuration	Percentage Count Rate Change in Rebuild								
	Det 1	Det 2	Det 3	Det 4	Det 5	Det 6	Det 7	Det 8	Det 9
196/33	-3.3	+3.1	+0.2	+4.6	+2.2	-1.1	-1.0	-2.1	-0.9
112/76 (CTD)	-1.0	+1.2	+0.4	-2.4	-1.8	-1.8	-1.8	+0.0	-2.2

From the above data the root mean square percentage change for the detectors outside the skip was 1.9%. For the detectors inside the skip the change was 2.7%, which reduced to about 2% r.m.s. when the detector positioning error of 2% was taken into account.

6.2 Effects of Changing the Detector Positions in the Reference Configuration

It was suspected that the movements of the detectors in the skip would produce small proportional changes in reactivity in the reference configuration by the same general argument outlined for temperature changes in the last chapter. As a measure of these effects and those due to temperature changes, the count rates for the detectors outside the skip (which were not repositioned) were recorded for each of the six positionings of the detectors inside the skip, and the percentage changes noted (Table 6.4). The first set of count rates for the standard detector postions was recorded at a temperature of 18.0°C which was close to the value of 18.3°C quoted for the calibration (section 5.1.1); the temperature changes in Table 6.4 are relative to this temperature.

Table 6.4 Percentage Count Rate Changes due to Reactivity Effects in the Reference Configuration

Detector Positions	Temp Change (°C)	Percentage Count Rate Change from 1st Set					
		Det 1	Det 2	Det 6	Det 7	Det 9	Mean
Standard	-	-	-	-	-	-	-
Alternative 1	-0.8	-2.0	-0.6	-0.8	-2.5	-0.4	-1.2
Alternative 2	-0.4	-1.2	-0.6	-0.6	-1.4	-0.4	-0.8
Alternative 3	-0.3	+1.4	+1.2	+1.8	+1.2	+2.4	+1.6
Alternative 4	-0.1	-1.4	+0.1	-1.0	-1.1	+0.0	-0.8
Alternative 5	+0.1	+0.0	-1.8	+0.6	+0.0	+1.2	-0.5
Standard (repeat)	-0.8	+1.9	+2.4	+2.2	+2.3	+2.4	+2.2

The root mean square change in count rate in the above table is about 1.5%. It is clear that temperature effects contribute significantly to this, since the repeat of the standard detector positions gives a mean change of +2.2%, due to the temperature change of -0.8°C. Accordingly an error of 1.5%, for each of the six detector positionings, was assigned to reactivity effects in the reference configuration.

6.3 Confirmation of the Source Decay

Since the measurements extended over several months, the changes in source strength due to the decay of californium 252 were significant (section 4.1.3). The rebuilds of the 196 pins per compartment and 112 pin clusters, centred configurations allowed tests to be made of the half-life of the sources. With the detectors in their standard positions, repeat count rates were taken in the rebuilds. These count rates, corrected where necessary for changes in detector sensitivity were compared with the count rates in the original builds. Their ratios were compared with that obtained from the predicted californium 252 decay over the time interval between the counts:

$$\frac{CR(t+t_o)}{CR(t)} = e^{-(0.693\ t_o)/t_{\frac{1}{2}}} \qquad (6.1)$$

where: $CR(t+t_o)$ is the count rate obtained from the rebuild;
$CR(t)$ is the count rate from the original build;
t_o is the time interval between the two counts; and
$t_{\frac{1}{2}}$ is the californium 252 half-life.

These ratios are shown in Table 6.5.

Table 6.5 Confirmation of Source Decay by Count Rate Changes

Configuration	Time Between Counts (years)	Mean Ratio of Counts	Predicted Ratio of Counts
112/76 (CTD)	0.116	0.959 ±0.026	0.970
196/33	0.399	0.901 ±0.020	0.901

These results provide experimental confirmation of the 2.65 year half-life of the sources, and a negligible error was thus assigned to each source decay factor used to obtain the corrected experimental count rates.

6.4 Symmetry of the Assemblies

In one of the fully flooded configurations, the 112 pin clusters, centred, count rates were recorded in the centres of 16 compartments to test the symmetry of the assembly. The 16 detector positions are shown in Figure 6.1. Table 6.6 gives the count rates which were normalised to count rates of 1.000 for the corresponding detectors in quadrant 1.

Table 6.6 Relative Count Rates in Symmetric Positions about the Axes of Symmetry

Quadrant	Count Rate Relative to Corresponding Detector in Quadrant 1			
	Det 3	Det 4	Det 5	Det 8
1	1.000	1.000	1.000	1.000
2	1.018	1.007	0.989	0.989
3	1.003	0.963	1.007	1.031
4	0.983	0.934	0.974	0.968

The relative count rates in Table 6.6 have a standard deviation of 2.5%. This standard deviation results from the assymmetries of the assembly, combined with detector positioning errors which have been shown to be about 2% (section 6.1.1). Accordingly the assymmetry errors can be given conservatively as about 2%. This is comparable with the count rate reproducibility errors from the rebuilds (section 6.1.3); it can be seen that both errors essentially result from the same origin, that is, imprecisions in the geometry of the assemblies. For example, one of the boron-steel walls was known to contain 0.9 w/o boron which is less than the average of about 1.04 w/o (Table 1.2).

6.5 Confirmation of Radial Detector Positioning

In order to obtain extra information on the sensitivity of the count rates to precise detector positioning for the detectors in the skip, an experiment was performed to assess the effects of displacing the tops of

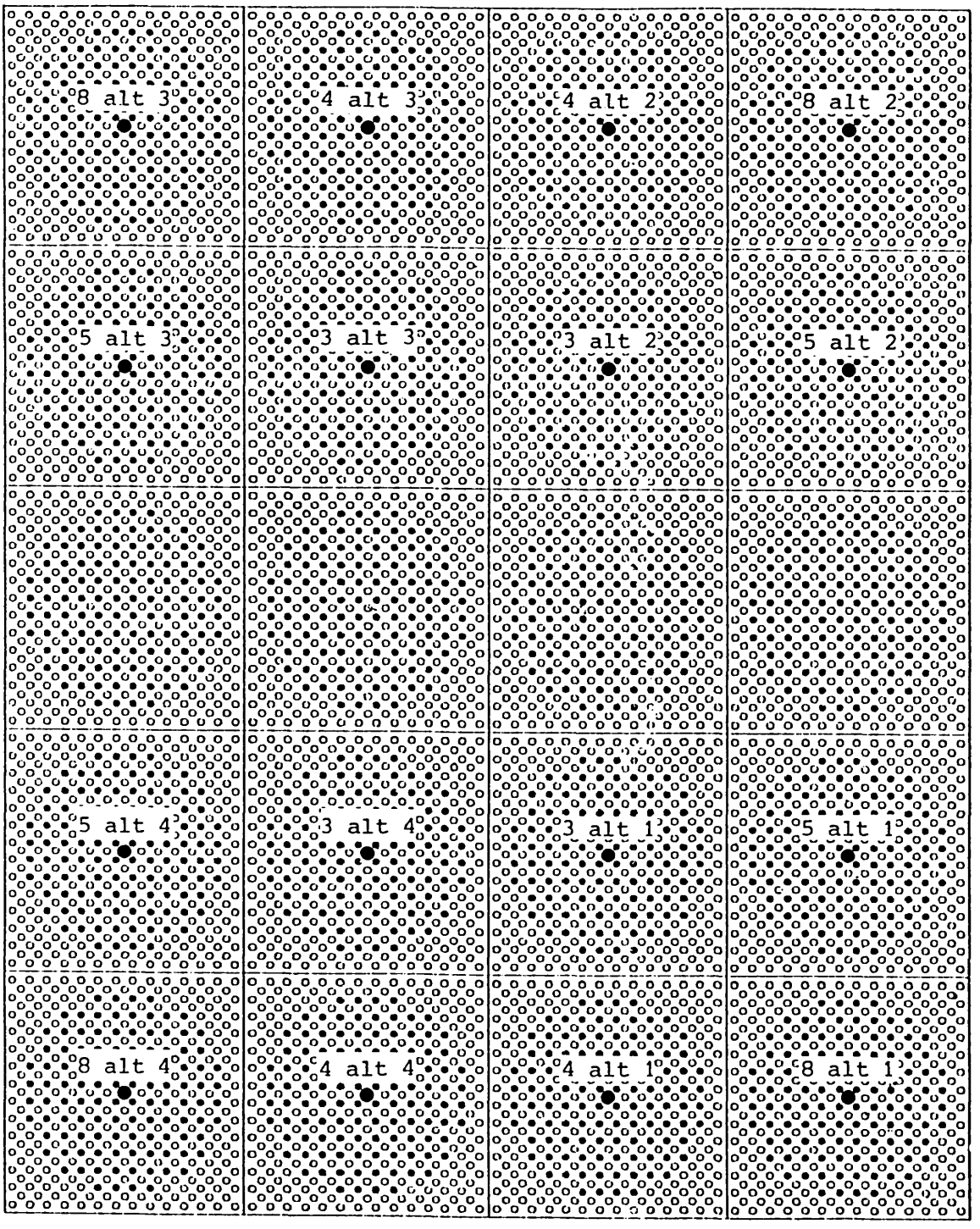

Fig. 6.1. Detector Positions Used to Test the Symmetry of the Assemblies.

the fuel pin cans (1). Count rates were taken for detectors 3, 4, 5 and 8 in their standard positions in the 112 pin clusters, groups of 4 configuration. The tubes were then displaced at their tops and the count rates taken again.

Measurements were made of the radial deflection of the tubes at the detector height, so that a count rate change per unit deflection could be computed for each detector. This count rate change was found to be about 2% per mm of detector deflection (1), which indicates that in the measurements the detectors were located radially to about 1mm.

6.6 Confirmation of Axial Detector Positioning

To confirm the axial positions of the active materials in detectors 7, 6, 9, 2 and 1, measurements were made with a special source positioning apparatus (2). The apparatus was clamped close to the pod containing a detector and counts were taken with the source at a variety of axial positions. The position giving the largest count rate corresponds to the centre of the axial material, provided the detector is of regular axial geometry. It was found that the active materials were indeed positioned according to the detector positions in the pods, and their specifications, to an accuracy of about 1cm (2).

6.7 Total Experimental Errors

The measurements in sections 6.1 to 6.4 enable an estimate of the total experimental error associated with the count rates appearing in the modified source multiplication equation. Firstly errors essentially random to every detector amount to about 2% and are dominated by the detector positioning errors (section 6.1). The reactivity effects in the reference configuration are about 1.5% and apply to groups of detectors (section 6.2). The assymmetries in the assemblies provide an error of about 2% for each count rate (section 6.4), which though partially systematic between the different configurations, should be considered conservatively as random. These errors amount to about 4% in combination for a count rate ratio derived from one detector in the reference configuration and in a well-subcritical configuration.

7. Subsidiary Calculations

In support of the correction factor calculations described in chapter 4, two sets of subsidiary calculations were carried out. These were:

(i) Comparisons of two-dimensional and three-dimensional calculations, to test the validity of using a two-dimensional model in the correction factor calculations (section 4.2.2).

(ii) Detector perturbation calculations, to give information on the effects of not including the detectors in the calculations (section 4.2.2).

7.1 Comparisons of Two-Dimensional and Three-Dimensional Calculations

7.1.1 Procedure for the Comparisons

Two aspects of the two-dimensional nature of the correction factor calculations required examination. These were:

(i) The validity of the source strength algorithm (Equation 4.12) which assumed a cosine function for the axial importance.

(ii) The assumption of the axial flux distribution to be a cosine function at detector locations (Equation 4.17).

The comparisons made to test these assumptions used the SNAP code in source mode. Two configurations were modelled in the comparisons:- the fully flooded 112 pin clusters, centred configuration and the 196 pins per compartment, 33cm water-height configuration. The former configuration was expected to be among the most subcritical of the configurations studied, and was thus expected to indicate any non-fundamental mode behaviour in the axial importance. The latter, having the smallest water height of the assemblies studied, was expected to show any effects due to the change of geometry both above and below the fuel pins.

Diagrams of each of the three-dimensional models are shown in Figures 7.1 and 7.2. The models are the same as those used in the correction factor calculations except that the axial bucklings are omitted and

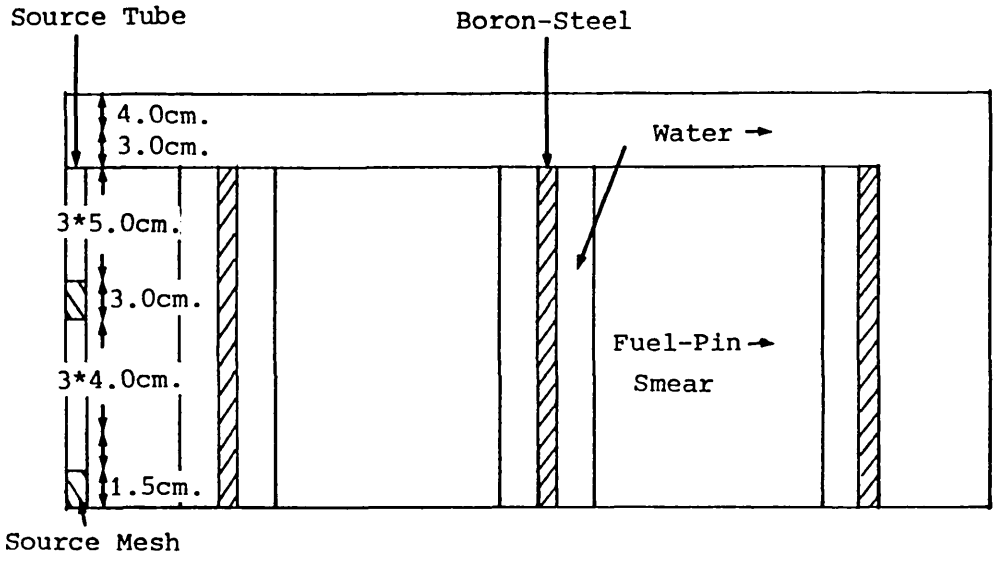

Fig. 7.1. Cross-Section of the Three-Dimensional Model of the 112 Pin Clusters, Centred Configuration.

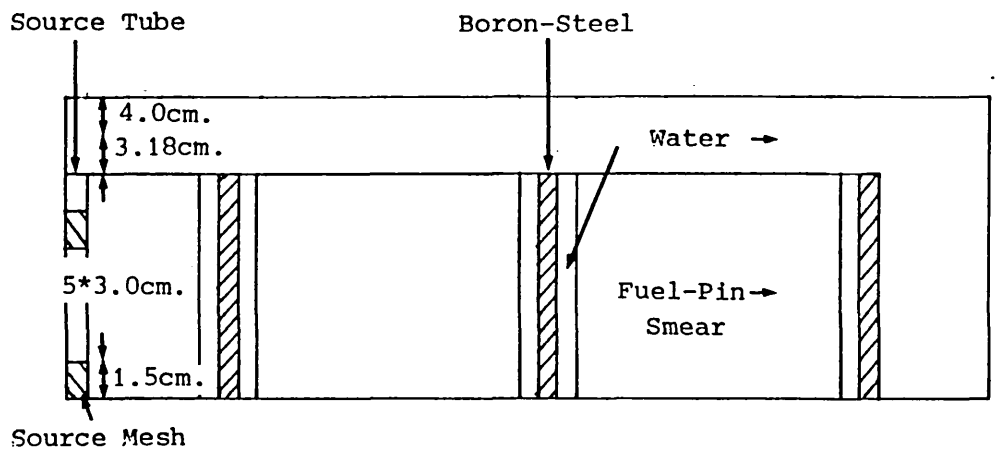

Fig. 7.2. Cross-Section of the Three-Dimensional Model of the 196 Pins per Compartment, 33cm. Water Height Configuration.

the axial geometry represented by 11 meshes in the fully flooded configuration and 8 meshes in the 33cm water height configuration. A plane of reflection was included half-way up the flooded part of the fuel pins, and a water region, of about 7cm thickness, was incorporated in each case.

In preparation for the source-mode comparisons testing the two assumptions above, calculations using the three-dimensional models and their corresponding two-dimensional models were run in eigenvalue mode. The axial bucklings for the two-dimensional models were adjusted to obtain the same k-eff values as those from the three-dimensional calculations, within small tolerances. This was to ensure the similarity of the three-dimensional models and the two-dimensional models, before introducing sources into the calculations.

Source-mode calculations were then run using both the three-dimensional models and the two-dimensional models. In the three-dimensional models, the experimental source positions were represented explicitly, as can be seen in Figs 7.1 and 7.2. The source strengths per unit volume were calculated from:

$$R_i = \frac{S_i}{Axh_i}, \qquad (7.1)$$

where: R_i is the strength of the i^{th} source in neutrons sec^{-1} unit $volume^{-1}$ in the calculations;
S_i is the experimental strength of the i^{th} pair of sources;
A is the horizontal area of the source meshes; and
h_i is the height of the i^{th} source mesh.

The source strengths in the corresponding two-dimensional calculations were computed using the source strength algorithm (Equation 4.12). Reaction rates were obtained from the source-mode calculations using the boron 10 cross-sections used in the correction factor calculations (section 4.2.3). Comparisons were then made of:

(i) The reaction rates at the standard detector positions (Fig. 4.2) from the three-dimensional and the two-dimensional calculations.

(ii) The axial reaction rate distribution at the standard detector positions in the three-dimensional calculations.

7.1.2 Eigenvalue Calculations

In Table 7.1 are given the k-eff values from the two sets of eigenvalue calculations. Also given are the effective heights of the assemblies.

Table 7.1 Comparison of Two-Dimensional and Three-Dimensional Eigenvalue Calculations

Configuration	3-D K-eff	Height of Assembly + Water (cm)	2-D K-eff	Axial Buckling (cm^{-2})	Effective Height of Assembly (cm)
112 pin clusters, centred	0.8150	69+(2x7) = 83	0.8157	0.00154	80.06
196 pins per compartment 33cm water height	0.9346	33+(2x7.18) = 47.36	0.9348	0.00502	44.34

The k-eff values are well matched in the above table. It can be seen, however, that the effective heights deduced from the required bucklings in the two-dimensional calculations are equal to the height of the flooded pins plus top and bottom extrapolation distances of about 5.5cm. In the correction factor calculations for the fully flooded configurations the axial bucklings corresponded to the height of flooded pins plus top and bottom extrapolation distances of about 7cm (section 4.2.2). This is illustrated schematically in Figure 7.3 and is a small discrepancy between the three-dimensional models and the two-dimensional correction factor models. Note that a similar type of discrepancy occurs in the correction factor models of the reference configuration which implied extrapolation distances of about 4.5cm (section 4.2.2). Consideration of the errors introduced by this discrepancy will be made later in this chapter.

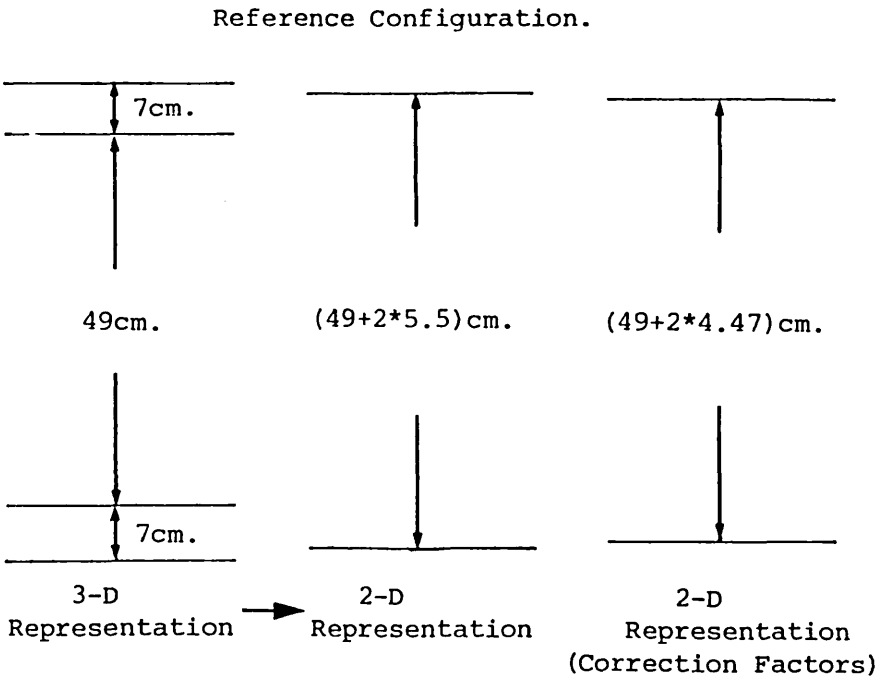

Fig. 7.3. The Discrepancy Between Axial Representations in Two-Dimensional and Three-Dimensional Calculations and in the Correction Factor Calculations.

7.1.3 Source Calculations

Considering firstly the axial reaction rate distribution at the standard detector positions, plots of this distribution for both of the three-dimensional source calculations are shown in Figures 7.4 and 7.5. The rates are expressed as fractions of the rate at the midplane, for ease of comparison with a cosine function. In each case the cosine function corresponds to the axial bucklings in Table 7.1.

The largest discrepancy observed between the axial reaction rate distribution and the corresponding cosine function was 4%. For all of the axial detector positions, the maximum discrepancy was, however, about 1% and the average discrepancy was of much smaller magnitude. The assumption of a cosine function for the axial reaction rate distribution can thus be assumed to introduce negligible errors into the correction factors. This can be attributed to the spreading of the sources and to the separation of the detectors from the sources, the closest being ~20cm or several migration lengths distant (Fig. 7.4).

The ratios of reaction rates from the two-dimensional and three-dimensional calculations of the two configurations are shown in Table 7.2. The reaction rates were calculated from midplane fluxes only, the confirmation of a cosine axial distribution already having been made.

Table 7.2 Ratios of Reaction Rates from Two-Dimensional and Three-Dimensional Calculations

Detector Position	112 Pin Clusters, Centred	196 Pins/Comp, 33cm Water Height
1 standard	1.010	0.989
2 "	1.010	0.990
3 "	1.010	0.996
4 "	1.010	0.996
5 "	1.010	0.992
6 "	1.010	0.992
7 "	1.011	0.995
8 "	1.015	1.010
9 "	1.010	0.990

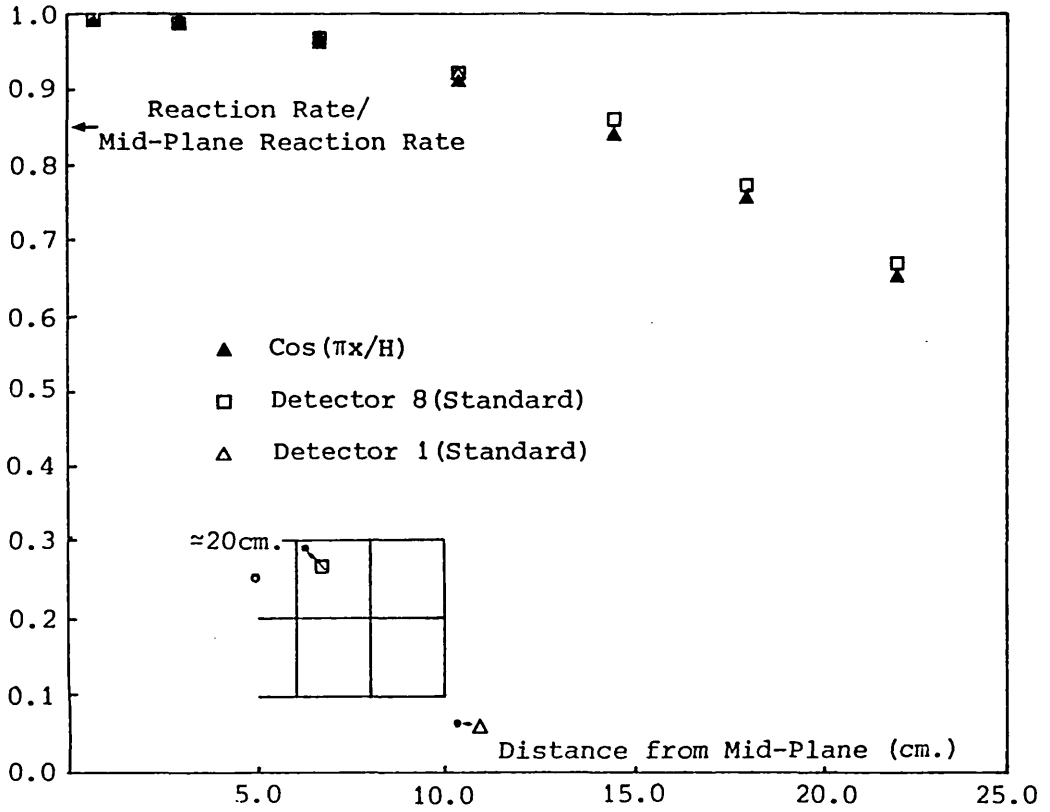

Fig. 7.4. Axial Behaviour of Calculated Reaction Rates: 112 Pin Clusters, Centred Configuration.

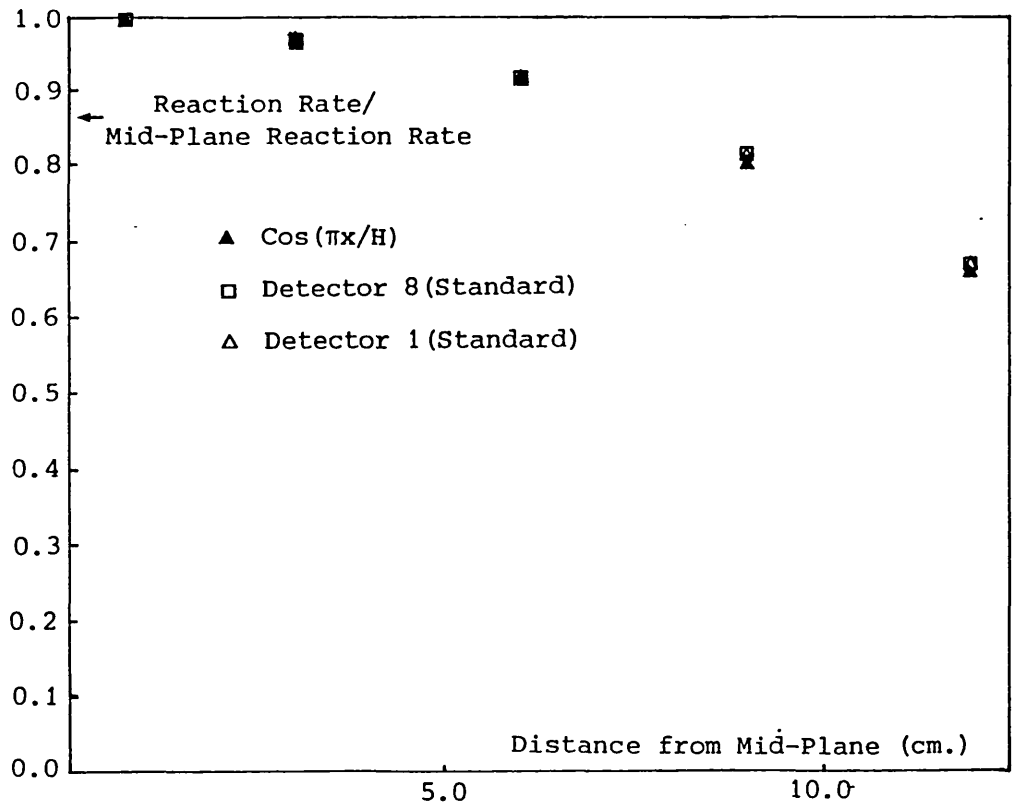

Fig. 7.5. Axial Behaviour of Calculated Reaction Rates: 196 Pins per Compartment, 33cm. Water Height.

The reaction rates agree within about 1% for both configurations. In the 112 pin clusters, centred configuration this is significant, since it means that the assumption of a fundamental mode axial importance (Equation 4.12) for the total effect of the sources is valid in spite of the large degree of subcriticality of this configuration. This validity is evidently due jointly to the degree of spreading of the sources (Figure 4.4) and to the fact that all the detector positions are at least several migration lengths' distance from the sources. In other words the source distribution, by being axially distributed, tends to reduce the effect of the higher importance modes.

Figure 7.6 shows an imaginary detector position close to the sources. The reaction rate ratio at this position was found to be 1.159 in the 112 pin clusters configuration; indicating that the assumption of fundamental mode axial importance for the total effect of the sources breaks down close to the sources in this well-subcritical configuration.

For the 196 pins per compartment, 33cm water height configuration, the reaction rates from the two calculations are in agreement to within 1% (Table 7.2). This indicates that the presence of the water region at the ends of the fuel pins does not significantly affect the assumption of a cosine function for the axial importance of the sources. This is probably due to the low importance of the water region, which occurs at the top and bottom of the assembly.

The comparisons of three-dimensional and two-dimensional calculations have thus shown the accuracy of the source strength algorithm and the assumed cosine axial flux distribution in the correction factor calculations. The three-dimensional models do not, however, precisely model the axial geometry of the assemblies studied. Firstly a depth of water greater than 7cm was present below the fuel pins (section 1.2.2). Secondly, and probably more significantly, the configuration with 33cm water height included dry fuel pins above the flooded regions and not a region of water alone, as in Figure 7.2. In order to show possible effects due to these discrepancies, comparisons of the three-dimensional models with experiment were made, as is now described.

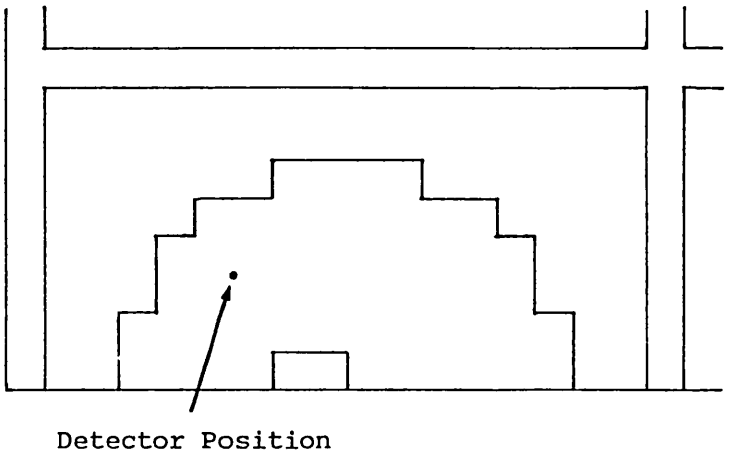

Fig. 7.6. Imaginary Detector Position Close to the Sources.

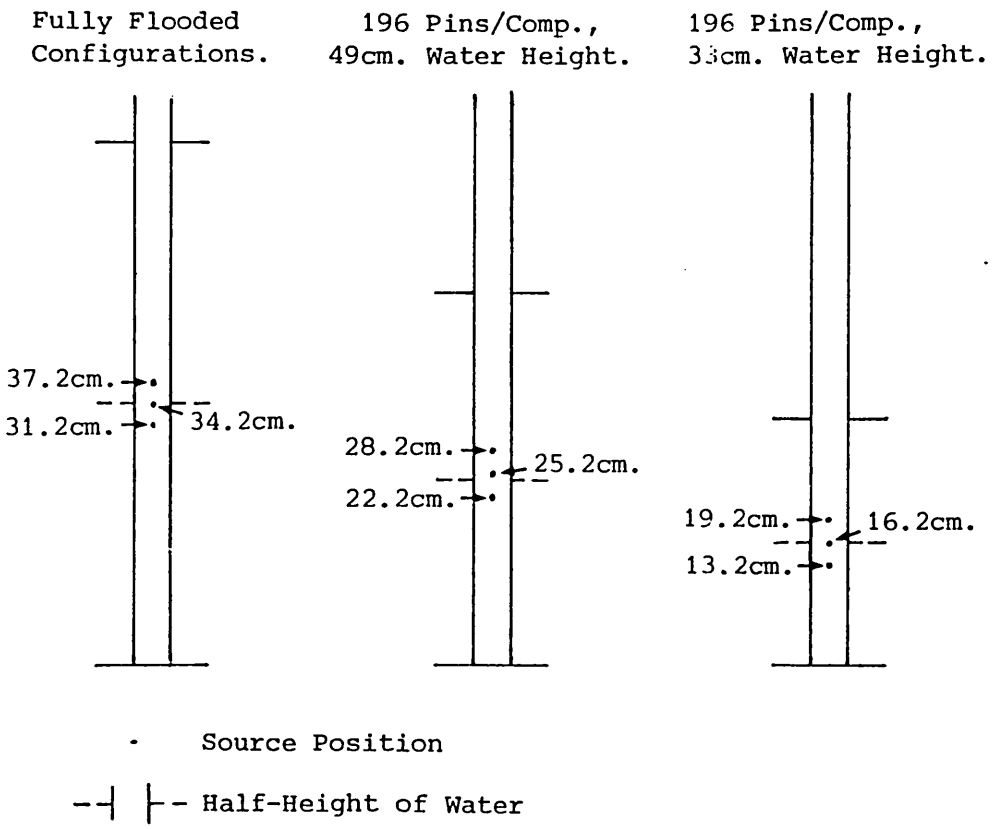

Fig. 7.7. The Clumped Source Dispositions.

7.1.4 Comparisons of Three-Dimensional Calculations with Experiment

With the source tubes in their standard positions, the sources were moved axially to a clumped disposition. This was done in all configurations. These source dispositions are illustrated in Figure 7.7 (previous page). Count rates were recorded from the detectors in the standard positions, and these count rates, corrected for changes in detector sensitivity if necessary, compared with the count rates obtained using the spread source dispositions which were illustrated in Figure 4.4.

The clumped source dispositions were included in each of the three-dimensional models of Figures 7.1 and 7.2, by moving the outermost two sources to positions adjacent to the central source. Reaction rates were computed for the clumped source dispositions and compared with the reaction rates resulting from the original source dispositions.

Table 7.3 shows the count rate ratios obtained from the two source dispositions in the 112 pin clusters, centred configuration.

Table 7.3 Comparisons of Count Rate Ratios. Spread/Clumped Sources. 112 Pin Clusters Centred.

Detector Position	Count Rate Ratio: (Spread/Clumped) Sources		Calculation/ Experiment
	Experiment	Calculation	
1 Standard	0.854	0.859	1.006
2 "	0.858	0.860	1.002
3 "	0.803	0.821	1.022
4 "	0.826	0.826	1.000
5 "	0.830	0.856	1.031
6 "	0.843	0.854	1.013
7 "	0.832	0.843	1.013
8 "	0.670	0.677	1.010
9 "	0.859	0.859	1.000

With the detector positioning errors of 2% (section 6.1.1) taken into account, the above results indicate excellent agreement between calculation and experiment. It is noticeable that the spread/clumped ratios increase from a value of 0.670 for detector 8 which is closest to

the sources to a value of about 0.860 for the detectors furthest away from the sources. This indicates that for the clumped source positions the assumption of a cosine function for the axial importance of the individual sources does not hold good within a large region around the sources. However this departure from a cosine function has no net effect on the total importance of the spread sources as has been observed. Experimentally, a similar variation of ratios was observed for all the fully flooded assemblies, with the count rate ratios tending to a value of about 0.860 for the detectors furthest away from the sources.

The spread/clumped count rate ratios from the 196 pins per compartment, 33cm water height configuration are given in Table 7.4.

Table 7.4 Comparisons of Count Rate Ratios. Spread/Clumped Sources. 196 Pins/Comp 33cm Water Height

Detector Position	Count Rate Ratio: (Spread/Clumped) Sources		Calculation/ Experiment
	Experiment	Calculation	
1 standard	0.840	0.816	0.971
2 "	0.812	0.816	1.005
3 "	0.823	0.816	0.991
4 "	0.801	0.815	1.017
5 "	0.805	0.815	1.012
6 "	0.812	0.816	1.005
7 "	0.821	0.816	0.994
8 "	0.812	0.800	0.985
9 "	0.817	0.816	0.999

Again the agreement between calculation and experiment is excellent, taking the detector positioning errors into account.

It can be concluded that the axial representation of the assemblies modelled by the three-dimensional calculations is accurate enough not to result in any significant systematic errors. This is a reasonable conclusion in view of the low importance of the regions affected by the modelling simplifications.

7.1.5 Contributions to Correction Factor Errors

The comparisons of two-dimensional and three-dimensional calculations have revealed that for the spread source dispositions used for the measurements, no explicit three-dimensional modelling is required. Instead, the two-dimensional models with the axial representations as described in section 4.2.2 are adequate. It remains to consider the small systematic errors occurring in the correction factors due to this simplified representation.

Provided that the two-dimensional models use bucklings which match with the three-dimensional models (Table 7.1), the only systematic errors which can be assigned to any of the correction factors are the 1% discrepancies appearing in the comparisons of reaction rates (section 7.1.3). However, the correction factor calculations used slightly different bucklings (Figure 7.3). This is also the case for the reference configuration, where extrapolation distances of about 4.5cm were assumed, instead of the distances of about 5.5cm resulting from the two-dimensional models in Table 7.1.

A convenient measure of the systematic errors resulting from a small change in the height of an assembly as modelled, can be gained from the source strength algorithm (Equation 4.12). The height change causes changes in both the importance of the sources on the right hand side of the equation, and in the extent of the cosine-shaped source on the left hand side. In fact, this is the only manner in which the axial geometry is effectively represented for most of the detectors, since the cosine factor used to correct the reaction rates (Equation 4.18) is nearly equal to one for detectors close to the midplane.

As a result of the height change, then, there is a slight change in the source strength per unit volume used in the calculations. This change in the source strength per unit volume, in turn affects the fluxes and reaction rates.

Table 7.5 Source Strengths in Comparisons of Two-Dimensional and Three-Dimensional Calculations and Correction Factor Calculations

Configuration	Source Strength/ Unit Vol, 2D/3D Cals ($ns^{-1}cm^{-3}$)	Source Strength/ Unit Vol, Correction Factor Cals ($ns^{-1}cm^{-3}$)	Ratio of Source Strengths, Correction Factor/ 'Correct' Models
112 pin clusters, centred (fully flooded)	3.426×10^4	3.345×10^4	0.976
196 pins/comp 33cm water height	5.702×10^4	5.519×10^4	0.968
196 pins/comp 49cm water height	3.960×10^4	3.996×10^4	1.009

Since every correction factor calculation used one of the first two source strengths in the appropriate column in Table 7.5, it appears that a systematic error of about 2-3% is indicated, due to the height discrepancies in the correction factor calculations. Combining this error with the 1% error assigned to the reaction rate comparisons (section 7.1.3) results in an overall error of 3% in each correction factor for the axial representation.

7.2 Detector Perturbation Calculations

7.2.1 Procedure for the Calculations

The conversion of source mode fluxes to reaction rates in the correction factor calculations disregarded the presence of any of the detectors (section 4.2.2) and used arbitrary densities for the cross-section preparation of the detection material (section 4.2.3). Hence no account was taken of the perturbation to the flux caused by each of the detectors. In addition the true spectrum required for producing the multigroup detection cross-sections was not necessarily represented. These deficiencies are not important, for a given detector, provided that they are of the same magnitude in both the reference and unknown subcritical assemblies. This occurs if the detector is in the same environment in both assemblies, though it was not clear how extensive this similarity of environment must be to ensure this condition.

It was apparent that many of the detectors were in the same environment in both reference and unknown subcritical configurations in the measurements; calculations were nevertheless required to show that the perturbations were common. Additionally, it was required to calculate relative perturbation factors for all detectors which were not in common environments (Equation 4.20).

For the detectors inside the skip, a total of 9 basic perturbations were evident; these are detailed in Figure 7.8. From these perturbations a total of 6 relative perturbations were possible, resulting from the three compartmental locations in either a 112 or a 221 pin clusters configuration relative to the reference configuration. This ignores the perturbations in the slumped and dropped-pin configurations, which will be considered later in this chapter. All 9 perturbations were calculated by models of the following detectors with their environments:

(i) 221 pin clusters, centre-of-cluster detector;
(ii) 221 pin clusters, corner-of-compartment detector;
(iii) 221 pin clusters, half-way detector;
(iv) 112 pin clusters, centre-of-cluster detector;
(v) 112 pin clusters, corner-of-compartment detector; and
(vi) 196 pins per compartment, corner-of-compartment detector.

It was assumed initially that the model for the centre-of-cluster detector (iv) in the 112 pin clusters would be representative also of the half-way detector in the 112 pin clusters and the centre-of-cluster and half-way detectors in the 196 pins per compartment configuration. This was because of the similar environment of these detectors (Fig. 7.8).

No models were set up for the detectors outside the skip. Three of these detectors (detectors 1, 2 and 9) were surrounded by more than 10cm of water throughout the measurements, a much greater distance than the migration length of neutrons in that medium, and so they were each assumed to have common perturbations in the measurements. For the other two detectors (detectors 6 and 7) the common environments were less extensive owing to the greater proximity to the pin clusters (Figure 4.2).

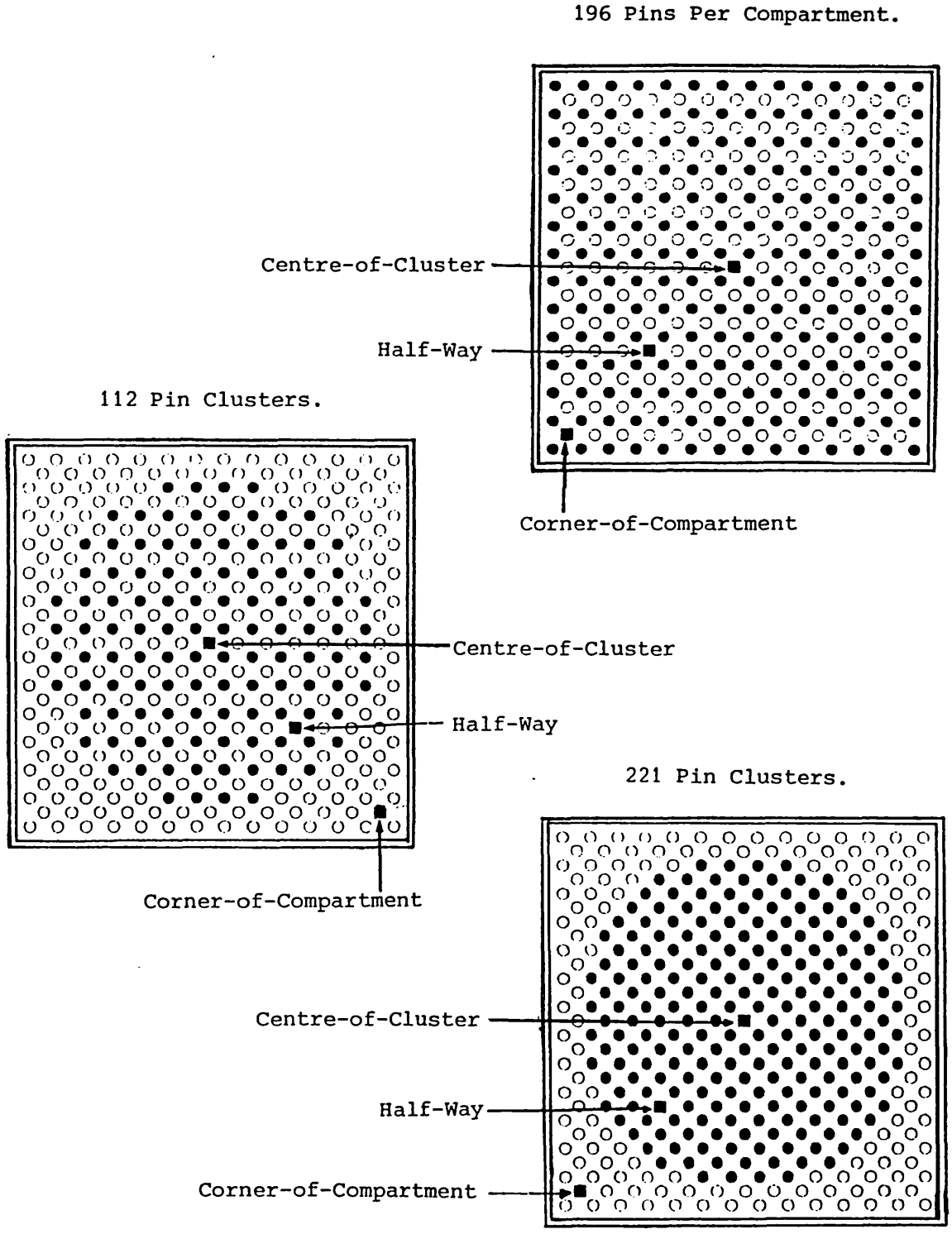

Fig. 7.8. The Nine Detector Perturbations in the Skip.

Two calculations were performed for each of the six models above. In one calculation, no detector was modelled. This gave a representation of the unperturbed fluxes and reaction rate at the detector position, corresponding to the correction factor calculations. In the other calculation, the inclusion of a detector gave the perturbed fluxes and reaction rate.

All the calculations employed localised models, in which one mesh point represented a pin cell, or a detector where included. Diagrams of the models are shown in Figure 7.9. The calculations used the transport theory code TWOTRAN in eigenvalue mode in all cases, with the same 8-group structure as for the correction factor calculations, and S-4 quadrature. They were thus different from the models used for the correction factor calculations, relying on the detector perturbations being local in nature, and not dependent on the position of the compartment in the skip. The boundaries for the models were infinitely reflecting, except those for the corner-of-compartment detectors which used repeating boundaries. Each detector was represented as a smear of steel, water, air and boron 10 and the material proportions were based on their estimated actual proportions, as shown in Table 7.6. A horizontal section through the pin cell containing a detector is shown in Figure 7.10.

Table 7.6 Detector Composition in the Perturbation Calculations

Material and Constituent Element	Fraction of Mass of Detector Smear (%)
Steel (as in Table 1.3)	51.1
Polythene (86% C, 14% H)	21.5
Water (as in Table 1.3)	27.4
Boron 10	0.002

A single perturbation factor was produced from each pair of calculations:

$$\text{Perturbation factor} = \frac{(\text{Reaction Rate at detector position})_{\text{TWOTRAN, detector}}}{\left(\sum_{g=1}^{G} \phi_g \text{ TWOTRAN, no detector} \times \Sigma_g\right) \times N}, \qquad (7.2)$$

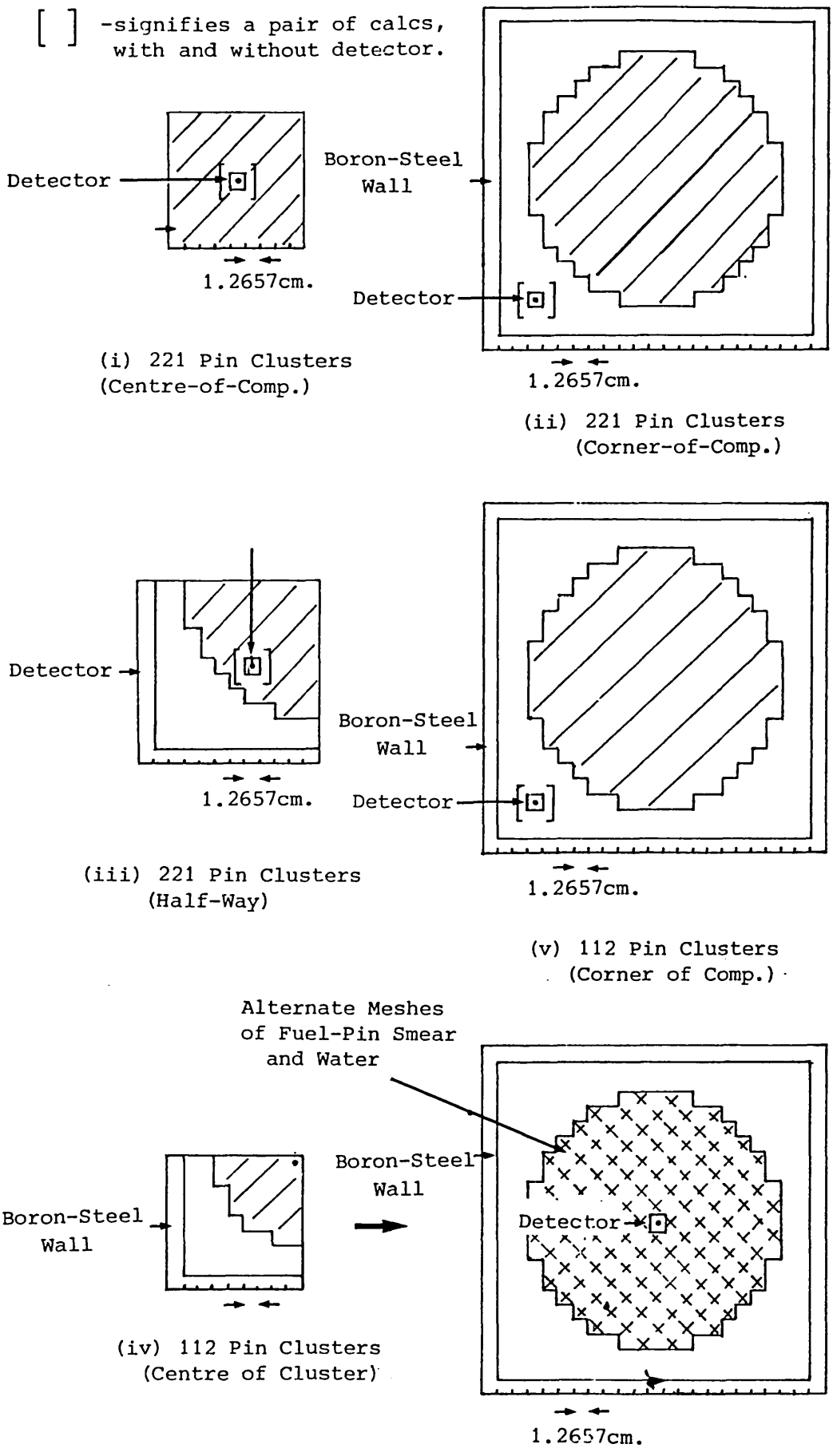

Fig. 7.9. The Detector Perturbation Models.

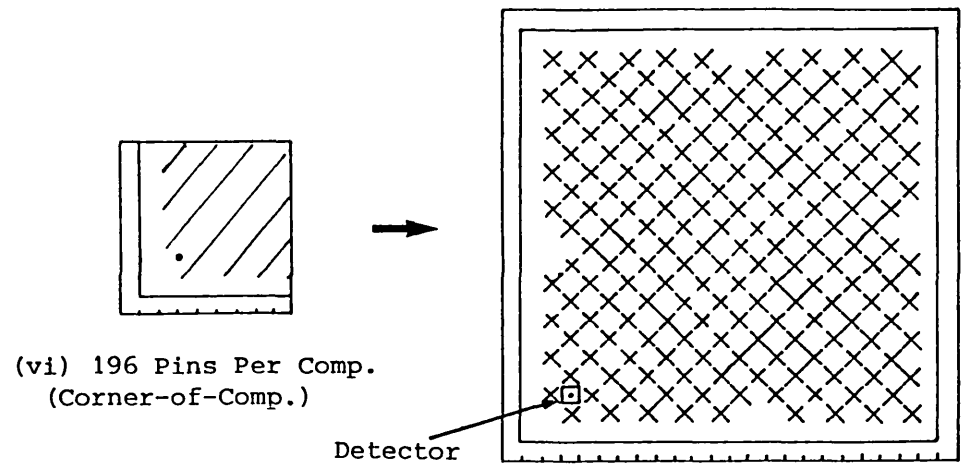

Fig. 7.9. (Contd.)

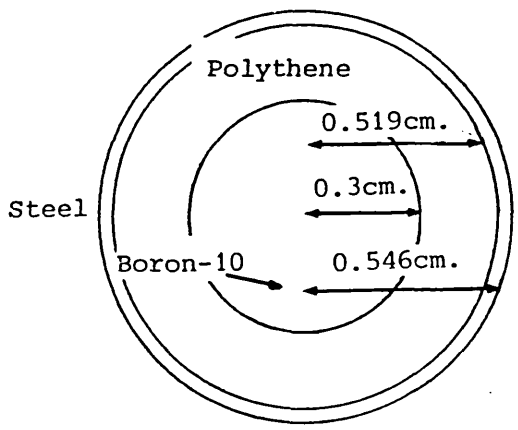

Fig. 7.10. Horizontal Section Through Detector Pin-Cell

where: ϕ_g is the flux in group g at the detector position resulting from the calculation with no detector included;
Σ_g is the detection cross-section in group g used for the corresponding detector in the correction factor calculations;
and N is a normalisation factor, to normalise the boron 10 number densities in the correction factor calculations to those in the perturbation calculations.

In the numerator of the above equation, the reaction rate at the detector position was produced directly from the TWOTRAN calculation using the REACTION edit (1).

Relative perturbation factors were then produced, where necessary, from the perturbation factors relevant to the unknown subcritical configurations and to the reference configuration:

$$RPF_d = \frac{PF_{d_2}}{PF_{d_1}}, \qquad (7.3)$$

where: RPF_d is a relative perturbation factor for a given detector; and
PF_{d2}, PF_{d1} are the perturbation factors for a given detector in an unknown subcritical configuration, and the reference configuration, respectively.

Equation 7.2 expresses the change from a normalised reaction rate produced from unperturbed fluxes and a somewhat arbitrary cross-section preparation, to a reaction rate taking the perturbation of the detector fully into account. The normalisation factor, N, in Equation 7.2, is clearly irrelevant to each relative perturbation factor, but gives perturbation factors which result from equal number densities of boron 10 and are thus physically meaningful.

7.2.2 Validity of the Models

The physical situation represented in each of the detector perturbation models illustrated in Fig. 7.9 differs in two respects from a two-dimensional model of the skip with imposed sources:

(i) Localised, fully reflected geometries were used, and in the case of the 221 pin clusters, centre-of-cluster detector, no account was made of the boron-steel walls or the water surrounding the clusters.

(ii) Eigenvalue mode was used. Physically this corresponds to a situation in which the source is distributed throughout the fuel (section 2.9) and is not localised as in the measurements.

Nevertheless, the perturbation calculations for the detectors in the clusters, at least, were expected to yield the same results as would source mode calculations using a full two-dimensional model of the skip. This was for two reasons.

Firstly, the neutron spectrum well inside the fuel clusters is not significantly changed by the use of localised geometry, and the use of eigenvalue mode instead of a true source-mode representation. This is demonstrated in Tables 7.7 and 7.8 which give the fluxes at detector positions, normalised for simplicity to give group-8 fluxes of 1.000.

Table 7.7 Neutron Energy Spectrum at Centre-of-Cluster Positions: 112 Pin Clusters, Centred

Energy Group	Flux by Group		
	Correction Factor Calculation (Source Mode)		Perturbation Calculation (No Detector)
	Det 8 Alt 1	Det 5 Standard	
1	6.795	6.798	7.306
2	7.153	7.155	7.466
3	5.504	5.503	5.611
4	1.178	1.178	1.201
5	0.628	0.628	0.637
6	2.103	2.103	2.103
7	2.251	2.251	2.251
8	1.000	1.000	1.000

Table 7.8 Neutron Energy Spectrum at Centre-of-Cluster Positions: 221 Pin Custers, Centred

Energy Group	Flux by Group		
	Correction Factor Calculation (Source Mode)		Perturbation Calculation (No Detector)
	Det 8 Alt 1	Det 5 Standard	
1	36.30	36.31	30.69
2	49.74	49.73	43.21
3	32.74	32.72	30.68
4	5.583	5.580	5.607
5	2.638	2.636	2.676
6	4.400	4.395	4.544
7	2.818	2.816	2.835
8	1.000	1.000	1.000

It can be seen from Table 7.7 that the spectrum resulting from the correction factor calculations for the 112 pin clusters case is the same for different detector positions in the centres of the clusters. Additionally, the spectrum given by the perturbation model differs from this spectrum by 2% or less in all but groups 1 and 2 , which have little contribution to the reaction rates. The spectrum given by the perturbation model in the 221 pin clusters case is somewhat more discrepant, though the difference in groups 4-8, which constitute 90% of the reaction rate, is at most 2%.

This similarity of spectrum in the different models is due to the respective detector environments being similar. In all of the models except the 221 pin clusters perturbation calculation, the detector environments differ only in the leakage effect from the full model of the skip. This is only likely, however, to have a slight effect on the fast part of the spectrum, it being noted that fast neutrons are most likely to leak from a finite system.

In the perturbation model for the 221 pin clusters, however, the compartmental environment is not represented (Fig. 7.9). Nevertheless the thermal spectrum is virtually unchanged as can be seen from Table 7.8. This is a result of the thermal scatter mean free paths being much smaller than the radius of the clusters. This is shown in Table 7.9 which lists the scatter mean free paths derived from the perturbation

calculation. The thermal neutrons at the detector position are likely to have undergone several scatters in the cluster environment and so to have attained the equilibrium spectrum for that environment.

Table 7.9 Comparison of Cluster Radius and Scatter Mean Free Paths

Cluster Radius (cm)	Energy Group	Approximate Scatter Mean Free Path (221 Pin Clusters)
11	2	16.7
	4	3.98
	8	1.75

The second reason for the validity of the perturbation models concerns the use, effectively, of a source spread throughout the fuel instead of a localised source. A localised source probably increases the radial anisotropy of the flux distribution. Now the isotropic flux distribution resulting from a distributed source probably does not affect the perturbation of a detector in a fuel cluster, since its immediate environment is radially symmetric.

Neither of the above arguments, however, holds for the corner-of-compartment detectors; this will be taken into account in the analysis of the perturbation factors.

7.2.3 Results of the Detector Perturbation Calculations

The six perturbation factors produced from the models illustrated in Figure 7.9 are shown in the table below.

Table 7.10 Calculated Perturbation Factors

Detector Perturbation Model	Perturbation Factor
221 pin clusters, centre-of-cluster	1.355
221 pin clusters, corner-of-compartment	0.878
221 pin clusters, half-way	1.356
112 pin clusters, centre-of-cluster	0.878
112 pin clusters, corner-of-compartment	0.892
196 pins per compartment, corner-of-compartment	0.912

7.2.4 Qualitative Analysis of the Perturbation Factors

Considering firstly the perturbation factors for the centre-of-cluster and half-way detectors in the 221 pin clusters, it is noticeable that the inclusion of a detector has caused an elevation of reaction rate. This is quite reasonable when it is considered that the detectors in these models replace fuel (Figure 7.9). The effect of this is to remove essentially a thermal absorber and replace it by the detector material which is a weak moderator. The loss of the fast neutrons emitted by the fuel pin which is removed has little effect on the thermal flux in its vicinity, since slowing down occurs on average over several times the migration area which is a much larger area (section 2.9) for the environment of fuel and water. In Table 7.11 are listed the changes in flux by energy group which contribute to the perturbation for the centre-of-cluster detector.

Table 7.11 Spectrum Changes for Centre-of-Cluster Perturbation: 221 Pin Clusters

Energy Group	Contribution to Unperturbed Reaction Rate (%)	Perturbed Flux/ Unperturbed Flux	Contribution to Perturbation (% of Unperturbed Rate)
1	0.3	0.94	-0.3
2	0.3	0.95	-0.3
3	9.0	1.04	+0.4
4	9.4	1.07	+0.7
5	8.6	1.11	+0.9
6	27.1	1.26	+7.0
7	27.7	1.51	+13.9
8	17.9	1.80	+14.3

It can be seen from Table 7.11 that the perturbation is dominated by the effects to neutrons in groups 6-8, that is, below about 0.25eV. This is evidently due to the small size of the detector (1cm diameter) in relation to the slowing-down area of neutrons in the medium.

In the case of the half-way detector, the unperturbed neutron spectrum is similar in the groups 6-8 to that for the centre-of-cluster detector, as shown in Table 7.12. The differences in spectrum in the fast

groups are, in view of the above reasoning, not important to the perturbation. Hence, the close similarity of these two perturbations is expected.

Table 7.12 Comparison of Neutron Spectra for Centre-of-Cluster and Half-way Detectors, 221 Pin Clusters

Energy Group	Normalised Flux	
	Centre of Cluster	Half-way
1	36.30	26.03
5	2.638	1.909
6	4.400	4.036
7	2.818	2.851
8	1.000	1.000

In contrast to the perturbation in the 221 pin clusters, the 112 pin clusters, centre-of-cluster perturbation involves a different geometry change. The in-cluster detectors in the 112 pin clusters fitted between the fuel pins (section 4.1.2). As a result, the perturbation model (Figure 7.9 (iv)) represents a change from smeared fuel and water to a situation in which the detector has replaced some of the water between several fuel pins.

The perturbation factor of 0.878 for this situation is reasonable, since the inclusion of the detector means a reduction in the amount of moderator in the region in question. It is quite certain that this perturbation is dominated by thermal neutron effects, since the 112 pin cluster environment has more moderator for each fuel pin that the 221 pin cluster environment, and so the spectrum is softer.

It can be said, confidently, that this perturbation applies also to the half-way detector in the 112 pin clusters and to the centre of cluster and half-way detectors in the 196 pins per compartment configuration. This is because their environments are sufficiently similar to result in similar thermal neutron spectra, as shown in Table 7.13.

Table 7.13 Comparison of Neutron Spectra for In-Cluster Detectors: 196 and 112 Pin Clusters

Energy Group	Normalised Flux at Detector Position			
	112 Pin Clusters, Centre-of-Cluster	112 Pin Clusters, Half-Way	196 Pins/ Comp, Centre-of-Cluster	196 Pins/ Comp, Half-way
1	6.795	4.566	6.648	6.600
5	0.628	0.442	0.634	0.637
6	2.102	1.949	2.122	2.124
7	2.251	2.247	2.254	2.254
8	1.000	1.000	1.000	1.000

It is clear that the neutron spectra are very similar, in three of the cases above, the only one showing some departure being the half-way detector in the 112 pin cluster. Its spectrum is still similar, however, in the groups of importance, that is groups 6 to 8.

It remains to consider the corner detectors. Interestingly their perturbation factors as shown in Table 7.10 are all similar to that of the centre-of-cluster detector in the 112 pin clusters. Yet, the thermal neutron spectra are markedly different in two of the three corner of compartment cases compared to this centre-of-cluster case. This behaviour is shown in Table 7.14.

Table 7.14 Comparisons of Neutron Spectra for Corner-of-Compartment Detectors

Energy Group	Normalised Flux at Detector Position			
	112 Pin Clusters Centre-of-Cluster	112 Pin Clusters Corner-of-Comp	221 Pin Clusters Corner-of-Comp	196 Pins/Comp Corner-of-Comp
1	6.795	1.450	0.944	7.881
5	0.628	0.192	0.172	0.777
6	2.102	1.398	1.411	2.204
7	2.251	1.968	1.975	2.204
8	1.000	1.000	1.000	1.000

Naturally the neutron spectra are much softer in the corner-of-compartment positions for the 112 and 221 pin cluster situations, since the environment is predominantly water, and not water and fuel.

It is believed that the similarity of perturbation factors for the above cases is fortuitous, and due to a cancellation of effects. The first effect concerns the thermal flux depression due to the replacement of water by a detector. This depression may be less for the corner environment than for the in-cluster environment. This is because the removal of moderator close to the strongly absorbing boron-steel wall reduces the thermal absoption in the boron, leaving neutrons with a higher chance of scattering into the detector.

The other effect lies in the nature of the in-cluster environment: it consists not only of the replacement of water by a detector, but also a transition from a smeared fuel and water environment to the water environment between the pins. This transition causes a thermal flux elevation which counteracts the flux depression due to the inclusion of the detector.

7.2.5 The Effects of the Detector Perturbations on the Correction Factors

The perturbation factors for the nine basic detector perturbations in the skip, with the associated relative perturbation factors are summarised in Table 7.15.

Table 7.15 Perturbation Factors with Relative Perturbation Factors

Configuration	Detector Environment	Perturbation Factor	Relative Perturbation Factor
196 Pins/ Compartment	Centre of Cluster	0.878	1.000
	Half-way	0.878	1.000
	Corner of Compartment	0.912	1.000
112 Pin Clusters	Centre of Cluster	0.878	1.000
	Half-way	0.878	1.000
	Corner of Compartment	0.892	0.978
221 Pin Clusters	Centre of Cluster	1.355	1.542
	Half-way	1.356	1.542
	Corner of Compartment	0.878	0.963

In the above table the relative perturbation factors quoted for the 196 pins per compartment array apply to the 33cm water height configuration. The factors for the 112 and 221 pin clusters models are assumed to apply to all variants of the centred configurations using these clusters.

The relative perturbation factors for the corner-of-compartment detectors were assumed, for simplicity, to be equal to 1.000. This represents a change of about 2-4%, but in fact has little importance to the overall results of the measurements, as will be seen.

Relative perturbation factors of 1.000 were also assigned to detectors 6 and 7 throughout the measurements on the strength of the fact that the perturbations calculated in the preceding sections appear to be decided predominantly by the geometric change due to the inclusion of the detector, and not so much by the environment more than a few centimetres away from it. This was observed both in the case of the corner-of-compartment detectors in the 112 and 221 pin clusters configuration, and the centre-of-cluster and half-way detectors in the 221 pin clusters configurations. This may not hold so well for detectors 6 and 7 which are larger than the detectors in the skip and thus presumably cause more

extensive perturbations. However, there appears to be little justification in the accurate calculation of their relative perturbation factors, since their proximity to the boron-steel walls probably renders flux predictions somewhat unreliable.

Finally, the perturbation factors for the detectors in the skip in the slumped and dropped-pin configurations were assumed to be the same as those generated from the centred cluster models. This is justified in view of the fact that in nearly all cases, the immediate environment around each of the detectors is unchanged by the movement of the clusters or the inclusion of extra pins (Fig. 7.8).

7.2.6 Sensitivity Studies of the Perturbation Factors

The relative perturbation factor of 1.542 (Table 7.15) for the in-cluster detectors in the 221 pin clusters, being representative of two quite different detector perturbations, clearly required substantiation. Additionally, it was felt necessary to directly demonstrate the sensitivity of the perturbation factors to the environment at some distance from a detector. It was on this assumed insensitivity of the perturbation factors that most of the in-cluster perturbation factors were based (section 7.2.2). Accordingly, three sensitivity studies were carried out:

(i) The calculations for the centre-of-cluster detectors in the 112 and 221 pin clusters were repeated using a finer mesh subdivision to assess the effect of a more detailed definition of flux in the detector region.

(ii) The composition of the detector smear was altered slightly in both of the above calculations, it being realised that the specification of the smeared detector material (Table 7.6) was somewhat approximate.

(iii) The centre-of-cluster perturbation in the 221 pin clusters was repeated using a model which included the water surrounding the clusters, and the boron-steel walls.

7.2.6.1 Sensitivity to Mesh Subdivision

Diagrams of the two models using a finer mesh subdivision are shown in Figure 7.11. The subdivision of meshes is into 25(5x5) per pin cell: the detector cell is divided according to the actual material regions listed in Table 7.6. Equation 7.2 was used to calculate the perturbation factors as before, though the perturbed reaction rate applied only to the mesh in the centre of the detector cell containing the detection material. The unperturbed reaction rate for the 112 pin cluster model was calculated, using for each group, the average of the 50 mesh fluxes appropriate to two central cells as shown in Figure 7.11.

The resultant perturbation factors of 1.000 from the 112 pin cluster model, and 1.492 from the 221 pin cluster model as listed in Table 7.16 differ significantly from the corresponding perturbation factors using single meshes for the pin cells in Table 7.15. However, the change in the relative perturbation factor is only about 3%. It may be that the perturbation factor is dependent on the detector geometry itself and not so much on the surrounding environment. This would indicate that the relative perturbation factors are insensitive to calculation, a fortunate situation for the relative perturbation in question.

Table 7.16 Sensitivity Studies of the Perturbation Factors

Perturbation Model	Perturbation Factors		
	112, Centre-of-Cluster	221, Centre-of-Cluster	Relative
Original (Fig.7.9)	0.878	1.355	1.542
Mesh subdivision	1.000	1.492	1.492
Hydrogen reduced by 4%	0.912	1.395	1.530

The above changes in the separate perturbation factors were investigated by means of two diagnostic calculations, the models for which are shown in Figure 7.12. A simplified group structure of 4 energy groups was

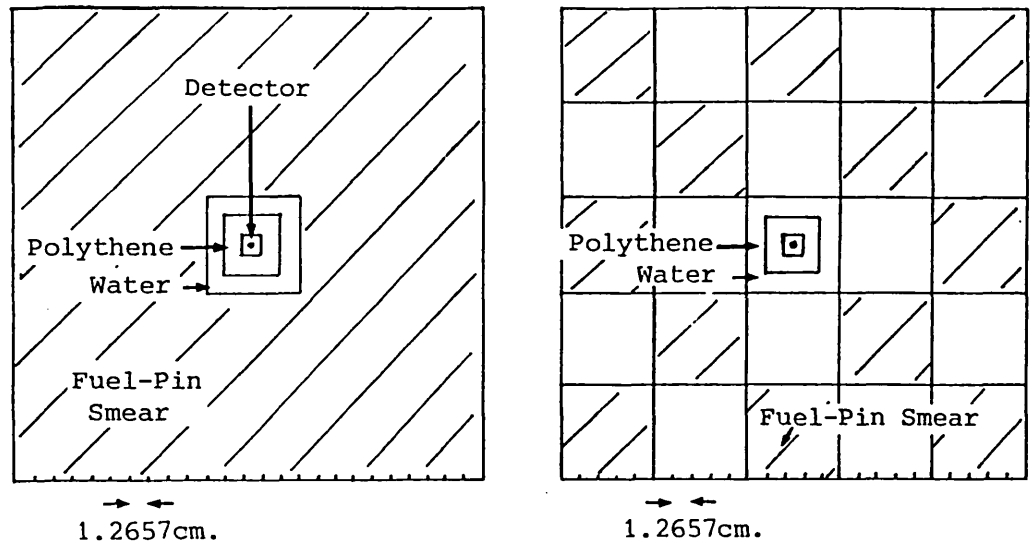

Fig. 7.11. Perturbation Models with Mesh Subdivision.

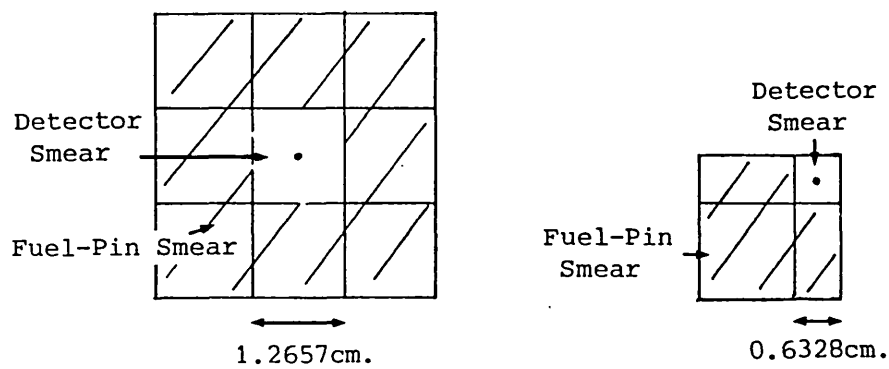

Fig. 7.12. Diagnostic Models of Mesh Subdivision.

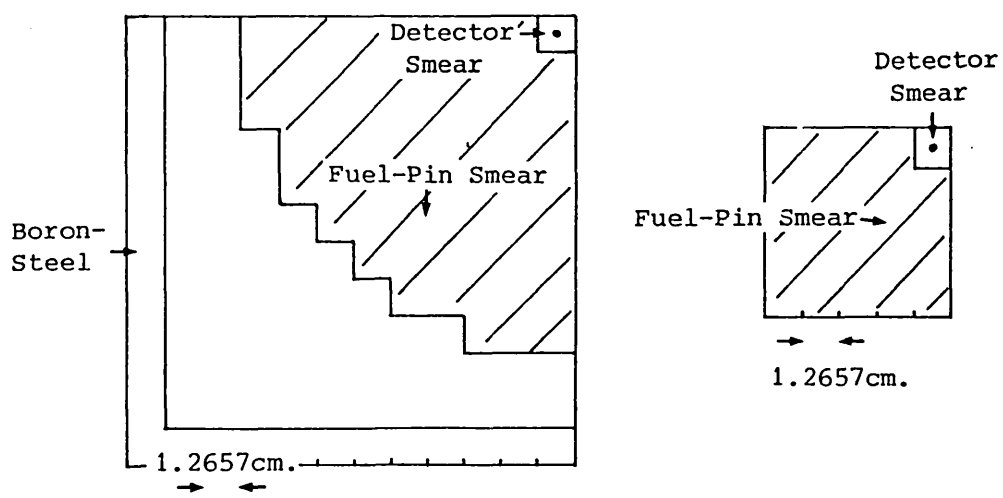

Fig. 7.13. Models to Test the Sensitivity of the Perturbations to the Out-of-Cluster Environment.

used, the method otherwise being similar to the other perturbation factor calculations. Inter-mesh neutron currents were also obtained, and it was because of the copious nature of this output that a reduced number of groups and surrounding meshes were used. Fluxes in the detector mesh for both models, one with no subdivision of the meshes, the other with the mesh size halved, are given in Table 7.17.

Table 7.17 Sensitivity of Perturbation to Mesh Subdivision: Detector Fluxes

Energy Group	LWRWIMS Groups	Flux: No Mesh Subdivision	Flux: Mesh Size Halved	Ratio of Fluxes
1	1-8	1.098	1.091	0.996
2	9-26	0.9196	0.9224	1.003
3	27-51	0.1826	0.1844	1.010
4	52-69	0.2543	0.2723	1.071

The 7.1% rise in thermal flux observed above is (rightmost column) similar in magnitude to the changes in perturbation factors observed in Table 7.16. Its cause can be seen from an examination of the neutron balance in group 4 in the detector mesh, as shown below.

Table 7.18 Neutron Balance in Group 4

Process	Number of Events		Ratio of Number of Events (Mesh Size Halved/no Mesh Subdivision)
	No Mesh Subdivision	Mesh Size Halved	
Scatter in	0.1067	0.01077	1.009
Net Leakage out	0.0879	0.0874	0.995
Absorption + Scatter out	0.0189	0.0202	1.070

It can be seen from the neutron balance that more than 80% of the neutron losses from group 4 in the detector mesh are due to leakage. As a result, the remaining losses due to absorption and upscatter are quite sensitive to changes in the leakage proportion. In the above table the leakage has dropped by a percent or so, due to the halving of the mesh size, yet this causes a 7% rise in the absorption and scatter-out processes, which are directly proportional to the neutron flux. It is quite conceivable that the subdivision of meshes in the region of a material discontinuity such as is a detector in a fuel region can cause a 1% change in the thermal leakage fraction.

7.2.6.2 Sensitivity to Detector Material Change

The most important uncertainty in the specification of the detector smear in the perturbation models was the proportion of polythene. The detector smear is primarily a moderator due to its significant hydrogen content (Table 7.6). The moderator outside the can containing the detector (Figure 7.10) has a well-defined volume, in contrast to the polythene which was loosely fitted around each detector (section 4.1.2). Using both models in Figure 7.9 (i) and (iv), the hydrogen content of the smeared detector material was reduced by 4% to simulate a 10% uncertainty in the polythene proportion. The resulting perturbation factors were 1.395 for the 221 pin clusters model and 0.912 for the 112 pin clusters model, giving a relative perturbation factor of 1.530 (Table 7.16). This change of about 1% in the relative perturbation factor indicates that the use of approximate material data for the perturbation calculations is probably justified.

7.2.6.3 Sensitivity to the Environment Outside the Clusters

Two perturbation factors were calculated for the centre-of-cluster detector in the 221 pin clusters using the models shown in Figure 7.13. The localised model (Fig. 7.13 (ii)) yielded a perturbation factor of 1.486 and the quarter-compartment model (Fig.7.13 (i))), which included the water and boron-steel outside the clusters, gave a corresponding factor of 1.478. This is a direct demonstration of the insensitivity of this detector perturbation to the out-of-cluster environment.

Implicitly it also gives assurance that the localised models are valid for the 112 pin cluster configurations. This is because a softer spectrum obtains in the clusters for these configuration, resulting in perturbations which are even more dependent on neutrons with short mean free paths.

7.2.7 The Relative Perturbation Factors and Errors

For all of the in-cluster detectors in the 112 pin cluster configurations, the relative perturbation factors are unity with negligible errors. This is due to common perturbations. The exceptions are the corner-of-compartment detectors, detectors 6 and 7, and the in-cluster detectors in the 221 pin cluster configurations. The relative perturbation factors for the corner of compartment detectors and detectors 6 and 7, though close to unity, possess errors which are difficult to define. As will be shown later, this uncertainty is not of great importance. Finally, a standard deviation of 3% was assigned to the relative perturbation factor of 1.542 for the in-cluster detectors in the 221 pin cluster configurations, based on the above sensitivity studies.

8. The Modified Source Multiplication Results and Preliminary Diagnostics

The reactivity of the reference configuration, the validity of the two-dimensional models used in the correction factor calculations and the relative perturbation factors have been established. The modified source multiplication results which resulted from the measurements and correction factor calculations as described in Chapter 4 can now be examined.

Results are given for all of the six configurations listed in Chapter 1. These results apply to both the standard and alternative source positions, where used. The configurations test the modifed source multiplication technique in well-subcritical assemblies with different positions of the clusters in relation to the boron-steel walls. Additionally, the 221 pin clusters configuration has no common environment in the skip compared with the reference configuration, and provides an opportunity to test the technique under this condition.

8.1 The Results and Comments

The form of the modified source multiplication equation:

$$\rho_2 = \rho_{1expt} \left(\frac{\rho_2 \, CR_2}{\rho_1 \, CR_1}\right)_{calc} \cdot \left(\frac{CR_1}{CR_2}\right)_{expt} \qquad (8.1)$$

suggests that at least three sets of results be given.

These are:

(i) The corrected experimental count rate ratios: $(CR_{1/CR_2})_{expt}$;

(ii) The calculated reactivities (ρ_{2calc}, ρ_{1calc}) and correction factors: $(\rho_2 CR_{2/\rho_1} CR_1)_{calc}$;

(iii) The reactivities (ρ_2) or the equivalent k-eff values from MSM.

Additionally, ratios of calculated and corrected experimental count rates ($CR_{2_{calc}}/CR_{2_{expt}}$) are listed; these give useful diagnostic information on the performance of the correction factor calculations. In the following tables of results, the detectors are grouped according to their environment; for each environment they are ordered with respect to their distances from the sources.

8.1.1 Corrected Experimental Count Rate Ratios

The ratios of corrected experimental count rates are shown in Tables 8.1 and 8.2. In addition, the corrected experimental count rates for several detectors in some of the configurations, including the reference configuration, are shown in Figure 8.1.

It is noticeable that the ratios for the 196 pins per compartment, 33cm water height configuration are much the smallest. This suggests that it is the least subcritical configuration. The experimental count rate ratios for the centre-of-cluster detectors in this configuration range from 7.5 to about 14.5, showing that its flux profile is somewhat different from that of the reference configuration.

In all the other configurations the ratios show a marked increase for each environment with distance from the sources. For example, the centre-of-cluster detectors in the 112 pin clusters, centred configuration, give a range from 40 to 287, with the sources in the standard positions. This behaviour indicates that the flux profile in each of these configurations is widely different from the flux profile in the reference configuration. In fact the flux distribution in each of the well-subcritical configurations is symptomatic of significant higher mode contamination. This is evident since the fundamental mode is expected to be a fairly even distribution throughout most of the configurations studied.

Table 8.1 Corrected Experimental Count Rate Ratios:

Standard Source Positions

Detector Environment	Detector Position	Corrected Experimental Count Rate Ratio, Reference/Well-Subcritical Configurations					
		196/33	112/76 (CTD)	112/76 (G4)	112/76 (CC)	112/76 (CCD)	221/76 (CTD)
Centre of Cluster	8 alt 1	7.913	44.32	72.97	31.39	14.12	137.49
	4 alt 4	7.866	42.27	29.87	37.95	25.98	132.66
	3 alt 5	7.504	40.54	29.26	36.77	24.68	130.19
	3 alt 1	10.51	99.77	113.73	83.56	47.66	337.78
	4 alt 5	9.977	95.73	102.73	79.08	45.30	314.75
	5 alt 4	10.42	98.44	48.63	83.32	47.96	320.41
	5 alt 5	10.03	94.50	48.31	78.24	47.07	318.85
	4 alt 1	13.11	184.16	169.01	134.15	60.44	712.30
	8 alt 4	14.59	286.80	213.64	265.60	132.21	1090.5
	8 alt 5	13.93	268.49	195.26	250.78	129.27	1009.4
	5 st	14.24	277.56	158.18	254.21	130.18	1058.5
Half-way	8 alt 2	6.920	33.89	26.99	23.40	9.921	81.21
	3 alt 2	10.88	107.64	114.66	86.95	46.65	307.27
	4 alt 2	12.33	163.09	150.61	110.85	50.34	478.61
	5 alt 2	13.40	239.41	134.16	230.39	117.16	700.37
Corner of Compartment	8 st	5.838	9.674	16.57	7.227	7.387	10.77
	3 alt 3	7.911	21.46	24.06	21.16	12.60	25.23
	3 alt 4	9.972	30.61	38.63	28.33	17.20	41.90
	8 alt 3	9.843	28.27	49.00	17.45	7.304	37.59
	3 st	11.22	47.55	52.19	41.55	21.16	68.18
	4 st	11.32	48.17	55.67	36.63	16.34	65.21
	4 alt 3	11.95	53.56	45.66	46.27	22.00	76.29
	5 alt 1	11.94	75.44	52.32	81.74	40.39	103.67
	5 alt 3	13.55	72.77	49.93	82.20	43.60	118.91
Outside Skip	7 st	12.20	145.90	205.19	165.86	96.89	217.86
	6 st	14.27	270.64	197.85	326.50	175.66	426.68
	9 st	13.78	372.31	295.55	474.13	247.06	602.27
	2 st	13.25	351.39	271.86	436.47	230.35	558.72
	1 st	14.68	356.09	366.20	419.21	219.73	552.92

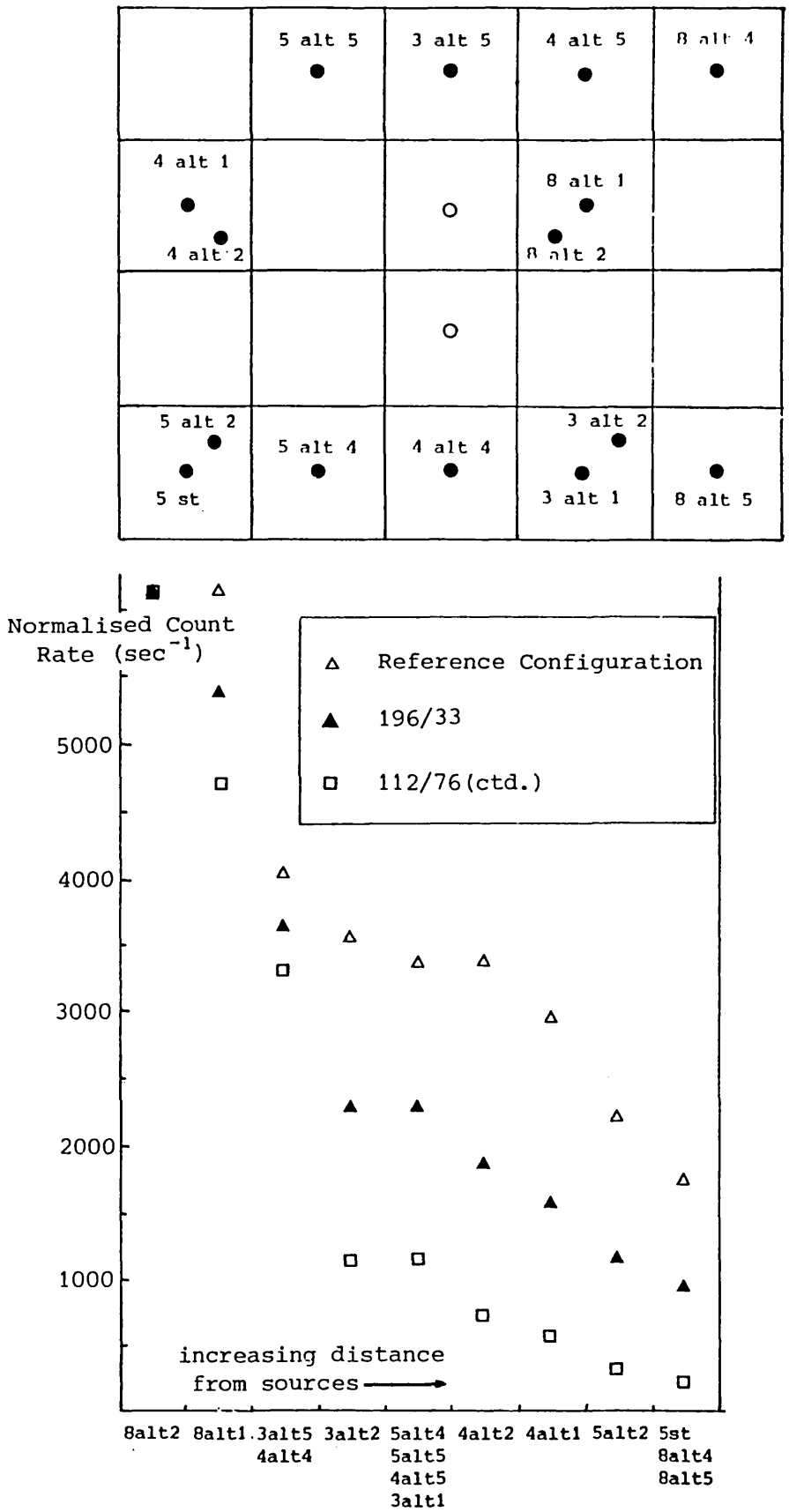

Fig. 8.1. Corrected Experimental Count Rates for Several of the Configurations.

The differences in flux profile have been caused by the creation of water gaps around the pin clusters. The likelihood of neutrons slowing down in the water and being captured in either the water or the boron-steel is greater in the well-subcritical configurations than in the reference configuration. The high flux attenuation with distance from the sources can be viewed in terms of the migration length of the neutrons and the approximate neutron multiplication ($^1/_\rho$) of each assembly. In the 112 pin clusters configurations, the migration length is about 6cm in the clusters (section 2.9), and so with a neutron multiplication of about 5 corresponding to k-eff ≅ 0.83, the average extent of the fission chains is expected to be about √5 x √6 x 6cm ≅ 33cm from the sources, which is somewhat greater than the width of one compartment.

Table 8.2 Corrected Experimental Count Rate Ratios: Alternative Source Positions

Detector Environment	Detector Positions in Combination	Corrected Experimental Count Rate Ratio		
		196/33	112/76 (CTD)	221/76 (CTD)
Centre of Cluster	4 st + 4 alt 2	7.227	37.15	113.83
	3 st + 3 alt 1	8.604	52.60	165.16
	3 alt 2	10.06	96.33	313.84
	8 alt 2	9.829	90.00	303.97
	5 st + 5 alt 2	9.386	79.18	267.91
Corner of Compartment	8 st + 8 alt 1	5.473	6.267	7.098
	4 alt 1 + 5 alt 1	7.373	19.43	23.59
Outside Skip	7 st + 7 alt 2	10.52	85.96	116.19
	6 st + 6 alt 2	10.17	107.71	151.12

As can be seen from Table 8.2, the range of count rate ratios is smaller for the alternative source positions. For example, the range for the centre-of-cluster detectors in the 112 pin clusters, centred configuration is from 37 to 96, which is three times smaller than the corresponding range for the standard source positions. This is experimental confirmation of the fact that the flux distribution in well-subcritical assemblies is evened out by a spreading of the source positions.

Finally, the ratios for the in-cluster detectors in the 221 pin clusters configuration are the greatest of all. This is due to the harder spectrum resulting from the smaller lattice pitch in this configuration (section 1.2.2), compared with the other configurations.

8.1.2 Calculated Reactivities and Correction Factors

In Table 8.3 are listed the calculated k-eff values and the equivalent reactivities used in the correction factor calculations. Values for both the standard and alternative source positions are given, it being known that the repositioning of the source tubes causes a small change in k-eff (section 4.1.1).

Table 8.3 Calculated Reactivities

Configuration	Standard Source Positions		Alternative Source Positions	
	Calculated k-eff	Calculated Reactivity	Calculated k-eff	Calculated Reactivity
196/49 (reference)	0.9929	-0.00719	0.9927	-0.00735
196/33	0.9489	-0.0538	0.9465	-0.0565
112/76 (CTD)	0.8132	-0.22974	0.8153	-0.2266
112/76 (G4)	0.8424	-0.18715	-	-
112/76 (CC)	0.8387	-0.19225	-	-
112/76 (CCD)	0.9047	-0.10536	-	-
221/76 (CTD)	0.7508	-0.33186	0.7517	-0.33032

It must be remembered that the calculational models for the two versions of the reference configuration included altered bucklings to produce reactivities close to the experimentally calibrated value of -0.00713 (section 4.2.2). The calculated reactivities for the well-subcritical configurations are in broad agreement with the implications of the count rate ratios in the previous section: the 196 pins per compartment, 33cm water-height configuration is the least subcritical.

Tables 8.4 and 8.5 show the correction factors for all detector and source positions. A relative perturbation factor of 1.542 (section 7.2.7) was used in the correction factors for the in-cluster detectors in the 221 pin clusters configuration; all other relative perturbation factors were equal to unity (section 7.2.7).

Table 8.4 Correction Factors: Standard Source Positions

Detector Environment	Detector Position	Correction Factor					
		196/33	112/76 (CTD)	112/76 (G4)	112/76 (CC)	112/76 (CCD)	221/76 (CTD)
Centre of Cluster	8 alt 1	1.185	0.605	0.288	0.745	1.015	0.304
	4 alt 4	1.243	0.693	0.827	0.619	0.527	0.353
	3 alt 5	1.243	0.693	0.827	0.619	0.527	0.353
	3 alt 1	0.958	0.265	0.197	0.270	0.282	0.124
	4 alt 5	0.958	0.265	0.197	0.270	0.282	0.124
	5 alt 4	0.958	0.265	0.504	0.270	0.282	0.124
	5 alt 5	0.958	0.265	0.504	0.270	0.282	0.124
	4 alt 1	0.755	0.127	0.127	0.270	0.219	0.0531
	8 alt 4	0.701	0.0850	0.102	0.158	0.0957	0.0344
	8 alt 5	0.701	0.0850	0.102	0.0790	0.0957	0.0344
	5 st	0.701	0.0850	0.102	0.0790	0.0957	0.0344
Half-way	8 alt 2	1.364	0.903	0.750	1.036	1.480	0.555
	3 alt 2	0.934	0.262	0.195	0.274	0.306	0.138
	4 alt 2	0.811	0.164	0.153	0.194	0.273	0.0849
	5 alt 2	0.749	0.106	0.161	0.0899	0.110	0.0543
Corner of Compartment	8 st	1.601	3.302	1.532	3.636	2.039	4.305
	3 alt 3	1.262	1.570	1.171	1.312	1.293	2.019
	3 alt 4	1.016	0.975	0.675	0.916	0.864	1.109
	8 alt 3	0.998	1.004	0.455	1.440	2.096	1.138
	3 st	0.905	0.642	0.473	0.619	0.738	0.723
	4 st	0.885	0.537	0.426	0.633	0.904	0.595
	4 alt 3	0.847	0.496	0.540	0.500	0.667	0.542
	5 alt 1	0.820	0.364	0.510	0.294	0.365	0.397
	5 alt 3	0.762	0.348	0.517	0.279	0.313	0.355
Outside Skip	7 st	0.852	0.176	0.106	0.134	0.135	0.188
	6 st	0.714	0.0795	0.108	0.0580	0.0648	0.0787
	9 st	0.707	0.0599	0.0753	0.0409	0.0480	0.0565
	2 st	0.739	0.0563	0.0700	0.0380	0.0445	0.0528
	1 st	0.643	0.0567	0.0497	0.0383	0.0449	0.0532

Table 8.5 Correction Factors: Alternative Source Positions

Detector Environment	Detector Positions in Combination	Correction Factor		
		196/33	112/76	221/76
Centre of Cluster	4 st + 4 alt 2	1.326	0.750	0.379
	3 st + 3 alt 1	1.126	0.549	0.281
	3 alt 2	0.987	0.282	0.134
	8 alt 2	0.987	0.282	0.134
	5 st + 5 alt 2	1.047	0.330	0.157
Corner of Compartment	8 st + 8 alt 1	1.640	4.702	6.116
	4 alt 1 + 5 alt 1	1.270	1.562	2.023
Outside Skip	7 st + 7 alt 2	0.975	0.322	0.362
	6 st + 6 alt 2	0.961	0.225	0.250

In the 112 and 221 pin cluster configurations it can be seen that the correction factors have a wide spread of values and inevitably depart significantly from unity in most instances. Considering the in-cluster detectors in the 112 pin clusters, centred configuration using the standard source positions, the correction factors range from about 0.9 to about 0.1. For the detectors outside the skip the ratios are still lower in most cases.

Now it is quite probable that many of these correction factors suffer from significant systematic errors. This is a very likely result of the calculation of the two different flux profiles for each correction factor, as was stated in the remarks on the modified source multiplication technique in section 3.2.3. Using the modal interpretation outlined in that discussion, it can be said that since the flux profile in each well-subcritical assembly is symptomatic of significant higher mode contamination, the correction factors derived from the calculation of that flux profile are sensitive, at least, to errors in calculated reactivity. This can alternatively be viewed in terms of the calculated representation of the absorption in the water surrounding the clusters and in the boron-steel walls. If this absorption is overestimated, then there will be an increasing tendency to underestimate correction factors as the distance from the sources increases. Such an effect is accompanied by a tendency to underestimate the k-eff of the assembly in question, which is equivalent to an error in calculated reactivity.

8.1.3 Ratios of Calculated and Corrected Experimental Count Rates

The possible systematic errors due to calculation can be examined by comparing the calculated and experimental count rates for each configuration.

In Tables 8.6 and 8.7 are the ratios of calculated and corrected experimental count rates for both source positions, though only the ratios for the detectors in the skip are given. It is only these

detectors, which, being intercalibrated (section 4.1.4) can be normalised to a common sensitivity and thus give meaningful information on the relations between the calculated and experimental flux profiles in the assemblies studied.

Table 8.6 Ratios of Calculated and Corrected Experimental Count Rates: Standard Source Positions

Detector Environment	Detector Position	Ratio of Calculated and Corrected Experimental Count Rates						
		196/49 (ref)	196/33	112/76 (CTD)	112/76 (G4)	112/76 (CC)	112/76 (CCD)	221/76 (CTD)
Centre of Cluster	8 alt 1	0.257	0.322	0.215	0.207	0.225	0.251	0.232
	4 alt 4	0.248	0.324	0.227	0.235	0.218	0.232	0.252
	3 alt 5	0.262	0.326	0.230	0.243	0.223	0.232	0.261
	3 alt 1	0.244	0.329	0.202	0.211	0.206	0.224	0.223
	4 alt 5	0.266	0.340	0.211	0.207	0.213	0.232	0.226
	5 alt 4	0.248	0.331	0.202	0.234	0.209	0.229	0.214
	5 alt 5	0.262	0.337	0.205	0.245	0.207	0.237	0.225
	4 alt 1	0.257	0.341	0.188	0.213	0.204	0.233	0.211
	8 alt 4	0.242	0.330	0.185	0.203	0.190	0.209	0.197
	8 alt 5	0.256	0.334	0.183	0.196	0.190	0.216	0.193
	5 st	0.236	0.314	0.174	0.203	0.177	0.201	0.186
Half-Way	8 alt 2	0.260	0.328	0.249	0.202	0.236	0.261	0.254
	3 alt 2	0.246	0.334	0.217	0.211	0.219	0.239	0.226
	4 alt 2	0.262	0.350	0.220	0.233	0.211	0.246	0.231
	5 alt 2	0.248	0.333	0.198	0.206	0.192	0.218	0.204
Corner of Compartment	8 st	0.295	0.369	0.295	0.288	0.290	0.304	0.297
	3 alt 3	0.278	0.371	0.294	0.301	0.289	0.309	0.307
	3 alt 4	0.276	0.374	0.258	0.277	0.268	0.280	0.278
	8 alt 3	0.289	0.379	0.257	0.247	0.271	0.302	0.268
	3 st	0.263	0.357	0.241	0.249	0.253	0.280	0.281
	4 st	0.302	0.404	0.251	0.275	0.262	0.304	0.254
	4 alt 3	0.296	0.401	0.246	0.280	0.256	0.296	0.265
	5 alt 1	0.267	0.349	0.229	0.273	0.240	0.269	0.238
	5 alt 3	0.291	0.401	0.231	0.288	0.249	0.270	0.265

Table 8.7 Ratios of Calculated and Corrected Experimental Count Rates: Alternative Source Positions

Detector Environment	Detector Positions in Combination	Ratio of Calculated & Corrected Experimental Count Rates			
		196/49 (ref)	196/33	112/76 (CTD)	221/76 (CTD)
Centre of Cluster	4 st + 4 alt 2	0.247	0.310	0.223	0.288
	3 st + 3 alt 2	0.239	0.301	0.224	0.246
	3 alt 2	0.234	0.302	0.207	0.219
	8 alt 2	0.252	0.318	0.207	0.228
	5 st + 5 alt 2	0.231	0.295	0.195	0.216
Corner of Compartment	8 st + 8 alt 1	0.286	0.334	0.273	0.276
	4 alt 1 + 5 alt 1	0.268	0.327	0.264	0.285

It can be seen that all of the ratios are much less than unity; this is probably due to an underestimation of the actual sensitivity of the detectors in the calculations (section 4.2.3). This underestimation is common to all the ratios in Tables 8.6 and 8.7, since each experimental count rate has been corrected by the relative detector sensitivity. This underestimation affects neither the correction factor nor the calculated reaction rate profile across each assembly. It only affects the level of the profile.

Figure 8.2 illustrates the ratios of calculated and corrected experimental count rates for representative detector positions in several of the configurations. It is evident that for each configuration there are two trends in these ratios: their behaviour in each environment across the whole configuration, and their behaviour across a single compartment, which encompasses the different environments.

For all of the 112 and 221 pin clusters configurations the ratios in Tables 8.6 and 8.7 decrease with increasing distance from the sources. This tendency to decrease is evident with some fluctuations, for each detector environment. Considering the 112 pins per compartment configuration with the standard source positions, the ratios for the centre of cluster detectors range from 0.230 for detector 3 (alternative 5) to 0.174 for detector 5 (standard). A similar range of ratios is apparent also for the slumped configurations showing that the relative

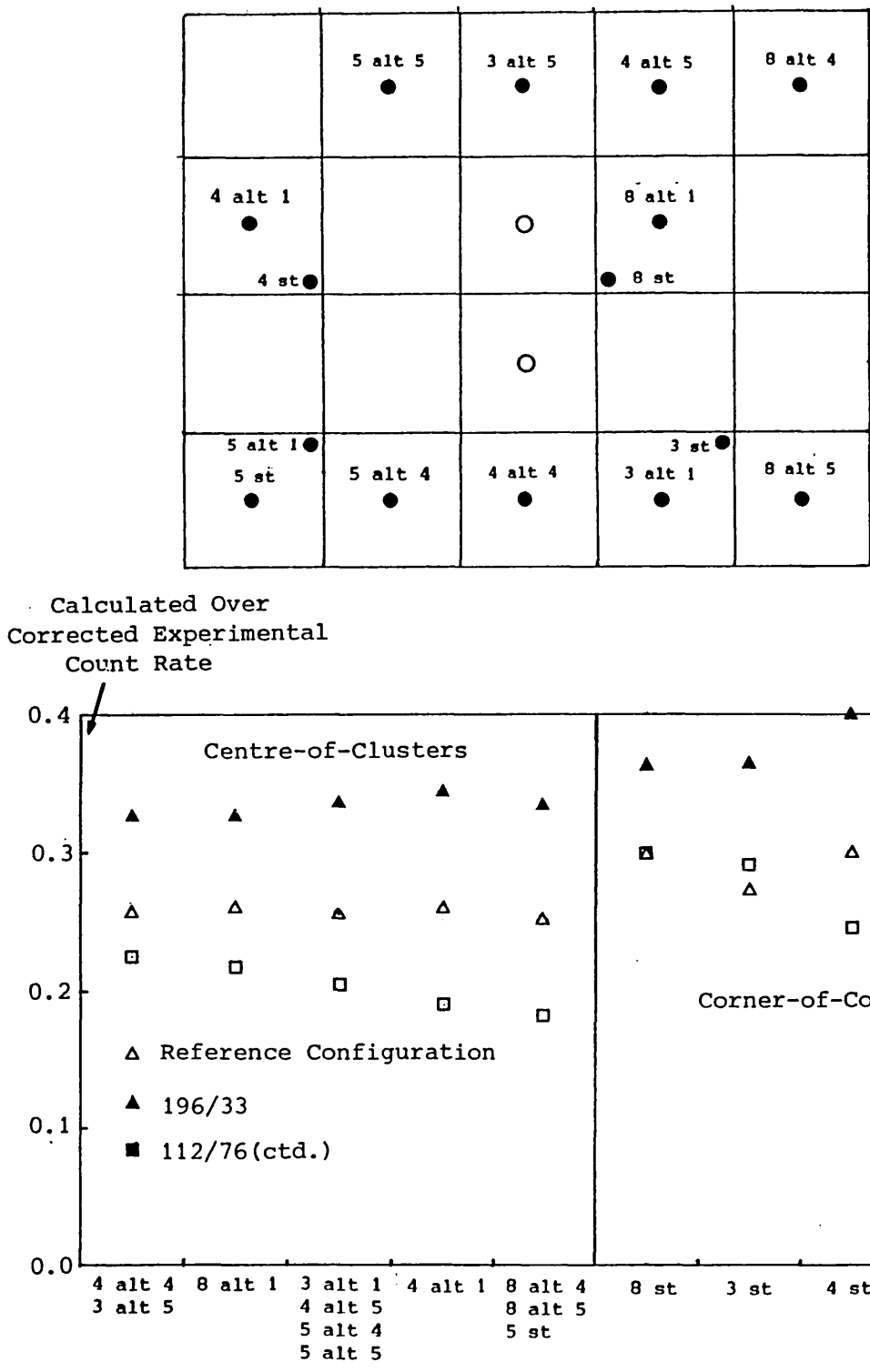

Fig. 8.2. Ratios of Calculated Over Corrected Experimental Count Rates for Several of the Configurations.

behaviour of the calculation and experiment is not much affected by the movements of the clusters.

This behaviour is, however, less marked with the alternative source positions. For example, the range for the centre-of-cluster detectors has reduced to 0.224 to 0.195. This is apparently due to the fact that the range of distances from the sources is smaller for the alternative source postions that it is for the standard source positions, it being remembered that the count rates in symmetric pairs of positions were combined when the alternative source positions were used (section 4.1.1).

The reason for the tendency of these ratios to decrease with increasing distance from the sources is evident, in part, from a comparison of the ratios in the clusters to those in the corners of compartments. The ratios in the compartmental corners are, on the whole, larger than those in the clusters, as can be seen in Figure 8.2. This points to an overestimation of thermal flux in the water surrounding the clusters compared to the thermal flux in the clusters themselves. Since water is a mild absorber of thermal neutrons, a significant overestimation of thermal flux in the water surrounding the clusters would mean an overestimation of the attenuation of neutron flux as an increasing number of water regions are crossed. There may also be a similar overestimation of thermal flux in the boron-steel walls.

By contrast, the ratios of calculated and corrected experimental count rates for the two 196 pins per compartment configurations show no consistent tendency to decrease with increasing distance from the sources and remain roughly constant. Nevertheless, the ratios in the corners of the compartments are greater than those in the centres of the compartments. The essential difference is that in the 196 pins per compartment configurations, the corners of the compartments are occupied by fuel pins, and not by water, as in the other configurations. Hence, the relative overestimation of thermal flux in the compartmental corners does not necessarily mean an overestimation in neutron absorption, relative to fission. In fact, there is some evidence that the overall absorption is underestimated for these configurations: in section 4.2.2

it was stated that the extrapolation distance in the calculational model for the reference configuration was reduced to 4.47cm from its estimated true value to give a subcritical reactivity equal to the calibrated value of -0.00713.

8.1.4 K-eff Values from Modified Source Multiplication

The reactivities and hence k-eff values from MSM relate in a simple fashion to the calculated over corrected experimental count rate ratios. The enforced similarity between the calculated and experimental reactivity of the reference configuration (section 4.2.2) enables the modified source multiplication equation to be written

$$\rho_2 \cong \rho_{2_{calc}} \frac{(CR_{2_{calc}}/CR_{2_{expt}})}{(CR_{1_{calc}}/CR_{1_{expt}})}. \qquad (8.2)$$

The calculated over corrected experimental count rate ratios in the reference configuration ($CR_{1_{calc}}/CR_{1_{expt}}$) show no tendency to increase or decrease with increasing distance from the sources as was shown in the previous section. Hence the reactivities from MSM for the well-subcritical configurations follow the same trends as the calculated over experimental count rate ratios in these configurations. The resultant k-eff values, shown in Tables 8.8 and 8.9, exhibit these trends, but in the reverse direction, tending thus to increase with distance from the sources in the 112 and 221 pin clusters configurations.

In Figure 8.3 are shown the spreads of k-eff values obtained for the 112 pin clusters, centred configuration. Of course, similar spreads of k-eff values are evident for all the 112 and 221 pin clusters configurations, since the calculated over experimental count rate ratios showed the smiliarity of these arrangements in the attenuation of neutrons in the water gaps between the clusters, and probably the boron-steel walls.

It is apparent from Figure 8.3 that the tendency of the calculations to overestimate the attenuation of neutrons with increasing distance from

the sources is continued into the regions outside the skip, since the k-eff values for the detectors outside the skip are the highest of all. The tendency of progressive overestimation of k-eff is, however, blurred somewhat by the experimental error of 4% r.m.s. in each count rate ratio (section 6.7). Also evident is the fact that the calculated k-eff value is lower than nearly all of the modified source multiplication k-eff values, which is consistent with the overestimation of thermal flux in the absorbent water regions around the clusters (section 8.1.3). Finally, the spread of k-eff values for each environment is reduced in the results from the alternative source positions.

Table 8.8 K-eff Values from MSM: Standard Source Positions

Detector Environment	Detector Position	k-eff Value from MSM					
		196/33	112/76 (CTD)	112/76 (G4)	112/76 (CC)	112/76 (CCD)	221/76 (CTD)
Centre of Cluster	8 alt 1	0.937	0.840	0.870	0.857	0.907	0.770
	4 alt 4	0.935	0.827	0.850	0.857	0.911	0.750
	3 alt 5	0.938	0.833	0.853	0.860	0.915	0.753
	3 alt 1	0.933	0.842	0.862	0.861	0.913	0.769
	4 alt 5	0.936	0.847	0.874	0.868	0.916	0.782
	5 alt 4	0.934	0.843	0.851	0.862	0.912	0.779
	5 alt 5	0.936	0.849	0.852	0.869	0.914	0.779
	4 alt 1	0.934	0.858	0.867	0.869	0.914	0.787
	8 alt 4	0.932	0.852	0.865	0.870	0.917	0.789
	8 alt 5	0.935	0.860	0.875	0.876	0.919	0.801
	5 st	0.934	0.856	0.862	0.875	0.918	0.794
Half-way	8 alt 2	0.937	0.821	0.874	0.853	0.905	0.756
	3 alt 2	0.932	0.833	0.862	0.855	0.908	0.768
	4 alt 2	0.933	0.840	0.859	0.867	0.911	0.775
	5 alt 2	0.933	0.847	0.867	0.871	0.916	0.787
Corner of Compartment	8 st	0.938	0.814	0.847	0.842	0.903	0.752
	3 alt 3	0.934	0.806	0.833	0.835	0.896	0.734
	3 alt 4	0.933	0.825	0.843	0.844	0.904	0.751
	8 alt 3	0.935	0.832	0.863	0.848	0.902	0.766
	3 st	0.933	0.827	0.850	0.845	0.900	0.740
	4 st	0.933	0.841	0.855	0.858	0.905	0.783
	4 alt 3	0.933	0.841	0.851	0.858	0.905	0.772
	5 alt 1	0.935	0.836	0.840	0.854	0.905	0.773
	5 alt 3	0.931	0.847	0.844	0.860	0.911	0.769
Outside Skip	7 st	0.931	0.845	0.866	0.864	0.915	0.774
	6 st	0.932	0.867	0.868	0.881	0.925	0.807
	9 st	0.935	0.863	0.863	0.878	0.922	0.805
	2 st	0.935	0.876	0.881	0.894	0.932	0.826
	1 st	0.937	0.874	0.885	0.897	0.934	0.827

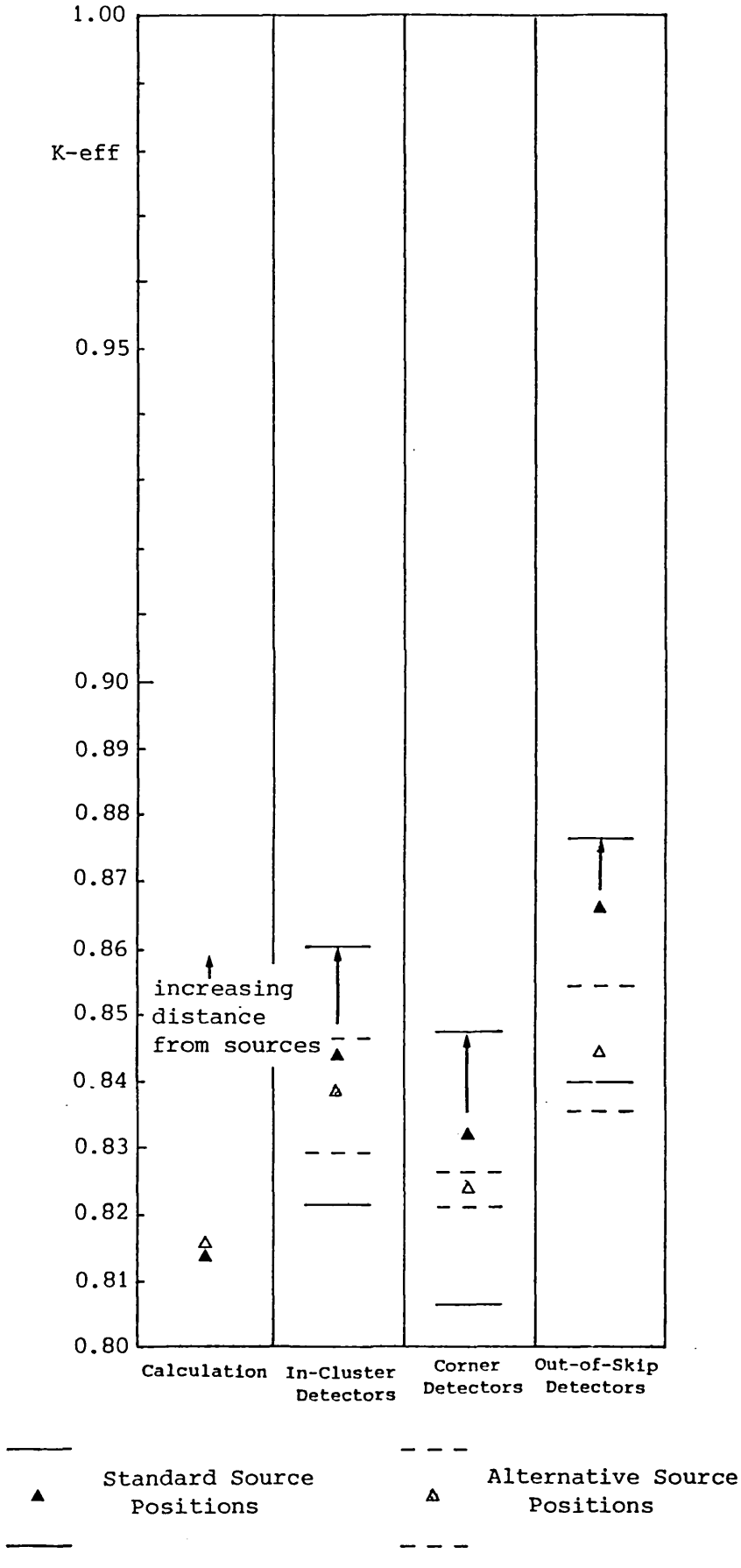

Fig. 8.3. Spreads of K-eff Values for the 112 Pin Clusters, Centred Configuration.

Table 8.9 K-eff Values from MSM: Alternative Source Positions

Detector Environment	Detector Positions in Combination	MSM k-eff Value		
		196/33	112/76 (CTD)	221/76 (CTD)
Centre of Cluster	4 st + 4 alt 2	0.936	0.834	0.764
	3 st + 3 alt 1	0.935	0.829	0.752
	3 alt 2	0.934	0.838	0.769
	8 alt 2	0.935	0.847	0.775
	5 st + 5 alt 2	0.935	0.843	0.770
Corner of Compartment	8 st + 8 alt 1	0.940	0.826	0.764
	4 alt 1 + 5 alt 1	0.937	0.822	0.746
Outside Skip	7 st + 7 alt 2	0.932	0.835	0.769
	6 st + 6 alt 2	0.935	0.853	0.788

The results in this chapter have shown that the large differences in flux profile between the well-subcritical configurations and the reference configuration have resulted in significant variations in the k-eff values obtained for different detector and source positions. This is due to the deficiencies of the calculations used to calculate, for each set of correction factors, two widely differing flux profiles. Since one of the principal aims of the modified source multiplication technique is to show the accuracy of the correction factors and that they are sufficiently accurate (section 3.2.3), it is evidently necessary to develop rules for the selection of preferred source and detector positions in this application.

8.2 Preliminary Assessment of Calculational Errors and Preferred Source and Detector Positions

8.2.1 Calculational Errors

It is necessary to provide a means of assessing the systematic errors due to calculational deficiencies. This was stressed in the discussion of the MSM technique in section 3.2.4. It seems reasonable that these errors are given, in some measure, by the spread of k-eff values obtained from detectors distributed throughout the skip (Figure 8.3).

This is because this spread of k-eff values results directly from the deficiencies of the calculations, as shown in the previous sections.

To clarify the relationship between the spreads of k-eff values and the systematic errors due to calculation, it can be postulated that the true k-eff value of each configuration lies somewhere in the range of k-eff values resulting from the detectors. The final estimate of this k-eff value is likely to be some average of these k-eff values, and so the likely difference between the estimate and the true value is influenced by the spread of the k-eff values.

Alternatively the systematic errors due to calculational deficiencies can be assessed by improving the correction factor calculations for selected configurations and examining the resultant changes in the k-eff values from the different detectors. To this end, it seems desirable to produce calculations which predict accurately the flux profile in the well-subcritical configuration.

Both of the above methods of assessing the calculational errors are used in the ensuing analysis.

8.2.2 Source Positions

It is clear from Figure 8.3 that the effective use of four radial source positions instead of two results in a smaller spread of modified source multiplication k-eff values. As long as the quantifiable errors from the modified source multiplication technique are dependent in some measure on the spread of k-eff values obtained from a range of detector positions, then the preference for the greater radial spreading of sources is clear.

This diagnosis does not mean, however, that the use of two radial source positions is inadequate for measuring the k-eff values of the well-subcritical skip configurations within acceptable errors. Nor does it mean, on the other hand, that the use of four radial source positions is itself adequate. This depends on the magnitude of the overall errors inherent in the measurements.

8.2.3 Detector Positions

The process of detector selection, as with that of preferred source positions in the last section, involves a reduction of the systematic errors due to calculation. Hence it is required to select a group of detectors which result in a sufficiently small range of k-eff values close to the true k-eff value. This is evidently desirable since the spread of k-eff values for the 112 pin clusters, centred configuration is from 0.806 to 0.876 for the standard source positions and from 0.821 to 0.854 for the alternative source positions (Fig. 8.3).

The justification for this selection should be in two parts, as with that for the preferred source positions. It should be demonstrable by calculation, and since calculations are inevitably approximate, it should have a physical basis. Fortunately, the physical meaning of source multiplication provides a means of detector selection. Equation 3.10 states that the reactivity of a subcritical assembly is defined by the ratio of the effective source strength to the total fission rate:

$$\rho = \frac{-WS_{eff}}{\overline{\nu}\, CR} = \frac{-S_{eff}}{\langle \nu\Sigma_f \phi \rangle}. \qquad (8.3)$$

The flux in regions outside the fissile regions of the assembly does not feature directly in this definition. Since the modified source multiplication equation (Equation 8.1) is merely a practical form of Equation 8.3, a physical interpretation of the technique is to include only the detectors situated in fissile regions of the assembly. The detectors situated outside the fissile regions are still useful in that they give information on the performance of the correction factor calculations, as was seen in section 8.1.3. The exclusion of the detectors outside the fuel regions has the additional advantage that the unquantified errors on their relative perturbation factors (section 7.2.7) are reduced in importance.

A first approach, then, to the question of detector selection is average the k-eff values from all detectors situated in the fissile regions of each configuration. In Table 8.10 are listed the k-eff values of each configuration resulting from this averaging, with their associated standard deviations.

Table 8.10 K-eff Values from Modified Source Multiplication: Averaging of In-Cluster Detectors

Configuration	Standard Source Positions		Alternative Source Positions	
	$\overline{k\text{-eff}}$	Standard Deviation	$\overline{k\text{-eff}}$	Standard Deviation
196/33	0.934	0.002	0.935	0.002
112/76(CTD)	0.843	0.011	0.838	0.007
112/76(G4)	0.863	0.009	-	-
112/76(CC)	0.864	0.008	-	-
112/76(CCD)	0.913	0.004	-	-
221/76(CTD)	0.776	0.015	0.766	0.008

This procedure for obtaining a k-eff value for each configuration has clearly brought the standard deviations resulting from the spreads of individual results down to quite small values. The above results, implicitly derived from several detectors, include the experimental count rate errors quantified in chapter 6.

It must be remembered, however, for simplicity the systematic error of 5.5% in the value of the reactivity of the reference configuration (Chapter 5), and the error of 3% resulting from the two-dimensional representations used in the correction factor calculations (Chapter 7) have not been included.

These errors will increase the errors given in Table 8.10 by an amount related to the departure of the k-eff values from unity. Hence, the total error in the value of k-eff for the 112 pin clusters, centred configuration increases from 0.011 to 0.014, for example.

It is possible to take the process of detector selection a stage further by noting the fact that Equation 8.3 relates the effective source strength to the total fission rate in the assembly, and not directly to the fission rate at certain positions. This suggests that the count rates from the detectors in the fissile regions should be treated as a single count rate, by summing them. This single count rate is an experimental representation of the total fission rate in the assembly.

The fission rate appearing in Equation 8.3 is, however, characteristic of a fundamental mode distribution and so its use can be questioned in the optimisation of measurements which involve neutron distributions far removed from a fundamental mode. The answer to this lies in the fact that although the neutron distribution in most of the skip configurations resulting from the localised sources is quite different from a fundamental mode, the total fission rate is probably fairly similar to that resulting from a fundamental mode distribution.

It has already been stated (section 3.2.3) that the higher modes, having both negative and positive values over the assembly, are not expected to contribute so much to the total fission rate as the fundamental mode. Alternatively, a comparison can be made of the total fission rate due to two source distributions of the same total strength, one being the localised distribution present in the modified source multiplication measurements and the other being a fundamental mode source distribution which, as explained in section 2.9, gives rise to a fundamental mode flux distribution, even in a well-subcritical assembly. Since the average extent of the fission chains is much smaller in the well subcritical configurations than the size of the whole assembly, and source neutrons are fast, it is to be expected that the average total number of fissions resulting from a source neutron, is not very strongly dependent on the position of the source neutron, at least near to the centre of the assembly. Hence, the localised source distribution is likely to result in a similar number of fissions to the fundamental mode source distribution. (This is further examined in Chapter 11).

The idea of summing the count rates from an ensemble of detectors spread over most of the assembly thus has the advantage of supressing the effects of the higher modes. However, it remains to be seen whether this leads to a decrease in the sensitivity of the correction factors to calculation.

The modified source multiplication results, derived from the aggregation of all count rates in the clusters for each configuration are given in Table 8.11. The resultant k-eff values are illustrated in Figure 8.4, together with the mean k-eff values of the in-cluster detectors as given in the last section. It can be seen that for all the 112 and 221 pin

clusters configurations, the effect of considering the in-cluster count rates as a single count rate is to increase the importance of the detectors closest to the sources, since these have the highest count rates. Hence, the k-eff values obtained by this method are lower in each case than those obtained by averaging the individual k-eff values resulting from the in-cluster detectors.

Table 8.11 Modified Source Multiplication Results: Aggregation of In-Cluster Count Rates

Configuration	Standard Source Positions			Alternative Source Positions		
	Ratio of Corrected Experimental Count Rates	Correction Factor	K-eff	Ratio of Corrected Experimental Count Rates	Correction Factor	k-eff
196/33	9.486	1.023	0.935	8.690	1.121	0.935
112/76(CTD)	67.96	0.4132	0.833	57.53	0.4831	0.835
112/76(G4)	66.65	0.3509	0.857	-	-	-
112/76(CC)	52.99	0.4400	0.857	-	-	-
112/76(CCD)	26.73	0.5292	0.908	-	-	-
221/76(CTD)	200.7	0.2196	0.760	182.1	0.2408	0.762

The above method of aggregating the count rates in the clusters has a potentially serious disadvantage in that the total count rate would be greatly influenced by the presence of a detector in the same fuel cluster as either of the tubes containing the sources. A calculation of the count rate resulting from a detector in the position shown in Figure 7.6 in the 112 pin clusters, centred configuration, gave a rate about 8 times that corresponding to detector 8 alternative 1, at a distance of one compartment from the sources. Hence it is quite possible that the k-eff value obtained for any of the well-subcritical configurations is significantly dependent on whether or not such a detector is included in the measurements.

An analysis of this question is pursued later, for the immediate issue is to give further information on the errors due to calculation and the detector selection described. This is achieved by a process of varying the correction factor calculations, and is outlined in the next two chapters.

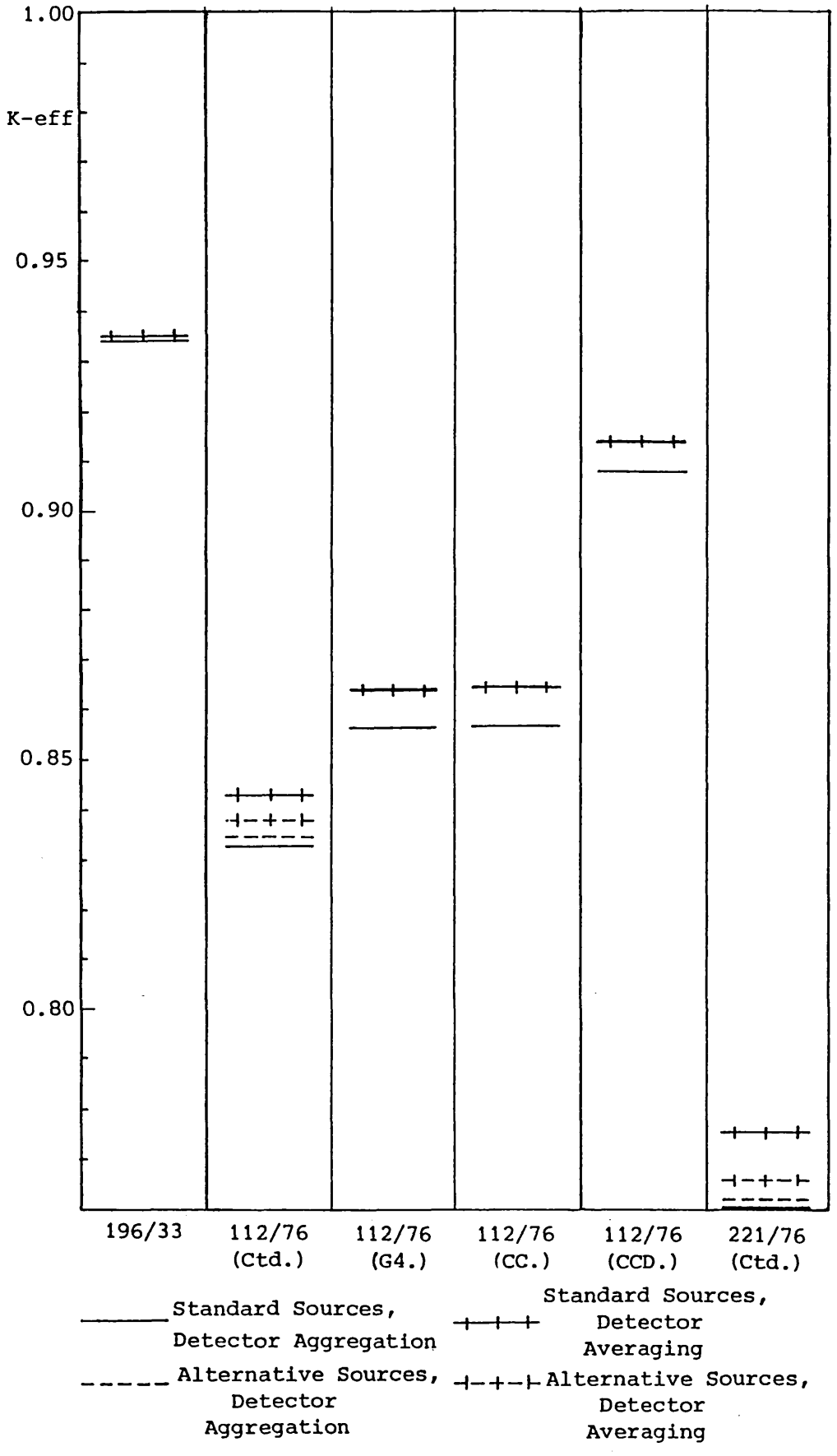

Fig. 8.4. Mean K-eff Values (In-Cluster Detectors.)

9. Correction Factor Calculations Using Transport Theory

9.1 Reasons for the Variation of the Correction Factor Calculations

The analysis of the previous chapter resulted in a selection of preferred source and detector positions, using physical considerations, to reduce the estimated systematic errors due to calculational deficiencies. The spread of k-eff values resulting from a distribution of detectors was used as a measure of these systematic errors. It is evident that the selection can be tested by producing a correction factor calculation which reduces this spread.

However, even calculations which predict accurately the flux profile in the configuration in question may still contain systematic errors related to the level of the flux in the well-subcritical configuration relative to the reference configuration.

In order to test for the presence of such systematic errors, a variety of sensitivity studies were carried out in which many of the specifications used in the correction factor calculations were varied. These sensitivity studies are described in the next chapter.

9.2 Differences Between Transport Theory and Diffusion Theory Calculations

With regard to the production of a correction factor calculation to represent more accurately the flux profile across each of the assemblies studied, it was expected that the principal deficiency in the original correction factor calculations was due to the performance of diffusion theory in the water regions surrounding the fuel clusters, and probably in the boron-steel walls. In such regions, diffusion theory is known to overestimate the thermal flux relative to the fuel regions (1). This is the case in the correction factor calculations, as indicated in the last chapter.

In order to ascertain whether this deficiency would be reduced by the use of transport theory calculations, a comparison of diffusion theory and transport theory eigenvalue calculations was made. These

calculations used an infinitely reflected, single compartment geometry representing the 112 pin clusters, centred configuration. The geometry is shown in Figure 9.1. Three calculations were performed. The first used the SNAP code in the eight-group structure of the original correction factor calculations. The second used the TWOTRAN transport theory code with S-4 quadrature and the same eight-group structure. The third calculation was similar to the second, except that a simplified four-group structure was used. This four-group structure is detailed in Table 9.1.

In Figure 9.2 is plotted the total flux in groups 5 to 8 of the eight-group calculations and group 4 of the four-group calculation, along the line AB in Figure 9.1.

Table 9.1 The Simplified Four-Group Structure

Energy Group: Four-Group Structure	Energy Groups: LWRWIMS 69-Group Library	Range of Energies (eV)
1	1-9	$>1.11\times10^{5}$
2	10-27	$4.0-1.11\times10^{5}$
3	28-52	0.625-4.0
4	53-69	0-0.625

This group 4 contains neutrons of energy 0.625 eV and below, which dominate the total absorptions in the compartment. It can be seen that the diffusion theory calculation significantly overestimates the thermal flux in the water relative to the fuel, compared to the transport theory calculations. This overestimation is also true, to a lesser extent, for the flux in the boron-steel walls. The thermal flux profile across the fuel cluster is predicted similarly by all three calculations. In Table 9.2 are shown the respective k-eff values resulting from the three calculations and the proportional neutron absorptions in the clusters, the water surrounding the clusters and the boron-steel walls.

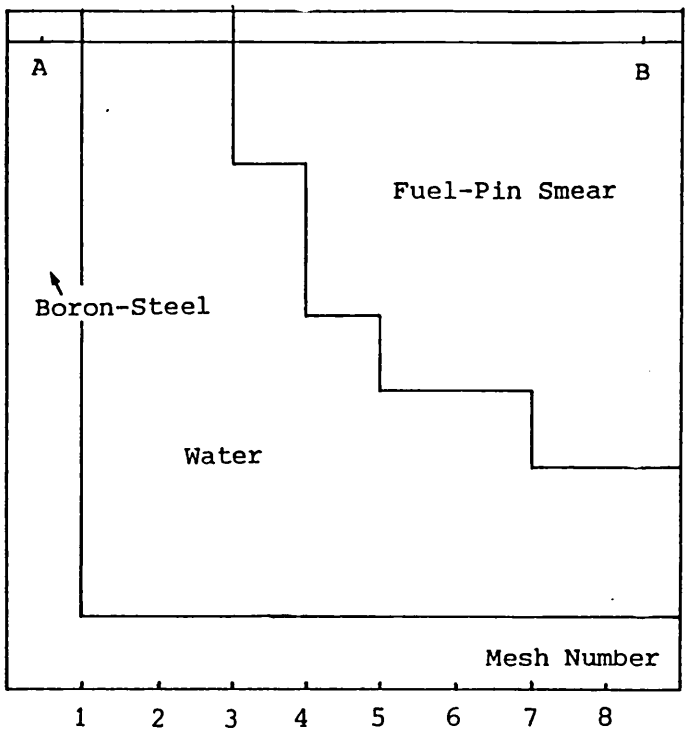

Fig. 9.1. Single Compartment Model of the 112 Pin Clusters, Centred Configuration.

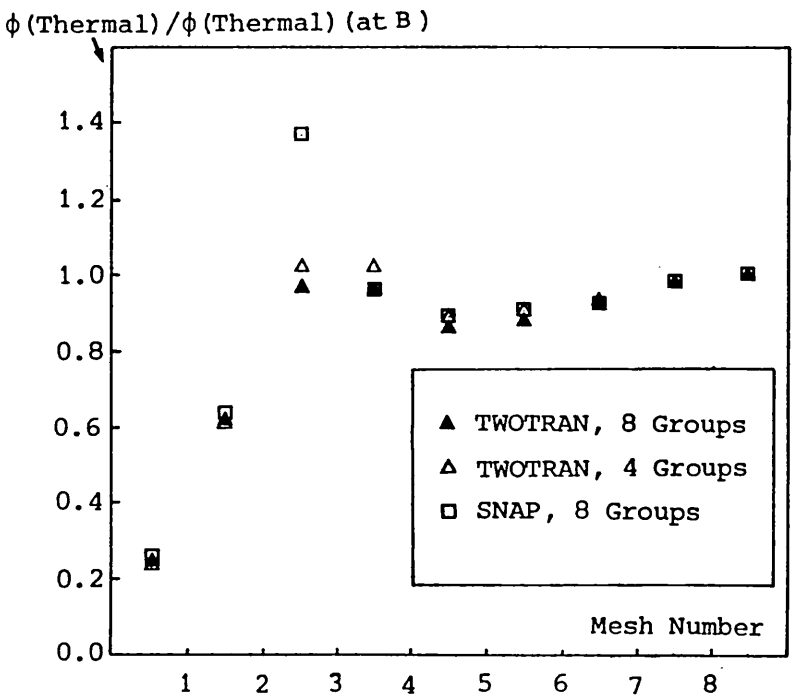

Fig. 9.2. Thermal Flux Along Line AB

Table 9.2 Comparisons of Diffusion Theory and Transport Theory Calculations

Calculation	k-eff	Cluster Absorptions (%)	Water Absorptions (%)	Boron-Steel Absorptions (%)
Diffusion theory, 8 groups	0.832	62.8	13.0	24.2
Transport theory, 8 groups	0.873	66.5	10.9	22.6
Transport theory, 4 groups	0.869	66.1	10.7	23.2

The k-eff values in Table 9.2 are in approximate proportion to the percentage of absorptions occurring in the fuel clusters, which consist of smeared fuel and water. The increased thermal flux in the water surrounding the clusters in the SNAP calculation is typical of diffusion theory fluxes in the region of strong absorbers (1).

Since a similar overestimation of thermal flux in the corners of the compartments was observed in the measurements (section 8.1.3), transport theory calculations were thus expected to estimate, more accurately than the diffusion theory calculations, the flux profile across the compartments. As a result of this, they were also expected to give an improved estimation of the flux profile across the skip.

9.3 Description of the Transport Theory Calculations

In view of the conclusions of the last section, it was decided to produce transport theory correction factors for two of the configurations used in the measurements. These correction factors were calculated using the TWOTRAN module of the LWRWIMS code, for the 112 and 221 pin clusters, centred configurations. A total of three pairs of eigenvalue and source mode calculations were thus required, including those for the reference configuration. These calculations used exactly the same geometry and nuclear data as the original correction factor calculations. An S-4 quadrature was employed. This account of neutron directionality was expected to provide the necessary improvement in the flux profile estimation as shown in the previous section.

The transport calculations were found, for reasons which will be shown presently, to be very cumbersome, and so the simplified four-group structure of Table 9.1 was adopted.

Eigenvalue calculations were run firstly for each of the three configurations. For the reference configuration, as with the original correction factor calculations, the axial buckling was adjusted to give a reactivity close to the calibrated value of -0.00713. The required buckling was $0.00263 cm^{-2}$ corresponding to the physical water height of 49cm with 6.13cm top and bottom extrapolation distances. For the two fully flooded configurations, top and bottom extrapolation distances of 7cm were assumed, as for the original correction factor calculations.

The source strength per unit volume used for the reference configuration was equal to $3.328 \times 10^{4} ns^{-1} cm^{-3}$ which is only 0.5% less than the value of $3.345 \times 10^{4} ns^{-1} cm^{-3}$ which is appropriate to the true extrapolation distance of 5.5cm as indicated by the two-dimensional and three-dimensional calculations (Table 7.1). The transport theory calculations thus have a smaller error in the axial representation than the original correction factor calculations, which had an estimated 1% error in the axial representation of the reference configuration (section 7.1.5).

The implementation of the source mode calculations presented a problem in that no source mode option existed in the TWOTRAN module of the LWRWIMS code. Accordingly the following procedure was adopted to simulate the source mode equations by using eigenvalue mode equations.

The multigroup transport theory equation in two-dimensional geometry can be written (2):

$$\mu \frac{\phi g}{dx} + \eta \frac{\phi g}{dy} + \Sigma_t^g(x,y,\mu,\eta) = S_g(x,y,\mu,\eta), \qquad (9.1)$$

where ϕ_g is the neutron flux at (x,y) in energy group g travelling in the direction $\overline{w}$, where $\frac{\overline{w}.\overline{x}}{x} = \mu$ and $\frac{\overline{w}.\overline{y}}{y} = \eta$.

The source term S_g in the above equation is composed of a fission source and a scattering source:

$$S_g = \frac{1}{k} \chi_g \sum_{h=1}^{G} \nu\Sigma_f{}^h(x,y)\phi_o{}^{ho}(x,y) + \sum_{n=0}^{IS}(2n+1)\sum_{h=1}^{G}\Sigma_n{}^{hg}(x,y)\sum_{j}^{n} R_n{}^j \phi_n{}^{hj}, \quad (9.2)$$

where $\phi_o{}^{ho}$ is the isotropic component of $\phi^h(x,y,\mu,\eta)$, the directional neutron flux at (x,y) in group h and the remaining term on the right hand side is a summation of polynomials to an order IS representing the scattering processes.

The corresponding source mode equation is:

$$\mu \frac{d\phi_g}{dx} + \eta \frac{d\phi_g}{dy} + \Sigma_t{}^g(x,y,\mu,\eta) = S_g{}'(x,y,\mu,\eta) + Q_g, \quad (9.3)$$

where $S_g{}'$ consists of the same two terms as S_g (Equation 9.2), without the multiplier ($^1/k$) in the fission source term and Q_g is the imposed source in group g, which is assumed to be isotropic.

Equation 9.1 can be made identical in form to the source mode equation (Equation 9.3), at all positions where there is no imposed source, by introducing an artificial fission cross-section with a fission emergence spectrum at the imposed source position and adjusting its magnitude so that the eigenvalue, $^1/k$, is equal to unity. At the imposed source position, this altered eigenvalue mode equation thus contains an extra term dependent on flux, instead of a true source term, which is independent of flux. This extra term is:

$$F_g{}' = \chi_g \sum_{h=1}^{G} \nu\Sigma_f{}^{h'}(x,y)\phi_o{}^{ho'}(x,y), \quad (9.4)$$

where: $\Sigma_f{}^{h'}(x,y)$ is the artificial fission cross-section; and

$\phi_o{}^{ho'}(x,y)$ is the isotropic flux component at (x,y) with the artificial fission source included.

If the imposed source extends over several meshes as is the case in the correction factor calculations (Figure 4.7), $F_g{}'$ varies over the source

meshes with $\phi_o^{ho'}(x,y)$. The total strength per unit height of the artificial imposed source is given by:

$$S_{art} = \sum_{m=1}^{NM} \sum_{g=1}^{NG} F'_{gm} A_m, \qquad (9.5)$$

where: S_{art} is the total strength per unit height of the artificial imposed source;

F'_{gm} is the artificial imposed source term in group g and mesh m;

A_m is the area of mesh m;

NM is the number of meshes over which the imposed source extends; and

NG is the total number of energy groups.

By normalising the values of $\phi_o^{ho'}(x,y)$ resulting from the artificial imposed source equations, the value of S_{art} can be made equal to the imposed source strength per unit height inherent in the original correction factor calculations. This source strength is related to the source strength per unit volume by:

$$S_{orig} = A \times \sum_{g=1}^{NG} R_g, \qquad (9.6)$$

where: S_{orig} is the total strength per unit height of the imposed source in the original correction factor calculations;

R_g is the imposed source strength per unit volume given by the source strength algorithm (Equation 4.12); and

A is the total area of the source meshes.

The imposed source in the original calculations is the same for each of the source meshes. Provided that the variation in $\phi_o^{ho'}$ is small over the source meshes, the spatial distribution of the artificial imposed source is similar to that of the original imposed source. Hence, the normalisation of S_{art} to S_{orig} renders the artificial source mode equations identical to the true source mode equation except for the dependence of the artificial imposed source, S_{art}, on the flux, $\phi_o^{ho'}(x,y)$.

It was not certain what effect, if any, this dependence of the artificial imposed source on the flux would have, and so a comparison of

the two types of calculation was made using the SNAP diffusion theory code. Starting from the eigenvalue calculation for the 112 pin clusters, centred configuration, an artifical fission cross-section was introduced in the source meshes, and adjusted to give a k-eff close to unity.

In Table 9.3 are shown the ratios of artificial source mode reaction rates to the true source mode reaction rates for several detector positions. Two artificial source mode calculations were performed; it can be seen by extrapolation that the required k-eff value of unity reproduces closely the true source mode reaction rates.

Table 9.3 Comparisons of Artificial and True Source Mode Calculations

Artificial Fission Cross-Section/Pin-Cell Fission Cross-Section	k-eff	Ratio of Reaction Rates at Detector Positions: Artificial/True Source Mode Calculations		
		8 alt 1	3 alt 1	5 st
6.90	1.030	0.980	0.970	0.959
6.95	1.015	0.990	0.985	0.980
7.00 *	1.000	1.000	1.000	1.001

* all the results in the last row were obtained by extrapolation.

The validity of the artificial source mode equations having been shown, TWOTRAN calculations were run using this method for the three configurations in question. The artificial fission cross-sections were entered using the MISCELLANY option in the LWRWIMS code (3). Convergence of these artificial source mode calculations was very slow, as a result of the increased flux gradients caused by the introduction of the artificial fission source term. This forced the use of the simplified four-group structure (Table 9.1) for these calculations.

Four-group detector cross-sections were produced using the PERSEUS module and the same models as for the original correction factor calculations. The reaction rates, correction factors and modified source multiplication reactivities were calculated as described in Chapter 4, with additionally the normalisation of the reaction rates for each configuration by the factor S_{orig}/S_{art}, to simulate the correct source strengths.

9.4 Modified Source Multiplication Results Using the Transport Theory Calculations

9.4.1 Calculated Reactivities and Correction Factors

In Table 9.4 are shown the k-eff values and reactivities resulting directly from the three transport theory eigenvalue calculations.

Table 9.4 Transport Theory Eigenvalues

Configuration	K-eff	Reactivity	K-eff (TWOTRAN)-K-eff (SNAP)
196/49 (reference)	0.99295	-0.00710	-
112/76 (CTD)	0.838	-0.1926	+0.025
221/76 (CTD)	0.771	-0.2979	+0.021

It can be seen that the eigenvalues for both well-subcritical configurations show roughly the same increase as that exhibited by the single compartment calculations (section 9.2) when transport theory calculations were used.

The correction factors resulting from the transport theory calculations, together with the percentage changes relative to the original correction factor calculations are listed in Table 9.5. Regarding the percentage changes, two distinct trends are evident:

(i) The percentage changes increase with distance from the sources. This is the case for each detector environment.

(ii) There is a general decrease of the correction factors for the corner-of-compartment detectors relative to the centre-of-cluster and half-way detectors.

Both trends can be explained in terms of the differences between the diffusion theory and transport theory calculations as diagnosed in section 9.2. It is convenient in diagnosing these trends to examine the ratios of calculated and experimental count rates.

Table 9.5 Transport Theory Correction Factors, Standard Source Positions

Detector Environment	Detector Position	Correction Factor 112/76(CTD)	% Change from Original	Correction Factor 221/76(CTD)	% Change from Original
Centre of Cluster	8 alt 1	0.601	-0.7	0.296	-2.5
	4 alt 4	0.713	+2.9	0.357	+1.3
	3 alt 5	0.713	+2.9	0.357	+1.3
	3 alt 1	0.285	+7.5	0.128	+3.4
	4 alt 5	0.285	+7.5	0.128	+3.4
	5 alt 4	0.285	+7.5	0.128	+3.4
	5 alt 5	0.285	+7.5	0.128	+3.4
	4 alt 1	0.147	+15.7	0.0591	+11.3
	8 alt 4	0.104	+21.8	0.0395	+14.8
	8 alt 5	0.104	+21.8	0.0395	+14.8
	5 st	0.104	+21.8	0.395	+14.8
Half-way	8 alt 2	0.849	-5.9	0.528	-4.8
	3 alt 2	0.281	+7.1	0.143	+3.9
	4 alt 2	0.182	+11.0	0.0922	+8.6
	5 alt 2	0.124	+16.7	0.0611	+12.5
Corner of Compartment	8 st	2.530	-23.4	3.392	-21.2
	3 alt 3	1.251	-20.3	1.641	-18.7
	3 alt 4	0.908	-6.9	1.009	-9.0
	8 alt 3	0.921	-8.5	1.034	-9.1
	3 st	0.595	-7.7	0.660	-8.8
	4 st	0.492	-8.4	0.548	-7.9
	4 alt 3	0.468	-5.7	0.508	-6.2
	5 alt 1	0.344	-5.5	0.375	-5.5
	5 alt 3	0.346	-0.7	0.337	-5.1
Outside Skip	7 st	0.196	+11.3	0.198	+5.3
	6 st	0.0943	+18.6	0.0840	+6.8
	9 st	0.0786	+31.2	0.0683	+20.9
	2 st	0.0833	+48.0	0.0717	+35.8
	1 st	0.0833	+46.9	0.0717	+34.8

9.4.2 Ratios of Calculated and Corrected Experimental Count Rates

Table 9.6 lists the ratios of calculated and corrected experimental count rates for all three configurations modelled in the transport theory calculations. Firstly, it is to be noted that no normalisation of the detector sensitivities to their nominal sensitivities was used in calculating the reaction rates. Hence the magnitude of the ratios are quite different to those resulting from the original correction factor calculations.

Table 9.6 Ratios of Calculated and Corrected Experimental Count Rates from the Transport Theory Calculations

Detector Environment	Detector Position	196/49 (reference)	112/76 (CTD)	221/76 (CTD)
Centre of Cluster	8 alt 1	1.352	1.327	1.313
	4 alt 4	1.260	1.400	1.424
	3 alt 5	1.328	1.415	1.473
	3 alt 1	1.249	1.309	1.289
	4 alt 5	1.359	1.367	1.307
	5 alt 4	1.267	1.311	1.240
	5 alt 5	1.338	1.329	1.304
	4 alt 1	1.377	1.373	1.381
	8 alt 4	1.252	1.368	1.282
	8 alt 5	1.324	1.357	1.257
	5 st	1.220	1.291	1.214
Half-way	8 alt 2	1.352	1.434	1.382
	3 alt 2	1.236	1.376	1.297
	4 alt 2	1.377	1.508	1.449
	5 alt 2	1.246	1.360	1.271
Corner of Compartment	8 st	1.355	1.222	1.180
	3 alt 3	1.175	1.163	1.159
	3 alt 4	1.189	1.219	1.198
	8 alt 3	1.356	1.301	1.256
	3 st	1.131	1.132	1.213
	4 st	1.396	1.253	1.192
	4 alt 3	1.287	1.189	1.190
	5 alt 1	1.133	1.084	1.083
	5 alt 3	1.253	1.163	1.197

Considering firstly the ratios for the in-cluster detectors in the reference configuration, there is no trend for their values to increase or decrease with distance from the sources. Their standard deviation is about 3%, which is roughly the standard deviation resulting from assembly asymmetries and detector positioning errors (section 6.7). This behaviour is quite reasonable in that the k-eff value and, therefore, the overall balance between neutron production and losses are well predicted for this configuration.

For the two well-subcritical configurations, however, there are two differences from the original correction factor calculations. Firstly, the trend of the ratios to decrease with distance from the sources has disappeared. The mean ratio for all the centre-of-cluster detectors in the 112 pin clusters configuration, for example, has a standard deviation of only 3%, about the same value as for the reference configuration.

Secondly, the ratios for the corner-of-compartment detectors are all reduced relative to those for the detectors in the clusters. This reduction can be assessed by examining the ratio for pairs of detectors, each pair in the same compartment, resulting from both the diffusion theory and the transport theory calculations. Nine such pairs were examined in the 112 pin clusters, centred configuration:

- 3 (standard), 3 (alt 3) and 3 (alt 4) in turn with 3 (alt 1);
- 4 (standard) and 4 (alt 3) in turn with 4 (alt 1);
- 5 (alt 1) and 5 (alt 3) in turn with 5 (standard); and
- 8 (standard) and 8 (alt 3) in turn with 8 (alt 1).

It can be seen from the average ratios for these pairs in Table 9.7, that on average, the ratio of the C/E's in the corners of compartments relative to the C/E's in the centres of the clusters is smaller using the transport theory calculations. This ratio is 27% less than for the diffusion theory calculations.

This behaviour was observed in the comparisons of diffusion theory and transport theory calculations in section 9.2. The smaller proportion of water absorptions in the transport theory calculations is consistent with the progressive rise in the correction factors with increasing distance from the sources. It appears likely that the thermal flux estimation in the boron-steel also contributes to this behaviour, though this cannot be readily diagnosed by means of experimental count rates.

Table 9.7 Comparisons of Count Rate Estimation in Cluster Centres and Compartmental Corners

Diffusion Theory: Average Corner (C/E)/ Centre (C/E)	Transport Theory: Average Corner (C/E)/ Centre (C/E)	Diffusion Theory/ Transport Theory
1.146	0.901	1.272

9.4.3 K-eff Values from MSM

The k-eff values from MSM using the transport theory calculations are listed in Table 9.8. These values reflect the behaviour of the ratios of calculated and corrected experimental count rates as noted in the last section. They are fairly constant for each group of detectors with the variation mostly resulting from experimental imprecisions. The selections of detector positions, as made in the last chapter, can now be evaluated.

Table 9.8 Modified Source Multiplication K-eff Values

Detector Environment	Detector Position	112/76 (CTD)	221/76 (CTD)
Centre of Cluster	8 alt 1	0.840	0.775
	4 alt 4	0.823	0.747
	3 alt 5	0.829	0.751
	3 alt 1	0.831	0.764
	4 alt 5	0.837	0.777
	5 alt 4	0.833	0.774
	5 alt 5	0.839	0.774
	4 alt 1	0.838	0.769
	8 alt 4	0.826	0.766
	8 alt 5	0.835	0.779
	5 st	0.830	0.771
Half-way	8 alt 2	0.830	0.766
	3 alt 2	0.823	0.761
	4 alt 2	0.825	0.761
	5 alt 2	0.826	0.766
Corner of Compartment	8 st	0.852	0.793
	3 alt 3	0.839	0.772
	3 alt 4	0.835	0.768
	8 alt 3	0.844	0.783
	3 st	0.838	0.757
	4 st	0.852	0.797
	4 alt 3	0.848	0.783
	5 alt 1	0.844	0.778
	5 alt 3	0.848	0.778
Outside Skip	7 st	0.831	0.765
	6 st	0.846	0.796
	9 st	0.827	0.773
	2 st	0.827	0.777
	1 st	0.826	0.780

9.5 Further Diagnostics of Detector Positions

In this evaluation the sensitivity to calculation of the two methods of averaging suggested in the last chapter is compared. Also compared are the selections of other groups of detectors, such as the corner-of-compartment detectors and the out-of-skip detectors.

The k-eff values resulting from several methods of detector selection are listed in Table 9.9. These estimates apply to both the 112 and 221 pin clusters, centred configurations. Results using both sets of correction factor calculations are given.

Table 9.9 Sensitivity to Calculation of Mean K-eff Values from Detector Selections

Detector Selection	112/76 (CID)			221/76/ (CID)		
	$\overline{k\text{-eff}}$ (Diffusion)	$\overline{k\text{-eff}}$ (Transport)	Δk (Transport-Diffusion)	$\overline{k\text{-eff}}$ (Diffusion)	$\overline{k\text{-eff}}$ (Transport)	Δk (Transport-Diffusion)
In-cluster (aggregated)	0.833	0.831	-0.002	0.763	0.763	+0.000
In-cluster (separate)	0.843	0.831	-0.012	0.778	0.768	-0.010
Corners (separate)	0.830	0.844	+0.014	0.760	0.779	+0.019
Out of Skip (separate)	0.865	0.831	-0.034	0.808	0.778	-0.030

It is apparent from the k-eff values in Table 9.9 that the k-eff resulting from an aggregation of the in-cluster count rates is scarcely changed by the use of correction factors derived from transport theory calculations. This results from the fact that the four detectors closest to the sources contribute most of the calculated reaction rate (69.3%, in the diffusion theory calculations) and these detectors have correction factors which are individually least sensitive to the change in the calculation method (Table 9.5). That their correction factors are the

closest to unity of the in-cluster detectors also indicates that the higher mode contamination is probably low.

The second detector selection, that of the in-cluster detectors considered separately, is much more sensitive to the change in the calculational method, the change being about -0.010 in k-eff. This change is a significant fraction of the change in calculated k-eff, equal to about 0.025 for both configurations (Table 9.4). It results from the fact that the in-cluster detectors which are farthest away from the sources and are individually most sensitive to the change in calculation method (Table 9.5), are weighted equally with the detectors closer to the sources.

The remaining two detector selections, for the corner-of-compartment detectors and the out-of-skip detectors, are even more sensitive to the change in calculational method. In fact, the mean k-eff value resulting from the selection of the out-of-skip detectors is as sensitive to calculation as the calculated k-eff values themselves.

It can thus be concluded that the use of aggregated in-cluster count rates results in correction factors which are least changed by the use of transport theory calculations. Note that this has not actually been demonstrated for the closest-to-centre, the groups-of-four and dropped-pin configurations. Since, however, the diffusion theory calculations show the same type of deficiency for these configurations as for the two centred configurations, it would appear that the use of aggregated count rates in the clusters is justified here also.

The use of transport theory calculations, though apparently eliminating the principal deficiency of the original calculations, is only one of several possible changes in the calculational method. Further correction factor changes are examined in the next chapter.

10. Further Studies of the Correction Factors

There were three areas in which the original correction factor calculations made approximations in their representation of the fuel storage configurations. These were:

(i) Material and geometric specifications;

(ii) Algorithmic and nuclear data specifications, that is, cross-section preparation, group structure and S-quadrature. The question of S-quadrature has already been studied using the transport theory calculations of the last chapter; and

(iii) Conversion of mesh fluxes to reaction rates. The representation of the detectors has already been examined in the detector perturbation calculations (Chapter 7). However, the calculations of the reaction rates involved linear interpolation between mesh fluxes. It is necessary to show the validity of this interpolation, which was described in section 4.2.4.

Studies were made of each of these approximations to ascertain whether any of them introduced significant systematic errors into the correction factors. These studies were also used to provide further evidence of the preference for the aggregation of in-cluster count rates as indicated by the use of transport theory calculations in the last chapter. The basis of each of the studies was to vary each specification towards its true value, wherever possible.

10.1 Material and Geometric Specifications

The geometric and material specificiations were approximated in several ways in the original correction factor calculations:

(i) The specifications of the skip and fuel pins were older and slightly less accurate than the up-to-date specifications of Tables 1.2 and 1.3. This was noted in the description of the correction factor calculations in section 4.2.1.

(ii) Each configuration was modelled using a regular, rectangular geometry. In fact, assymmetries were inevitably present giving an estimated error of 2% in each count rate (section 6.4).

(iii) The source tubes were represented using a smeared material approximating the proportions of steel, air and water occupying the source tube meshes (section 4.2.1).

(iv) The source neutrons were assumed to originate from the whole area of the source tube meshes instead of from their centre (section 4.2.2).

10.1.1 Specifications of the Skip and Fuel Pins

The only changes in the specification of the skip and fuel pins amounting to more than a fraction of one per cent are listed in Table 10.1.

Table 10.1 Differences Between Original and Revised Specifications of the Skip and Fuel Pins

Specification	Original Specification	Revised Specification
Boron-steel wall thickness (cm)	0.546	0.523
Water gap between outermost lattice position and boron-steel walls (cm)	0.447	0.390
w/o of boron in boron-steel	0.9	1.12*

*This figure was later revised to 1.04.

In order to examine the effect of these changes together with the slight changes in the pin and can specifications, two additional correction factor calculations were performed for the 112 pin clusters, centred configuration.

The first calculation incorporated all the revised specifications, apart from the boron weight proportion, for which the original proportion of 0.9% was used. The second calculation differed from the first only in the inclusion of the revised weight proportion of 1.12% boron in Table 10.1.

These calculations included the corresponding models of the reference configuration. As before, the axial buckling was altered in each case to give a reactivity close to the calibrated value. The greatest resultant departure in the source strength per unit volume from that corresponding to an extrapolation distance of 5.5cm (section 7.1.2) was 1.6%, that is, no more than in the original calculations.

In Table 10.2 are listed the k-eff values resulting from these correction factor calculations, alongside those resulting from the original correction factor calculations. The in-cluster detectors are considered, both aggregated and separate.

Table 10.2 Results of Sensitivity Studies of Skip and Fuel Pin Specifications. 112 Pin clusters, Centred Configuration

Correction Factor Calculation	K-eff Value from MSM: In-Clusters, Aggregated	K-eff Value from MSM: In-Clusters, Separate	Calculated k-eff Value
Original	0.833±0.010	0.843±0.011	0.813
Revised Materials	0.830±0.007	0.835±0.008	0.818
Revised materials + boron proportion	0.830±0.008	0.838±0.008	0.816

The results in Table 10.2 provide confirmation of the preference for the aggregation of in-cluster count rates over their separate treatment. It can be seen that the use of the revised geometrical material specifications, with or without the revised boron-steel proportion, causes a change of -0.003 in the modified source multiplication k-eff value from MSM. The small effect of these uncertainties can be explained as follows.

Firstly, the changes in water gap and boron-steel wall thickness in Table 10.1 are quite small dimensionally, and thus are expected to have

only a small effect. On the other hand, the small reduction in the calculated k-eff value (Table 10.2) resulting from the increase in boron weight percentage from 0.9 to 1.12 (or 24%) seems surprising in view of the fact that about 20% of the total absorptions occur in the boron-steel walls. This was shown by the single compartment calculations of section 9.2. The small size of this reduction in k-eff is partly due to the self-shielding of the boron. This can be seen from Table 10.3, which lists, by energy group, the percentage of boron-steel absorptions, the boron-steel mean free path for absorption, and the estimated percentage increase in absorptions caused by the 24% increase in boron proportion.

Table 10.3 The Absorption Properties of the Boron-Steel Walls. 112 Pin Clusters, Centred Configuration

Energy Group	Percentage of Boron-Steel Absorptions	Absorption Mean Free Path (cm)	Estimated Percentage Increase in Absorption Probability Caused by Increase in Boron w/o
1	0.2	500	24
2	0.2	500	24
3	5.6	14.3	24
4	7.1	2.32	21
5	6.4	1.21	18
6	30.0	0.633	14
7	36.5	0.399	10
8	14.0	0.229	4

The figures in Table 10.3 were taken from the appropriate single compartment calculation described in section 9.2. The fractional increases in absorptions were calculated from the formula,

$$\text{Ratio of absorptions, } (0.9 \rightarrow 1.12)\text{w/o} = \frac{1 - e^{-\Sigma_a' d}}{1 - e^{-\Sigma_a d}}, \qquad (10.1)$$

where: Σ_a' is the macroscopic absorption cross-section in the boron-steel with 1.12 w/o boron;

Σ_a is the macroscopic absorption cross-section in the boron-steel with 0.90 w/o boron; and

d is the thickness of the boron-steel wall.

This formula applies to neutrons striking the boron-steel walls perpendicularly and ignores scattering in the walls. It can be seen from Table 10.3 that the average increase in absorption probability is around 10% for groups 6-8 in which most of the absorptions take place. This reduction occurs because the boron does not act as a volume absorber for thermal neutrons.

Additionally, the boron-steel walls are separated from the fuel clusters by about 2.5cm to 6cm or more. This compares with the thermal diffusion length of about 2.6cm for neutrons in water (1). It is thus likely that many of the extra neutrons absorbed in the boron-steel walls due to the increase in boron concentration would have been absorbed in any case in the water surrounding the clusters. So the decrease in k-eff is, thus, much less than expected from the increase in boron-steel absorptions.

The above conditions still hold for the groups-of-four, closest-to-centre and dropped pin configurations, since the average size of the water gaps is undiminished by the movements of the clusters.

Finally, considering the model of the reference configuration, since this also figures in the correction factors, there is a smaller overall proportion of absorptions in the boron-steel walls (about 15%). The water gaps between the fuel pins and the walls are much smaller for this configuration, however, so that fuel absorptions tend to be more effected by the increase in boron proportion. On balance, the effect of the extra boron is quite small, the calculated k-eff value decreasing by only 0.3% prior to the change in axial buckling.

In addition to their small effects on the calculated reactivities, the geometric and material changes in Table 10.2 have a correspondingly small effect on the attenuation of neutrons through the skip, and thus on the source mode reaction rates. Hence, the correction factors are, as a result, little changed.

10.1.2 Specifications of the Source Tubes and Sources

The composition of the source tube and its surrounding water represented as a smeared material in the original correction factor calculations,

a diameter of 2.3cm instead of 3.1cm (Table 4.4); the latter was the diameter specified in its original design. This decrease in assumed diameter corresponded to the replacement of about 1 mesh of steel and air by water in the 196 and 112 pins per compartment configurations. In the 221 pin clusters configuration, however, the extra space was occupied by 4 fuel pins and the source tube and surrounding water could be considered to occupy 5 instead of 9 meshes.

In order to test the effect of this inaccuracy on the correction factors, new correction factors were generated for the 112 and 221 pin clusters, centred configurations; a source tube and water smear based on the revised diameter of 2.3cm was used in each case. In the model of the reference configuration it was found that the use of this revised specification changed the k-eff value only slightly, from its former value of 0.9929 to 0.99353. This was still close to the calibrated value of k-eff and so the axial buckling was not altered. The results of these calculations for the 112 and 221 pin clusters configurations are shown in Table 10.4.

Table 10.4 Results of Sensitivity Studies of Source Tube Specification

a) 112 Pin Clusters, Centred

Correction Factor Calculation	K-eff Value from MSM: In-Clusters, Aggregated	K-eff Value from MSM: In-Clusters, Separate	Calculated k-eff Value
Original	0.833±0.010	0.843±0.011	0.813
Revised source Tube Specification	0.830±0.008	0.840±0.009	0.816

b) 221 Pin Clusters, Centred

Correction Factor Calculation	K-eff Value from MSM: In-Clusters, Aggregated	K-eff Value from MSM: In-Clusters, Separate	Calculated k-eff Value
Original	0.778±0.016	0.765±0.015	0.751
Revised source Tube Specification	0.779±0.015	0.767±0.015	0.752

For both configurations, the MSM k-eff value is only slightly changed by the use of the revised source tube specifications. There is no marked preference in this study for the aggregation of detectors; this can be explained as follows. Changes in the source tube specifications effect cross-sections in the area of the sources alone. So the fission chains are affected only at their origin, or at subsequent times if they pass through this area. There is no change in absorption or production across the skip and, as a result, the level of the flux profile is affected and not its shape. The individual detector correction factors are thus all changed in the same proportion and so their weighting makes no difference to the change.

The low sensitivity of the correction factors to the changes in source tube specifications can be explained as follows. The inclusion of one extra mesh of water in the 196 and 112 pins per compartment configurations has little effect on the correction factors for two reasons. Firstly, since the area over which the fast neutrons from the sources slow down (~6x2 5cm^2 (section 2.9)) is much greater than the extra area of water included (~3cm^2) the effect on the moderation of the source neutrons is likely to be small. Secondly, the moderator-to-fuel ratio is close to its optimum for the 1.79cm pin pitch (2) and so the extra absorption in the water significantly counteracts the extra moderation.

For the 221 pins per compartment, centred configuration, the use of the revised source tube specifications is equivalent to the replacement of four-ninths of the source tube smear by fuel pin cells. This has the effect of both increasing the amount of fuel in the vicinity of the source and of decreasing the fuel-to-moderator ratio. Since the 221 pin clusters configuration is distinctly undermoderated (section 1.2.2), the reduction in fuel-to-moderator ratio tends to counteract the effect of the extra fuel. Hence, neither the calculated reactivity nor the source mode reaction rates are expected to be much effected.

Regarding the remaining configurations it should be noted that, since the source tubes and their immediate environment are unaffected by the movement of the clusters, the effect of the revised source tube

specifications on the correction factors must be of the same magnitude as indicated in Table 10.4 (a).

10.1.3 The Extent of the Source Emissions

In the original correction factor calculations, the source term was assumed to extend over the entire area of the source tube meshes, whereas the sources were in reality smaller than their inner capsules of diameter 0.6cm (3).

As a test of possible errors arising from this representation, the source mode calculation for the 112 pin clusters, centred configuration was repeated. Meshes of extent 0.3cm x 0.3cm were created in the centre of the source tube smear and the imposed source term was limited to these meshes. The source strength per unit volume was normalised to provide the same total source strength as in the original calculations.

It was found that this more localised representation of the source emission made virtually no difference to the reaction rates at any of the detector positions. This can be explained in terms of the contribution of the source neutrons to each reaction rate, or their importance (section 2.7). Since the fission chains in the 112 pin clusters, centred configuration are, on average, fairly short, the importance is expected to decrease somewhat with distance from the detector, even over the extent of the source meshes. Now the localisation of the source term scarcely changes the mean distance of the source term from each of the detectors. This is because the source term is merely concentrated in the centre of its previous area. As long as the decrease in importance over the source meshes is close to being linear, the average importance is unchanged by the localisation.

The removal mean free path of the source neutrons in the source tube smear and the fuel pin and water environment is about 10cm. Even in an entirely attenuative system, the importance thus only changes by a fraction of $e^{-(d/10)}$ over the source tube meshes, where d is equal to the width of the source tube meshes (3.58cm). The exponential function up to a power of about $\frac{3.58}{10} = 0.36$ is a fairly linear function, so the

importance is also linear. In fact, the importance is almost certainly more slowly varying than this, because the environment is fissile as well as being attenuative.

Note should be made also of the effect of increased source localisation in the reference configuration since this can also potentially effect the correction factors, through the source mode reaction rates. In fact, the importance of the source to any detector count rate is expected to be only a slight variation over the source meshes in this configuration. Since all fission chains in this configuration extend over the whole skip because of its high neutron multiplication, the importance is expected to be slowly varying across a single compartment and even more slowly varying in the centre of the 196 fuel pins in a compartment. This behaviour was verified by a similar study to that described above, which yielded no change in the reaction rates.

10.2 Algorithmic Specifications

10.2.1 Cross-Section Preparation

In the cross-section preparation for each of the eigenvalue and source mode calculations (section 4.2.1), some allowance for fine-group spectrum differences with environment were made by the incorporation of two fuel types and two water types. This allowance was arbitrary and so a study was made to demonstrate the sensitivity of the correction factors to the fine group spectrum used to generate the multigroup cross-sections. This study involved repeats of the eigenvalue and source mode calculations for the 112 pin clusters, centred configuration. The multigroup cross-sections used, however, were those for the reference configuration. The cross-sections for the reference configuration were symptomatic of a slightly less thermalised spectrum over the entire fuel in view of the greater amount of fuel present in this configuration.

The results of this sensitivity study are listed in Table 10.5.

Table 10.5 Results of Sensitivity Study of Cross-Section Preparation. 112 Pin Clusters, Centred Configuration

Correction Factor Calculation	K-eff Value from MSM: In-Clusters, Aggregated	K-eff Value from MSM: In-Clusters, Separate	Calculated k-eff Value
Original	0.833±0.010	0.843±0.011	0.813
Changed cross-section prepartion	0.836±0.011	0.848±0.013	0.815

From the above results, which indicate a 0.3% change in k-eff, or a 2% change in reactivity, it is evident that the change in multigroup cross-sections makes very little change to the correction factor for the aggregated detectors. In fact, the cross-sections themselves are very similar, showing differences of 1% or less.

The above study does not, however, guarantee the absence of a significant systematic change which might result from the use of a different nuclear data set to produce the multigroup cross-sections.

10.2.2 Group Structure and S-Quadrature

Both the energy-group structures of 8 and 4 groups used in the correction factor calculations are gross simplifications of the energy dependence of the neutronic processes. The 69-group spectrum for each cell type or material is implicitly included in the calculations, however, in that the 8-and 4-group cross-sections were generated from this spectrum, represented in a simplified geometry.

Nevertheless, it was considered necessary to give some indication of the probable effects of using a finer energy-group structure in the correction factor calculations. Accordingly, several calculations were undertaken using the TWOTRAN code, with 20 energy groups as detailed in Table 10.6. Though the choice of 20 groups was quite arbitrary, the calculations were intended to show whether the use of a finer group structure would predict accurately the thermal flux profile across a compartment of the skip. It was shown in section 9.4.2 that the 4-group transport theory calculations appeared to overpredict the thermal flux in the fuel clusters relative to the corners of the compartments by as much as 10%.

Table 10.6 The Energy-Group Structure of 20 Groups

Energy Group (20 Groups)	Energy Group (4 Groups)	Energy Groups (69 Group Library)	Energy Range (eV)
1	1	1-3	1.0×10^{7}-2.231×10^{6}
2	"	4-5	2.231×10^{6}-8.21×10^{5}
3	"	6-9	8.21×10^{5}-1.11×10^{5}
4	2	10-14	1.11×10^{5}-9.12×10^{3}
5	"	15-17	9.12×10^{3}-2.24×10^{3}
6	"	16-20	2.24×10^{3}-3.67×10^{2}
7	"	21-23	3.67×10^{2}-4.81×10^{1}
8	"	26-27	4.81×10^{1}-4.0
9	3	28-31	4.0-1.5
10	"	32-36	1.5-1.071
11	"	37-40	1.071-0.972
12	"	41-45	0.972-0.625
13	4	46-48	0.625-0.350
14	"	49-52	0.350-0.250
15	"	53-55	0.250-0.140
16	"	56-58	0.140-0.067
17	"	59-61	0.067-0.042
18	"	62-64	0.042-0.025
19	"	65-67	0.025-0.010
20	"	68-69	0.010-0.0

The 20-group calculations used a single compartment model representative of the reference configuration, and the 112 and 221 pin clusters, centred configurations. So no correction factors were generated from these calculations, which were in eigenvalue mode only. In order to show the probable differences between the 20-group calculations and 4-group calculations, single compartment calculations were also performed using the 4-group stucture.

The results of the 20-group calculations are summarised in Table 10.7. In this table are included 'estimated C/E profiles'. These refer to the ratios of calculated to corrected experimental count rates (C/E's) and are explained as follows. The transport theory correction factor calculations resulted in comparisons of corner-of-compartment C/E's with center-of-cluster C/E's (Table 9.7). From the single compartment calculations, the change in flux profile resulting from the 20-group structure was noted. This change was used to adjust the C/E profiles in Table 9.7:

Estimated C/E profile, corner/centre (20 groups)=

$$\frac{[C_{corner}/C_{centre}]_{20\ groups}}{[C_{corner}/C_{centre}]_{4\ groups}} \times \frac{(C/E)_{corner}}{(C/E)_{centre}}, \qquad (10.2)$$

where the C/E values result from the transport theory correction factor calculations, and C_{corner} and C_{centre} are reaction rates at the corner and centre of the single compartment models.

Table 10.7 Studies of the Use of a More Detailed Energy-Group Structure: 20 Groups

Configuration	Calculated Δ(k-eff) (20 Groups - 4 Groups)	C/E Profile, Corner/Centre	
		Estimated, 20 Groups, S-8	Transport Theory Correction Factor Calculations (4 groups)
196/49 (reference)	+0.0016	0.948±0.029	0.968±0.030
112/76 (CTD)	+0.0057	0.948±0.031	0.901±0.030
221/76 (CTD)	+0.0031	1.009±0.034	0.913±0.030

The small changes in calculated k-eff resulting from the increase to 20 energy groups indicates that the correction factors are probably little effected by this change. The reason for this was noted earlier in the chapter: a small change in calculated k-eff means a small change in the balance between neutron absorption and production through the skip. This, is turn, means the flux profile and also the correction factors are little effected.

The estimated C/E profiles in Table 10.7 are generally closer to unity for the 20-group structure than for the 4-group structure. It thus appears that the more detailed energy group structure estimates the flux profile more accurately than the 4-group structure. However, the improvement may not be particularly great. It can thus be concluded that there exists some uncertainty about the presence of systematic errors due to the simplified energy group structure and S-quadrature.

10.3 Interpolation of Mesh Fluxes

Of the detector positions represented in the correction factor calculations, all except the centre-of-cluster detectors in the 221 pin clusters, centred configuration were between the centres of meshes. Interpolation was thus required in the calculation of reaction rates (section 4.2.4). The accuracy of this interpolation was tested by examination of the reaction rates corresponding to the mesh points around selected detector positions. Only in-cluster detector positions were included in this analysis, the results for the out-of-cluster detectors having been categorised for diagnostic purposes only.

Figure 10.1 shows plots of the reaction rates around three representative detector positions. These positions include both centre-of-cluster and half-way positions in the 112 pin clusters, centred configuration and a half-way position in the 221 pin clusters, centred configuration. The two configurations chosen were the most subcritical and were expected to provide the steepest flux gradients present in the fuel clusters.

It can be seen from Figure 10.1 that, for a centre-of-cluster position in the 112 pin clusters, centred configuration (8 alternative 1), the flux gradient is linear, giving a negligible error in the interpolation. Figure 10.1, for a half-way detector in this configuration (8 alternative 2), indicates that the linear interpolation may overestimate the reaction rate at this position by about 1-2%. This is a result of the increase in thermal flux gradient as the water region is approached.

Now the half-way detectors contribute about 30% of the aggregated count rate in each of the 112 pin clusters configurations. So the error in the aggregated count rate resulting from the linear interpolation is less than 1%.

Figure 10.1 shows that for the half-way position in the 221 pin clusters, centred configuration (8 alternative 2), the linear interpolation probably causes an overestimation of reaction rate of about 8%. This is a result of the increased spectrum differences

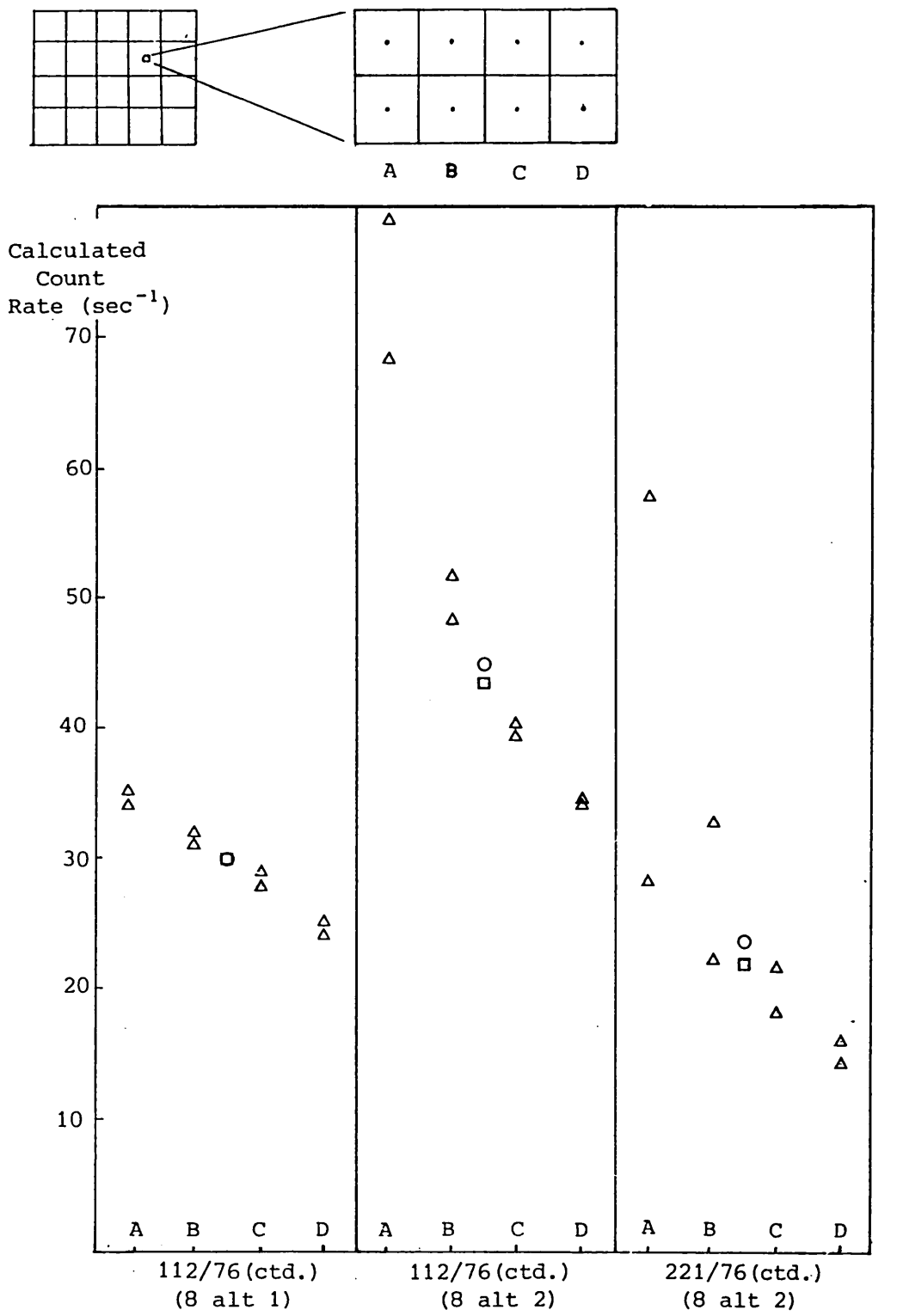

Fig. 10.1. Reaction Rates Around Detector Positions.

between the water regions and the in-cluster regions in this configuration. As the water region is approached, the thermal flux gradient becomes very steep, and non-linear.

In fact, the failure of the linear interpolation for the half-way detectors in the 221 pin clusters, centred configuration may be reason enough to exclude them from the aggregated count rate for this configuration, leaving the 11 centre-of-cluster detectors only.

10.4 The Significance of the Sensitivity Studies

The sensitivity of the correction factors to many of the specifications used in the calculations has thus been tested. No change in the specification produces a change in the modified source multiplication k-eff value greater than about 0.003, corresponding to a 2% change in the correction factor at a k-eff of 0.813. This is provided that the correction factor applies to the aggregate of the in-cluster count rates, which are symptomatic of reduced higher mode contamination (section 9.5).

However, in only one case, that of the use of transport theory calculations, (Chapter 9) has the sensitivity to a large change in calculated reactivity been tested. This may be the only such test needed, since the use of transport theory calculations largely resolves the main deficiency of the original calculations. Moreover, several specifications, such as the choice of nuclear data and the use of a very fine group structure have not been adequately tested.

In the next chapter it is shown that the spread of k-eff values of the in-cluster detectors is in fact a conservative measure of the systematic errors due to calculation, as was proposed in section 8.2.1. As will be seen, the sensitivity studies of this chapter are of value in the forthcoming analysis.

11. Analysis of the Overall Errors

11.1 The Significance of the Total Neutron Production Rate

The need to quantify the systematic errors due to calculational deficiencies requires the relation of the calculated correction factor for each configuration to a well-predicted correction factor. Ideally, the designation of a well-predicted correction factor must be by physical arguments. These arguments can be aided by sensitivity studies.

Now there is one correction factor which relates simply to physical arguments. It is the correction factor appropriate to the total neutron production rate in each configuration. This is also an idealised extension of the count rates in the measurements. Instead of considering localised reaction rates, the entire neutron production rate is considered.

The definition of the 'total neutron production rate' correction factor can be considered. It can be denoted by $\rho_2 PR_2 / \rho_1 PR_1$, where PR_2 and PR_1 are the total neutron production rates in both configurations in question. The significance of this correction factor can be seen from the following derivation, which applies to both of the products $\rho_2 PR_2$ and $\rho_1 PR_1$:

$$\rho PR = \frac{\langle \phi_o^* S \rangle}{\langle \phi_o^* \nu\Sigma_f n_o \phi_o \rangle} \times \sum_n \nu\Sigma_f n_n \phi_n \quad , \tag{11.1}$$

by the definition of reactivity and total source mode flux (Equations 3.10 and 2.29).

$$\text{Hence} \quad \rho PR = \langle \phi_o^* S \rangle \left(1 + \frac{\sum_{n \neq 0} \langle \nu\Sigma_f n_n \phi_n \rangle}{\langle \nu\Sigma_f n_o \phi_o \rangle}\right), \tag{11.2}$$

since the importance-weighted fission rate is equal to the fission rate, by the normalisation of ϕ^* (section 2.8).

The 'total neutron production rate' correction factor can thus be denoted by:

$$\frac{\rho_2 PR_2}{\rho_1 PR_1} = \frac{\langle \phi_o^* \, S_2 \rangle}{\langle \phi_o^* \, S_1 \rangle} \times \frac{1 + \alpha_2}{1 + \alpha_1}, \qquad (11.3)$$

where α_2 and α_1 are the net contributions of the higher modes to the total fission rate:

$$\alpha_m = \frac{\sum_{n \neq 0} \langle \nu\Sigma_f n_n \phi_n \rangle_m}{\langle \nu\Sigma_f n_o \phi_o \rangle_m} \quad m = 1 \text{ or } 2. \qquad (11.4)$$

So this correction factor can be seen as the ratio of importance-weighted source strengths in the two configurations, adjusted by the respective higher mode proportions. The importance in this context is the fundamental mode importance, that is, the contribution of the source to a fundamental mode distribution. In the following sections the prediction of this correction factor is considered.

11.1.1 The Well-Subcritical Configurations

How well predicted is the 'total neutron production rate' correction factor? It is convenient in the forthcoming analysis, firstly to give calculated values of the correction factor and then to proceed to a discussion of its physical characteristics. Calculations were performed of both its numerator and denominator, for the 112 pin clusters centred configuration relative to the reference configuration. All of the different two-dimensional specifications as described in Chapters 4, 9 and 10 were used. A program, 'FISSR', computed the total neutron production rate from each set of source mode fluxes and geometry and cross-section data stored on disk, using the following equations:

$$MR = \sum_{g=1}^{NG} \sum_{x=1}^{NX} \sum_{y=1}^{NY} \nu\Sigma_{fxyg} \, \phi_{xyg} \, A_{xy}, \qquad (11.5)$$

where: MR is the midplane neutron production rate per unit height;

$\nu\Sigma_{fxyg}$ is the macroscopic neutron production cross-section in mesh (x,y) and group g;

ϕ_{xyg} is the flux in mesh (x,y) and group g;

A_{xy} is the area of mesh (x,y); and

NX, NY, NG are the numbers of groups and meshes in the x and y directions respectively;

and

$$PR_{3-D} = MR \times \int_{-H/2}^{+H_2} \cos \frac{\pi x}{H} \, dx, \qquad (11.6)$$

where: PR_{3-D} is the total neutron production rate in the three-dimensional equivalent of the two-dimensional model; and

H is the effective height of the assembly, given by $\pi/\sqrt{Ba}$, where Ba is the axial buckling.

The products ρPR_{3-D} were divided by the total experimental source strength so as to give values of source importance. It should be noted that the relation of the ρPR_{3-D} products to the experimental source strength takes account of the axial importance weighting used in the source strength algorithm (Equation 4.12).

In Table 11.1 are listed the calculated values of the source importance for the 112 pin clusters, centred configuration. Also given are the corresponding values of the quantity ρMR, which relates to the midplane on which the in-cluster detectors are situated. This quantity bears a constant relationship to $\rho PR_{3-D/S}$, since the effective axial height, H, is the same for all the calculations. The percentage change of each value of ρMR from the original correction factor calculation is given and can be compared with the corresponding change in the product $\rho\sum CR$, where $\sum CR$ is the total reaction rate of the in-cluster detectors used in the measurements.

Table 11.1 Source Importance Values: 112 Pin Clusters Centred Configuration

Calculation	Source Importance $\rho PR_{3-D}/S$	ρMR ($cm^{-1}s^{-1}$)	% Change in ρMR (from original Calc)	$\rho\sum$Count Rates: % Change from Original Calc
Original	1.257	9.990×10^5	-	-
Transport theory	1.266	1.006×10^6	+0.7	+7.4 *
Changed materials and boron density	1.248	9.918×10^6	-0.7	+1.5
Revised source tube specification	1.266	1.006×10^6	+0.7	+4.4
Changed cross-section preparation	1.244	9.887×10^6	-1.0	-1.7

* Including normalisation for detector sensitivity, corresponding to original calculations (section 4.2.3). As will be seen, a similar change occurs in the same quantity in the reference configuration.

The above results show that the value of the source importance is less sensitive to calculation than the numerator of the 'in-cluster aggregate' correction factor. This reduced sensitivity to calculation can be interpreted in terms of the higher mode contamination present, it being recalled that higher mode contamination tends to make correction factors sensitive to reactivity (section 3.2.3).

Accordingly, the higher mode contamination was estimated for the numerators of both the above correction factors. The level of the fundamental mode in a subcritical assembly driven by a steady state source is given by (section 2.8):

$$n_o = \frac{1}{\rho} \frac{\langle \phi_o^* S \rangle}{\langle \phi_o^* \nu\Sigma_f \phi \rangle}. \qquad (11.7)$$

The fundamental mode level, n_o, was calculated by a program, 'FM', which utilised the numerical equivalent of Equation 11.7:

$$n_o \text{ (calc)} = \frac{1}{\rho} \frac{\sum_{g=1}^{NG} \sum_{x=1}^{NX} \sum_{y=1}^{NY} \phi^*_{xyg} \; R_{xyg} \; A_{xy}}{\sum_{g=1}^{NG} \sum_{x=1}^{NX} \sum_{y=1}^{NY} \phi^*_{xyg} \; \nu\Sigma_{fxyg} \; \phi_{xyg}}, \qquad (11.8)$$

where: ϕ^*_{xyg} is the adjoint eigenvalue mode flux in mesh (x,y) and group g;

R_{xyg} is the imposed source strength per unit volume in mesh (x,y) and group g; and

ϕ_{xyg} is the eigenvalue mode flux in mesh (x,y) and group g.

The fundamental mode neutron production rate was calculated using n_o (calc) from Equation 11.8:

$$PR_{3\text{-}D} \text{ (fundamental mode)} = n_o \text{ (calc)} \sum_{g=1}^{NG} \sum_{x=1}^{NX} \sum_{y=1}^{NY} \nu\Sigma_{fxyg} \; \phi_{xyg}. \qquad (11.9)$$

It is noted that the normalisation of ϕ_{xyg} makes no difference to the value of $PR_{3\text{-}D}$.

The resulting value of $[\rho PR_{3\text{-}D}$(fundamental mode) ÷ experimental source strength] was 1.483. So the total neutron production rate (Table 11.1) is smaller than its fundamental mode component, by a proportion of about 15%, their ratio being 1.257/1.483.

The above proportion, due to the higher modes, can be compared with the higher mode proportion of the total count rate of the in-cluster detectors. This was calculated using the fundamental mode flux component, $n_o \phi_o$, which was converted to reaction rates in the same manner as for the original correction factor calculations. Table 11.2 lists the in-cluster reaction rates and their fundamental mode components. They are plotted in Fig. 11.1.

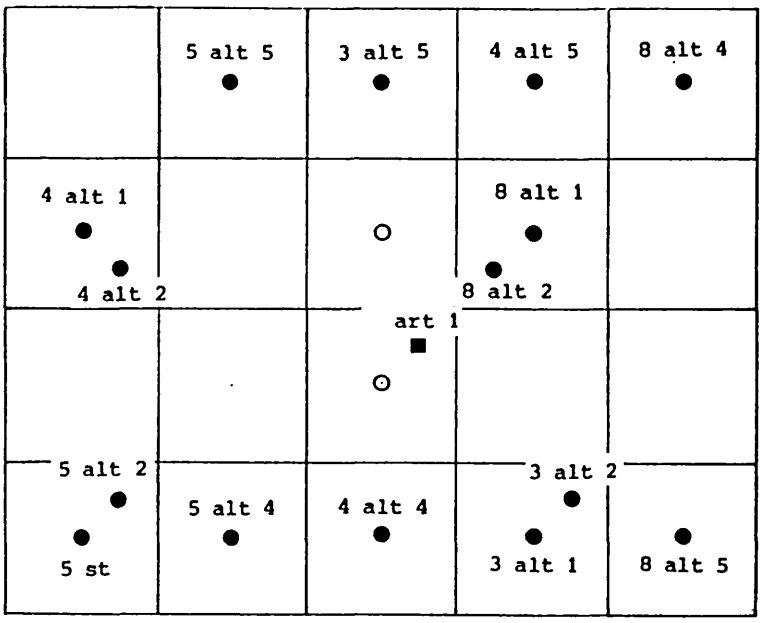

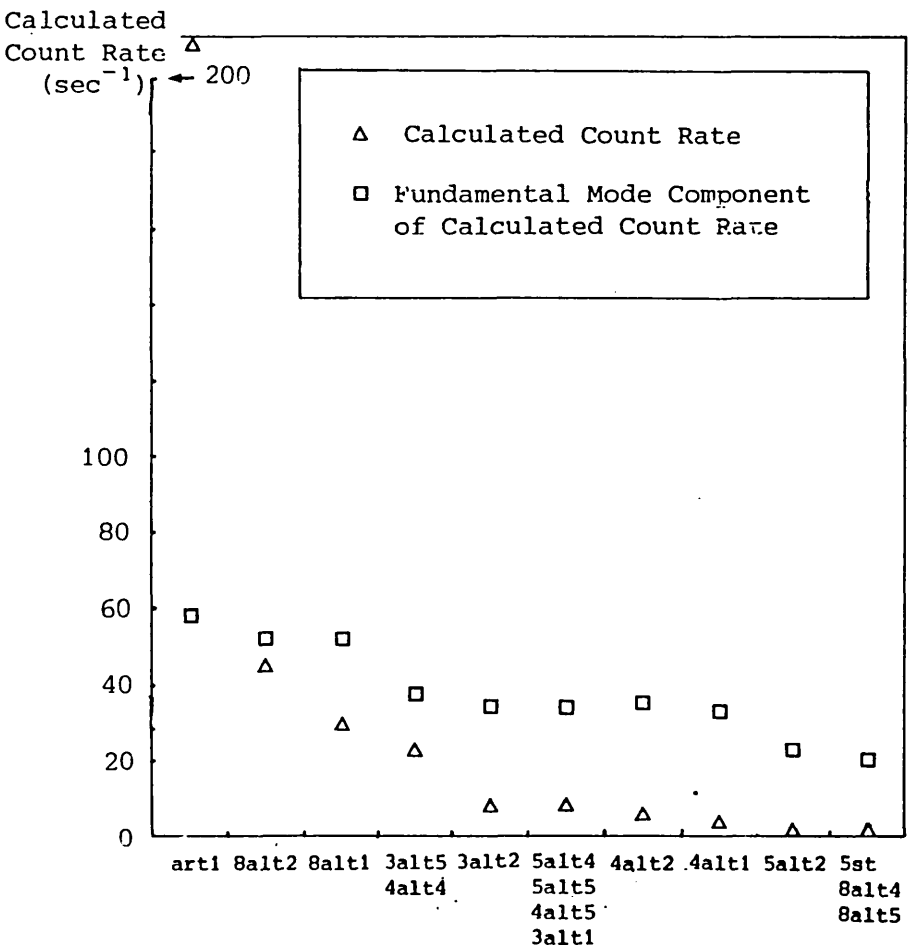

Fig. 11.1. The Fundamental Mode Component of the Count Rates in the 112 Pin Clusters, Centred Configuration.

Table 11.2 In-Cluster Detectors: Reaction Rates and their Fundamental Mode Components

Detector Position	Reaction Rate	Fundamental Mode Component of Reaction Rate
8 alt 2	44.83	52.21
8 alt 1	29.27	55.46
4 alt 4	22.24	37.29
3 alt 5	22.24	37.29
3 alt 2	7.14	34.00
3 alt 1	7.05	34.71
4 alt 5	7.05	34.71
3 alt 4	7.05	34.71
5 alt 5	7.05	34.71
4 alt 2	4.49	34.99
4 alt 1	3.01	33.54
5 alt 2	1.84	23.13
8 alt 4	1.10	20.15
8 alt 5	1.10	20.15
5 st	1.10	20.15
Total	167.0	497.4
Position close to sources (Fig.7.6)	208.8	56.00

Again the higher modes have an overall negative effect. This effect is much larger here than for the total neutron production rate; this is because the in-cluster detector positions are not evenly distributed throughout the fuel. In particular, no detector is positioned in either cluster containing the sources. It can be seen from Table 11.2 that the inclusion of such a detector would greatly reduce the net proportion of the higher modes in the total reaction rate.

It can be seen from Fig. 11.1 that the aggregation of in-cluster count rates, by the decreasing contribution of detectors with distance from the sources, decreases the higher mode contamination in the correction factors. This decrease in higher mode contamination results in the reduction of the sensitivity of the correction factors to calculation (section 9.5).

Fortunately this sensitivity to calculation appears to be small (section 9.5) even though the level of higher mode contamination is still large.

Returning to a consideration of the total neutron production rate, the level of higher mode contamination can be related to physical considerations. This can be done by making a comparison between the total importance of a source neutron, due to all modes, and the fundamental mode importance of that neutron.

Firstly, the value of the source importance, which was found to be about 1.26 (Table 11.1) can be assessed. This can be done by imagining the effect of lumping a fundamental mode source distribution into the localised positions used in the measurements. A source distribution which is itself a fundamental mode, results in a fundamental mode flux distribution, by orthogonality. The resultant total neutron production rate is thus equal to S/ρ and the source importance, $\rho PR/S$, is equal to unity.

Now the lumping of the source is not likely to increase its importance greatly, for the following reasons. Firstly, the fission chains extend radially, on average, over a fraction of the total volume of the skip, as demonstrated by the experimental count rates for all of the 112 and 221 pin clusters configurations. Hence, the effect of leakage on the total fission rate due to a source neutron is only likely to be marked for sources close to the outer boundaries of the skip.

Secondly, the extent of the fission chains, though much smaller than the skip itself, is larger on average than the area of one compartment. Hence the average total fission rate due to a source neutron may not be affected too greatly by the horizontal position of the source neutron in a compartment.

So the source importance is fairly constant radially over the entire skip. In fact, its calculated value of 1.26 at the central position is greater than that which would be obtained if the source distribution were of a fundamental mode axially. Such an axial distribution, of the form $S\cos(\pi x/H)$, has an average axial importance relative to the midplane, of

$$\frac{\int_{-H/2}^{+H/2} S\cos\left(\frac{\pi x}{H}\right)\cos\left(\frac{\pi x}{H}\right)dx}{\int_{-H/2}^{+H/2} S\cos\left(\frac{\pi x}{H}\right)dx} = 0.7854.$$

The axial importance of the sources used in the measurements is, relative to the midplane,

$$\frac{\sum SS_i\cos(\pi x_{i/H})}{\sum_i SS_i} = 0.8537.$$

Accordingly, if the source were of an axial fundamental mode distribution, its importance would be $\frac{0.7854}{0.8537} \times 1.257 = 1.156.$

This importance, which includes the net contribution of the higher modes, can be compared with the importance which would be obtained if a fundamental mode only were present. This is given by the value of the fundamental mode adjoint flux, ϕ_o^*, at the source position, relative to the average value of ϕ_o^* for a fundamental mode source distribution.

To consider the value of the importance for a central source, one can firstly imagine a rectangular homogeneous system. For each dimension across such a system, both forward and adjoint fluxes are cosine distributions, with boundaries determined by the extrapolation distance at the edges. For a fundamental mode source distribution the average value of the importance along the axial dimension is given by:

$$\bar{\phi}_o^* = \frac{\langle \phi^* \nu\Sigma_f \phi_o \rangle}{\langle \nu\Sigma_f \phi_o \rangle} = \frac{\int_{-B/2}^{+B/2}\int_{-L/2}^{+L/2} \phi_{oc}^* \nu\Sigma_f \phi_{oc} \cos^2\left(\frac{\pi x}{L}\right)\cos^2\left(\frac{\pi y}{B}\right)dxdy}{\int_{-B/2}^{+B/2}\int_{-L/2}^{+L/2} \nu\Sigma_f \phi_{oc} \cos\left(\frac{\pi x}{L}\right)\cos\left(\frac{\pi y}{B}\right)dxdy} = \frac{\pi^2}{16} = 0.617,$$

where: ϕ_{oc}^* and ϕ_{oc}^* are the forward and adjoint fluxes at the centre of the system, both normalised to unity; and

L and B are the length and breadth of the system respectively.

Hence, the importance of a central source is equal to $^{1}/0.617 = 1.621$.

For the 112 pin clusters, centred configuration, the fundamental mode importance of the source is expected to be smaller than this value, for the following reasons. Firstly, the skip is surrounded by water, resulting in a significant extrapolation distance of about 6.5cm for both forward and adjoint fluxes. Hence the above integration does not occur over the full range of the two distributions. This tends to raise the average, $\bar{\phi}^*_o$, though the value at the centre is unaffected.

Secondly, the presence of the source tube necessitates the removal of fuel pins, which tends to reduce the importance of the source neutrons. This is shown by a plot of the adjoint flux for neutrons above 0.821MeV, which includes most of the source neutrons in Figure 11.2. The adjoint flux in the central compartments is lower than in two of the adjacent compartments. In opposition to this effect, however, is the central positioning of the sources in the clusters, as can be seen from Figure 11.2. Apparently, this effect is not large, and so the importance of the sources is expected to be somewhat lower than 1.617 and thus not much greater, if at all, than the value of 1.156 derived previously. In fact, the calculated value of this importance, assuming a fundamental mode axial distribution, is equal to 0.7854/0.8537 x 1.483 = 1.364.

So from the above considerations, it can be seen that the higher mode contamination in the total neutron production rate is bound to be fairly small. The value of the source importance, including the effect of the higher modes, is thus predominantly determined by the shape of the fundamental mode importance. However, it should be noted that the value of ϕ^*_o at the source position is dependent also on the thermal flux distribution in the fundamental mode, ϕ_o. This is because the value of ϕ^*_o at the source position is relative to a value of unity for a fundamental mode fission source (section 2.8):

$$\langle \phi^*_o \ \nu\Sigma_f \ \phi_o \rangle = \langle \nu\Sigma_f \phi_o \rangle \qquad (11.10)$$

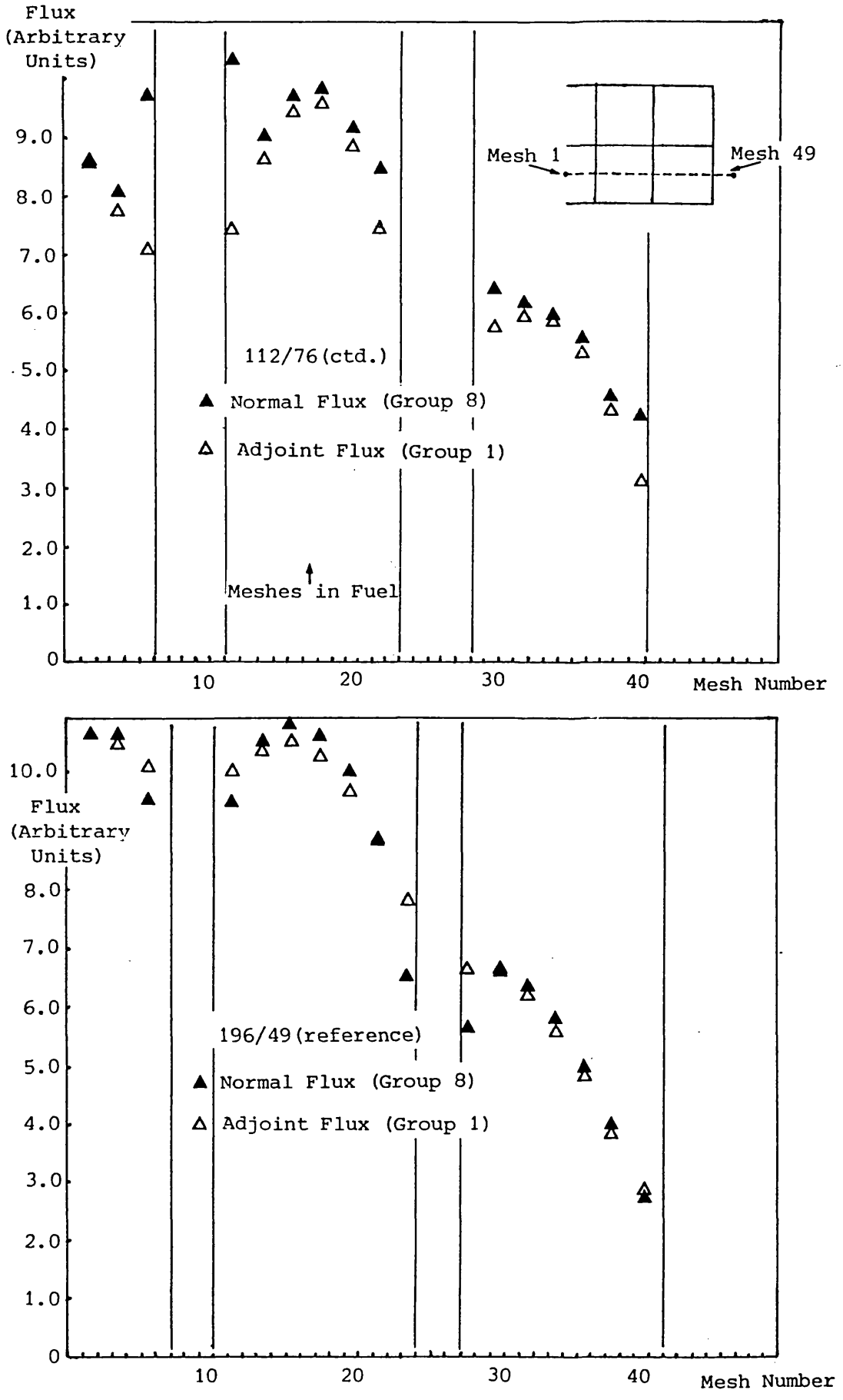

Fig. 11.2. Normal and Adjoint Fundamental Mode Flux in the 112 Pin Clusters, Centred Configuration and the Reference Configuration.

The apparent insensitivity to calculation of ϕ^* at the source position (including the effects of the higher modes) can probably be attributed to its dependence on ϕ_o^* in the fuel regions and source tube alone. Both the fuel specification and distribution are well defined. In addition, diffusion theory difficulties with flux anisotropy are not experienced in fuel regions (Fig. 9.2).

It can be seen from Fig. 11.2 that both the functions ϕ_o^* for fast neutrons and ϕ_o for thermal neutrons correspond roughly to cosine functions across the skip with variations across the compartments superimposed. Hence a large error in the prediction of ϕ^* at the source position seems unlikely, given the accurate representation of the replacement of fuel pins by the source tubes.

The prediction of ϕ^* at the source position is substantiated by the performance of the transport theory calculations (Chapter 9) and is illustrated in Fig. 11.3. The flux profile is accurately predicted in the 112 pin clusters, centred configuration (Fig. 11.3 (i)). This assumes that the accurate prediction of flux profile applies also to the clusters containing the source tubes. This is reasonable since the calculations predict accurately the flux attenuation from compartment to compartment and across each compartment, the skip geometry being a repeating geometry.

Now the value of ϕ^* at the source position depends on the fission rate profile at the source position relative to the fission rate profile at all positions in the fuel (Fig. 11.3 (ii)), the average value of ϕ^* being unity. Since the fission rate at any position depends on the fission rate at positions between this position and the source (Fig. 11.3 (iii)), it is likely that the fission rate profile at the source position relative to other positions in the fuel is well predicted. It should also be noted that in this argument the predictions of ϕ_o and ϕ^* have been related to the experimental situation. Hence any disparity in the flux prediction resulting from the use of the eigenvalue mode equation containing the factor ^{1}/k-eff (section 2.3) is probably small.

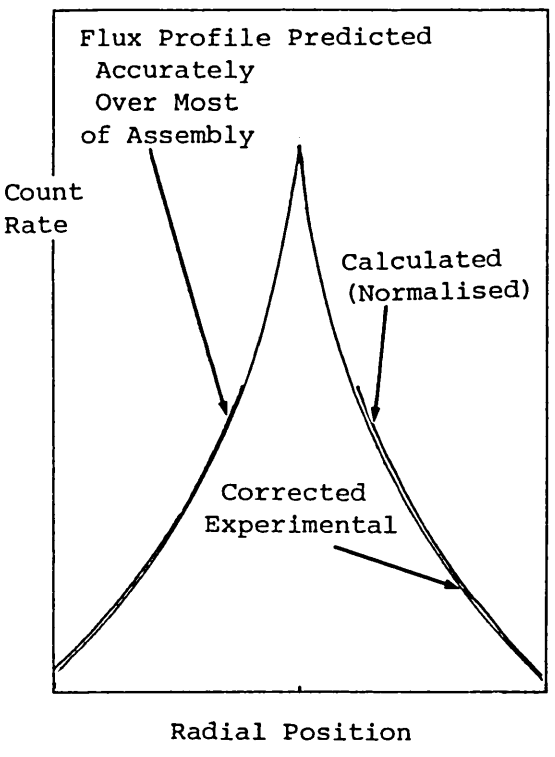

(i) Prediction of Flux Profile

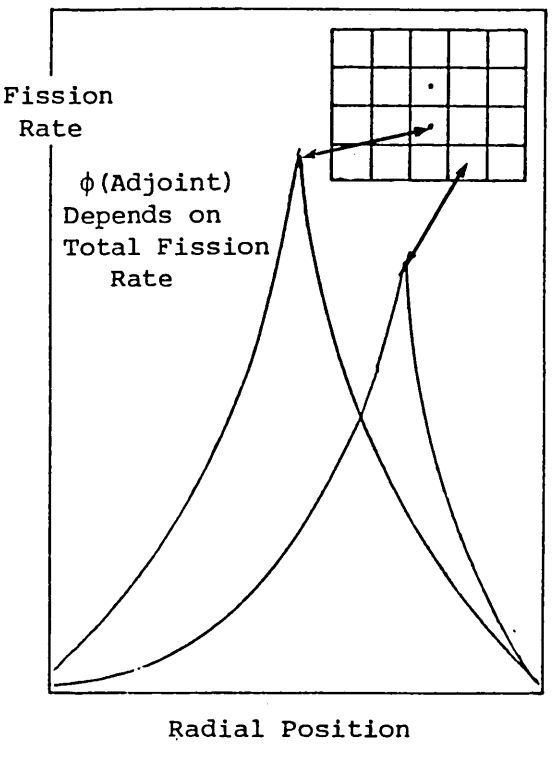

(ii) Relation of Source Importance to Total Fission Rate

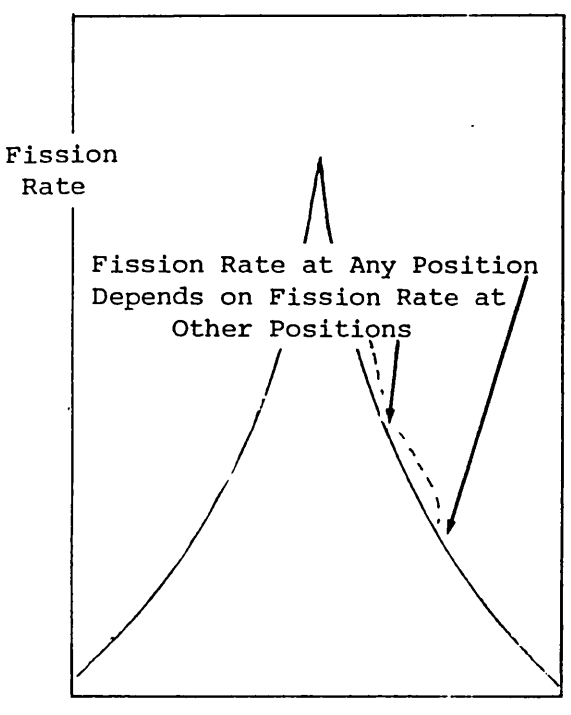

(iii) Fission Rate Profile

Fig. 11.3. The Prediction of the Source Importance by the Transport Theory Calculations.

Regarding the source importance values for the closest-to-centre, groups-of-four and dropped-pin configurations, these are expected to be well predicted also since the above conditions are unchanged.

11.1.2 The Reference Configuration

Calculated values of the product $\rho PR_{3-D}/S$, or source importance, for the reference configuration, are listed in Table 11.3. It should be noted, however, that the calculations of the reference configuration used different axial bucklings to maintain a reactivity close to the calibrated value. This causes an extra variation in the value of the ρPR_{3-D} product since the value of importance-weighted source strength (appearing as $\sum_i SS_i \cos(\pi x i/H)$ in Equation 4.12) changes with the effective height, H, which is derived from the axial buckling. Fortunately, the corresponding product ρMR, which relates more directly to the in-cluster detectors, is less sensitive to the calculational method.

Table 11.3 Source Importance Values: Reference Configuration

Calculation	Source Importance $\rho PR_{3-D}/S$	ρMR ($cm^{-1}s^{-1}$)	% Change (Orig. Calc)	$\rho\sum CR$: % Change from $\rho\sum CR$ (Orig. Calc)
Original	1.326	1.499×10^6	-	-
Transport Theory	1.406	1.503×10^6	+0.3	+5.3 *
Changed materials and boron density	1.319	1.536×10^6	+2.5	+3.0
Revised source tube specification	1.358	1.535×10^6	+2.4	+2.4

* Including normalisation for detector sensitivity, corresponding to original calculations (section 4.2.3).

It can be seen from Table 11.3 that the value of ρMR for the reference configuration is only slightly less sensitive to calculation than the value of $\rho\sum CR$. This is because of the small contribution of the higher modes to the aggregated count rate for this configuration. The fundamental mode component of $\rho PR_{3-D}/S$ was computed using the same

method as in section 11.1.1, giving a value of 1.350, which is only 2% higher than the source importance of 1.326 (Table 11.3).

Again, the value of ϕ^*_o at the source position, relative to the average value for a fundamental mode source distribution, is well predicted. This is for the same reasons as those given for the 112 pin clusters, centred configuration. Plots of the adjoint flux in group 1 and the normal flux in group 8 are shown in Figure 11.2.

11.1.3 'The Total Neutron Production Rate' Correction Factor

A correction factor which probably has a small sensitivity to calculation has been defined. Were it not for the empirical buckling changes in the reference configuration, this correction factor would be the 'total neutron production rate' correction factor. It was found, however, that the midplane component of this correction factor, $\frac{\rho_2 MR_2}{\rho_1 MR_1}$, is largely insensitive to the axial height changes in the reference configuration. The values of the numerator and denominator of this correction factor show no more than a 2% spread (Tables 11.1 and 11.3). It is thus reasonable to say that the correction factor $\frac{\rho_2 MR_2}{\rho_1 MR_1}$ is calculated to an accuracy of about 3%, for all of the configurations studied.

11.2 The Application of the 'Total Neutron Production Rate' Correction Factor to the Measurements

11.2.1 The General Behaviour of the Correction Factors

Several important characteristics of the correction factors for all the 112 and 221 pin clusters configurations have thus been established. Firstly, the original calculations tend to progressively underestimate the individual correction factors for the in-cluster detectors with increasing distance from the sources (section 8.1.4). This is due to the flux profile estimation in the well subcritical configurations. By contrast, the flux profile estimation in the reference configuration is accurate for the centre-of-cluster and half-way detectors (section

8.1.3). Finally, the 'total neutron production rate' correction factor is well predicted for each configuration (section 11.1.3).

Now the 'total neutron production rate' correction factor is equivalent to a summation of correction factors, each applying to a region of fuel in the well-subcritical configuration in question:

$$\frac{\rho_2 MR_2}{\rho_1 MR_1} = \sum_{\substack{\text{all fuel} \\ \text{regions}}} \left(\frac{\rho_2 MR_{2_{reg}}}{\rho_1 MR_1}\right), \qquad (11.11)$$

where $MR_{2_{reg}}$ is the neutron production rate in a region of fuel. The quantity $\rho_2 MR_{2_{reg}}/\rho_1 MR_1$ can be referred to as a partial correction factor.

The terms involved in the above summation can be related to the calculated correction factors by the following steps. Firstly the relation for the well-subcritical configurations, resulting from the flux profile estimation by the diffusion theory calculations is:

$$\left(\frac{CR_{2_{calc}}}{CR_{2_{expt}}}\right)_{d_1} < \left(\frac{CR_{2_{calc}}}{CR_{2_{expt}}}\right)_{d_0}, \qquad (11.12)$$

where the subscripts d_0 and d_1 refer to detector positions and d_1 is more distant from the source than d_0.

Relation 11.12 can be converted to a similar relation for neutron production rates in the immediate vicinity of the detector positions. Considering the calculated count rates first, each bears a constant relationship to the calculated local neutron production rate for the detector position. This is because the thermal spectrum is virtually the same for all in-cluster detector positions in each of the configurations in question (section 7.2.4) as are the thermal detector and neutron production cross-sections. Also invariant with detector position is the relationship between the corrected experimental count rates and the actual neutron production rates. It should be noted that this relationship itself is not known, but must be invariant with

detector position because of the similarity of detector environment and the correction for the different detector sensitivities (section 4.1.3).

So Relation 11.12 becomes:

$$\left(\frac{MR_2\ (calc)}{MR_2\ (true)\ r_1}\right) < \left(\frac{MR_2\ (calc)}{MR_2\ (true)\ r_0}\right), \qquad (11.13)$$

where MR_2 is the regional neutron production rate and regions r_1 and r_0 apply to small regions around detector positions d_1 and d_0 respectively.

Now each of the four neutron production rates in Relation 11.13 can be converted to a partial correction factor by multiplying both sides of Relation 11.13 by the terms $(\rho_2/\rho_1 MR_1)_{calc}/(\rho_2/\rho_1 MR_1)_{true}$.

Hence,

$$\left(\frac{\rho MR_{2reg}}{\rho MR_1}\right)_{calc} \Big/ \left(\frac{\rho MR_{2reg}}{\rho MR_1}\right)_{true\ (r_1)} < \left(\frac{\rho MR_{2reg}}{\rho MR_1}\right)_{calc} \Big/ \left(\frac{\rho MR_{2reg}}{\rho MR_1}\right)_{true\ (r_0)}. \qquad (11.14)$$

Relation 11.14 states that the partial correction factors are progressively underestimated with distance from the sources. But in section 11.1 it was established that:

$$\sum_{reg} \left(\frac{\rho_2 MR_{2reg}}{\rho_2\ MR_1}\right)_{calc} \cong \sum_{reg} \left(\frac{\rho_2 MR_{2reg}}{\rho_1 MR_1}\right)_{true}. \qquad (11.15)$$

to an accuracy of 3%.

That is,

$$\sum_{reg} \left(\frac{\rho_2 MR_{2reg}}{\rho_1\ MR_1}\right)_{calc} \Big/ \sum_{reg} \left(\frac{\rho_2 MR_{2reg}}{\rho_1\ MR_1}\right)_{true} \cong 1.00. \qquad (11.16)$$

This relationship can be satisfied if for some regions, the partial correction factor is overestimated and in other regions, the partial correction factor is underestimated. If, however, for all regions:

$$\left(\frac{\rho_2 MR_{2reg}}{\rho_1 MR_1}\right)_{calc\ (r)} < \left(\frac{\rho_2 MR_{2reg}}{\rho_1 MR_1}\right)_{true\ (r)}$$

$$\text{or } \left(\frac{\rho_2 MR_{2reg}}{\rho_1 MR_1}\right)_{calc\ (r)} > \left(\frac{\rho_2 MR_{2reg}}{\rho_1 MR_1}\right)_{true\ (r)}, \qquad (11.17)$$

then the 'total neutron production rate' correction factor is either overestimated or underestimated since it is equal to the sum of the partial correction factors.

So the following is true:

$$\left(\frac{\rho_2 MR_{2reg}}{\rho_1 MR_1}\right)_{calc} \Big/ \left(\frac{\rho_2 MR_{2reg}}{\rho_1 MR_1}\right)_{true\ (r)} \begin{matrix} > 1 \text{ for some regions and} \\ < 1 \text{ for other regions.} \end{matrix} \qquad (11.18)$$

Relation 11.18 can be converted to a corresponding relation for the actual correction factors used in the measurements. This can be done by multiplying by a conversion factor:

$$\frac{\left(\frac{CR_2}{MR_{2reg\ calc}}\right) \Big/ \frac{CR_1}{MR_{1calc}}}{\left(\frac{CR_2}{MR_{2reg\ true}}\right) \Big/ \frac{CR_1}{MR_{1true}}}. \qquad (11.19)$$

which converts all neutron production rates in Relation 11.17 to detector count rates. It can be shown that for the original correction factor calculations, this conversion factor is close to unity. Consider firstly the calculated terms in the above conversion factor. Firstly for the well-subcritical configuration:

$$\left(\frac{CR_2}{MR_{2reg}}\right)_{calc} = \left(\frac{\overline{\Sigma_d}\ \phi_d}{\overline{\nu\Sigma_f}\ \phi_d} \times P.F.\right)_{calc} = \left(\frac{\overline{\Sigma_d}}{\overline{\nu\Sigma_f}} \times P.F.\right)_{calc}, \quad (11.20)$$

where in the region of a detector,

$\overline{\Sigma_d}$ is the spectrum-averaged detector cross-section;

$\overline{\nu\Sigma_f}$ is the spectrum-averaged cross-section for neutron production;

ϕ_d is the total flux at the detector position; and

P.F. is the detector perturbation factor.

Secondly for the reference configuration:

$$\left(\frac{CR_1}{MR_1}\right)_{calc} = \left(\frac{\overline{\Sigma_d}\ \phi_d}{\overline{\nu\Sigma_f}\ \phi_d} \times P.F. \times W\right)_{calc} = \left(\frac{\overline{\Sigma_d}}{\overline{\nu\Sigma_f}} \times P.F. \times W\right)_{calc}, \quad (11.21)$$

where $\overline{\Sigma_d}$, $\overline{\nu\Sigma_f}$, ϕ_d and P.F. are defined as above and W is the ratio of the neutron production rate at the detector position to the total midplane neutron production rate per unit height.

Now on the right hand sides of Equations 11.20 and 11.21, Σ_d is common to both configurations as are $\overline{\nu\Sigma_f}$ and P.F. since the thermal neutron spectrum is common to the fuel regions of both configurations, as shown by the detector perturbation calculations (section 7.2.4). This is not the case in the 221 pin clusters configuration; reliance is thus placed on the accuracy of the perturbation factor calculations in this case.

Hence, dividing Equation 11.20 by 11.21:

$$\left(\frac{CR_2}{MR_{2reg}}\right)_{calc} / \left(\frac{CR_1}{MR_1}\right)_{calc} = \frac{1}{W}_{calc}. \quad (11.22)$$

Considering likewise the 'true' terms in the conversion factor (Equation 11.19) results in:

$$\left(\frac{CR_2}{MR_{2reg}}\right)_{true} / \left(\frac{CR_1}{MR_1}\right)_{true} = \frac{1}{W}_{true} \qquad (11.23)$$

where W_{true} is the ratio of the actual neutron production rate at a detector position (assuming the detector to be replaced by fuel) to the total midplane neutron production rate per unit height in the reference configuration.

Now it is noted that both terms W_{calc} and W_{true} in Equations 11.22 and 11.23 depend almost solely on the thermal neutron flux distribution in the reference configuration. This is because the spectrum is virtually constant throughout the fuel regions. In addition it was observed (section 8.1.3) that the thermal flux distribution in the reference configuration is accurately predicted by the original calculations. Hence $W_{calc} \approx W_{true}$ for any detector position. The conversion factor (11.19) is thus equal to unity for each in-cluster detector, to an accuracy of a few percent.

So Relation 11.18 can be converted to:

$$\left(\frac{\rho_2 CR_2}{\rho_1 CR_1}\right)_{calc\ (r)} / \left(\frac{\rho_2 CR_2}{\rho_1 CR_1}\right)_{true\ (r)} \begin{array}{l} > 1 \text{ for some regions r and} \\ < 1 \text{ for other regions r.} \end{array} \qquad (11.24)$$

Relation 11.24 is important and is illustrated schematically in Figure 11.4. Its application to the original correction factor calculations can thus be explained qualitatively, by considering the prediction of the quantities ρ_2 and CR_2/CR_1.

Since the original correction factor calculations overestimate the neutron absorption through the skip for the well-subcritical configurations, it is natural to assume that they also underestimate k-eff. Hence, they overestimate the subcritical reactivity, ρ_2. But the subcritical reactivity is merely a measure of the fundamental mode neutron production rate:

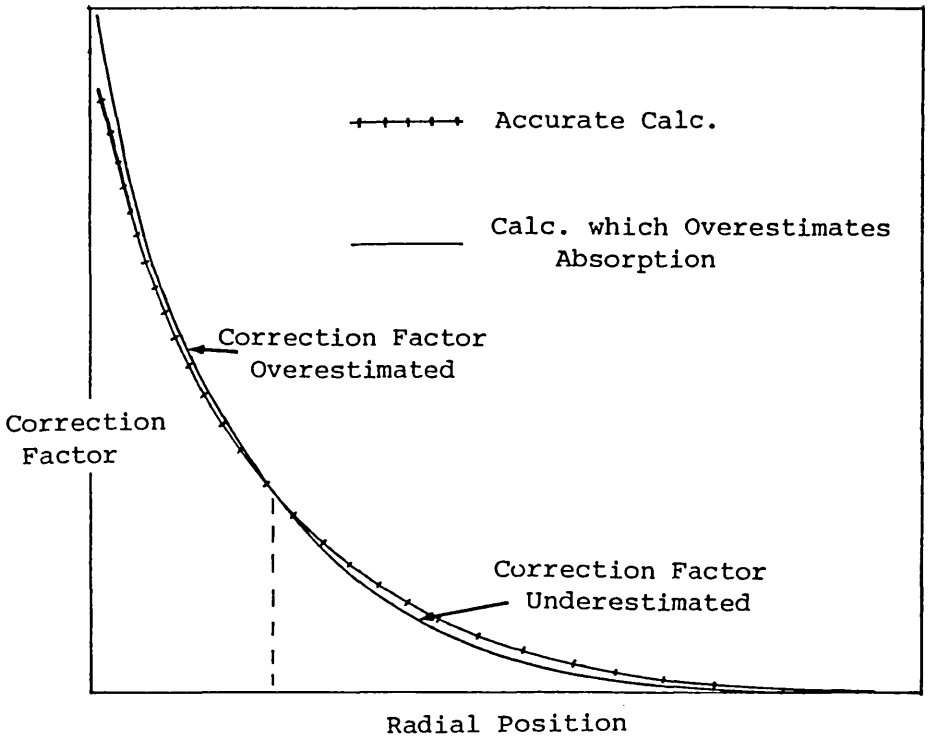

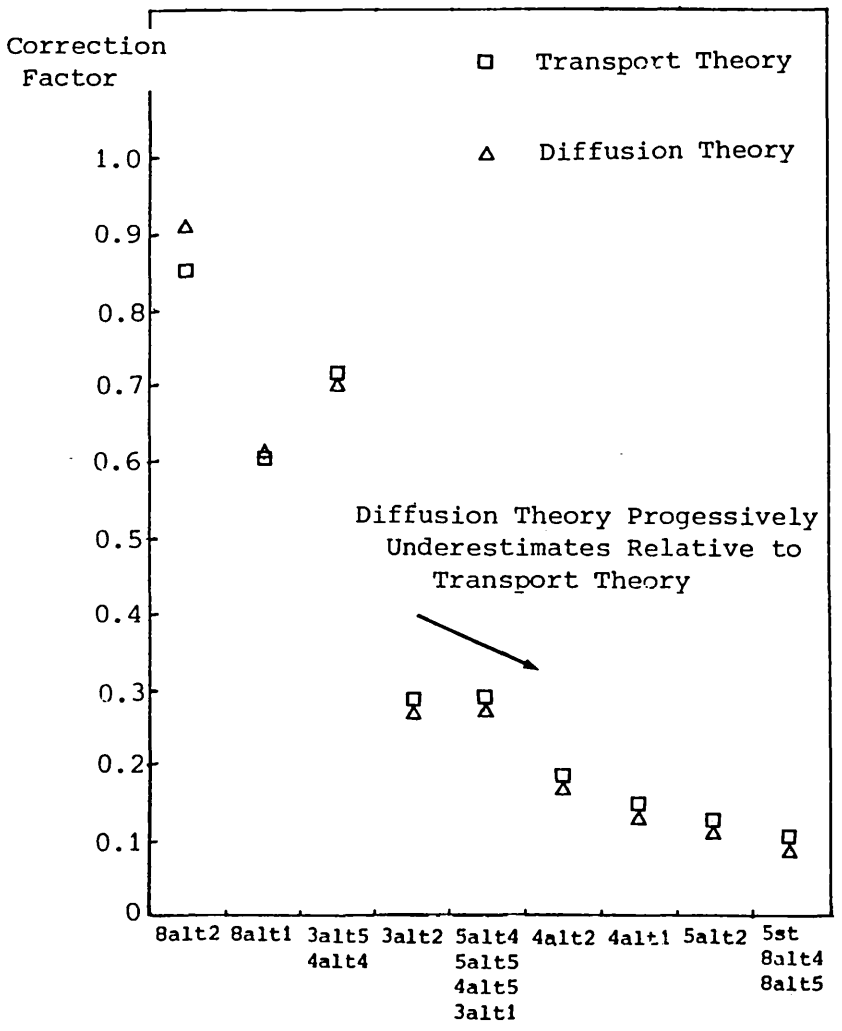

Fig. 11.4. The Variation of the Correction Factor Calculations with Absorption Through the Skip.

$$\rho = \frac{\langle \phi^* S \rangle}{\langle \phi \nu \Sigma_f \phi \rangle}.$$

This neutron production rate at any point has contributions from sources at all points in the fuel, since the required source distribution must itself be a fundamental mode for a well-subcritical assembly. These contributions are either overestimated or underestimated in relation to the estimation of subcritical reactivity, according to their distance from the point in question. This is because the overestimation of absorption occurs progressively throughout the skip.

The skip is thus divided roughly into two regions in which the $\rho_2 CR_2 / \rho_1 CR_2$ is either overestimated or underestimated though the performance of the calculations across the individual compartments may complicate this behaviour. The division between these two regions occurs at a distance from the sources at which the underestimation of the count rate ratio is great enough to counteract the overestimation of subcritical reactivity. Clearly, with the progressive underestimation of the correction factors by the original calculations covering a range of about 15% or more for some configurations (Table 8.4), the correction factors are in all probability overestimated close to the sources and underestimated far away from the sources.

For the transport theory calculations, however, the trend in the individual k-eff values has disappeared. It can only be concluded in view of the accurate prediction of the 'total neutron production rate' correction factor that all of the correction factors are well predicted. The error due to any calculational deficiencies (which are probably small) and the experimental count rate errors, can thus reasonably be expressed in terms of the spread of k-eff values from the in-cluster detectors.

11.2.2 Evaluation of the Systematic Errors due to Calculation

If it is assumed that the calibrated reactivity is equal to its true value, then Relation 11.24 applies directly to the reactivities from

MSM. Superimposed on it, however, is a random error resulting from the experimental count rate ratio $((CR_1/CR_2)_{expt})$ for each detector.

This error was examined in Chapter 6 and is due largely to the asymmetry of each configuration and the reproducibility of each count rate.

Unfortunately, the in-cluster detectors in the measurements are not situated at all distances from the sources. Most conspicuously there is no detector in either of the clusters containing the source tubes. There is thus no obvious guarantee that the closest detector to the sources, detector 8 alternative 2 (Figure 4.2) has a correction factor which is overestimated.

There is other evidence, however, that the original correction factor for detector 8 alternative 2 is overestimated. This evidence is provided by the transport theory calculations, which predict a reduction of the correction factor for this detector from 0.903 (Table 8.4) to 0.849 (Table 9.5). Since the transport theory calculations accurately predict the flux profile in the well-subcritical configurations, all the resultant k-eff values from MSM are in all probability close to the true k-eff value of each configuration. The modified source multiplication k-eff values from detector 8 alternative 2 are shown in Table 11.4.

Table 11.4 The Range of Measured k-eff Values

Configuration	k-eff Values from MSM			
	8 alt 2	Aggregated In-Cluster Detectors	5st, 8 alt 4 8 alt 5 (mean)	Range of k-eff Values
112/76 (CTD)	0.821	0.833±0.010	0.856	0.035
112/76 (G4)	0.850 *	0.861±0.009	0.867	0.017
112/76 (CC)	0.853	0.857±0.007	0.874	0.021
112/76 (CCD)	0.905	0.908±0.004	0.918	0.013
221/76 (CTD)	0.750 *	0.765±0.015	0.795	0.045

*Detector 3 alt 5

Also listed in Table 11.4 are the k-eff values resulting from the in-cluster detectors farthest away from the sources, using the original

correction factor calculations (Table 8.8). Together with the k-eff values resulting from detector 8 alternative 2 they give a range of k-eff values within which the true k-eff of the configuration probably lies, assuming there are no errors in the calibrated reactivity of the reference configuration.

It would be convenient to express the above ranges in terms of a standard deviation, referring to the probable departure of the k-effective value given by the aggregated in-cluster count rates from the true k-eff value. This standard deviation would then combine easily with the error of 5.5% associated with the calibrated reactivity, the axial calculational errors and the perturbation errors where appropriate.

The only obvious standard deviation to use is that resulting from the individual k-eff values from the in-cluster detectors, which has been the assumed error so far. However the variances resulting from the individual detectors are weighted by their experimental count rates in the well-subcritical configuration:

$$\sigma_{k\text{-eff}} = \left[\sum_{i=1}^{ND} W_i (k\text{-eff}_i - \overline{k\text{-eff}})^2 / \sum_{i=1}^{ND} W_i \right]^{\frac{1}{2}}, \qquad (11.25)$$

where: ND is the number of detectors;
W_i is the experimental count rate from detector i in the well-subcritical configuration; and
$k\text{-eff}_i$ is the k-eff derived from detector i.

It is noted that this weighting accounts for the large variation in the contributions of the detectors to the total count rate in the well-subcritical configuration. However the derived standard deviation is, for each configuration, only slightly smaller than that derived from equal weighting of the detectors (Table 8.10).

This standard deviation can be compared with the range of k-eff values for each configuration (Table 11.4), which is about 3 times as great in each case. Remembering that the use of a standard deviation implies a

range of values equal to about one and a half standard deviations on either side of the measured value for roughly a 86% confidence limit, it would appear that the standard deviations are a conservative expression of the errors.

It is important to note that the sensitivity studies of Chapters 9 and 10 which yielded smaller changes in k-eff (~0.003) than the standard deviations (~0.010) quoted in Table 11.4, provide substantiation of the statement that these errors are conservative.

Hence the proposed use of the spread of k-eff values as a measure of the systematic errors due to calculation as proposed in section 8.2.1 is vindicated, provided that the k-eff values result from detectors distributed throughout the fuel regions. The weighting of these k-eff values in calculating the standard deviation (Equation 11.25) reflects the aggregation of count rates used in deducing the mean k-eff value.

11.3 Evaluation of the Overall Errors

The total error associated with the measured k-eff value of each configuration (ie that derived from the aggregation of in-cluster count rates) can now be evaluated. Since the error resulting from the correction factor deficiencies and the experimental count rate uncertainties is expressed in the form of a standard deviation (section 11.2), it can be added, in quadrature, to the standard deviation of 5.5% associated with the calibrated reactivity (section 5.1.2). The systematic error of 3% associated with the simplified axial representation (section 7.1.5) must also be included. Finally for the 221 pin clusters, centred configuration, an additional error of 3% for the relative perturbation factor (section 7.2.7) is also added.

A summary of the errors associated with the measured k-eff value of each configuration is given in Table 11.5. Since the error from the correction factor calculation combined with the experimental count rate error is derived from a particular correction factor calculation for each configuration, separate errors result from the transport theory calculations, and the use of the alternative source positions.

Table 11.5 The Errors of the Measurements

Configuration	Source Positions	Correction Factor Calculation	Correction Factor + Count Rate Error (% of Reactivity)	Total Error (% of Reactivity)	k-eff Value with Error (σ total)
196/33	Standard	Diffusion	3.3	7.0	0.935±0.004
	Alternative	"	1.5	6.7	0.935±0.004
112/76(CTD)	Standard	Diffusion	8.6	10.4	0.833±0.014
	"	Transport	4.4	7.3	0.831±0.010
	Alternative	Diffusion	5.2	7.8	0.835±0.010
112/76(G4)	Standard	Diffusion	7.5	9.5	0.861±0.011
112/76(CC)	Standard	Diffusion	6.1	8.4	0.857±0.010
112/76(CCD)	Standard	Diffusion	3.9	7.4	0.908±0.006
221/76(CTD)	Standard	Diffusion	9.6	11.9	0.765±0.022
	"	Transport	5.7	9.0	0.763±0.016
	Alternative	Diffusion	4.1	8.1	0.762±0.014

There are several remarks to be made regarding the magnitude of the overall errors. Firstly, the overall errors, expressed as a percentage of subcritical reactivity, have a minimum of about 7%, as can be seen from the appropriate column in Table 11.5. This minimum is largely dictated by the error of 5.5% in the calibrated reactivity. However, its presence also reduces the sensitivity of the total error to the correction factor and count rate errors. It can be seen that the correction factor and count rate errors range from 1.5% to 9.6%, yet the total errors have a smaller range, from 6.7% to 11.2%.

It is thus evident that, though it is preferable to use transport theory calculations or four radial source positions in the measurements, the resultant gain in precision is not particularly great. This can be seen from the errors for the 112 and 221 pin clusters, centred configurations.

Also evident is the decreasing size of the total error in k-eff as a k-eff of unity is approached. This results from the fact that as the subcritical reactivity becomes smaller, the magnitude of the error in

reactivity also diminishes because it remains a roughly constant fraction of the reactivity.

Finally consideration should be made of the probable effect of including a detector in the same cluster as the sources on the mean k-eff values and their errors. In the 112 pin clusters, centred configuration, such a detector would roughly double the total count rate (Table 11.2). The k-eff value resulting from this detector alone will probably be slightly less than the value of 0.821 for detector 8 alternative 2 (Table 11.4), taking account of the trend for these values to increase with distance from the sources, for the original calculations. This would result in a k-eff value of about 0.825, considering the total in-cluster count rate. This is not greatly different from the value of 0.831 using the transport theory calculations (Table 11.4). It should be noted that the absence of a trend in the k-eff values derived from the transport theory calculations probably means that a detector in the source cluster will not affect the mean k-eff value greatly if these calculations are used.

11.4 Comparisons of Measured and Calculated K-eff Values

The measured k-eff values for each configuration (Table 11.5) can be compared with the k-eff values obtained directly from the diffusion theory and transport theory calculations. The calculated k-eff values from diffusion theory have been listed in Table 8.3 and those from transport theory, for the two centred configurations, are given in Table 9.5. The transport theory k-eff values for the remaining configurations were calculated using the same group structure, S-quadrature, and geometrical and material specifications as in the transport theory calculations already described (section 9.2).

In addition, comparisons can be made with k-eff values obtained from Monte Carlo calculations. These calculations used the code MONK6.2 (1). Together with the diffusion theory and transport theory k-eff values, these k-eff values form the full range of comparisons described in the aims of the measurements (section 3.1).

The measured and calculated k-eff values are listed in Table 11.6. Where more than one measured k-eff value is available (from transport theory calculations or the alternative source positions) the value with the smallest standard deviation is given.

Table 11.6 Measured and Calculated k-eff Values

Configuration	k-eff (Measured)	k-eff (Diffusion Theory and ΔK (Diffusion-Measured)	k-eff (Transport Theory) and ΔK (Transport-Measured)	k-eff (Monte Carlo)* and ΔK (Monte Carlo-Measured)
112/76(CTD)	0.831±0.010	0.813 (-0.018)	0.845 (+0.014)	0.836 (+0.005)
112/76(G4)	0.861±0.011	0.842 (-0.019)	0.862 (+0.001)	0.878 (+0.017)
112/76(CC)	0.857±0.010	0.839 (-0.018)	0.868 (+0.011)	0.875 (+0.018)
112/76(CCD)	0.908±0.006	0.905 (-0.003)	0.924 (+0.016)	0.938 (+0.030)
221/76(CTD)	0.762±0.013	0.751 (-0.011)	0.778 (+0.016)	0.788 (+0.026)
196/49 (reference)	0.9929	1.007 (before axial buckling change)		*standard deviation 0.006 ΔK in each case

Considering firstly the calculated k-eff value from diffusion theory for every 112 and 221 clusters configuration, the k-eff value is, in all probability, underestimated. This is evidently due to the overestimation of thermal flux in the water around the clusters and possibly the boron-steel walls relative to the fuel regions. This was observed in the preliminary analysis of the measurements (section 8.1.3). It also appears that the underestimation of k-eff is significantly reduced for the configuration involving the dropped pins. A likely reason for this trend is indicated by the diffusion theory k-eff value for the reference configuration. When there is no water gap between the fuel pins and boron-steel walls, it appears that diffusion theory has a slight tendency to overestimate k-eff. The presence of dropped pins adjacent to the boron-steel walls in the centre of the skip would thus certainly tend to reduce the underestimation of k-eff.

By contrast, most of the transport theory calculations probably overestimate k-eff. This is consistent with the fact that the transport theory calculations appear to underestimate the thermal flux in the water around the cluster relative to the fuel regions. This was

observed in the analysis of the transport theory calculations in section 9.4.2. The probable overestimation of k-eff by the transport theory calculations may well be quite small, a fact supported by their accurate prediction of the flux profile in the 112 and 221 pin clusters, centred configurations (Table 9.6).

The validation of the WIMS nuclear dataset (2) indicates that with the most recent adjustments, the prediction of k-eff for simple assemblies of enriched uranium oxide pins in water is very accurate. It is not possible to say for the skip configurations, precisely how accurate the k-eff predictions are, since the measured k-eff values have errors which are not insignificant. Nevertheless, it can be said that transport theory calculations employing a simple four- or eight-group structure and an S-4 quadrature predict the k-eff of a variety of skip configurations to an accuracy of less than 1-2%. This prediction appears to be largely independent of the size of water gaps between the clusters and boron-steel walls, and of the pitch of the fuel pins.

Finally, the MONK6.2 k-eff values in Table 11.6 seem to be overpredictions of k-eff for the most part. There is no clear evidence that MONK6.2 overpredicts k-eff for uranium systems (1). However the overprediction may be smaller than is apparent from Table 11.6, in view of the errors in the MSM k-eff value and the standard deviation of each of the MONK k-eff values.

12 Applications of the Measurements, and their Limitations

The implementation of the modified source multiplication technique in well-subcritical fuel storage assemblies has thus been demonstrated. It is worthwhile to indicate further applications of the technique and to give recommendations as to its implementation on other assemblies. It is also desirable to indicate the limitations of the technique in a plant situation.

12.1 The Application of the Measurements to Other Assemblies

12.1.1 Applications

The range of application of the measurements is restricted by the necessity of using a reference configuration which is slightly subcritical. This has already been noted in previous references (1). In fact, in a plant situation involving a fuel storage array or a dissolver, it is virtually certain that no convenient reference configuration will be available. Nevertheless the technique used in the DIMPLE measurements does have other potential applications.

Provided that an assembly of unknown subcriticality can be built in a well-controlled environment such as DIMPLE, and a reference configuration can be built also, preferably by making a reactivity insertion to the assembly in question, its reactivity and hence k-eff can be measured. Though this is not a plant situation, such a measurement has two principal uses. Firstly, it serves to validate calculations for a situation which resembles the plant situation more closely than the critical assemblies, upon which most validation of k-eff calculations is based. Secondly, if the measured configuration represents the most reactive credible configuration which is likely to occur in a plant situation, then the measurement can confirm the safety of the plant situation, even though the exact specification, however, would probably require some form of monitoring the configuration in the plant situation as it is assembled.

Among the assemblies which may be built in DIMPLE and upon which the modified source multiplication technique will be of use, are fuel

storage arrays involving boron-poisoned water, voids around the clusters and situations involving dissolvers.

12.1.2 Recommendations for the Implementation of the Technique in DIMPLE

12.1.2.1 Characteristics of the Configurations

Both the well-subcritical configuration in question and the reference configuration should preferably have the following characteristics, all indicated by the DIMPLE measurements. Since it is necessary to make use of a well-predicted correction factor in the interpretation of the errors, the 'total neutron production rate' correction factor should be well predicted (section 11.1). As indicated in section 11.1 this is probably the case for assemblies with a fairly regular distribution of fuel, since the importance of fast neutrons is thus a slowly varying function of position (Figure 11.1). With regard to assemblies containing uneven fuel distributions, for example pins of widely different enrichments, the 'total neutron production rate' correction factor may be less well predicted.

It is also desirable to have a common fuel environment in both the reference and well-subcritical configurations. This makes the detector perturbations common to both configurations, provided the common environment is extensive enough (section 7.2.4). The calculation of relative perturbation factors is thus unneccessary. If no common fuel environment is present, then relative perturbation factors must be calculated. This adds an extra component to the total error (section 7.2.7).

12.1.2.2 Sources

Before discussing the use of imposed sources, it should be noted that it may be possible to use the inherent source from irradiated fuel if it is present. In previous references (2), this was noted as reducing higher mode contamination in well-subcritical configurations and thus to make correction factor calculations more reliable. However, the need for

accurate knowledge of this inherent source may make its use inconvenient.

If localised sources are used, it may be necessary to distribute them radially. This tends to reduce the magnitude of flux attentuation with distance from the sources. Inevitably, the decision to distribute the sources depends on the configuration in question and the calculations used to model it.

Axially, the sources should be distributed to ensure that the flux approximates to a fundamental mode axially (section 7.1.3). This is probably a simple requirement, given that a vertical holder such as a tube is used to locate the sources.

The sources should be of sufficient strength to limit counting statistics for detectors in the fuel regions to about 1-2% or less (section 4.1.3).

Finally, note that if localised sources are used in a configuration with an inherent neutron source, and it is required to ignore the effect of the inherent neutron source, count rates can be taken both with and without the imposed sources in place, to deduce the count rates due to the imposed sources:-

$$CR(\text{imposed source}) = CR(\text{inherent source} + \text{imposed source}) - CR(\text{inherent source}). \quad (12.1)$$

12.1.2.3 Detectors

The detectors should, as far as possible, be evenly distributed throughout the fuel regions. This ensures a reasonable representation of the 'total neutron production rate' correction factor.

The correction factor for all of the in-cluster detectors in the fuel regions is thus most likely to be insensitive to the calculational method. In addition, the spread of measured k-eff values from all the in-fuel detectors provides a true measure of the systematic errors due to calculation (section 11.3).

It is also useful to situate detectors outside the fuel regions to give diagnostic information on the correction factor calculations (sections 8.1.3 and 9.4).

If the axial flux distribution is a cosine shape, then the detectors should be positioned close to the midplane where the flux varies least with axial position. This minimises uncertainties arising from the position of the detector active material (section 4.1.2).

Finally, the detectors should be sufficiently sensitive to give counting statistics of about 1-2%.

12.1.2.4 Calculations

The principal restraint on the correction factor calculations is that they must estimate the flux profile within a certain accuracy. This is particularly the case for well-subcritical configurations in which the attenuation of flux away from localised sources is likely to be significant.

Obviously, the adequacy of a particular calculational model will depend on the characteristics of the configuration in question. The DIMPLE measurements indicate the following requirements for correction factor calculations of thermal systems:

(i) Diffusion theory is adequate provided that the attenuation with distance from the sources is not too great. High attenuation would make the spread of k-eff values very susceptible to errors in the estimation of this attenuation.

(ii) A group structure of 4 groups is probably adequate.

(iii) Errors in the geometric and material specifications can be tolerated, to a certain degree (Section 10.1).

Finally, it should be noted that there is some advantage in producing a correction factor calculation which is as accurate as possible (section 11.4).

12.2 The Implementation of the Technique in a Plant Situation

The purpose of this section is to indicate how the modified source multiplication technique might be implemented, if at all, in a plant situation. It should be emphasised, however, that the following guidelines are only tentative.

12.2.1 Restraints on the Technique

There are several restraints, applying to CAGR skips in a plant situation, which will effect the implementation of the technique.

The first of these restraints is the lack of a convenient reference configuration. This leaves two options: either the measurements are made using sources and detectors which have been used for a calibration on another site, or they are made with no calibration at all. The former option involves the transporting of the sources and detectors and associated electronics from one site to another. The latter option implies, as will be shown, that extra information on the sources and detectors is needed.

Another restraint concerns the positioning of sources and detectors in and around the skip. Safety restrictions may not allow either sources or detectors to be placed inside the skip. Hence, the technique must involve out-of-skip detectors alone, with the source neutrons either being provided by the inherent source in the irradiated fuel, or by sources placed outside the skip.

A third restraint concerns the specification of the skip and its contents. In a plant situation it is usually not practical to perform detailed measurements on a skip and its fuel pins similar to those performed in the DIMPLE measurements. Furthermore, the fuel pins being irradiated, are likely to be of a variety of enrichments. This would probably make their accurate specification impossible.

Accordingly, any calculation used to support a subcritical reactivity measurement must be based on an approximate model of a skip and its contents. Any calculated factors used must be fairly insensitive to the uncertainties in the model.

12.2.2 Guidelines for the Implementation of the Technique

Given the likely presence of all three of the aforementioned restraints, the resulting feasibility of modified source multiplication measurements can be examined.

Firstly, the possibility of employing the technique without a reference configuration can be examined using the results of the DIMPLE measurements, together with some extra data. The basic modified source multiplication equation is (Equation 3.10):

$$\rho = - \frac{WS_{eff}}{\overline{\nu}CR} \qquad (12.2)$$

The quantity $(-WS/\overline{\nu})$ is equal to the product (ρCR). Hence, we have:

$$\rho_{2expt} = (\rho_2 CR_2)calc/_{CR_{2expt}} \qquad (12.3)$$

where the well-subcritical configuration has been given the subscript '2' as in Chapter 3.

Effectively, the reliance is now on the product $(\rho_2 CR_2)calc$. Provided that a fundamental mode is predominant, there is still latitude for errors in the calculation of ρ_2, since CR_2 is proportional to $1/\rho_2$ for a fundamental mode distribution. The calculation of CR_2, however, must now take into account the absolute source strength, the detector sensitivity and the detector flux perturbation (section 3.2.1). This is because these quantities are not common to both the numerator and demominator of the equation giving the unknown reactivity as they are when a reference configuration is used.

For the sources and detectors used in the DIMPLE measurements, these three quantities are, fortunately, known. The total strength of the californium sources was measured as $27.8 \times 10^{7} ns^{-1}$ ±2%rms on a date 7.25 years before the start of the measurements (3). Since the half-life of californium-252 is accurately known, it is possible to calculate the actual source strength applicable to any of the measurements.

Regarding the detector sensitivities, these can be calculated, using a knowledge of the amount of active material contained in each of the detectors, and the microscopic neutron absorption cross-section of boron 10. A summary of this calculation is given in Table 12.1.

Table 12.1 The Absolute Sensitivity of the In-Cluster Detectors

Dimension of BF_3 gas in detector
Length : 5cm Diameter : 0.5cm Volume : $0.982 cm^3$
Pressure of BF_3 gas : 0.526 atmospheres Proportion of boron-10 in boron : 90% Microscopic neutron absorption cross-section (group 8) : $5600 \times 10^{-24} cm^2$
Group 8 Sensitivity (= no of boron-10 atoms x σ_{abs}): 0.07 $cps/ncm^{-2}s^{-1}$

However, the above sensitivity is only nominal and individual variations are expected for the different detectors issued in the measurements. Account can be made of this variation by assigning the above sensitivity to the average sensitivity of the detectors used, which was previously known only on a relative scale (section 4.1.4). On the relative scale used for the detector sensitivities, the average sensitivity was found to be 1.120.

So for detector 3 at the start of the measurements, for example, the sensitivity is given by

$$S = \frac{1.000}{1.120} \times 0.07 \text{ cps/neutron } cm^{-2}s^{-1}, \qquad (12.4)$$

where S is the sensitivity to group-8 neutrons.

Finally, for the in-cluster detectors in the 112 pin clusters configurations, the perturbation factor was calculated as 0.878 (section 7.2.3). This figure probably has an error of about 3% associated with it, as indicated in section 7.2.7.

An estimate of the subcritical reactivity of any of the well-subcritical configurations can now be given. For the 112 pin clusters, centred configuration; this estimate is summarised in Table 12.2.

Table 12.2 The Absolute MSM Reactivity: 112 Pin Clusters, Centred Configuration

Corrected experimental count rate (total for in-cluster detectors): $747.3 sec^{-1}$ (Appendix A)
Calculated count rate (original calculations) : $167.0 sec^{-1}$ (Appendix A)
Factor to account for detector sensitivity and perturbation: $\left(\frac{1.000}{1.120} \times \frac{0.07}{0.015} \times 0.878\right)$: 3.658
Calculated count rate (including above factor): $610.9\ sec^{-1}$
Calculated reactivity (Table 8.3) : -0.22974
Reactivity, using absolute MSM (Equation 12.3) : -0.188 (cf -0.200 from relative MSM)
K-eff, using absolute MSM : 0.842 (cf 0.831 from relative MSM)

It can be seen from Table 12.2 that there is a difference of 6.6% between the subcritical reactivities deduced from the relative and absolute modified source multiplication methods. This difference is not large when it is considered that the relative method includes an error of 5.5% from the calibration (Chapter 5) and the absolute method includes a possibly larger error from the source and detector data just described.

The apparent similarity between the reactivities derived from the relative and absolute methods suggests that the absolute method may be feasible. The situation would be clearer if the absolute sensitivities

of the detectors were known more accurately. An experimental determination of these sensitivities is thus recommended. This could be achieved by calibration against activation foils (4).

So the absolute method may be feasible when in-cluster sources and detectors are used. Unfortunately, the probable restraints on the positioning of sources and detectors force a consideration of the feasibility of the absolute method for detectors outside the skip, using the inherent source in the fuel. Can the product ρCR be accurately predicted in this situation?

It should firstly be noted that the fact when the source is spread throughout the fuel, the higher mode contamination is reduced. So it may well be that the ρCR product is accurately predicted for any point in the fuel regions, since the flux is proportional to $^1/\rho$ for a fundamental mode distribution and the source mode flux prediction thus depends only on the fundamental mode flux prediction throughout the fuel.

Unfortunately, the flux prediction in the water regions surrounding the clusters was found to vary greatly with calculation (section 9.2).

Clearly, there will have to be several exploratory calculations and experiments to ascertain whether the ρCR product can be accurately predicted for detectors outside the skip. Such calculations might initially model a fixed skip geometry and source distribution. Variations in the calculational method such as changes in the S-quadrature and group structure would then be tried.

Several subsidiary points should be made concerning the above configuration of sources and detectors. Firstly, the irradiated fuel may well possess a high γ-ray source in addition to its neutron source. The presence of a high γ-ray source can give rise to pulses in the detectors which cannot be distinguished from the pulses resulting from neutrons reacting with the detector active material. It may thus be preferable to use fission detectors which have better γ-ray discrimination than boron triflouride detectors.

The question of detector perturbations must also be considered. The calculations of Chapter 7 showed that perturbation factors can be calculated, though the reliability of the calculations is not absolutely certain. There is, however, the possibility that a small detector in a completely thermalised neutron spectrum may cause only a small flux perturbation. This is because a thermal spectrum is in equilibrium as regards neutron slowing-down and so the displacement of moderator by the detector presumably may make little difference to the thermal spectrum. Again some exploratory calculations could test this hypothesis.

Finally, consideration must be made of the effect the approximations in the calculational model have on the product ρCR. Detectors placed outside the skip are effectively monitoring the neutron leakage from it. Unfortunately the leakage from a CAGR skip depends, for instance, on the separation of the fuel clusters from the boron-steel walls, and thus is probably sensitive to the calculational model. The leakage may not, however, be particularly sensitive to the fuel enrichment since the migration area tends to be controlled by the proportion of water which is the dominant moderator.

To conclude then, the possibility of employing an absolute modified source multiplication technique should be investigated. Exploratory calculations which should be undertaken are:

(i) Calculations of ρCR for detectors outside the skip and an inherent source in the fuel. Different calculational methods should be investigated.

(ii) Calculations of detector perturbations for detectors deep in a water region.

(iii) Calculations of ρCR for varying fuel irradiations in the skip.

It is expected that the variations in the likely fuel irradiation and distribution in the skip will probably limit the absolute MSM technique to use, at best, as an approximate measurement. Such a measurement would, however, still be of significant worth, for the following reason.

A CAGR skip containing highly irradiated fuel has a k-eff which is much lower than the values of 0.80 to 0.86 which featured in the DIMPLE meausurements. This is because its enrichment may be only between 1 and 2%. Approximate measurements may at least be able to confirm that the k-eff is below a certain threshold, say about 0.8.

12.2.3 The Direction of Further Work

It is presumed that further measurements and calculations will take place to show the limits of the modified source multiplication technique in a plant situation. This technique, however, is only one of the possible types of subcritical reactivity measurement which can be made. Nevertheless, it is the obvious first choice to provide a basis for the possible validation of other techniques.

Of the other types of measurement, noise measurements and pulsed neutron measurements, particularly the former, have already been noted for possible use (5). At the present time, none of these have been validated in well-subcritical water-moderated assemblies such as the CAGR skips.

Some exploratory measurements using a noise or neutron correlation technique, were carried out in DIMPLE at the time of the modified source multiplication measurements. Since no conclusive results were obtained, these measurements are not detailed in this work, but will be described in a separate paper.

13. Summary and Conclusions of the Measurements

13.1 Summary

It was required to measure the k-effective of arrays of 3% enriched uranium oxide pins contained in a CAGR skip insert and flooded by water. The modified source multiplication technique was used for this purpose. This technique involves the comparison of experimental count rates in a well-subcritical configuration relative to those in a slightly subcritical configuration of known reactivity (the reference configuration). Both assemblies contained fixed neutron sources. Calculated correction factors are used to account for differences in source importance and detector effeciency between the two configurations.

The modified source multiplication technique had not been systematically validated for measurements of well-subcritical assemblies in which the flux distribution is significantly different from the flux distribution in the reference configuration. For the CAGR skip measurements the differences in flux distributions were severe in view of the large size of the skip in relation to the average length of the fission chains in a water-moderated environment. This was symptomatic of significant higher mode contamination. A crucial part of the validation of the technique was thus to quantify the errors resulting from deficiencies in the correction factor calculations (Chapter 3).

The reactivity of the reference configuration was determined using the period technique (Chapter 5). The experimental errors in the count rate ratios were determined (Chapter 6). The errors inherent in the use of two-dimensional calculations were found to be small (Chapter 7). Factors to account for the detector perturbations were derived, though these were unity for the in-cluster detectors in most of the configurations (Chapter 7).

The main diagnostics followed. Firstly, using physical arguments, a preferred type of source and detector distribution was indicated (Chapter 8). Then by performing sensitivity studies on the correction factor calculations, the preferred type of detector distribution was

verified (Chapters 9 and 10). In addition, it was demonstrated that systematic errors in the correction factors were probably small for this type of distribution (Chapters 9 and 10).

Finally, it was shown that the correction factor derived from the total neutron production rates in both the well-subcritical and reference configurations was well predicted (Chapter 11). This allowed the following interpretation of the systematic errors resulting from the correction factor calculations. The error can be expressed in terms of the spread of measured k-eff values resulting from each of a distribution of detectors over the fuel regions. Combined with the errors resulting from the experimental count rates, it is equal to the root mean square standard deviation resulting from this spread of k-eff values (section 11.2).

13.2 Conclusions

The conclusions reached from the measurements can be grouped according to the different aspects of the modified source multiplication technique. These aspects are three-fold:

(i) The use of a well-predicted correction factor to interpret the systematic errors due to calculational deficiencies.

(ii) The preferred positioning of sources and detectors to minimise the above errors.

(iii) The characteristics of different correction factor calculations and comparisons of predicted and measured k-eff values.

Regarding the first of the above aspects, it can be concluded that the correction factor derived from the total neutron production rate in the skip is predicted to an accuracy of about 3% or less (section 11.1).

It is concluded that the original correction factor calculations overestimate the correction factors close to the sources and underestimate the correction factors distant from the sources. This enables an interpretation of the systematic errors due to calculation in terms

of the standard deviation resulting from the individual k-eff values given by the detectors (section 11.2).

Regarding the source locations, it was found that the use of sources in four central compartments rather than two, reduced the errors slightly (section 11.3). However, the use of two source positions was found to be adequate.

It is concluded that by spreading the sources axially in their tubes, it is possible to calculate the source mode fluxes required for the correction factor calculations by means of two-dimensional models (section 7.1.5).

Using the aggregate count rate from all detectors in the fuel regions resulted in correction factors which were least sensitive to the calculational method. It is concluded that other weightings of detector count rates result in correction factors which are significantly more sensitive to the calculational method (Chapters 9 and 10). It would probably be desirable to include an additional detector in the clusters containing the source tubes.

It is concluded that the optimum axial positioning of the detectors is on the midplane of the configuration. This minimises uncertainties arising from the positioning of the detector active material. The flux perturbations caused by the in-cluster detectors are concluded to be constant in all of the configurations with a common lattice pitch. This is due to the common local environment of the detectors, coupled with their small physical size (section 7.2.4).

The total error associated with the measured k-eff value of each configuration is concluded to be in the range of 1% to 2%. It consists of three components (section 11.3):

(i) The error due to calculational deficiencies in the correction factors, including the simplified axial representation;

(ii) The error arising from the reproducibility of the experimental count rates (section 6.1) and assembly asymmetries (section 6.4);

(iii) The error associated with the delayed neutron data used in the calibration of the reference configuration (section 6.7).

Regarding the predictions of the k-eff for the skip configurations, the following is concluded (section 11.4):

(i) Diffusion theory calculations probably underestimate k-eff for all of the configurations with sizeable water gaps between the fuel clusters and the boron-steel walls;

(ii) Transport theory calculations probably slightly overestimate the corresponding k-eff values.

The modified source multiplication measurements have thus advanced the study of the modified source multiplication technique in the following ways:

(i) They have provided a means of quantifying the calculational errors for well-subcritical assemblies in which the flux distribution is widely different from the flux distribution in the reference configuration;

(ii) They have indicated how the sources and detectors should be employed in such assemblies;

(iii) They have shown how to treat some subsidiary aspects of the calculations, notably the representation of three-dimensional calculations by two-dimensional calculations (Chapter 7), the calculation of perturbation factors for the detectors (Chapter 7) and the provision effectively of source mode calculations from eigenvalue mode calculations (Chapter 9);

(iv) They have shown the accuracy of standard calculational methods of predicting the k-eff of certain fuel storage arrays.

REFERENCES

Chapter 1

1 FLAGG, J. F. Chemical Reprocessing of Reactor Fuels. Nuclear Science and Technology Monographs. Academic Press. 1961.

2 HYDE, PERLMAN & SEABORG. The Nuclear Properties of the Heavy Elements II. Prentice Hall. 1964.

3 LEDERER SHERLEY et al. Table of Isotopes, Edition 7. Wiley and Sons. 1967.

4 BARTTELOT, C., HARRISON, S. Thorp Inlet and Receipt Building: Shielding Design Basis. ANS Report SHF-302/6. 1983.

5 FRANKLIN, B., STEVENSON, J. M. Notes in Support of the Lattice Certificate for the First Dimple Core in the CAGR Skip Insert. Internal Reactor Physics Division Note.

6 FRANKLIN, B. Notes on the Safety Calculations for 152, 137 and 52 Pin Clusters in the CAGR Skip Insert. Internal Reactor Physics Division Note.

7 KEAY, R., DUNN, M. A Criticality Assessment for 3.0 W/O Fuel in the CAGR Dismantler Facility Under Accident Conditions. Internal BNFL Report.

8 KEAY, R. The Sensitivity of System Reactivity to Major Criticality Parameters in the CAGR Dismantler Inlet Facility. Internal BNFL Report.

9 INGRAM, G. Dimple and its Current Experimental Programme. Paper for International Seminar on Criticality Studies Programs and Needs. Dijon, Sept 1983.

10 FRANKLIN, B. DIMPLE Technical Note.

11 MILLER, G. DIMPLE Technical Note.

Chapter 2

1 DUDERSTADT & HAMILTON. Nuclear Reactor Analysis, Ch. 4. Wiley & Sons. 1976.

2 DAVISON. Neutron Transport Theory, Ch. 2 and Appendix A. Oxford University Press. 1958.

3 DAVISON. Neutron Transport Theory, Ch. 3. Oxford University Press. 1958.

4 LEWINS, J. Importance: The Adjoint Function. Pergamon. 1965.

5 MIHALCZO et al. Subcriticality Measurements in the FFTF Test Facility. ORNL Internal Report.

6 WEINBERG, A., WIGNER, E. The Physical Theory of Neutron Chain Reactors. P330. University of Chicago Press. 1958.

7 DUDERSTADT & HAMILTON. Nuclear Reactor Analysis. P367. Wiley & Sons. 1976.

Chapter 3

1 INGRAM, G. Dimple and its Current Experimental Programme. Paper for International Seminar on Criticality Studies, Programs and Needs. Dijon. Sept 1983.

2 Status of LMFBR Safety Technology. Reactivity Monitoring in an LMFBR at Shutdown. OECD Report. March 1981.

3 STEVENSON, J. M. et al. Experience With Subcritical Monitoring in Large Subcritical Assemblies. International Symposium on Fast Reactor Physics. Aix en Provence. Sept 1979.

4 MARSHALL, J. Internal Communication.

5 FLEISCHMAN, R. M. Evaluation of the Modified Source Multiplication Technique for Subcritical Reactivity Assessments in FTR. US/UK Fast Reactor Exchange. HEDL-TME74-53. 1974.

6 MIHALCZO, J. T., et al. Recommendations for Implementation of Modified Source Multiplication Method for Reactivity Surveillance in Refuelling the FTR. US/UK Fast Reactor Exchange. ORNL/TM-5168. 1976.

7 PAXTON, H. C., KEEPIN, G. R. Criticality. The Technology of Nuclear Reactor Safety, Vol 1. 1964.

8 GREENSPAN. A Source Multiplication Reactivity. Nuclear Science and Engineering. 1975. (56:103).

9 MARSHALL, J. Internal Communication.

10 FRANKLIN, B. DIMPLE Technical Note.

Chapter 4

1 INGRAM, G. and JAMIESON, G. R. Safety Aspects of the Use of Cf252 Sources at Zebra. Internal AEE Winfrith Paper.

2 STEVENSON, J. M. Internal Communication.

3 20th Century Electronics Ltd. Neutron Counters for Reactor Control. Technical Bulletin. May 1960.

4 BROWN, W. et al. Measurements of Material Buckling and Detailed Reaction Rates in a Series of Low Enrichment UO_2 Fuelled Assemblies Moderated by Light Water. AEEW - R502. P7. Sept 1967.

5 McCALLIEN, G. W. J. SNAP 2-D; A Two-Dimensional Neutron Diffusion Code. TRG 1990(R). 1970.

6 HALSALL, M. J. LWR-WIMS, A Computer Code for Light Water Reactor Lattice Calculations. AEEW-R1498. 1982.

7 FRANKLIN, B. Internal Communication.

8 The Radiochemical Centre, Amersham. Californium 252 Neutron Sources. Technical Bulletin 72/7.

9 THORNTON, D. E. J. A Method for Speeding Convergence in Near Critical Source Calculations. Internal UKAEA Risley Memorandum.

Chapter 5

1 MARSHALL, J. DIMPLE Technical Note.

2 MARSHALL, J. DIMPLE Technical Note.

3 MADDISON, R. J. Delayed Neutron Data for Reactor Kinetics. Internal AEE Winfrith Report.

4 JAKEMAN, D. Physics of Nuclear Reactors. P96. English Universities Press. 1966.

5 FRANKLIN, B. M. and STEVENSON, J. M. Notes in Support of the Lattice Certificate for the First Dimple Core in the CAGR Skip Insert. Internal Reactor Physics Division Note.

6 WEINBERG, A., WIGNER, E. The Physical Theory of Neutron Chain Reactors. P487-488. University of Chicago Press. 1958.

7 STEVENSON, J. M. Internal Communication.

8 LATHROP, K. D. TWOTRAN - A FORTRAN Program for Two-Dimensional Transport. GA-8747. 1968.

Chapter 6

1 MILLER, G. DIMPLE Technical Note.

2 MILLER, G. DIMPLE Technical Note.

Chapter 7

1 HALSALL, M. J. LWR-WIMS, A Computer Code for Light Water Reactor Lattice Calculations. P182. AEEW - R1498. 1982.

Chapter 9

1 HALSALL, M. J. LWR-WIMS, A Computer Code for Light Water Reactor Lattice Calculations. P126. AEEW-R1498. 1982.

2 Ibid, P71.

3 Ibid, P198.

Chapter 10

1 DUDERSTADT & HAMILTON. Nuclear Reactor Analysis, P367. Wiley & Sons. 1976.

2 FRANKLIN, B. Internal Communication.

3 INGRAM, G. and JAMIESON, G. R. Safety Aspects of the Use of Cf 252 Sources at Zebra. Internal AEE Winfrith Paper.

Chapter 11

1 The Monk Code User's Manual. SRD Document. 1985.

2 HALSALL, M. J. and TAUBMAN, C. J. Adjustments to the WIMS Nuclear Data Library. AEEW-R1492. May 1982.

Chapter 12

1 Status of LMFBR Safety Technology. Reactivity Monitoring in an LMFBR at Shutdown. OECD Report. March 1981.

2 ACKERMANN, N. J. Subcriticality Measurements on an LMFBR. Nuclear Safety, Vol 12, No 6. Nov-Dec 1971.

3 Certificate of Measurement of a Californium Neutron Source. N110a. National Physical Laboratory. 1982.

4 INGRAM, G. Internal Communication.

5 BUDD, C. An Outline of the Use of Noise Analysis for Reactivity Measurements in Zero-Power Systems. Internal Reactor Physics Division Note.

Appendix A. Tables of Experimental and Calculated Count Rates

The corrected experimental count rates in Tables A.1 and A.2 were derived from the actual experimental count rates by dividing by factors to account for the relative detector sensitivity and source decay.

The detector sensitivities of the 5EB40 detectors inside the skip varied from values of 0.336 to 1.430, with an average value of 1.120. These values were all relative to a value of 1.000 for detector 3 at the beginning of the measurements.

The source decay factors were assigned a value of 1.000 at the beginning of the measurements. They reached a minimum value of 0.7 for the count rates in the 221 pins per compartment, centred configuration with the alternative source positions. This configuration was built approximately six months after the beginning of the measurements.

Table A.1 Corrected Experimental Count Rates: Standard Source Positions

Detector Environment	Detector Position	Configuration and Corrected Experimental Count Rate (counts sec^{-1})						
		196/49 (REF)	196/33	112/76 (CTD)	112/76 (G4)	112/76 (CC)	112/76 (CCD)	221/76 (CTD)
Centre of Cluster	8 alt 1	6116.7	773.04	138.01	83.83	194.85	433.20	44.49
	4 alt 4	4135.4	525.69	97.83	138.45	108.98	159.20	31.17
	3 alt 5	3922.0	522.66	96.75	134.04	106.66	158.91	30.13
	3 alt 1	3484.1	331.54	34.92	30.64	41.70	73.11	10.31
	4 alt 5	3201.6	320.90	33.44	31.17	40.49	70.67	10.17
	5 alt 4	3433.7	329.46	34.88	70.61	41.21	71.60	10.72
	5 alt 5	3249.8	323.90	34.39	67.28	41.54	69.05	10.19
	4 alt 1	2964.4	224.97	16.02	17.45	21.99	48.80	4.141
	8 alt 4	1715.0	117.57	5.980	8.028	6.457	12.97	1.573
	8 alt 5	1619.3	116.25	6.031	8.293	6.457	12.53	1.605
	5 st	1758.9	123.49	6.337	11.12	6.919	13.51	1.662
Half-way	8 alt 2	6101.9	881.80	180.06	226.04	260.73	615.04	75.14
	3 alt 2	3542.9	325.49	32.91	30.90	40.75	75.94	11.53
	4 alt 2	3329.1	270.05	20.41	22.10	30.03	66.13	6.956
	5 alt 2	2228.0	166.25	9.306	16.61	9.671	19.02	3.181
Corner of Compartment	8 st	3846.2	658.86	397.57	232.06	532.23	520.70	357.12
	3 alt 3	2995.0	378.59	139.54	124.47	141.52	237.79	118.70
	3 alt 4	1183.7	118.71	38.67	30.64	41.78	68.79	28.25
	8 alt 3	2915.2	296.16	103.10	59.50	167.04	399.10	77.55
	3 st	2372.4	211.41	51.99	45.46	57.09	112.14	34.80
	4 st	2316.2	204.67	46.77	41.60	63.23	141.75	35.52
	4 alt 3	2042.6	170.97	38.14	44.74	44.15	92.86	26.78
	5 alt 1	1941.9	162.63	25.74	37.12	23.76	48.08	18.73
	5 alt 3	704.8	52.00	9.686	14.12	8.574	16.16	5.927
Out of Skip	7 st	12728.0	1043.1	87.24	62.03	76.74	131.37	58.42
	6 st	25044.6	1754.4	92.54	126.59	76.71	142.57	58.70
	9 st	27054.9	1820.1	67.35	84.84	52.89	101.50	41.63
	2 st	1138.0	85.87	3.239	4.186	2.607	4.940	2.034
	1 st	1749.7	119.20	4.914	4.778	4.174	7.693	3.165
Total count rate in fuel clusters		50788	5354	747.3	896.5	958.5	1900	253.0

Table A.2 Corrected Experimental Count Rates: Alternative Source Positions

Detector Environment	Detector Position	Configuration and Corrected Experimental Count Rate (Counts sec^{-1})			
		196/48 (REF)	196/33	112/76 (CTD)	221/76 (CTD)
Centre of Cluster	3 alt 2	2943.1	493.0	97.94	31.87
	4 alt 1	2790.7	586.7	129.52	42.44
	3 alt 3	3286.2	326.8	34.11	10.47
	8 alt 3	3056.9	311.0	33.96	10.06
	5 alt 1	1587.7	250.3	34.32	10.20
	3 alt 1	2536.8	143.9	6.420	1.315
	4 alt 3	2092.4	84.37	1.907	0.4546
	5 alt 3	1207.6	47.52	0.982	0.2348
Corner of Compartment	8 alt 2	3482.5	906.0	939.39	836.2
	5 alt 2	1785.3	355.7	153.19	126.8
	8 alt 1	2691.7	222.1	45.84	33.62
	4 alt 2	1253.2	56.43	3.230	1.994
Out of Skip	7 alt 3	10601	1411.9	211.32	158.3
	6 alt 1	21882	3081.7	340.55	244.4
	7 alt 1	9093.6	460.9	17.80	11.24
	6 alt 3	16304	673.6	13.98	8.143
	9 st	22221	3425.7	303.05	218.4
	2 st	1008.6	152.5	14.37	10.28
Centre-of-Cluster Combinations	3 alt 2, 3 alt 1	5479.9	636.9	104.18	33.19
	4 alt 1, 4 alt 3	4883.1	671.1	131.43	42.90
	5 alt 1, 5 alt 3	2795.3	297.8	35.30	10.43
Corner Combinations	8 alt 1, 8 alt 2	6174.2	1128.0	985.23	869.84
	5 alt 2, 4 alt 2	3038.5	412.1	156.42	128.78
Out-of-Skip Combinations	7 alt 1, 7 alt 3	19695	1872.7	229.12	169.51
	6 alt 1, 6 alt 3	38186	3755.2	354.53	252.51

Table A.3 Calculated Count Rates: Standard Source Positions

Detector Environment	Detector Position	Configuration and Corrected Experimental Count Rate (counts sec^{-1})						
		196/49 (REF)	196/33	112/76 (CTD)	112/76 (G4)	112/76 (CC)	112/76 (CCD)	221/76 (CTD)
Centre of Cluster	8 alt 1	1570.4	248.6	29.72	17.37	43.75	108.7	10.33
	4 alt 4	1026.3	170.5	22.24	32.59	23.76	36.90	7.852
	3 alt 5	1026.3	170.5	22.24	32.79	23.76	36.90	7.852
	3 alt 1	851.0	109.0	7.053	6.450	8.607	16.39	2.294
	4 alt 5	851.0	109.0	7.053	6.450	8.607	16.39	2.294
	5 alt 4	851.0	109.9	7.053	6.450	8.607	16.39	2.294
	5 alt 5	851.0	109.0	7.053	6.450	8.607	16.39	2.294
	4 alt 1	759.3	76.65	3.007	3.716	4.481	10.37	0.8740
	8 alt 4	414.6	38.83	1.103	1.628	1.225	2.709	0.3092
	8 alt 5	414.6	38.83	1.103	1.628	1.225	2.709	0.3092
	5 st	414.6	38.83	1.103	1.629	1.225	2.709	0.3092
Half-way	8 alt 2	1586.8	289.3	44.83	45.72	61.50	160.31	20.96
	3 alt 2	871.6	108.8	7.142	6.535	8.921	18.18	2.857
	4 alt 2	782.4	94.50	4.485	5.144	6.345	16.27	1.759
	5 alt 2	553.3	55.38	1.839	3.421	1.860	4.140	0.7133
Corner of Compartment	8 st	1135.9	243.0	117.40	66.87	154.48	158.0	105.94
	3 alt 3	833.5	140.5	40.96	37.51	40.89	73.55	36.46
	3 alt 4	326.9	44.40	9.974	8.478	11.19	19.26	7.856
	8 alt 3	841.7	112.26	26.45	14.67	45.33	120.37	20.75
	3 st	623.7	75.39	12.53	11.34	14.44	31.41	9.774
	4 st	698.6	82.66	11.75	11.43	16.55	43.12	9.013
	4 alt 3	605.2	68.49	9.401	12.55	11.32	27.57	7.108
	5 alt 1	518.3	56.83	5.904	10.15	5.702	12.92	4.457
	5 alt 3	204.8	20.86	2.233	4.068	2.134	4.37	1.573
Out of Skip	7 st	10814	1231.6	59.59	44.02	54.05	99.85	44.02
	6 st	21124	2300.7	60.02	100.29	52.35	106.69	41.11
	9 st	24826	2344.4	46.54	71.85	38.00	81.21	30.39
	2 st	27693.0	759.6	13.55	20.69	10.93	23.37	8.795
	1 st	1949.2	167.5	3.458	3.723	2.794	5.967	2.246

Table A.4 Calculated Count Rates: Alternative Source Positions

Detector Environment	Detector Position	Configuration and Corrected Experimental Count Rate (Counts sec^{-1})			
		196/48 (REF)	196/33	112/76 (CTD)	221/76 (CTD)
Centre of Cluster	3 alt 2	708.5	149.10	22.19	7.860
	4 alt 1	683.5	182.70	29.04	10.13
	3 alt 3	769.6	98.79	7.047	2.294
	8 alt 3	769.6	98.79	7.047	2.294
	5 alt 1	359.4	74.37	6.769	2.217
	3 alt 1	601.7	42.76	1.135	0.3172
	4 alt 3	523.5	25.47	0.3188	0.0774
	5 alt 3	286.4	13.59	0.1448	0.0343
Corner of Compartment	8 alt 2	957.9	295.8	257.20	231.01
	5 alt 2	454.9	114.9	40.57	36.22
	8 alt 1	805.9	80.49	11.79	9.027
	4 alt 2	360.1	19.88	0.7231	0.4576
Out of Skip	7 alt 3	8909.4	1599.6	161.80	126.37
	6 alt 1	20487	3809.9	262.91	201.74
	7 alt 1	76296	498.3	10.76	6.995
	6 alt 3	16741	843.9	9.017	5.310
	9 st	21394	4188.8	250.92	187.03
	2 st	6642.0	1360.3	73.15	54.16
Centre of Cluster Combinations	3 alt 2, 3 alt 1	1310.2	191.9	23.33	8.180
	4 alt 1, 4 alt 2	1207.0	208.2	29.36	10.14
	5 alt 1, 5 alt 3	645.8	87.96	6.914	2.251
Corner Combinations	8 alt 1, 8 alt 2	1763.8	376.3	268.99	240.04
	5 alt 2, 4 alt 2	815.0	134.8	41.29	36.68
Out of Skip Combinations	7 alt 1, 7 alt 3	16534	2098.0	172.56	133.36
	6 alt 1, 6 alt 3	37228	4653.8	271.93	207.00

Appendix B

The reactivity of the reference configuration was also determined using the summation:

$$\rho_{reference} = \overline{d\rho/dB^2} \times \Delta B^2, \qquad (B1)$$

where B^2 is the axial buckling and $\overline{d\rho/dB^2}$ is the average value of $d\rho/dB^2$ over the bucklings between the critical water height and the water height of the reference configuration. This determination is summarised in Table B.1. Extrapolation distances of both 5.5cm and 6.5cm have been used to show the sensitivity of the result to the extrapolation distance.

It should be noted that:

$$d\rho/dB^2 = d\rho/dh \times dh/dB^2. \qquad (B2)$$

Since $B^2 = (\pi/h)^2$, where h includes the top and bottom extrapolation distances,

$$dB^2/dh = -2\pi^2/h^3, \qquad (B3)$$

so $dh/dB^2 = -h^3/2\pi^2$.

Table B.1 Determination of the Reactivity of the Reference Configuration

Water Height of fuel pins (cm)	$d\rho/dh$ (cm^{-1})	λ = 5.5cm		λ = 6.5cm	
		B^2 (cm^{-2})	$d\rho/dB^2$ (cm^2)	B^2 (cm^{-2})	$d\rho/dB^2$ (cm^2)
52.26 (critical)	0.001960	2.466×10^{-3}	-25.14	2.317×10^{-3}	-27.60
50.52	0.002108		-24.87		-27.40
49.96	0.002239		-25.69		-28.31
49.00 (reference)	-	2.742×10^{-3}	-	2.568×10^{-3}	-
		$\Delta B^2 = 2.76 \times 10^{-4} cm^{-2}$		$\Delta B^2 = 2.51 \times 10^{-4} cm^{-2}$	
		$\overline{d\rho/dB^2} = -25.23 cm^2$		$\overline{d\rho/dB^2} = -27.77 cm^2$	
		$\rho_{ref} = -0.000696$		$\rho_{ref} = -0.00697$	

It is noted that the function $d\rho/dB^2$ is less sensitive to water height than $d\rho/dh$. This is because the k-eff and hence the reactivity is directly related to the buckling through the approximate relation:

$$k\text{-eff} = k_\infty / (1 + M^2 B^2). \qquad \text{(B4)}$$

The above values for the reference configuration reactivity of -0.00696 -0.00697 are 2% less than the value of -0.00713 in section 5.1.2, which is good agreement, taking into account the error of 1.5% in the determination of the area under the $d\rho/dh$ curve (Table 5.3).